Metal/insulating transitions in V O systems probed in situ and at the nanoscale by monochromated electron spectromicroscopy

El Khalil Ibrahim Koita

▶ **To cite this version:**

El Khalil Ibrahim Koita. Metal/insulating transitions in V O systems probed in situ and at the nanoscale by monochromated electron spectromicroscopy. Strongly Correlated Electrons [cond-mat.str-el]. Université Paris-Saclay, 2023. English. NNT : 2023UPASP007 . tel-04413705

HAL Id: tel-04413705

https://theses.hal.science/tel-04413705v1

Submitted on 24 Jan 2024

HAL is a multi-disciplinary open access archive for the deposit and dissemination of scientific research documents, whether they are published or not. The documents may come from teaching and research institutions in France or abroad, or from public or private research centers.

L'archive ouverte pluridisciplinaire **HAL**, est destinée au dépôt et à la diffusion de documents scientifiques de niveau recherche, publiés ou non, émanant des établissements d'enseignement et de recherche français ou étrangers, des laboratoires publics ou privés.

université PARIS-SACLAY

Metal/insulating transitions in V_2O_3 systems probed *in situ* and at the nanoscale by monochromated electron spectromicroscopy

Transitions métal/isolant dans les systèmes de V_2O_3 sondées in situ et à l'échelle nanométrique par spectromicroscopie électronique monochromatée

Thèse de doctorat de l'université Paris-Saclay

École doctorale n° 564, Physique en Île-de-France (EDPIF)
Spécialité de doctorat: Physique
Graduate School : Physique. Référent : Faculté des sciences d'Orsay

Thèse préparée au **Laboratoire de Physique des Solides** (Université Paris-Saclay, CNRS), sous la direction d'**Odile STÉPHAN**, Professeure, et le co-encadrement de **Laura BOCHER**, Chargée de recherche

Thèse soutenue à Paris-Saclay, le 23 Janvier 2023, par

El Khalil Ibrahim KOITA

Composition du jury

Membres du jury avec voix délibérative

Philippe LECOEUR Professeur, Université Paris-Saclay (Centre de Nanosciences et Nanotechnologies)	Président
Claire COLIN Maîtresse de Conférences (HDR), Université Grenoble Alpes (Institut Néel)	Rapporteure & Examinatrice
Philippe MOREAU Professeur, Université de Nantes (Institut des Matériaux de Nantes)	Rapporteur & Examinateur
Etienne JANOD Directeur de recherche, Institut des Matériaux de Nantes	Examinateur

THESE DE DOCTORAT

NNT : 2023UPASP007

université PARIS-SACLAY | ÉCOLE DOCTORALE Physique en Île-de-France (PIF)

Titre: Transitions métal/isolant dans les systèmes de V_2O_3 sondées *in situ* et à l'échelle nanométrique par spectromicroscopie électronique monochromatée

Mots clés: V_2O_3, spectroscopie de perte d'énergie des électrons, 4D-STEM nanodiffraction, classification en K-moyennes, microscopie *in situ*, phase paramagnétique isolante

Résumé: Ce travail de thèse en microscopie électronique vise à répondre aux récentes préoccupations portant sur les mécanismes structuraux et/ou électroniques associés à la séparation de phase électronique observée dans le V_2O_3 à des résolutions spatiales allant jusqu'à quelques dizaines de nanomètre. La microscopie électronique, grâce aux récents développements instrumentaux permettant d'investiguer les propriétés électroniques et structurales à des résolutions spatiales de l'ordre du nanomètre, se trouve être ici l'outil adéquat pour répondre à de telles problématiques.

Dans un premier temps, nous avons étudié à température ambiante, les propriétés locales structurales, électroniques et chimiques dans un film mince de V_2O_3 sur un substrat de Al_2O_3. Nous avons mis en évidence dans le film, des inhomogénéités structurales caractérisées par des variations locales du paramètre de maille dans le plan, entre 4.946 Å et 4.988 Å. Nous avons également montré en spectroscopie des pertes d'énergie des électrons (EELS), par l'application de techniques telles que la classification en K-moyennes, des inhomogénéités électroniques s'étendant sur des domaines d'environ 50 nm. Ces observations structurales et électroniques suggèrent la coexistence de la phase paramagnétique métallique (PM) et d'une phase de grand volume analogue à la phase paramagnétique isolante (PI), induite ici par les contraintes imposées par le substrat. Nous avons également mis en évidence des propriétés électroniques homogènes dans la région interfaciale, même si des variations de proportion en vanadium sont observées dans certaines régions à l'interface. Ces résultats suggèrent donc de très fortes corrélations entre degrés de liberté électronique et structural dans les films minces de V_2O_3.

Dans un second temps, nous avons étudié, *in situ*, les mécanismes de nucléation structuraux et/ou électroniques associés à la transition en température entre les phases PM et antiferromagnétique isolante (AFI) dans les monocristaux de V_2O_3. Nous avons mis en évidence des mécanismes de transition différents pendant le refroidissement (de PM vers AFI) et pendant le chauffage (de AFI vers PM). Pendant le refroidissement, nous observons une transition électronique abrupte en spectroscopie EELS et la coexistence de structures monoclinique et hexagonale en 4D-STEM nanodiffraction et microdiffraction. L'observation de la phase hexagonale isolante à basse température suggère la présence d'une phase analogue à la phase PI, comme le confirme d'ailleurs les sauts de paramètre de maille observés à la transition. Cette phase serait ici induite par les contraintes uniaxiales imposées par les contacts en platine qui maintiennent l'échantillon, pendant cette transition de phase qui est accompagnée d'une augmentation abrupte du volume. Pendant le chauffage, nous observons la propagation d'une paroi de domaines séparant les régions PM et les régions où coexistent la phase AFI et la phase similaire à la phase PI. L'investigation de la région interfaciale révèle encore une fois la présence d'une phase analogue à la phase PI, précurseur à la phase PM. Ces résultats suggèrent les degrés de liberté électroniques comme degrés de liberté pilotes de cette transition de phase.

université PARIS-SACLAY | ÉCOLE DOCTORALE Physique en Île-de-France (PIF)

Title: Metal/insulating transitions in V_2O_3 systems probed *in situ* and at the nanoscale by monochromated electron spectromicroscopy

Keywords: V_2O_3, electron energy-loss spectroscopy, 4D-STEM nanodiffraction, K-means clustering, *in situ* microscopy, paramagnetic insulating phase

Abstract: This thesis in electron microscopy aims to address recent concerns about the structural and/or electronic mechanisms associated with the observed electronic phase separation in V_2O_3 at spatial resolutions down to a few tens of manometer. Electron microscopy, thanks to recent instrumental developments allowing the investigation of electronic and structural properties at nanometer spatial resolutions, is the appropriate tool to address such issues.

In the first step, we studied, at room temperature, the local structural, electronic, and chemical properties of a V_2O_3 thin film on an Al_2O_3 substrate. We have highlighted structural inhomogeneities in the film, characterized by local variations in the in-plane lattice parameter between 4.946 Å and 4.988 Å. We have also shown in electron energy-loss spectroscopy (EELS), by applying techniques such as K-means clustering, electronic inhomogeneities extending over domains of about 50 nm. These structural and electronic observations suggest the coexistence of the paramagnetic metallic phase (PM) and a large volume phase similar to the paramagnetic insulating phase (PI), induced here by the strains imposed by the substrate. We also found homogeneous electronic properties in the interfacial region, although variations in the vanadium proportion are observed in some regions at the interface. These results, therefore, suggest very strong correlations between electronic and structural degrees of freedom in V_2O_3 thin films.

In a second step, we studied, *in situ*, the structural and/or electronic nucleation mechanisms associated with the temperature-induced transition between the PM and antiferromagnetic insulating (AFI) phases in V_2O_3 single crystals. We have highlighted different transition mechanisms during cooling (from PM to AFI) and heating (from AFI to PM). During cooling, we observe an abrupt electronic transition in EELS spectroscopy in the low-loss region and the coexistence of monoclinic and hexagonal structures in 4D-STEM nanodiffraction and 4D-STEM microdiffraction. The observation of the insulating hexagonal phase at low temperatures suggests the presence of a phase analogous to the PI phase, as confirmed by the jumps in lattice parameter observed at the phase transition. This phase would be induced here by the uniaxial strains imposed by the platinum contacts that hold the sample during the phase transition from PM to AFI, which is accompanied by an abrupt increase in volume. During heating, we observe the propagation of a domain wall separating the PM regions and the regions where AFI and PI-like phases coexist. The investigation of the interfacial region again reveals the presence of a phase analogous to PI, precursor to the PM phase. These results suggest the electronic degrees of freedom as driving degrees for this phase transition.

Acknowledgements

J'aimerais d'emblée remercier mes rapporteurs, à savoir Claire Colin et Philippe Moreau, pour le temps consacré à la lecture et l'évaluation de mon travail. J'aimerais également remercier Etienne Janod et Philippe Lecoeur pour leur participation à mon jury de thèse. Je souhaite témoigner à chacun d'entre eux ma reconnaissance pour la qualité de nos échanges, me permettant notamment de porter un regard plus profond sur le travail que j'ai eu à réaliser.

Je souhaite évidemement remercier mes encadrantes, Laura Bocher et Odile Stéphan, qui ont su m'accompagner et me guider pendant toutes ces années, tant sur le plan scientifique que personnel. La bonne humeur et la bonne ambiance qu'elles ont su dégager et surtout leurs patiences à mon égard m'a permis de surmonter les nombreuses difficultés pendant cette thèse. Je souhaite leur témoigner toute ma gratitude.

Je voudrais également dire merci à toute l'équipe STEM, avec laquelle j'ai eu à passer de très bons moments. Je ne pense pas qu'il puisse exister un groupe aussi chaleureux que ce dernier. Je souhaite remercier notamment Luiz Galvao Tizei, Nathalie Brun, Jean-Denis Blazit, Marcel Tence, Steffi Woo, Mathieu Kociak et bien d'autres encore, pour leurs aides précieuses dans le cadre de mes travaux de thèse. Je remercie tous les doctorants de l'équipe (Malo, Maeva, Jassem, Chia-Ping, Fuhui, Laura, Yves, Noemie, Marc, désolé pour les oublis.....), mais également Steffi et Jean-Denis pour tous ces moments de détente passés en leur compagnie. Je n'oublie surtout pas Michele Amato, membre permanent de l'équipe, qui a bien voulu m'accueillir dans son bureau et avec qui j'ai eu des discussions très sympathiques tant sur le plan scientifique que celui de la vie quotidienne.

J'aimerais également dire un grand merci à Adrien Teurtrie, ancien doctorant dans l'équipe et qui a participé à l'encadrement de mon stage de Master 1. Il a su susciter encore plus en moi cette passion pour la microscopie électronique, et pour cela je souhaite lui témoigner toute ma gratitude. Je lui souhaite plein de réussites dans ses futurs projets.

Je voudrais aussi remercier toute l'équipe PMN de l'institut des matériaux de Nantes, particulièrement Laurent Cario, Benoit Corraze et Julien Tranchant pour ces nombreuses discussions scientifiques, qui m'ont permis d'en savoir un peu plus sur le V_2O_3.

Enfin, je voudrais dire un grand merci à toute ma famille (ainsi qu'au Professeur Atheba) pour leur soutien constant tout au long de mon cursus académique.

Contents

List of Abbreviations

AFI	antiferromagnetic insulating phase
APB	antiphase domain boundary
ARPES	angle-resolved photoemission spectroscopy
BF	bright field
CLC	center of the Laue circle
DFT	density functional theory
DMFT	dynamical mean field theory
EELS	electron energy-loss spectroscopy
ELNES	energy-loss near-edge structure
EXAFS	x-ray absorption fine structure
FFT	fast Fourier transform
FIB	focused ion beam
FWHM	full width at half maximum
GPA	geometric phase analysis
HAADF	high angle annular dark field
IMT	insulator-to-metal transition
LDA	local density approximation
LHB	lower Hubbard band
MIT	metal-to-insulator transition
MLLS	multiple linear-least square fitting
NMF	non-negative matrix factorization
PCA	principal component analysis
PDF	magnetic pair distribution function
PEEM	photoemission electron microscopy
PI	paramagnetic insulating phase
PSF	point spread function
QOCM	quadrupole-octupole coupling mode

R-L	Richardson-Lucy
SNR	signal-to-noise ratio
Spim	spectrum-image
STEM	scanning transmission electron microscopy
UHB	upper Hubbard band
VCA	vertex component analysis
XAFS	x-ray absorption fine structure
XAS	x-ray absorption spectroscopy
XRD	x-ray diffraction
ZLP	zero loss peak

Chapter 1

Introduction

Strongly-correlated materials exhibit multiple physical properties due to the significant electronic correlations that take place within. In these systems, electron-electron interactions are the key ingredient [1], through which the application of external stimuli, such as temperature (T), pressure (P), or chemical doping, can access, for instance, metal-insulator transitions (MITs) within these materials. V_2O_3, a prototypical system of this class of correlated-oxide materials, is no exception to this rule. This model system presents a very rich phase diagram where two types of MITs, namely that between the paramagnetic metallic (PM) and paramagnetic insulating (PI) phases on the one hand, and between the PM and antiferromagnetic insulating (AFI) phases on the other hand, are particularly illustrated [2–4]. These transitions are associated with abrupt changes in resistivity, respectively, of about two and seven orders of magnitude. Interesting functions exploitable in resistive switching devices, for instance, could thus arise from these MITs, notably from the transition between PM and PI, which can occur at room temperature. The understanding of V_2O_3 physical properties could therefore be of great interest as regards the potentialities of this system.

Competitive structural and/or electronic mechanisms associated with phase transitions in V_2O_3 have emerged enormously in recent years at spatial resolutions ranging from micrometers to tens of nanometers. For the first time, Lupi *et al.* [5] have shown in T-dependent photoemission, the coexistence of micrometric insulating/metal domains in the PM phase of the chromium-doped V_2O_3 single crystal, during the T-induced transition between PM and PI. The T-activated transition from PM to AFI, often neglected because of its cracking issues (due to the abrupt increase in volume at the transition),

has also recently been the subject of intense investigations, particularly in thin films. The observations made in micro-XRD and nano-IR [6] (spatial resolution of about 25 nm) also indicate electronic phase separation during this phase transition between PM and AFI. However, as we have noted, the experimental techniques used cannot provide direct answers to questions related to the local mechanisms governing the formation of the structural and/or electronic domains, which are strongly involved in this transition [6, 7] and could be at the origin of these observations. Indeed, these domains can arise, for example, from structural defects or chemical clustering, all mechanisms ranging from the nanometer to the angström. The local modulations of electronic or atomic configurations that govern macroscopic physical properties in multiferroic [8, 9], magnetoelectric [10] or thermoelectric [11] systems illustrate this perfectly. It is also difficult to study, through these techniques, the local interfacial mechanisms involved in this temperature-induced transition when we know that the strain states generated in V_2O_3 thin films by Al_2O_3 substrates, for instance, can annihilate the electronic transition from PM to AFI [12]. These observations raise, therefore, many questions about the nucleation mechanisms of the phase transition between PM and AFI, which are still poorly understood in thin films and single crystals at a very local scale. Finally, we are entitled to ask the following questions: How can the evolution of electronic and structural properties during this transition between PM and AFI be precisely probed and correlated, when we know that the nucleation mechanisms are generally of the order of the nanometer or even the angström? What are the strain states at the interface or globally in V_2O_3 thin films? How does strain locally influence the structural and electronic properties of the system? What role can stoichiometry play in these potential strained systems? These are, therefore, some major questions in thin films but also in single crystals (particularly concerning the transition nucleation mechanisms), which we must strive to answer.

This thesis project is explicitly dedicated, within this framework , to studying V_2O_3 structural and electronic properties by electron microscopy. Aberration-corrected scanning transmission electron microscopes (STEMs) equipped with monochromators allow today to efficiently answer such problems in nanomaterials [13]. Indeed, monochromated experiments in electron energy-loss

spectroscopy (EELS) with ultra-high spectral resolution (down to a few meV) and spatial resolution (from the nanometer to the angström) allow access to the local optical, electronic, and chemical properties of the probed materials. In addition, imaging and electron diffraction techniques are also able to provide information about the materials's structural properties at spatial resolutions of a few nanometers or even angström. These experimental techniques, which can be coupled within the electron microscope, are therefore relevant for investigating the local correlations between structural and electronic properties in thin films or single crystals. Furthermore, thanks to recent instrumental developments concerning cryo sample holders in STEMs [14, 15], we can perform *in situ* experiments at variable temperatures while ensuring high stability and spatial resolution ranging from nanometer to angström. All these findings concerning the evolution of the system's electronic and structural properties can also be mapped using data analysis techniques such as non-negative matrix factorization (NMF), or more recently clustering, applied to electron microscopy experiments. These technological advances should therefore allow us to probe and map the intrinsic local structural and/or electronic mechanisms associated with the phase transition between PM and AFI. The STEM microscopes used in the present investigations, namely the NION ULTRASTEM and especially the NION CHROMATEM fitted with the HennyZ cryo sample holder [15] and which presents all the above characteristics, are unique tools, capable of providing answers to the concerns raised in this thesis.

The samples studied in this project, namely V_2O_3 thin films deposited on Al_2O_3 substrates and thin lamellas from V_2O_3 single crystals, come, respectively, from collaborations with KU Leuven and IMN (Nantes).

This manuscript is presented as follows:

In chapter 2, we start by presenting the strongly correlated systems to which V_2O_3 belongs, the Mott-Hubbard transition, and the dynamical mean field theory (DMFT), which explain some physical properties of this material. Then, we present the phase diagram of this system and the major findings, such as the recent works on the electronic structure, the electric field-driven and the photoinduced experiments.

In Chapter 3, we present in detail experimental techniques such as EELS

spectroscopy and 4D-STEM nanodiffraction or microdiffraction. We also present the tools such as geometric phase analysis (GPA) or K-means clustering, which we used to process and analyze the acquired data.

In chapter 4, we first discuss the local structural properties investigated by GPA, in a V_2O_3 thin film on an Al_2O_3 substrate at room temperature. We then discuss, still at room temperature, the local electronic properties investigated by EELS spectroscopy, which we then correlate with the structural properties. Finally, we investigate the local chemical properties of V_2O_3, mainly in the interfacial region. We also discuss in this chapter the structural and electronic interfacial properties in V_2O_3 thin films.

In chapter 5, we present the local evolution of electronic (in EELS spectroscopy) and structural (in 4D-STEM nanodiffraction and microdiffraction) properties in V_2O_3 single crystals during the phase transition between PM and AFI. We discuss correlations between these two degrees of freedom and the role of strain on the local mechanisms governing this phase transition. We also discuss the degrees of freedom that drive this phase transition.

In Chapter 6, we finally present the conclusions of our work and outline the perspectives for future studies.

Chapter 2

V_2O_3, a strongly-correlated material

2.1 . Introduction

Studied for several decades, vanadium sesquioxide or V_2O_3 has been the subject of constant debate and remarkable discoveries. The chapter aims to revisit this system and present its main physical properties, which are essential for understanding the investigations carried out in this thesis.

Firstly, the strongly correlated systems to which V_2O_3 belongs, the Mott-Hubbard transition, and the Dynamical Mean Field Theory (DMFT) which account for some essential properties in this system, will be introduced. We will present, in the following, the rich phase diagram of V_2O_3 and its different associated phases. Finally, we will discuss in detail these phase transitions and the main findings in V_2O_3.

2.2 . Strongly-correlated systems, Mott-Hubbard transition and DMFT

At T = 0 K, an insulator can be clearly distinguished from a metal by its zero electrical conductivity. For Temperatures above 0 K, where the conductivity still prevails, the distinction between these two entities, for analytical purposes, can be more or less made by a significant difference in the order of magnitude of conductivity. In this case, we can use the terms "good" or "bad" electrical conductors, respectively for metals or insulators [16, 17].

Electrical conductivity is determined by electronic transport, which in turn depends on the ionic potential, the coulomb interaction, and any eventual external electric or magnetic fields applied [16, 18]. In the absence of or

under weak external fields, two main classes of insulators emerge. We observe a first family of insulators resulting from the interaction between ions and electrons. Band insulators, where the electrons are taken as independent and interact with the periodic ionic potential, are a typical example. The second family, which is of particular interest in the context of this PhD thesis, namely Mott insulators, results from the strong interaction between electrons. We dissociate among Mott insulators, Mott-Hubbard insulators where the insulating state involves neither symmetry breaking nor long-range spin or charge order, and Mott-Heisenberg insulators involving these long-range orders [16, 18].

In strongly correlated systems, where we can classify Mott insulators, electron-electron interactions are relatively important and play a decisive role in describing the material's physical properties [1]. Many transition metal oxides such as NiO, VO_2, or even V_2O_3, which is the main subject of this study, belong to this class. In these d-electron systems, the radius of d-orbitals is relatively small compared to the lattice constants. As a result, the hybridization of transition metal d-orbitals via overlapping with oxygen ligands generally leads to a very narrow bandwidth, where electrons are confined [18, 19]. Significant electronic correlation effects can thus occur in these materials.

Despite the complexity of predicting the behavior of these systems due to electronic correlations, theoretical models exist to account for the metal-insulator transitions that some materials in this class may undergo. In the case of V_2O_3 considered as a canonical Mott system and exhibiting a Mott-Hubbard metal-insulator transition (MIT) which will be discussed in the following sections, the Hubbard model is seen as an exciting point for the theoretical description of this system.

2.2.1 . Hubbard model

The Hamiltonian in the Hubbard model is given by the following expression:

$$H = \sum_{<ij>\sigma} (t_{ij} c^{+}_{i\sigma} c_{j\sigma} + h.c.) + U \sum_{i} (n_{i\uparrow} n_{i\downarrow}) \tag{2.1}$$

In this Hamiltonian, t_{ij} represents the transfer or overlapping integral between sites i and j. If they are nearest-neigbor sites, $t_{ij} = -t$; otherwise

$t_{ij} = 0$. $c^{+}_{i\sigma}$ and $c_{j\sigma}$ correspond respectively to the creation and annihilation operators of an electron of spin σ on sites i and j; $h.c.$ represents the Hermitian conjugate; U corresponds to the electron-electron coulomb repulsion; $n_{i\uparrow}$ and $n_{i\downarrow}$ represent respectively the spin up and spin down populations on site i.

The Hubbard model [20–22], which is a relatively simplified view where each on-site atom has only one orbital, physically reflects a competition between kinetic energy (t) or bandwidth[1] (W) and Coulomb repulsion (U); as shown in figure 2.1 . The first term which describes this model represents the hopping of electrons between the nearest-neighbors atomic sites, attributing an itinerant behavior to these latter. The second term reflects the Coulomb interaction between the two electrons of opposite spins on the same atomic site, indicating the localized character of these electrons. The physics described by this hamiltonian can therefore be summarised by the relative electron correlation strength, represented here by the U/W or W/U ratio.

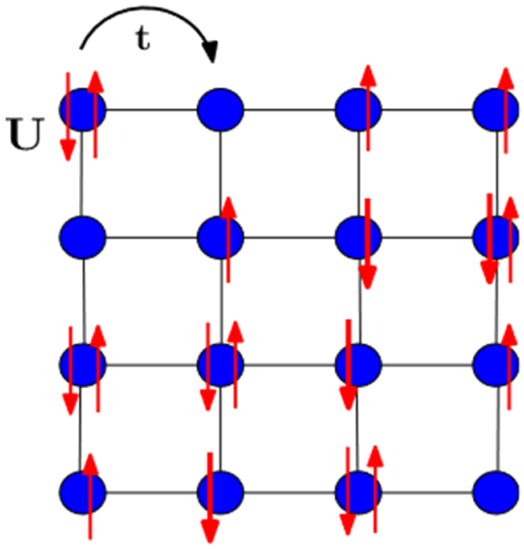

FIGURE 2.1: Representation on a square lattice of Hubbard model. The interaction between two electrons on the same site is given by U. Electrons can also move towards a nearest-neigbor site with an amplitude t. The figure is adapted from [23].

[1] $W = 2zt$; where z is the number of nearest-neighbors atomic sites.

Two exact limits exist for this model. We distinguish the band limit when $(U/W)\sim 0$. In this configuration, where the kinetic energy term largely predominates, there are no interactions, and the electrons can be described as independent, as in the classical band theory [17]. The system becomes metallic, obviously when the band is not entirely filled (in a half-filled system for example). Conversely, we are in the atomic limit when the $(W/U)\sim 0$. In this situation, where the Coulomb interaction term becomes predominant, the double occupation of an atomic site amounts to increasing its energy level by U. For a half-filled system (one electron per site), the minimization of the energetically costly Coulomb term U leads to the hopping suppression between nearest-neighbors sites and to the single occupation of these latter [17]. The Mott insulator state therefore appears in the half-filled system, when the electronic correlation term becomes very large compared to the kinetic energy one.

The Hubbard model gives, in general, a simple overview of the electronic states related to the Mott transition. Other ingredients such as electronic or lattice structure, or even orbital degeneracy, for example, have to be taken into account to properly model the behavior of real materials, which is not the case of this model [18, 24, 25].

Moreover, in the intermediate case where $U\sim W$, there are no exact solutions for this model beyond one dimension [26]. More sophisticated approximations or methods such as DMFT, presented in the next section, are thus employed.

2.2.2 . Dynamical Mean Field Theory (DMFT)

Intrinsically, the idea behind DMFT is to map the lattice electron problem to that of a quantum impurity on a single atomic site immersed in a self-consistent effective medium [27]. The localized atomic environment that dynamically interacts with a bath of free electrons, as presented in this model, makes it possible to capture the configuration fluctuations of the system over time while ignoring the spatial fluctuations. The approach proposed here allows the observation of the system's evolution, whatever the amplitude of the correlations [18]. This approximation used in DMFT becomes exact for infinite coordination [27, 28].

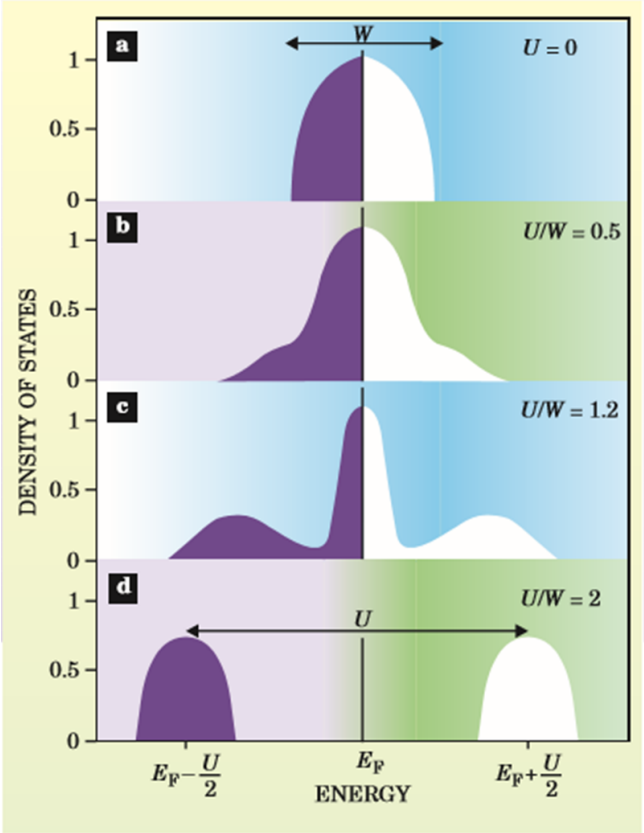

FIGURE 2.2: Evolution of the density of states obtained in DMFT for the Hubbard model, as a function of electronic correlations. The figure is adpated from [29].

DMFT can predict or represent not only the metallic or insulating states associated with the one-band Hubbard model but also the intermediate states where the orders of magnitude for electronic correlations and bandwidth are nearly similar; as presented in figure 2.2. Thus, when $(U/W) = 0$, the local density of states obtained in DMFT for the Hubbard model is that of a metal as in the band approximation. For weak electronic correlations where $(U/W) = 0.5$, the electrons are represented as quasiparticles, with a density of states close to the previous case. In the regime of strong electronic correlations $(U/W) = 1.2$, we observe the appearance of a quasiparticle peak close to the Fermi level, and the so-called lower (LHB) and upper (UHB) Hubbard bands. Finally, the insulating state appears when the electronic correlations become sufficiently large $(U/W) = 2$. The quasiparticle peak then vanishes, and we observe an energy gap with a value U separating the Hubbard bands

[29]. This quasiparticle feature observed in DMFT has been experimentally confirmed in photoemission in the metallic state of V_2O_3 [30].

In the case of real materials such as the one studied in this thesis, LDA+DMFT (LDA for Local Density Approximation) approaches are generally used. They allow to introduce the band structure by LDA before DMFT calculations. The combination of these two methods thus makes it possible to deal with weak electronic correlations using LDA, on the one hand, and strong correlations caused by electrons in the narrow d or f bands, using DMFT [24, 31], as in the case of V_2O_3 with an incomplete d-shell.

2.3 . About phase transitions in $(V_{1-x}M_x)_2O_3$ ($M = Cr, Ti$)

V_2O_3, a prototypical Mott system, has been widely studied because of its diverse physical properties. The work carried out over the years has contributed to understanding certain physical phenomena, although many contradictions and concerns remain. In the following sections, we propose to present this system and discuss the significant findings in the literature about this material.

2.3.1 . Some generalities in V_2O_3

$(V_{1-x}M_x)_2O_3$ ($M = Cr, Ti$) presents paramagnetic metallic (PM), paramagnetic insulating (PI) and antiferromagnetic insulating (AFI) phases, under external parameters such as temperature (T), pressure (P) or chemical substitution. The phase diagram of this system, presented in figure 2.3, was established in the 1970s by McWhan *et al.* [2–4] partly by transport and X-ray diffraction measurements, i.e., by measurements on a macroscopic scale.

The PM phase appears at room temperature, in the pure V_2O_3 compound, or possibly for the chemical substitution of vanadium (V^{3+}) by chromium (Cr^{3+}) below 1 %. The material, isostructural to corrundum $\alpha - Al_2O_3$ in this phase [32], has a rhombohedral structure but the hexagonal representation is generally used, with a space group corresponding to $R\bar{3}c$ (figure 2.4). In this structure, the vanadium atoms occupy 2/3 of the octahedral sites. The lattice parameters are given in table 2.1.

Starting from the PM phase, we distinguish two types of MIT. First, we

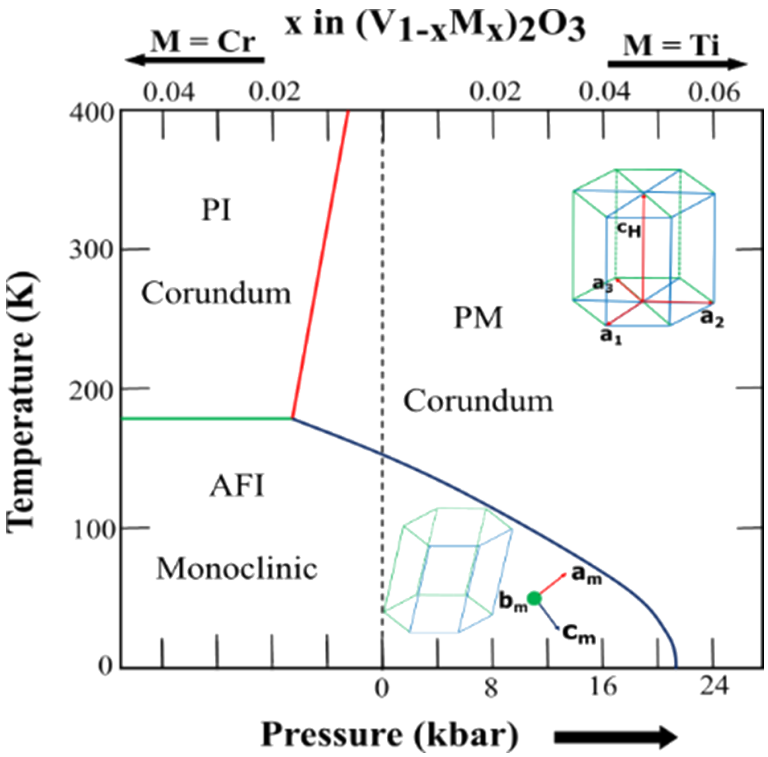

FIGURE 2.3: Phase diagram of $(V_{1-x}M_x)_2O_3$ (M for Cr or Ti) function of external parameters (T,P, chemical substitution), adapted from McWhan *et al.* pioneer works [2–4].

observe a first-order transition from PM to AFI when the temperature is lowered below $\sim$ 150 K - 160 K, for the pure compound, for instance. As shown in the phase diagram, this transition can also be achieved at different temperatures for chromium or titanium substitutions of less than 1 % or 5 %, respectively. This transition is both structural, electronic, and magnetic. Structurally, we find a symmetry breaking with an AFI phase described this time in the monoclinic system and possessing a space group $I2/a$ (see figure 2.4). At the transition, the vanadium atoms along the hexagonal c_h-axis move almost perpendicularly to the latter, towards the empty octahedral sites (figure 2.5). This structural change, characterized by the hexagonal threefold symmetry breaking, is mainly represented by the tilt of the c_h-axis by about 1.8° [33] (see the structure in inset in figure 2.3). As the tilt can occur in 3 directions at 120° to each other and at 30° to a_h and b_h directions (still in the plane

(a_h, b_h)), it may form twin monoclinic domains in the AFI phase. Finally, an abrupt and significant increase in volume (+1.4 % from PM to AFI) accompanies this transition [2]. The monoclinic lattice parameters obtained in the AFI phase are also given in table 2.1. Electronically, we observe an increase in resistivity of about 7 orders of magnitude during this transition [2–4] (figure 2.5). In addition, the antiferromagnetic order, established in the AFI phase, leads to magnetic moments ordered ferromagnetically in the (010) planes, which are themselves antiferromagnetically arranged in the monoclinic lattice [34]. The exact mechanism leading to the PM - AFI transition is still debated.

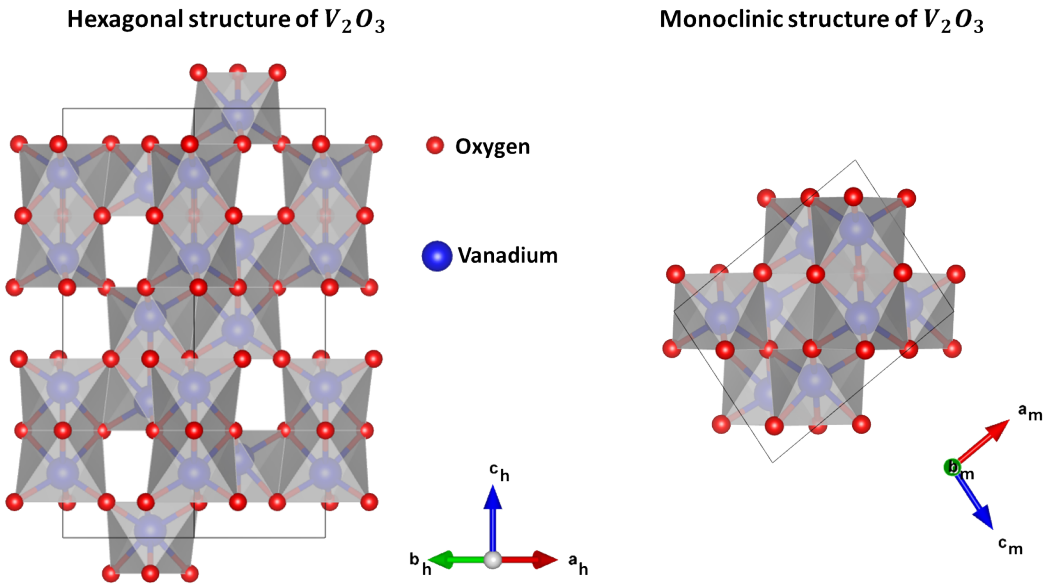

FIGURE 2.4: Hexagonal structure observed in the $[\bar{1}\bar{1}0]_h$ direction for PM and PI, and monoclinic structure observed in the $[020]_m$ direction for AFI phase in V_2O_3.

Secondly, we observe another first-order transition from the PM to the PI phase at room temperature, for vanadium substitution by chromium around 1 %, for instance [2]. This transition from PM to PI can also be achieved by increasing the temperature for a given chromium substitution, as shown in

[2]This percentage increase is obtained by comparing the volume of the rhombohedral lattice in the PM phase with that of the monoclinic primitive lattice in the AFI phase.

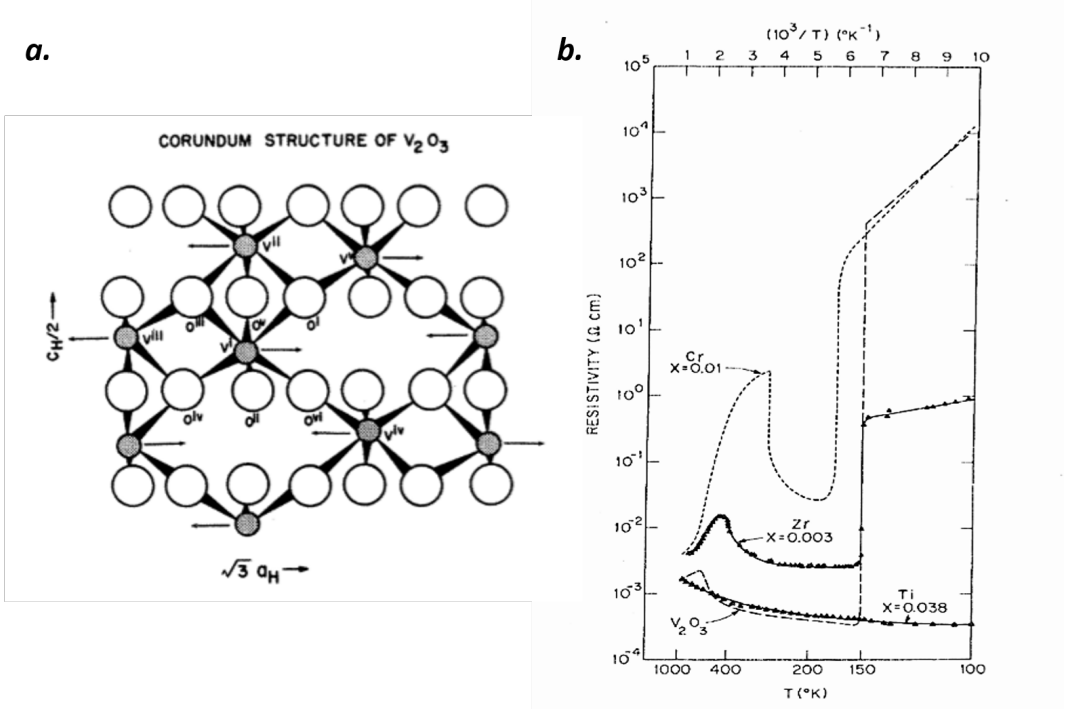

FIGURE 2.5: *a*. Hexagonal structure of V_2O_3. Oxygen and vanadium are represented respectively in white and grey. The arrows indicate the displacement direction of vanadium at the monoclinic structural transition. This figure is adapted from [33]. *b*. Resistivity curves, observed mainly for pure V_2O_3 and 1 % Cr-doped V_2O_3. This figure is adapted from [3].

the phase diagram. This phase change, a prototypical Mott-Hubbard transition, involves neither symmetry breaking nor magnetic order. However, we note an abrupt increase in the volume of about 1.2 % from PM to PI [4]. The lattice parameters obtained for the PI phase thus show, respectively, an expansion and compression of a_h and c_h, compared to those of the PM phase. These lattice parameters, found for an approximately 1.1 % Cr-doping are given in table 2.1. Finally, we observe an increase in resistivity of 2 orders of magnitude during this transition (figure 2.5). Hassan *et al.* suggest electronic degrees of freedom as the driving force in the PM - PI transition [35]. Rodolakis *et al.* also indicate inequivalent mechanisms leading to the PM state under chemical substitution, temperature, or pressure [36]. Chemical substitution or temperature would lead to the metallic state via the reduction of the crystal field. The metallic state obtained under pressure would

Sample	V_2O_3 [3]	$(V_{0.989}Cr_{0.011})_2O_3$ [18]	V_2O_3 [2]
***T* (K)**	300	300	77
Phase	PM	PI	AFI
Symmetry	Hexagonal	Hexagonal	Monoclinic
Space group	$R\bar{3}c$	$R\bar{3}c$	$I2/a$
***a* (Å)**	4.951	4.997	7.255
***b* (Å)**	4.951	4.997	5.002
***c* (Å)**	14.003	13.926	5.548
α **(°)**	90	90	90
β **(°)**	90	90	96.75
γ **(°)**	120	120	90
Volume (Å^3)	297.261	301.145	199.939

TABLE 2.1: Lattice parameters for $(V_{1-x}Cr_x)_2O_3$ in the PM, PI and AFI phases [2, 3, 18].

rather result from an increase in the bandwidth.

2.3.2 . Metal-to-insulator transition (MIT) and non-stoichiometry in V_2O_3

Phase transitions in V_2O_3 have been studied in the case of non-stoichiometric samples, particularly for the PM - AFI phase transition. When the system is deficient in vanadium ($V_2O_{3+\delta}$), the transition temperature is lowered [37, 38]. Below a vanadium proportion given by $\delta = 0.04$ ($\delta = 0.026$ in another work [38]), the MIT vanishes completely. However, the compound still shows a magnetic transition at about 10 K, from PM to AFM (antiferromagnetic metallic), when $0.04 < \delta < 0.08$ [37]. Above this limit, another compound, V_3O_5, emerges [39]. The application of a hydrostatic pressure on pure V_2O_3 compound has almost the same effect. It reduces the transition temperature and suppresses it above 26 kbar [4].

The oxygen vacancies system has only been studied in thin films due to

the instability of $V_2O_{3-\delta}$ bulk sample. Brockmann *et al.* generated and stabilized these vacancies by growing thin films in an oxygen-reduced environment [40]. These oxygen vacancies, whose estimated proportion is given by $\delta = 0.006$, would induce, contrary to the vanadium vacancies, an increase in the transition temperature up to 50 K.

2.3.3 . Elastic properties in $(V_{1-x}Cr_x)_2O_3$

The evolution of the elastic properties was also probed during these transitions. Ultrasonic sound waves [41] and neutron scattering measurements [42] show a softening of the elastic coefficient c_{44} related to the direction perpendicular to the hexagonal c_h-axis; when the temperature gradually decreases from PI to AFI (figure 2.6). An extrapolation performed from experimental data highlights a value $c_{44} \approx 0$ (hexagonal lattice instability condition [43]) at the transition temperature $T \sim 180K$ between PI and AFI. This softening of c_{44} is not observed during cooling for the PM to AFI transition.

Here, the hardening of c_{44} appears to be closely related to the PM phase, as shown particularly in the 1.5 % Cr-doped sample in figure 2.6. Indeed, the latter allows to carry out during the sample cooling, the PI to PM transition around 200 K, then the PM to AFI transition around 150 K. When the temperature is lowered, the decrease of c_{44} is first observed in the PI phase. Then, it stops when we enter the PM phase and does not evolve in temperature, as in the case of pure V_2O_3 samples. As mentioned above, the monoclinic structure is achieved by the movement of vanadium atoms in the direction perpendicular to c_h, therefore in the same direction related to c_{44}. These results would thus suggest the existence of a brief and transient precursor PI phase in the PM - AFI transition, where the softening of c_{44} could take place before the appearance of the AFI phase [42, 44]. Transport measurements performed by Carter *et al.* in pure V_2O_3 under pressure would also suggest the presence of an intermediate or persistent (above 15 kbar) PI phase during the PM to AFI transition [45].

2.3.4 . Electronic structure

V_2O_3 is a transition metal oxide and belongs to the family of strongly correlated systems, as mentioned above. In these systems, the electrons in the incomplete narrow d-band of the transition metal, in this case, vanadium,

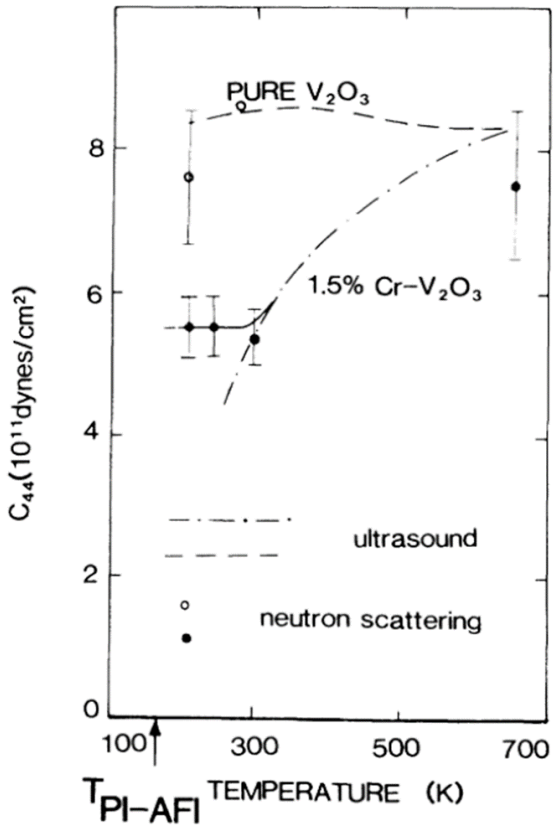

FIGURE 2.6: Evolution of the elastic coefficient c_{44} as a function of temperature, obtained by ultrasound and neutron scattering for V_2O_3 and 1.5 % $Cr - V_2O_3$. The figure is adapted from [42].

predominantly determine the electronic properties [18, 19]. The electronic structure of the latter in V_2O_3 is $[Ar]3d^2$, with a V^{3+} oxidation state.

Due to the cubic crystal field in the octahedral environment of oxygen anions in V_2O_3, the fivefold degenerate 3d orbitals of vanadium split and form the twofold degenerate e_g^σ (higher energy) and the threefold degenerate t_{2g} (lower energy) orbitals. Thanks to the trigonal distortion of these octahedral sites, the lower t_{2g} orbital splits again to finally give rise to the twofold degenerate e_g^π and the non-degenerate a_{1g} orbitals, oriented respectively in the hexagonal basal plane and along the c_h-axis [18, 46]. The model proposed by Castellani *et al.* to describe the electronic structure of V_2O_3 involves the dimerization of vanadium ions along the c_h-axis [18, 46, 47]. The sharing of one of the two electrons of vanadium involved in this process would lead

to the complete occupation of the molecular orbital a_{1g} resulting from the V - V bond, the latter being found in this description at lower energy. The corresponding electronic structure is presented in figure 2.7. We would finally obtain a 1/2 spin state for vanadium, where the remaining electron would partially occupy the twofold degenerate e_g^π orbital. The description of Castellani *et al.* would thus support the one-band Hubbard model, where the electron remaining on the e_g^π orbital would be mainly responsible for the electronic properties of the system in this configuration [18].

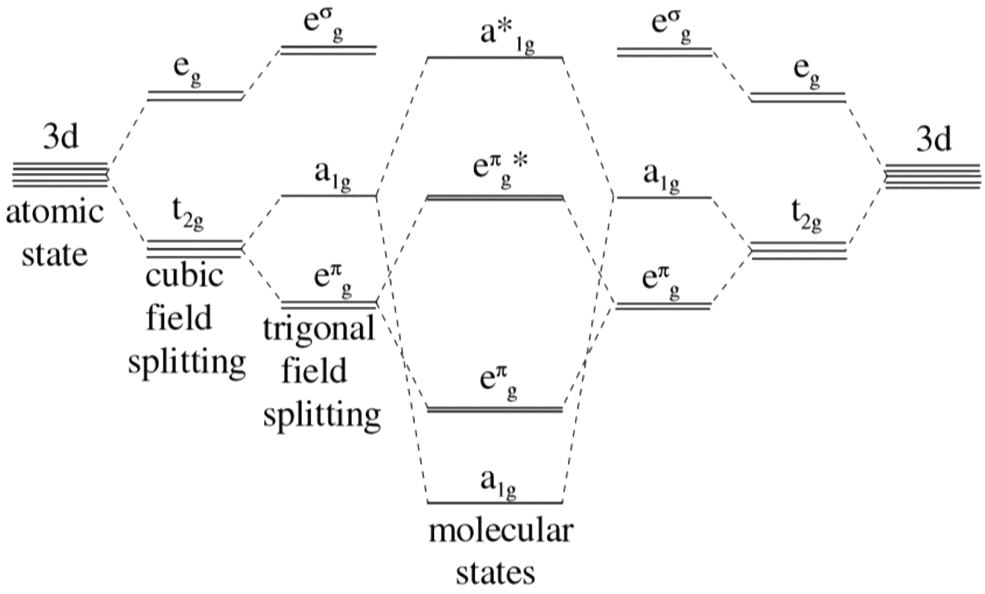

FIGURE 2.7: Electronic structure proposed by Castellani *et al.* for V_2O_3, adapted from [46].

However, Park *et al.*, using polarization-dependent X-ray absorption spectroscopy (XAS) and multiplet calculations, found an S = 1 spin configuration instead for vanadium ions, with an admixture of $e_g^\pi e_g^\pi$ and $e_g^\pi a_{1g}$ states in the ground state [49]. The occupation ratio $e_g^\pi e_g^\pi : e_g^\pi a_{1g}$ obtained by Park *et al.* are 2:1 for AFI, 1:1 for PM and 3:2 for PI. These variations in the occupation ratio of the orbitals in the AFI, PM and PI phases would point towards the necessary introduction of a multi-orbital Hubbard model for the description of $(V_{1-x}Cr_x)_2O_3$. The LDA+DMFT calculations of Keller *et al.* [50], taking into account this multiband or multi-orbital character, have subsequently made

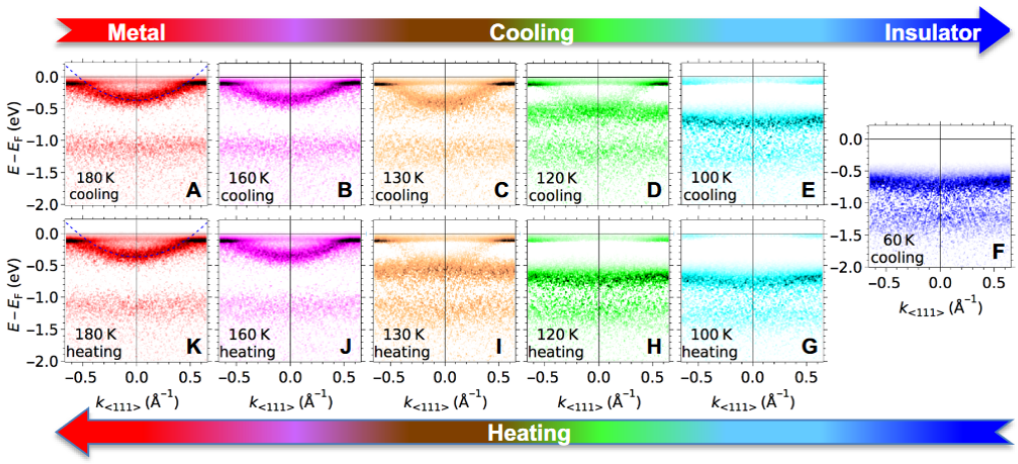

FIGURE 2.8: Evolution of the energy bands obtained in ARPES, in V_2O_3 thin film, near the Fermi level, during the transition between PM and AFI. The figure is adapted from [48].

it possible, for example, to recover the spin state S = 1 and to find spectra at 300 K that are almost in agreement with those obtained in photoemission. The spectral function in the insulating state, calculated in LDA + DMFT by Poteryaev *et al.* [51], still using multiband considerations, is also found to agree with that obtained in photoemission for $(V_{0.962}Cr_{0.038})_2O_3$.

Another important fact concerning the electronic structure is the recent observation in ARPES, by Thees *et al.* [48], of the band structure evolution through the PM - AFI transition on V_2O_3 thin films. They show a gradual transfer of spectral weight from the dispersive conduction band to a quasi-localized state as the MIT approaches (see figure 2.8). This quasi-localized state also shifts to lower energies during the transition to finally give rise to the opening of a gap of about 0.7 eV in the insulating state, when the dispersive conduction band has wholly vanished.

Finally, regarding the gap in the insulating phases, the values given in the literature are 0.1 eV $\sim$ 0.2 eV for PI [52, 53], and 0.5 eV $\sim$ 0.7 eV for AFI [53–55].

2.3.5 . Decoupling between degrees of freedom during the temperature-induced structural transition

Probing and mapping physical properties at relatively small scales, down to the nanometer or even atomic level, would show a much more complex

picture than the phase diagram established by McWhan *et al.*. X-ray absorption fine structure (XAFS) measurements carried out in the late 1990s by Frenkel *et al.* [56] on a V_2O_3 single crystal would indicate the presence of local monoclinic regions in the PM phase, after the T-induced insulator-to-metal transition (IMT), upon heating. These regions would have a coherence length of up to 40 Å in the PM phase. The existence of a structural precursor has also been proposed by Pflazer *et al.* [57]; this time for the T-induced MIT from PM to AFI, upon cooling. Using coupled extended x-ray absorption fine structure (EXAFS) and transport measurements, they deduced a smooth increase and continuous tilt of the c_h-axis a few Kelvins before the MIT; this in a slightly non-stoichiometric V_2O_3 single crystal.

Much more recent experiments by McLeod *et al.* [6], and Majid *et al.* [58], on V_2O_3 thin films, would also suggest the existence of an intermediate metallic monoclinic phase. The results obtained by McLeod *et al.*, in micro-XRD and nano-IR (with a probe size of about 25 nm) would indicate the co-existence of metallic/insulating domains but also a 6 K decoupling between the electronic and structural transitions during this T-induced MIT. Majid *et al.* would observe a much larger decoupling of about 23 K between both degrees of freedom using Raman and resistivity measurements, noting that all their observations are made in strained thin films.

According to Kalcheim *et al.* [7], this observed decoupling between electronic and structural transitions should be discussed in light of the experimental tools and methods used in the previous data acquisition. Indeed, the structural (micrometer scale) and spectroscopic (nanometer scale) probes used in [6] would investigate slightly different volumes. As Kalcheim *et al.* show, physical properties can vary from one volume to another in these thin films, as observed in figure 2.9. Beyond this aspect, the resistivity measurements made in [58] would also be a poor barometer of the electronic state of the samples, due to the percolative character of the phase transition; according to Kalcheim *et al.*. The re-examination of this transition by the latter in XRD with a penetration depth of about 13 μm, and in IR spectroscopy with a penetration depth of up to 760 nm would indicate this time a strong coupling between structural and electronic degrees of freedom in thin films. The strong coupling shown here would be in agreement with the results obtained

by Frandsen *et al.* [59], in XRD and nano-IR, still in thin films. However, their muon spin relaxation (μsr) measurements would show antiferromagnetic fluctuations as the phase transition approaches.

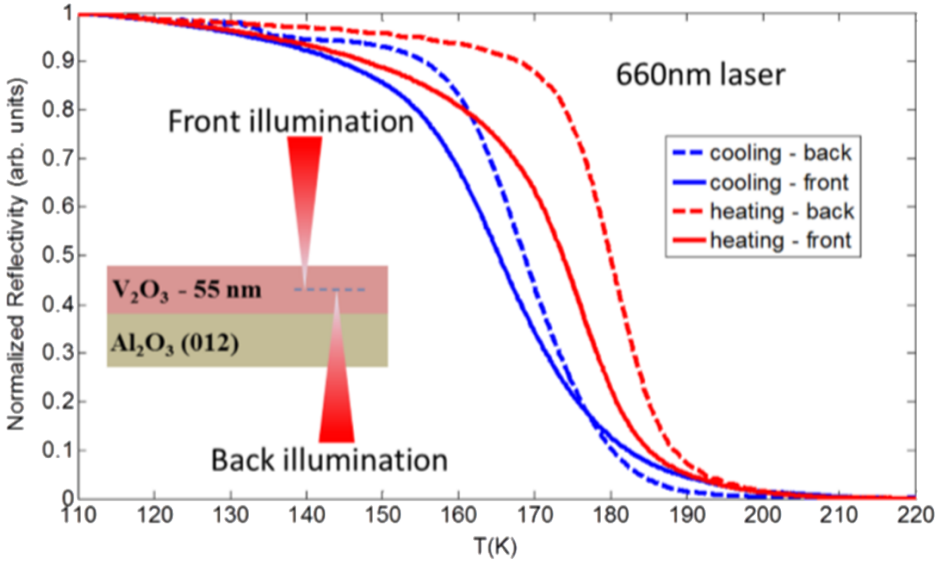

FIGURE 2.9: Evolution of reflectivity as a function of temperature in V_2O_3 thin film. Differences, as for the transition temperature, are observed when the film is probed at top or bottom. The figure is adapted from [7].

The central role that the magnetic degree of freedom could play in this T-induced phase transition in V_2O_3 has been increasingly discussed in the literature these last years. The change of sign at about 200 K (from positive to negative) and the decrease of the magnetoresistance well before the MIT in PM - AFI transition, observed by Trastoy *et al.* in thin films [60], would indicate the non-negligible role of antiferromagnetic fluctuations in this transition. The decrease of the magnetic pair distribution function (PDF) at least 25 K before the IMT, shown by Fletcher *et al.* [61], would seem furthermore support this hypothesis. Such fluctuations were also observed in Carter's susceptibility measurements in V_2O_3 single crystals, but only when the sample is under pressure.

Leiner *et al.* [62] also addressed the question of the magnetic degree of freedom in $(V_{1-x}Cr_x)_2O_3$ compounds. Using inelastic neutron scattering

measurements and density functional theory (DFT) calculations, they conclude that a magnetic frustration state would exist in the rhombohedral or hexagonal structure and would be induced by exchange interactions between nearest and next-nearest neighbors in the honeycomb basal plane. The monoclinic distortion that occurs at the transition would lead to lifting this frustration and, thus, to the antiferromagnetic state in the AFI phase. There would be, therefore, a close link between symmetry and magnetic properties.

2.3.6 . Impact of pressure, strain and Cr-doping in V_2O_3

As mentioned above, strongly correlated systems like V_2O_3 exhibit various physical properties upon external stimuli such as temperature. In addition, Ding *et al.* [63] demonstrated a few years ago the existence of a metallic monoclinic phase in pure V_2O_3 (powder sample) under a hydrostatic pressure at room temperature. Beyond 32.5 GPa, they would observe a structural transition, from the rhombohedral to the monoclinic structure represented here in the $P2_1/c$ space group. The absence of an electronic transition accompanying this structural transition would indicate a decoupling between these two degrees of freedom under high pressure at room temperature.

Strains in thin films are also not without effect. Dillemans *et al.* [12] indicate that V_2O_3 thin films would show no T-induced MIT when the film thickness would be less than 6 nm. On the other hand, the use of a buffer layer of Cr_2O_3 before film deposition would indicate an MIT for a V_2O_3 thickness of approximately 3.5 nm. These differences would be explained by the clamping effect to the substrate and by differences in lattice mismatch (4.2 % between V_2O_3 and Al_2O_3 and 0.1 % between V_2O_3 and Cr_2O_3), inducing strains more or less important in the thin film.

Other interesting effects occur upon Cr-doping in V_2O_3. In $(V_{0.989}Cr_0.011)_2O_3$ single crystals, Lupi *et al.* [5] indicate an electronic phase separation in the PM phase; during the T-induced transition between PI and PM. They would observe at the micrometer scale, in T-dependent photoemission microscopy, a coexistence of insulating and metallic domains in the PM phase, which would be not the case for the PI phase where the insulating state would be homogeneous throughout the sample. The most striking fact here is the memory effect observed in the PM phase. Indeed, the different electronic domains

would always reappear in the sample in the same regions at the transition. These results could be explained by the presence of structural defects associated with the insulating domains, which would serve as nucleation sites in the phase transition. These structural defects, in turn, could originate from the introduction of Cr impurities into the V_2O_3 matrix, as suggested by Hansmann *et al.* [64]. Additionally, Lechermann *et al.* [65] indicate that Cr impurities would induce local monoclinic distortions and would enhance crystal field effects, as observed in their DFT + DMFT calculations. The realization of the PM - PI transition in pure V_2O_3 would therefore make it possible to elucidate some concerns.

Until recently, Cr doping was necessary to achieve the PM-PI transition in V_2O_3. Hu *et al.* [66], recently showed, according to their resistivity measurements, that it is possible to achieve a PI phase and carry out this transition in V_2O_3 thin films. They achieved this by acting only on the temperature of the Al_2O_3 substrate during film deposition in order to generate so-called "thermal" strains and stabilize the PI phase in the film. The trigonal distortion mechanism (increase or decrease respectively for PI or PM) would drive this transition in the pure thin films obtained. Homm *et al.* [67] also demonstrated the PM to PI transition in V_2O_3 thin films at room temperature, just by heteroepitaxy ($V_2O_3//Cr_2O_3//(Cr_{1-y}Fe_y)_2O_3//Cr_2O_3//Al_2O_3$). The PI phase observed in their strained thin films would exhibit gap variations of up to 0.5 eV, in contrast to the approximate 0.1 eV generally encountered in this phase. The real part of the optical conductivity also obtained would be much closer to that observed for the AFI phase in single crystals than that of the PI phase obtained in single crystals by chromium substitution.

As a last point related to strains, the PM to AFI phase transition can also serve to control the magnetic behavior in $V_2O_3/CoFeB$ heterostructures, as shown by Polewczyck *et al.* [68]. Thanks to the interfacial strains generated by V_2O_3 due to the large volume increase at the transition, they would obtain a reversible variation of up to 330 % of $CoFeB$ coercive field.

2.3.7 . Previous work in EELS

Some works have also been carried out with electron energy-loss spectroscopy (EELS), which is one of the main techniques used in our investigations. The work of Abe *et al.* [69, 70] in EELS, in the PM, PI, and AFI phases, for pure V_2O_3 and 1.2 % Cr-doped V_2O_3, reveals the presence of a 1 eV spectroscopic signature present only in the PM phase, which they attribute to an interband plasmon. They also observed during the transition from the metallic to the insulating state an upward shift of about 0.4 eV on the oxygen O-K edge, the latter corresponding to electronic transitions from O 1s core level states to O 2p hybridized with vanadium V 3d orbitals. These observations align with those of Muller *et al.* [71] in XAS, with a shift value of about 0.3 eV. These results will be discussed in more detail in the following chapters.

2.3.8 . Electric-field and photoinduced experiments in $(V_{1-x}Cr_x)_2O_3$

In addition to the temperature-induced transition, as discussed previously, $(V_{1-x}Cr_x)_2O_3$ compounds are also privileged exploration materials within the framework of electric-field-driven or photoinduced experiments. When $(V_{1-x}Cr_x)_2O_3$, in the insulating state, is submitted to electrical pulses above a certain threshold (about 6 kV/cm for x=0.15), metallic conducting filaments are created in the insulating matrix [72]. The mechanism involved in this transition would be avalanche breakdown, which would induce the displacement of electrons and would lead locally to the creation of unoccupied and doubly occupied sites (by analogy with the Hubbard model), and therefore to the establishment of a local metallic state.

Immediately after the electrical pulse, the stabilization (non-volatile resistive switching) of these filaments above a certain critical size, as shown in the modelizations carried out, or their dissolutions (volatile resistive switching) below this size, would depend on the characteristics of the pulse [72, 73] (see figure 2.10). Indeed, the voltage applied in these experiments would induce competition between the electric field's avalanche breakdown mechanism, which would favor the creation of metallic regions, and the Joule effect relaxation mechanism, which would contribute to the dissolution of these metallic regions. Applied to MIM (metal-insulator-metal) structures [73] of the type

$TiN/(V_{1-x}Cr_x)_2O_3/TiN$ (800 nm thick V_2O_3), a lower voltage of 3.5 V for 1.5 μs would stabilize filaments and would lead to a low resistance state ('SET' transition). On the other hand, a higher voltage of 4.5 V for 250 ns would induce dissolution of the filaments and would lead to the high resistance state ('RESET' transition). These "SET" and "RESET" transitions shown here would present a great interest. It would make it possible to produce logical "0" and "1" states and thus develop resistive switching devices [72].

Another interesting application would arise from the volatile resistive switching. Experiments carried out in this framework would also make it possible to reproduce the 3 sequences of a biological neuron [74, 75]. Indeed, in the mammal brain, the neuron receives electrical impulses from neighbors neurons via its membrane in the **Integrate** sequence. Then, it discharges or relaxes between impulses in the **Leaky** sequence and finally, it sends an impulse or action potential to other neurons in the **Fire** sequence when its membrane potential reaches a certain threshold. Under a train of electrical pulses, according to modeling carried out, the steps leading to the volatile resistive switching; namely the creation of metallic sites in the insulating matrix, the decay or relaxation of given sites between pulses, and finally, the percolation giving rise to the metallic filament, would perfectly reproduce the Integrate, Leaky and Fire sequences, respectively [75]. From all these observations, $(V_{1-x}Cr_x)_2O_3$ would therefore represent a potential candidate for non-volatile memories and neuromorphic applications.

Regarding photoinduced-IMT experiments, Singer *et al.* [76], through x-ray scattering and x-ray nanodiffraction experiments, point out the existence of a transient non-equilibrium phase from AFI to PM phase transition, in V_2O_3 thin films grown on R-plane sapphire substrate. This phase would present a quasi-analogous structure to the PI state. The recent observations of Ronchi *et al.* [77] are different from the previous one. Using reflectivity and time-resolved photoemission electron microscopy (PEEM) measurements, they showed the presence of a non-equilibrium metallic monoclinic phase instead. These observations are made on a V_2O_3 thin film grown on a c-cut sapphire substrate and probed under a laser fluence of 22 mJ/cm^2 (up to 6 mJ/cm^2 in Singer *et al.* experiments). According to the latter, this new phase would result from the twinning nanotexturation observed in their AFI

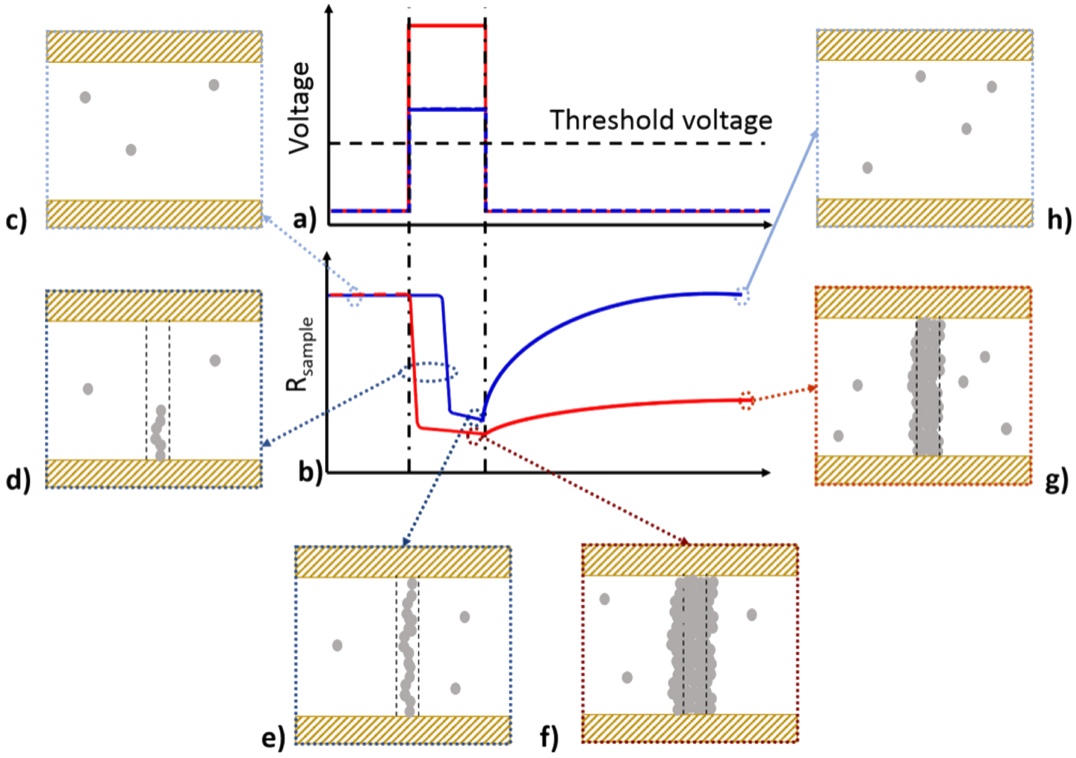

FIGURE 2.10: Representation of the switch mechanism in the insulator $(V_{1-x}Cr_x)_2O_3$ under electrical pulse. Above a critical voltage threshold, we observe the creation of metallic sites (grey dots) in the insulating matrix, which accumulate and then percolate to give rise to a metallic conducting filament finally. If the voltage is high enough (red curve), the filament reaches a critical size and stabilizes in the insulating matrix. Otherwise (blue curve), it dissolves immediately after the electrical pulse. The figure is adapted from [75].

phase, which would consolidate and preserve this out-of-equilibrium photoinduced metallic monoclinic state.

2.4 . Conclusion

V_2O_3, belonging to the family of strongly correlated systems, shows a diversity of phase transitions, between PM, PI and AFI phases, when it is submitted to external parameters such as temperature or pressure. This system also shows an exciting potential for non-volatile memories and neuromorphic applications. As we have seen in this chapter concerning electronic

phase separation, structural precursors, or magnetic fluctuations, phase transitions in V_2O_3 still raise several questions (about nucleation mechanisms or correlations between the degrees of freedom, for instance), especially on relatively small scales (the nanometer). Therefore, the understanding and accurate description of this system require investigations by tools with at least a nanometric resolution, and that allow the simultaneous correlation of information on the essential degrees of freedom involved in these transitions. In the next chapter, we will present the techniques and methods used in our investigations on this material.

Chapter 3

Experimental techniques and tools for data analysis

3.1 . Introduction

Phase transitions in V_2O_3, as discussed in the previous chapter, are still not well understood, especially when dealing with relatively small scales like the nanometer. Explaining the underlying mechanisms related to these phase transitions requires using tools with a good spatial resolution. Techniques such as nano-IR or IR-spectroscopy have been widely used in recent years for this purpose.

In this chapter, we will present the experimental techniques in electron energy-loss Spectroscopy (EELS), microdiffraction, and nanodiffraction, employed in our investigations on V_2O_3. We will also present tools such as Geometric Phase Analysis (GPA), Principal Component Analysis (PCA) or K-means clustering, for instance, used in analyzing and processing our data.

3.2 . Electron microscopy, diffraction and spectroscopy

Electron-matter interactions are proving to be powerful tools for understanding and describing matter. Indeed, electrons carrying negative electrical charges can interact electrostatically with the nuclei and other electrons in the explored sample [78]. This interaction provides information on the sample's structural, chemical, or electronic properties, depending on the different regions through which the electrons pass.

Electrons can be elastically scattered during these processes as they interact with atomic nuclei. This interaction involves almost no energy loss for the incident electrons due to the mass difference between these two entities [78]. Inelastic scattering can also occur during electron-electron interactions. This mechanism, resulting from the interaction between particles of the same mass, involves a transfer of energy which can be significant in some instances.

These two processes, widely used in electron microscopy, are genuine sources of information, as we shall see in this chapter.

3.2.1 . Elastic scattering

As mentioned above, this phenomenon arises from the electrostatic interaction of incident electrons with atomic nuclei. A substantial quantity in describing this interaction is the differential cross section, which represents an electron's scattering probability per unit solid angle Ω [78]. The latter, considering the interaction with fast incident electrons with a kinetic energy of several tens of keV, and also the screening effects of the electronic cloud around the atom, is defined by :

$$\frac{d\sigma_e}{d\Omega} \approx \frac{4\gamma^2 Z^2}{a_0^2 k_0^4 (\theta^2 + \theta_0^2)^2} \tag{3.1}$$

In this expression, $\gamma = (1 - \frac{v^2}{c^2})^{-1/2}$ is the relativistic factor with v and c representing respectively the velocities of electrons and light in vacuum; Z is the atomic number, and $a_0 = 0.529$ Å is the Bohr radius. k_0 is the momentum of the incident electron with m_0 its rest mass and $\hbar$ the reduced Planck constant. θ is the scattering angle and $\theta_0 = (k_0 r_0)^{-1}$ is the elastic scattering angle. For incident electrons with an energy of 100 keV, θ_0 is of typically 20 mrad for carbon samples. Finally, r_0 is the screening radius. An illustration of the scattering process is given in Figure 3.1. As we can see, the angular distribution of this interaction is Lorentzian, with a full width at half-maximum (FWHM) $\sqrt{2}\theta_0$.

The atomic model presented in equation 3.1 is a good approximation for

amorphous materials because of the weak diffraction effects [78]. In crystalline materials, however, this angular dependence can vary greatly and deviate from the model proposed in the equation 3.1 due to diffraction focusing the scattered elastic intensity mainly in the Bragg constructive interference directions.

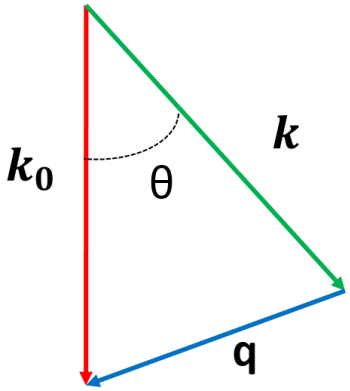

FIGURE 3.1: Representation of the scattering phenomenon undergone by the incident electrons. $\mathbf{k_0}$ represents the wave vector of the incident electron, $\mathbf{k}$ is the wave vector of the electron after scattering and $\mathbf{q}$ is the momentum transferred to the atom during the process. The figure is adapted from [78, 79].

Diffraction studies are an important part of this thesis. In crystalline samples, where the atomic arrangement is periodic, diffracted intensities are observed when Bragg's law is satisfied. This law is given by $n\lambda = 2d_{hkl}sin\theta_B$. In other words, under an electron beam and for a given interference order n, a set (hkl)[1] of crystal lattice planes with an inter-reticular distance d_{hkl} will produce a reflection for a given direction θ_B. For electrons accelerated to 100 keV, the scattering angles associated with these reflections are greater than 10 mrad.

Another tool generally used to understand and represent the diffraction phenomenon is the construction of the Ewald sphere. In this description, a reflection (hkl) will be observed in the diffraction pattern when a node corresponding to (hkl) in the reciprocal lattice will intercept the Ewald sphere, centered on the sample and of radius $r = 1/\lambda$ (λ being the wavelength of the incident electron beam), as shown in the figure 3.2. Several methods, such

[1] h, k and l are Miller indices

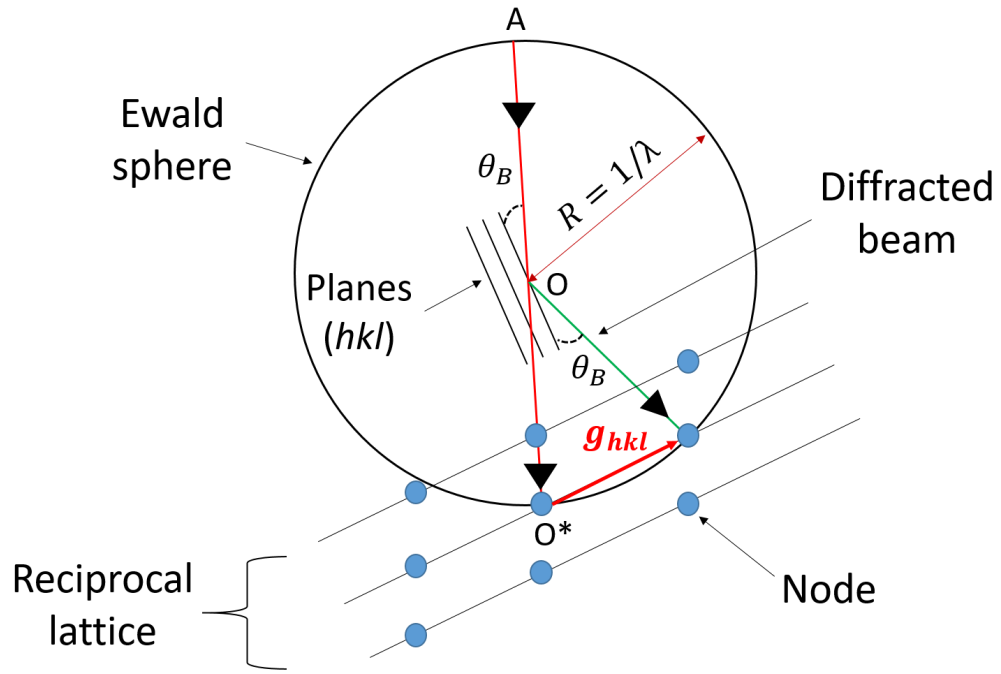

FIGURE 3.2: Representation of Bragg's law with the Ewald sphere. Bragg's law is satisfied if the sphere intercepts a node of the reciprocal lattice. The figure is adapted from [80].

as nanodiffraction or microdiffraction, also used in our investigations, allow us to map these diffraction phenomena occurring in the material and thereby deduce information about the symmetry and parameters of the crystal lattice. We will come back to this later in this chapter.

3.2.2 . Inelastic scattering

Inelastic scattering results from the electrostatic interaction between incident electrons and electrons in the atomic outer or inner shells, involving a more or less substantial transfer of energy during the interaction. From Bethe's theory, this interaction can be very well described by the double differential cross section, which takes into account the angular and energy dependence resulting from this process [78]. This expression, still considering the interaction with fast incident electrons with a kinetic energy of several tens of keV, is given by :

$$\frac{d^2\sigma_e}{d\Omega dE} \approx \frac{4\gamma^2 R}{Ek_0^2(\theta^2+\theta_E^2)^2}\frac{df}{dE} \tag{3.2}$$

In this equation, E and R represent the energy loss and the Rydberg energy, respectively. $\frac{df}{dE}$ is the generalized oscillator strength[2] (GOS) and depends on the scattering vector $\mathbf{q}$ (the momentum transferred to the atom during the interaction, see figure 3.1) and the energy loss E. This quantity is also proportional to the energy loss function in electron energy-loss spectroscopy (EELS), which will be introduced later. $\theta_E = \frac{E}{\gamma m_0 v^2}$ is the characteristic angle of inelastic scattering. In the non-relativistic approximation, $\theta_E = \frac{E}{2E_0}$, with E_0 the energy of the incident electron.

The angular distribution of this interaction is also lorentzian at small scattering angles. For incident electrons with energy E_0 = 100 keV, the FWHM of this inelastic angular distribution, extending to a few milliradians, is much smaller than that obtained for elastic scattering [78] (exceeding 10 mrad). As a result, this interaction contributes slightly to the broadening of the diffraction patterns. However, the inelastic lorentzian distribution's tail may lead to this interaction's participation in the background of the recorded diffraction pattern [78]. Inelastic scattering can lead to the excitation of entities such as phonons, interband transitions, plasmons, or core-level excitations, for instance, in the sample under investigation.

3.2.3 . About scanning transmission electron microscopy (STEM)

The STEM is an electron microscope in which a focused beam of electrons accelerated to a few keV probes the analyzed sample point by point or pixel by pixel [81] . Modern STEMs incorporating aberration correctors (Cs-STEM), such as those used in this thesis, have excellent spatial capabilities, in the nanometer or angström range. This tool, therefore, allows us to access the sample's local structural, electronic, or chemical properties, in particular by exploiting the signals resulting from the elastic and inelastic scattering phenomena. All these elements will be explained in the rest of this section.

[2]The GOS models the atomic behaviour with respect to the interaction with the electron beam.

Aberrations and spatial resolution

In theory, the spatial resolution limit should depend on the wavelength of the electrons used in an electron microscope, which is about 3.7 pm when the electrons are accelerated to 100 keV. Unfortunately, in practice, we have to consider the aberrations of the electromagnetic lenses used, and the size of the source, in order to determine the spatial resolution [82]. The spatial resolution limit due to diffraction is defined by the Rayleigh criterion whose expression is given by :

$$d_d = 0.61\frac{\lambda}{\alpha} \tag{3.3}$$

Here λ is the wavelength of the incident electrons and α is the convergence half-angle of the electron microscope (see figure 3.3). For electrons accelerated to 100 keV and an α value of 30 mrad generally used on one of our electron microscopes (NION ULTRASTEM 200) which we will describe in the following, d_d is 75 pm [82]. This value would correspond to the resolution achieved by our microscope if there were no other limiting factors as mentioned above.

Aberrations negatively influence spatial resolution, as we see, for instance, with the spherical geometric aberration, which turns out to be significant. Indeed, the resolution limit imposed by the latter admits an α^3 dependence, meaning its effects become dramatic as α increases. This observation, in contrast to the diffraction limit resolution (which improves as α increases), necessitates a compromise in choosing this angular value. In aberration-corrected STEMs (Cs-STEMs) such as those used in these investigations, high spatial resolution can be achieved by correcting and compensating for aberrations up to 5th order. This is made possible by using magnetic multipoles, such as the coupling in series of quadrupoles and octupoles [81]. Chromatic aberrations, which admit an angular dependence in α, can also be important at low primary energies [83]. They can be minimized, for instance, by using a monochromator.

The source size, which contributes to the spatial resolution, also has an angular dependence, but this time in $1/\alpha$ according to the expression :

$$d_s = (\frac{4I}{B\pi^2\alpha^2})^{1/2}, \tag{3.4}$$

where I and B represent the probe current and the brightness of the electronic source, respectively.

Finally, the spatial resolution is given by [82] : $d = \sqrt{(d_a^2 + d_s^2)}$, where d_a is the size of the probe taking into account the diffraction limit and aberrations.

NION ULTRASTEM 200 and NION CHROMATEM

The two Cs-STEM electron microscopes used in this thesis are the NION ULTRASTEM 200 and the NION CHROMATEM.

For the NION ULTRASTEM 200, we find mainly from the bottom of the column the cold field emission (CFEG) electron gun, 3 condenser lenses (CL1 to CL3), a C3/C5 aberration corrector, an objective lens, projector lenses (PL1 to PL4) and different signal detectors such as BF (Bright field), HAADF (High Angle Annular Dark Field) or EELS detectors [84] (see figure 3.3). The CFEG electron gun provides emission stability, high brightness of about $10^9 A.cm^{-2}.sr^{-1}$, and a low energy spread of about 0.35 eV [84]. The condenser lenses are beneficial for illuminating the material being probed and adjusting the probe size and the beam half-angle convergence (α in figure 3.3.**b**). The C3/C5 corrector corrects or attenuates geometric aberrations up to 5th order thanks to a set of magnetic quadrupoles and octupoles. The objective lens defines the collection angular range of electron to obtain a fine electron beam on the probed material [79]. The projector lenses allow the optical coupling of the transmitted electrons resulting from the different processes in the sample to the different HAADF, BF, or EELS detectors of the electron microscope. A full description of the column can be found in [84, 85]. With this instrument, we typically achieve at 100 keV, spatial and spectral resolutions of about 0.8 Å and 0.35 eV, respectively.

Another essential element is the Ronchigram or shadow image, which gives an overview during the microscope's alignment and aberration correction steps. This image is obtained from a CCD camera (retractable) [79] placed before the EELS spectrometer. This camera is also used to acquire

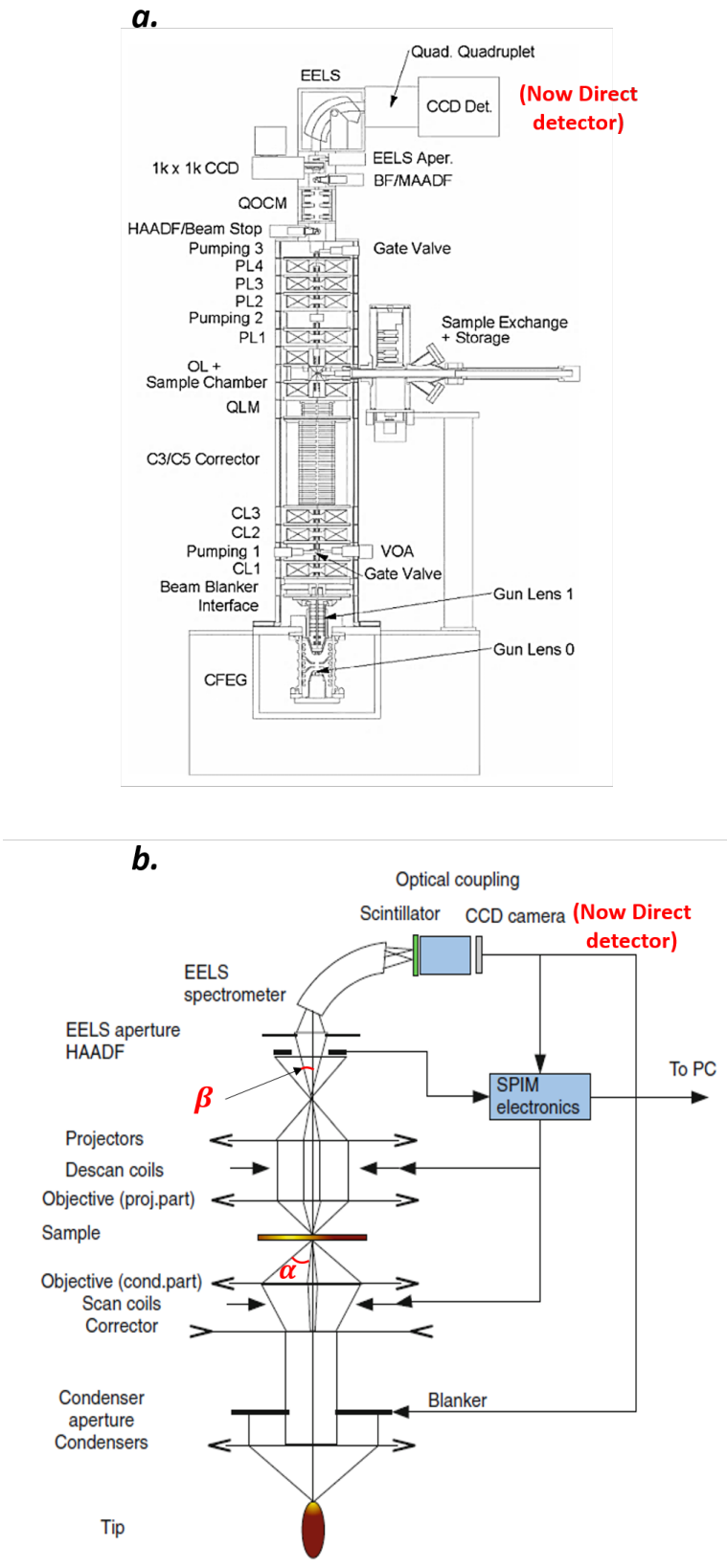

FIGURE 3.3: *a*. Scheme of the NION ULTRASTEM 200 electron microscope column. The figure is adapted from [84]. *b*. Simplified representation of a Cs-STEM, with the path followed by the electron beam in the column. The figure is adapted from [83].

diffraction information in reciprocal space in our experiments carried out on NION CHROMATEM.

The NION ULTRASTEM 200 and the NION CHROMATEM share almost the same elements in the microscope column, except for the sample insertion modes, the presence of a monochromator on the NION CHROMATEM microscope, and the possibility to perform on the NION CHROMATEM *in situ* experiments under liquid nitrogen. The α-monochromator[3] used on the NION CHROMATEM (see figure 3.4), placed before the CL1 condenser lens, consists of 21 optical layers [13]. The monochromator essentially disperses the beam in energy, then filters or selects it in energy, and finally recombines it for re-injection into the electron column. With this built-in system, Krivanek *et al.* [13] obtained spatial and spectral resolutions of about 12 meV and 1.2 Å at 60 keV, respectively. The insertion of the sample holder is also different, depending on whether we are working with the NION ULTRASTEM 200 or the NION CHROMATEM. On the NION ULTRASTEM 200, the sample holder containing the investigated specimen is deposited in a removable magazine and placed in the microscope in the "Sample exchange + Storage" area in the figure 3.3. Then, an automatically controlled retractable arm picks up the side-entry sample holder and takes it to the microscope column [84]. On the NION CHROMATEM, the side-entry sample holder is inserted manually. This specificity allows, for instance, for the sample to be subjected to external stimuli, such as cooling under liquid nitrogen, from the outer part of the sample holder which is not in the microscope.

Both microscopes have single and double-tilt sample holders. The double-tilt sample holders, widely used in our experiments, allow the sample to be tilted up to plus or minus 30 degrees [82] in two different directions. These double-tilt versions allow us to place in zone axis conditions, equivalent to placing in the direction of high crystal symmetry and thus in the conditions for observing atomic columns at resolutions of the order of the angström.

The NION CHROMATEM also has special HennyZ sample holders using MEMS systems, which have allowed us to perform experiments at variable

[3] It is so called because of the trajectory described by the beam in the monochromator, evoking a similarity with the Greek letter α

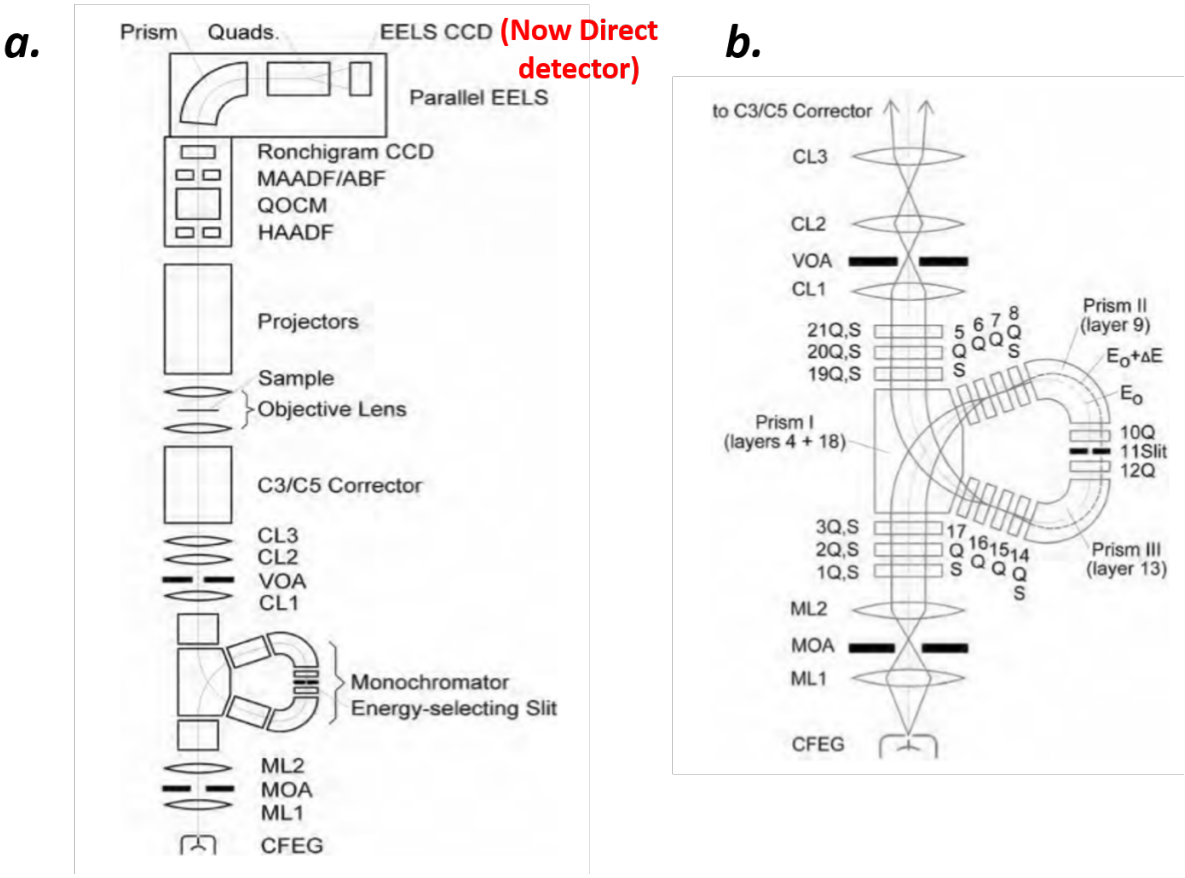

FIGURE 3.4: *a*. Scheme of the NION CHROMATEM column. *b*. Representation of the monochromator incorporated in the NION CHROMATEM. The figure is adapted from [13].

temperature between about 125 K and 300 K, at spectral resolutions of a few tens of meV and spatial resolutions in the nanometer range.

As mentioned above, the informations gathered from these microscopes, i.e., the structure, chemistry, or electronic properties of the sample being probed, come from signals explicitly obtained on the HAADF detectors, the EELS spectrometer, and the Ronchigram CCD camera for diffraction. In the following sections, we will describe these in more detail.

High Angle Annular Dark Field (HAADF) imaging

The transmitted electrons resulting from the elastic scattering process are incoherent in nature when they are scattered at high angles, at several tens of mrad. We exploit this effect with the HAADF high-angle annular detector,

ranging from 80 to 240 mrad [84], which is used here to collect these electrons.

The intensity obtained from the HAADF detector [78] is proportional to $I_{HAADF} \propto NtZ^{4/3}$. Here, N is the number of atoms per unit volume, t the thickness of the material probed, and finally, Z the atomic number.

The HAADF intensity is directly related to the atomic number for uniform sample thickness and sample homogeneity. In these conditions, the image contains a chemical contrast. Therefore, the higher the atomic number Z, the brighter the element will appear on the HAADF image. For example, we can observe in the figure 3.5, a HAADF image acquired on one of V_2O_3 thin lamellas in the $[\bar{1}\bar{1}0]_h$ zone axis . We clearly distinguish the atomic columns of vanadium (Z = 23), which appear bright on the image. Oxygen (Z = 6) does not almost contribute due to its low atomic number.

The images acquired from the HAADF imaging mode are generally easier to interpret than those acquired in the BF mode. BF imaging mode represents a coherent mode producing phase contrast images whose interpretation requires simulations [81]. However, the image acquired in HAADF can encounter a reversal of contrast due to significant variations in thickness. The samples investigated in this thesis were prepared to obtain a uniform thickness as best as possible.

Electron Energy-Loss Spectroscopy (EELS)

EELS spectroscopy exploits the inelastic scattering effects that occur during the interaction of the incident electron beam with the probed sample. It studies the energy loss spectrum of the transmitted electrons resulting from this process and can inform about the material's optical, electronic, or chemical properties.

The spectrometer used for EELS is a magnetic prism. It is used to separate the inelastically scattered transmitted electrons along different trajectories depending on their energy and, therefore, the losses encountered in the material. This separation or dispersion takes place along a direction called the dispersion direction [83]. Before the spectrometer, there is the quadrupole-octupole coupling module (QOCM in figure 3.3) composed of

3 pairs of quadrupoles-octupoles, whose role is to correct the electronic spectrum's first, second, and third order aberrations essentially [84].

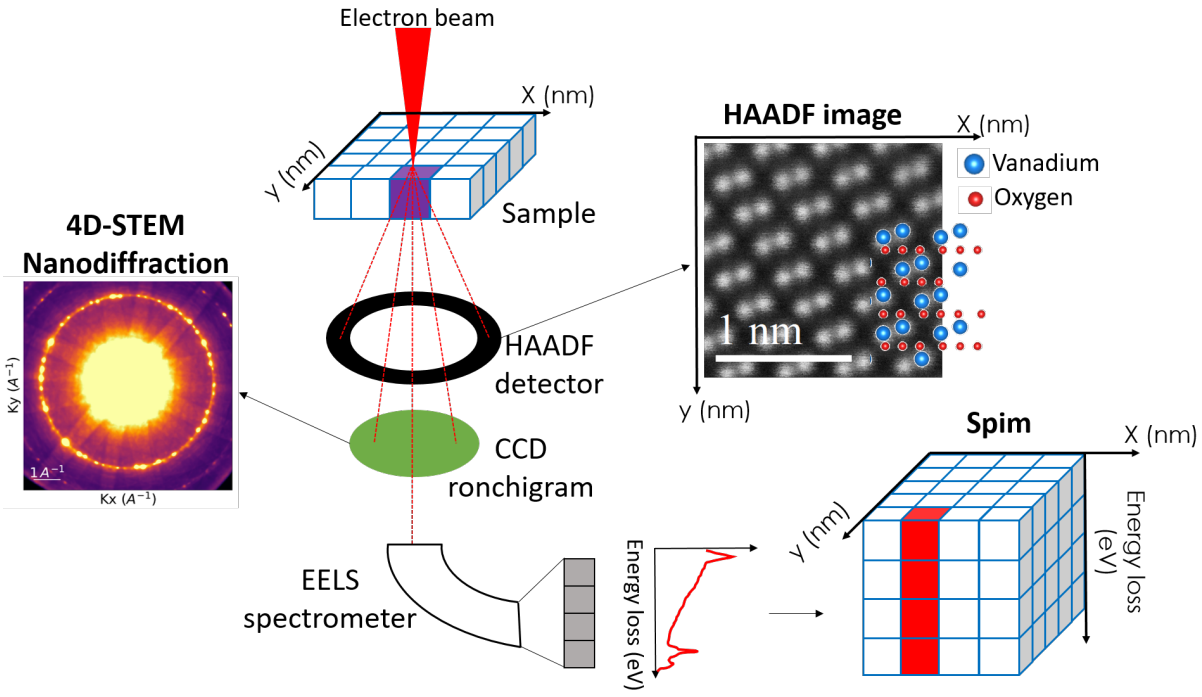

FIGURE 3.5: Representation of the electron-sample interaction and the resulting detection of different signals. HAADF, diffraction and EELS informations are obtained. The figure is adapted from [82, 86].

The electrons separated in the spectrometer and focused according to this energy dispersion or losses are finally transferred to the **Medipix 3** direct detection camera (installed on both the NION ULTRASTEM 200 and the NION CHROMATEM) to form the EELS spectrum. This direct detection camera has a better PSF (point spread function) or instrumental response than traditional CCD or CMOS cameras due to the direct detection of electrons, and also has negligible readout noise [87, 88]. The only limiting factor (with shot noise) for this camera is the gain variation noise, corresponding to the non-uniform amplification of the signal in the different channels of the detector. This problem is solved, in our case, by acquiring an image during uniform illumination of the camera without sample, at the same accelerating voltage of the microscope used during the experiments (100 keV for our acquisitions). The

correction of the gain variations is finally obtained by dividing the acquired EELS spectra by this image. Therefore, the EELS spectra acquired from the **Medipix 3** have a much better signal-to-noise ratio (SNR) compared to a CCD camera. Nevertheless, we would like to point out that the first monochromated EELS experiments at NION CHROMATEM were carried out using the KURO CMOS camera before the installation of the Medipix 3 in September 2021. The KURO CMOS, which uses a scintillator to convert electrons into photons before detection, has a worse PSF than the Medipix 3. In addition, the SNR of the KURO CMOS, compared to the Medipix 3, is worse due to the presence of readout noise or dark current [4], for instance. We would also like to point out that EELS noise is considered as a mixture of Poisson and Gaussian noise [89] (although predominantly Poissonnian). Statistical methods such as PCA (principal component analysis), which we will present later, are used to limit the influence of noise in the data analysis.

EELS spectrum-image (Spim)

The spectroscopic information acquired during this thesis was obtained by making spectrum-images (spims). The spim is a data cube (see figure 3.5), where each pixel of coordinates (x,y) representing the probe's position in the investigated region is associated with the corresponding EELS spectrum [90]. The spim is, therefore, the mapping of the spectroscopic signatures resulting from the electron-sample interaction and coming from EELS spectrometer.

About EELS spectrum

The energy loss encountered by the incident electrons as they pass through the material is given by [91]:

$$\Delta E = \int_0^\infty \hbar\omega\Gamma(\omega)\, d\omega \tag{3.5}$$

$\Gamma(\omega)$ here represents the probability for the electrons to loose an energy of amount $\hbar\omega$. This $\Gamma(\omega)$ probability for bulk excitations is also proportional

[4] The dark current is the thermal electronic leakage current, generated by the CCD camera [81].

to $Im(\frac{-1}{\epsilon(\omega)})$, representing the electron energy loss function introduced above. This loss function is the quantity measured in EELS [78].

In the expression given above, $\Gamma(\omega)$ or $\epsilon(\omega)$ do not admit any dependence on $\mathbf{q}$, the momentum transferred by the electrons. Indeed, in the experiments carried out in EELS in this thesis, we work at $q \approx 0$, i.e., under conditions where the electrons mainly collected are scattered inelastically at very small angles, thus leading to a nearly zero momentum transfer. These conditions are determined by the EELS aperture at the entrance to the spectrometer, which defines the collection half-angle β (see figure 3.3) of these inelastically scattered transmitted electrons [78].

An important point to consider in EELS is the delocalization effect of inelastic scattering due to the long-range electrostatic behavior of this interaction. The impact parameter b, which represents the maximum distance between the atom and the incident beam, from which the beam can induce an energy loss ΔE , can be approximated by $b \approx \frac{hv}{\Delta E}$, where h is Planck's constant and v the velocity of incident electrons [92, 93]. Thus, for a given incident beam, the impact parameter b decreases when the energy losses increase. It is of the order of a few nanometers for the plasmonic excitations, which occur for losses of a few eV or even a few tens of eV, and around 0.5 nm for energy losses beyond 100 eV [81].

The EELS spectrum consists of three regions, namely, the zero loss peak (ZLP), the low-loss region, and the core-loss region, as shown on figure 3.6 . The ZLP, which we can also include in the low-loss region, is the most intense peak in an EELS spectrum. It is produced by electrons that encounter almost no energy loss during electron-sample interaction. Its FWHM gives us an indication of the spectral resolution of the spectrometer [78]. In monochromated experiments conducted in EELS on the NION CHROMATEM, the ZLP FWHM ranges from 40 meV to 80 meV.

The low-loss region

The low-loss region extends from 0 to 50 eV and includes excitations such as excitons, interband transitions, or collective oscillation modes such as phonons or plasmons [81]. This region can also provide information on the optical gap of the probed material, provided that the ZLP tail does not extend too far into

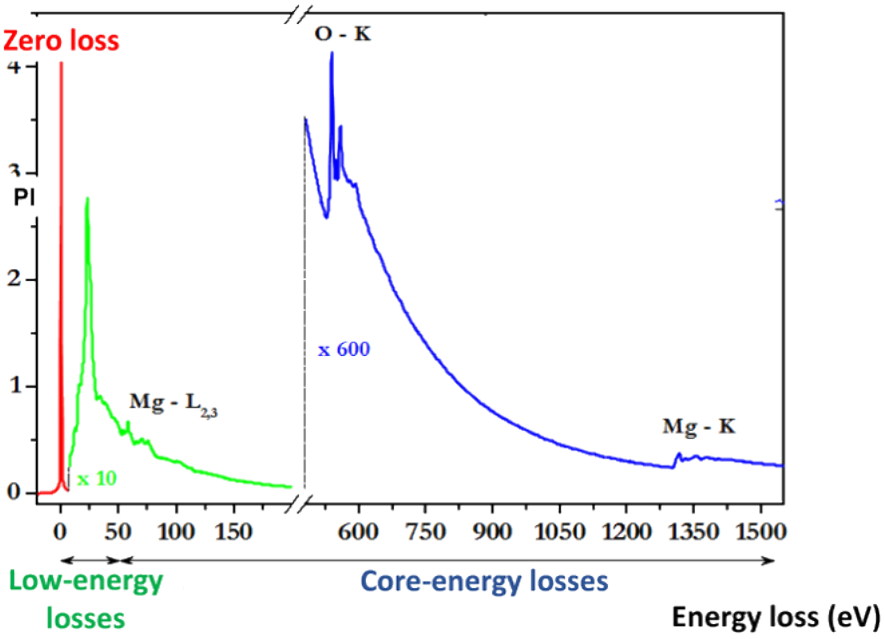

FIGURE 3.6: Representation of the ZLP, low-loss and core-loss regions of the EELS spectrum. The figure is adapted from [90].

the observation area. The optical and electronic properties of the sample are investigated in the low-loss region.

We were particularly interested in this region during this thesis. Indeed, previous EELS studies were conducted by Abe *et al.* in the low-loss region on pure V_2O_3 [69] (PM and AFI phases investigated) and on 1.2 % Cr-doped V_2O_3 [70] (PI, PM, and AFI phases investigated). These studies indicate the presence of a spectroscopic signature at about 1 eV, observed only in the PM phase or the metallic state, as shown on figure 3.7. They attribute this signature to an interband plasmon. Kramers-Kronig calculations for the dielectric function $\epsilon(\omega) = \epsilon_1(\omega) + i\epsilon_2(\omega)$ reveal both the existence of a volume plasmon (obtained for $\epsilon_1(\omega) = 0$) and an interband transition (obtained for a maximum of $\epsilon_2(\omega)$); this at about 1 eV. Experiments carried out at variable temperature on our side in the low-loss region for the PM and AFI phases in pure V_2O_3, also indicate the presence of a spectroscopic signature at 1 eV only in the PM metallic state (see figure 3.7).

As we have noted, this spectroscopic feature is an ideal probe for determining our samples' metallic or insulating state. We used it for this purpose

during the investigations carried out on the electronic state.

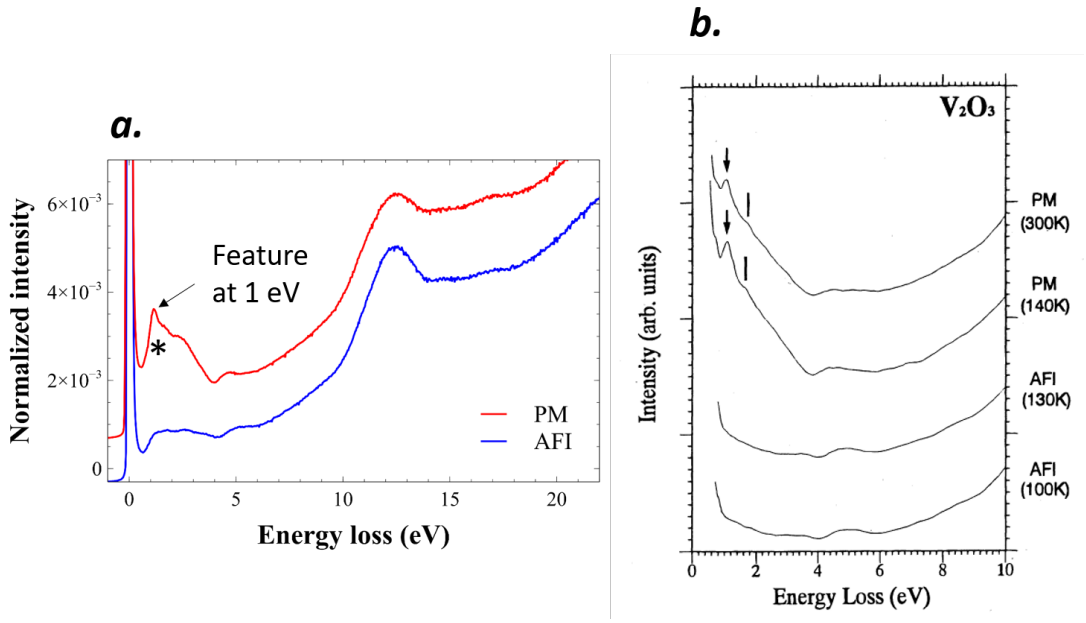

FIGURE 3.7: *a*. Low-loss spectra obtained in the PM and AFI phases on pure V_2O_3 thin films. The spectroscopic feature at 1 eV is observed only in the metallic state. *b*. Low-loss spectra in the PM and AFI phases obtained by Abe *et al.*. The 1 eV spectroscopic characteristic is also observed only in the metallic state. The figure is adapted from [69].

The core-loss region

The core-loss region results from the electronic excitation of the inner atomic shells in the sample to unoccupied electronic states [81]. It extends from 50 eV to a few keV. Considering the dipole approximation, where $q \approx 0$, the loss function $Im(\frac{-1}{\epsilon(\omega)})$ for these high energy losses is proportional to the complex part of the dielectric function $\epsilon_2(\omega)$, the absorption term [78]. EELS spectra in the core-loss region are thus often compared with spectra obtained in XAS. The core-loss region can tell us about the chemical elements present in the sample, their oxidation states, and the nature of the atomic hybridizations [81], for instance.

The spectra acquired for a thin lamella of pure V_2O_3 in the PM and AFI phases are shown in Figure 3.8 . The spectra are almost similar to those of

Abe *et al.* [69] (see figure 3.8). We distinguish the vanadium L_3 and L_2 edges ($V - L_{2,3}$) at 516 and 522 eV, respectively. They result from the spin-orbit splitting of the vanadium 2p states and correspond to transitions from $2p_{3/2}$ to 3d vanadium orbitals for the L_3 edge, and from $2p_{1/2}$ to 3d vanadium orbitals for the L_2 edge. The regions observed above these edges also show some spectroscopic features, indicated by arrows. These regions are included or belong to the so-called energy-loss near-edge structure (ELNES). The features observed in ELNES are influenced by various effects such as local coordination or atomic valence states and can therefore provide information about these effects [81]. The ELNES, extending over the first 50 eV of the ionization threshold, represents in a first approximation, the local density of unoccupied states in the conduction band [78]. However, this interpretation is no longer valid for transition metals L edge, as in this case where electronic correlations are important. Indeed, in these situations, the shape observed in ELNES (for vanadium in this case) emanates from 2p - 3d Coulomb, 3d - 3d coulomb, and exchange interactions [94, 95]. It is, therefore, difficult to directly assign the structures (indicated by arrows in figure 3.8) observed in this region. We can, however, make qualitative observations between the metallic PM and insulating AFI phases. The shoulders at 512 eV and 519 eV (indicated by arrows) on the V-$L_{2,3}$ edge (see figure 3.8) in the PM phase transform into peaks in the AFI phase. The shoulder at about 514 eV (indicated by an arrow) is also much less marked in the PM phase than in the AFI phase. Finally, we observe a change in shape on the V-L_2 edge at about 522 eV (also indicated by an arrow). All these observations perfectly agree with Abe *et al.*'s core-loss observations on pure V_2O_3.

In these spectra, we also distinguish the O-K edge, producing peaks at 529 and 532 eV in the PM phase. It corresponds to the electronic transitions from 1s to 2p oxygen core level states hybridized with vanadium 3d orbitals (t_{2g} for the 529 eV peak and e_g^σ for the 532 eV peak). Comparing the core-loss spectroscopic signatures for the PM and AFI phases, we notice an upward shift of about 0.4 eV on the O-K edge during the metal to insulating state transition. These results are still in agreement with those of Abe *et al.*.

All these changes presented on the V-$L_{2,3}$ and O-K edges are also observed during the phase transition between PM and PI. Indeed, the spectroscopic

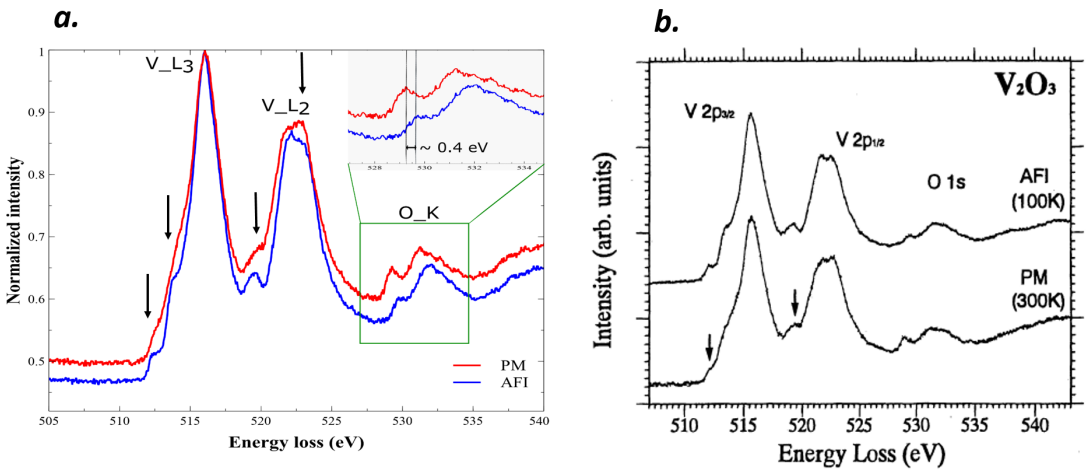

FIGURE 3.8: *a*. Core-loss spectra in the PM and AFI phases, acquired on V_2O_3 thin films. An upward shift of about 0.4 eV is observed on the O-*K* edge from PM to AFI. *b*. Core-loss spectra in PM and AFI phases of V_2O_3, acquired by Abe *et al.*. Identical observations are made. The figure is adapted from [69].

measurements carried out by Park *et al.* [49] in XAS on the one hand, and by Abe *et al.* [69] in EELS core-loss on the other hand, presented in figure 3.9, show relative similarities between the spectra acquired in the AFI and PI phases. However, the peak at around 512 eV and the change in the shape of the V-L_2 edge are much less marked for the PI phase. These small differences could be due, in a first approximation, even if we cannot assign these structures, by the differences in a_{1g} orbital occupation rate [5] between these two phases, which also contribute partly to these observations. Finally, all the spectroscopic changes observed in the core-loss region can, therefore, also be used to determine the electronic state of our samples.

Nanodiffraction and microdiffraction experiments

The observation of the structural properties in variable temperature on V_2O_3 thin lamellas investigated during this thesis was made possible thanks to nanodiffraction and microdiffraction measurements.

[5] We recall that, according to Park *et al.*, the ground state for vanadium is given by an admixture of $e_g^\pi e_g^\pi$ and $e_g^\pi a_{1g}$ states. The occupation ratio $e_g^\pi e_g^\pi : e_g^\pi a_{1g}$ are 2:1 for AFI and 3:2 for PI.

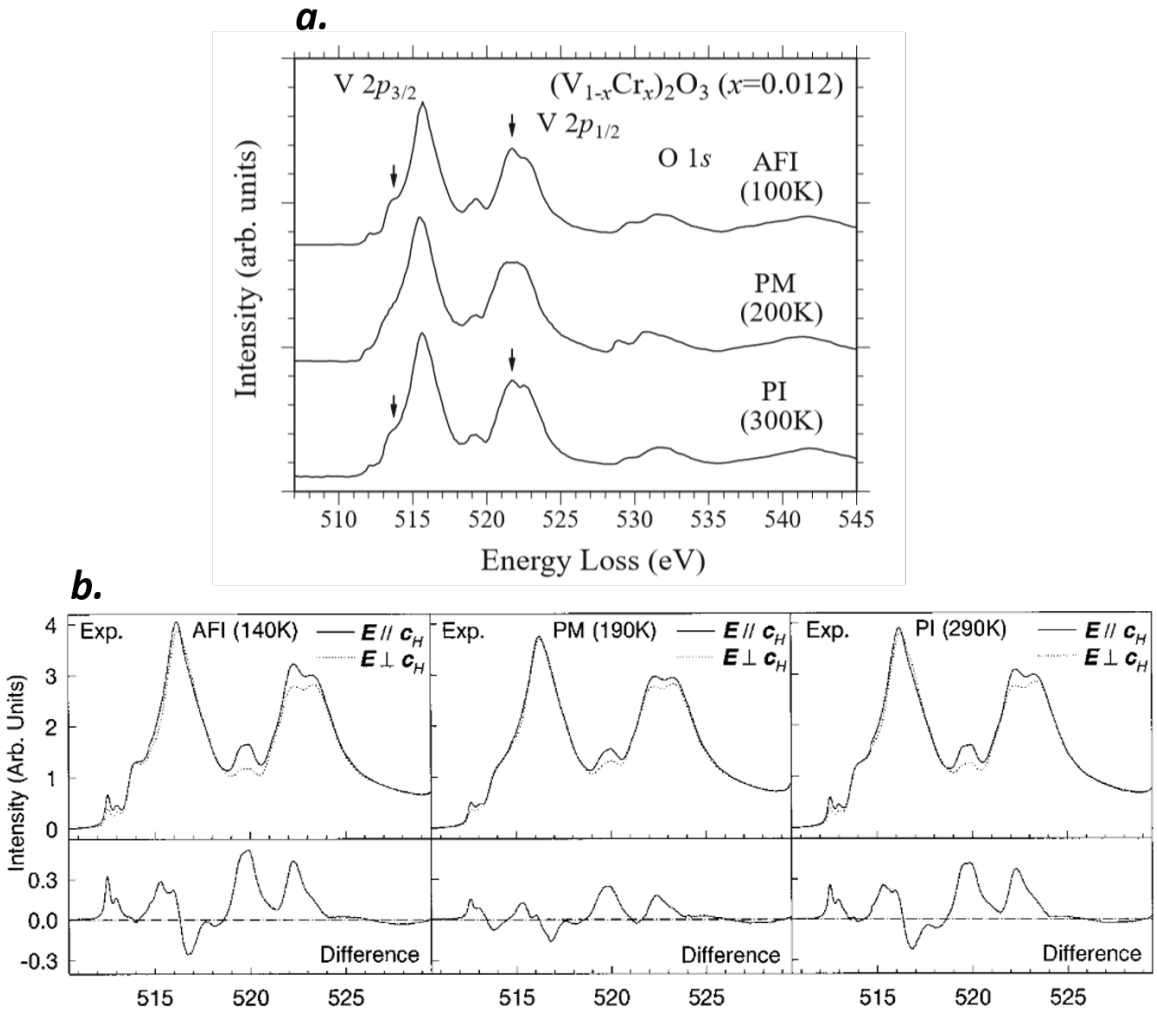

FIGURE 3.9: *a*. EELS core-loss spectra in the PM, PI, and AFI phases (for 1.2 % *Cr*-doped V_2O_3). The figure is adapted from [70]. *b*. XAS spectra in the PM, PI and AFI phases (for 1.2 % *Cr*-doped V_2O_3). The figure is adapted from [49].

Nanodiffraction consists of using a convergent electron beam to produce the diffraction pattern associated with the structural phases present in the sample at a given temperature. The convergence half-angle α used in our case is about 3 mrad. With the convergent beam used in this technique, the reflections produced in diffraction and observed on the Ronchigram's CCD camera form discs whose diameter is proportional to α [80].

Nanodiffraction is essentially used to probe the position of the center of the Laue circle (CLC). Indeed, in crystalline materials, the reflections observed on the diffraction patterns associated with the different Laue zones[6] are organized around concentric circles, called Laue circles [96, 97]. These circles result from the intersection of the Ewald sphere with the Laue zones of different orders. When we are in zone axis conditions, i.e., when the incident beam is perpendicular to a family of planes (hkl), the CLC coincides with the position of the transmitted beam (see figure 3.10). However, when the crystal experiences a tilt of angle Φ with respect to the zone axis conditions, the CLC shifts this time from the position of the transmitted beam (see figure 3.10). Probing the position of the CLC is, therefore, an efficient way to determine the structural transition in our material, where this structural transition is mainly characterized by the tilt of the hexagonal c_h axis, from the hexagonal structure in PM towards the monoclinic structure in AFI.

This is what we have implemented in our nanodiffraction investigations by remaining throughout the variable temperature experiments in the zone axis $[\bar{1}\bar{1}0]_h$, and thus perpendicular to c_h. Under these conditions, we can determine from the CLC shift of the transmitted beam position at the structural transition, the crystal's tilt angle, and the direction associated with this tilt, as shown on the figure 3.11. We can therefore probe the structural transition. All these parameters are determined using the crystallographic software **JEMS** [98]. The spatial resolution achieved in these nanodiffraction experiments is about 5 nm.

We use a quasi-parallel electron beam to form the diffraction pattern for microdiffraction. This nearly parallel beam is obtained by performing a Kohler illumination mode. In this mode, by adjusting the focal planes of the condenser lenses, the beam is focused on the object focal plane of the objective

[6] The Laue zones represent the reciprocal lattice plane layers perpendicular to the beam.

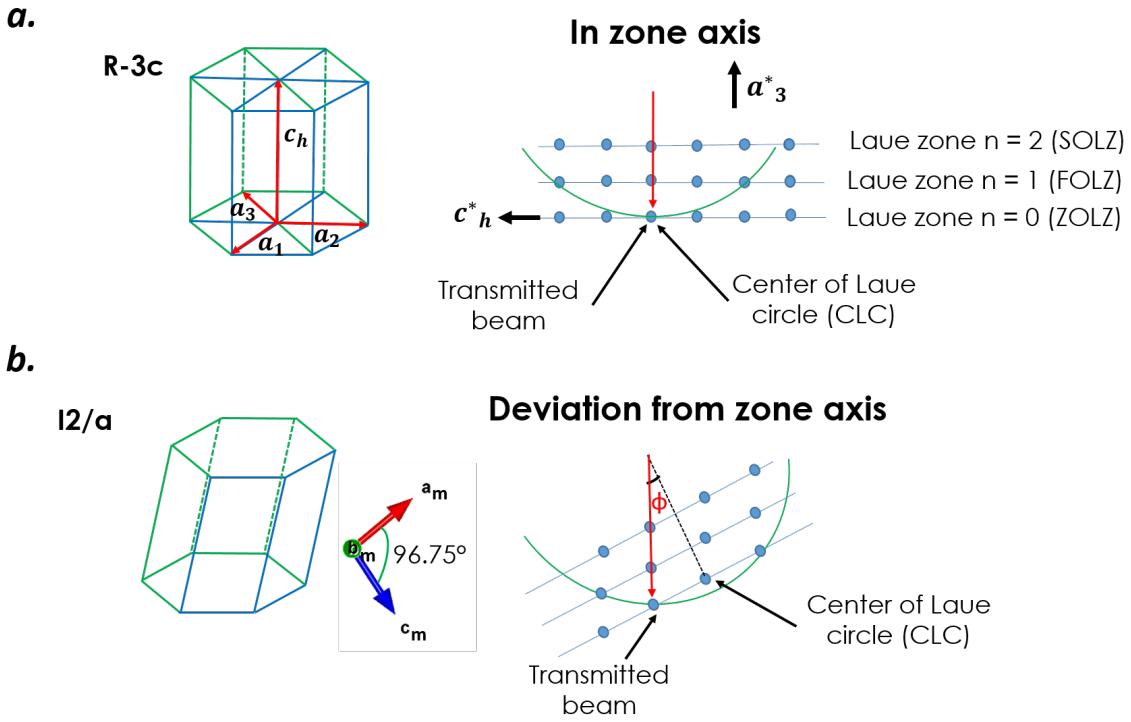

FIGURE 3.10: *a*. Representation of the Laue zones and circles in the zone axis. The positions of the transmitted beam and the CLC are identical. *b*. Representation of the Laue zones and circles after a deviation from zone axis. The transmitted beam and the CLC do not coincide anymore.

lens, leading to a nearly parallel illumination on the probed sample [99]. The reflections observed in microdiffraction correspond this time to spots and no longer to discs [80], as shown on the figure 3.12. This technique is mainly used to determine the crystal symmetry and lattice parameters (using the Pyxem python library [100, 101]). The diffraction pattern indexing is also performed using the crystallographic software JEMS. The spatial resolutions achieved in microdiffraction are about 120 nm and 10 nm (the latter was produced to observe the evolution of the material near the structural transition on a better scale).

All the optimization of the optical settings for nanodiffraction and microdiffraction acquisitions were carried out by Dr. Luiz Galvao Tizei, a researcher in the STEM group at the Laboratoire de Physique des Solides (LPS).

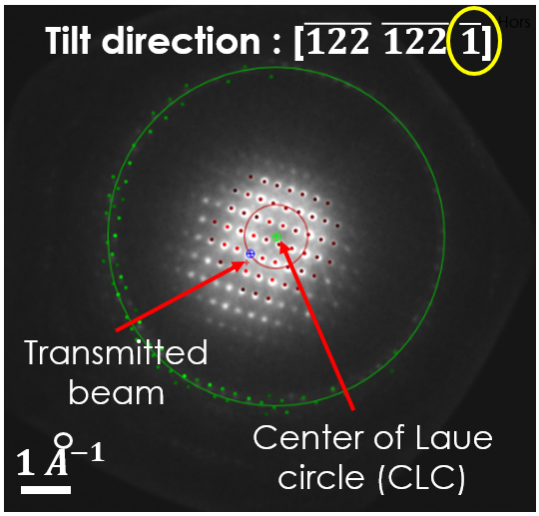

FIGURE 3.11: 4D-STEM nanodiffraction in $[\bar{1}\bar{1}0]_h$ zone axis, in AFI after structural transition, acquired on V_2O_3 thin lamella. As expected, the positions of the transmitted beam and the CLC no longer coincide.

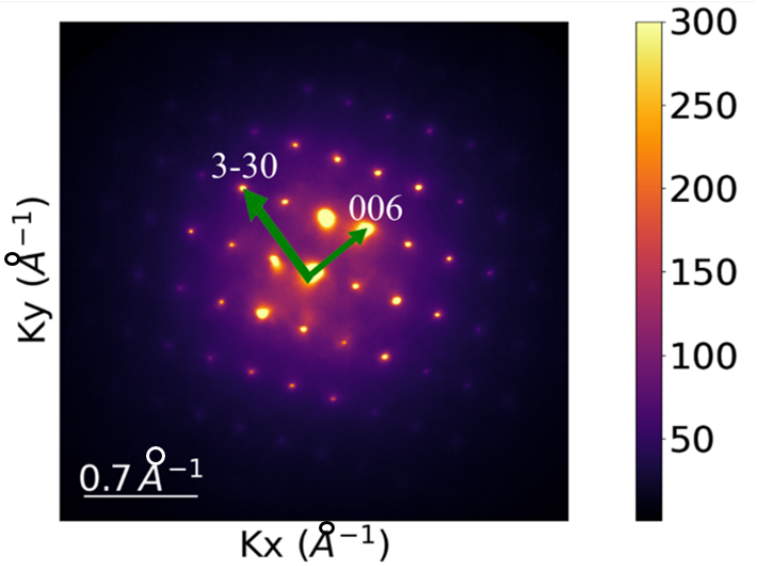

FIGURE 3.12: 4D-STEM microdiffraction in $[\bar{1}\bar{1}0]_h$ zone axis, in hexagonal symmetry, acquired on V_2O_3 thin lamella.

4D-STEM acquisition mode

The data acquired in nanodiffraction and microdiffraction were performed in the 4D-STEM mode.

4D-STEM corresponds to an acquisition mode where each position (x,y) or pixel of the probed region is associated with the corresponding diffraction pattern in the reciprocal space (k_x, k_y) [102]. This results in information in 4D, i.e., 2D information for the probed region and 2D information for the corresponding diffraction patterns.

The data acquired in 4D-STEM are generally big, each over 10 GB for those acquired in this thesis. They, therefore, require a relatively long processing time depending on the tools used for this purpose[7].

Sample growth and preparation

The V_2O_3 thin films and single crystals investigated were obtained from collaboration with the KU Leuven in Belgium and the Institut des Matériaux de Nantes (IMN) in France.

The heteroepitaxial V_2O_3 thin films from Leuven are obtained by deposition using the oxygen-assisted Molecular Beam Epitaxy (MBE) technique. The vanadium metal, which is in an evaporation cell, is deposited at a rate of 0.1 Å/s and under an oxygen partial pressure of $6.2.10^{-6}$ Torr, on a (0001)-oriented Al_2O_3 substrate at a temperature of 700°C [67]. A 56 nm V_2O_3 thin film with the hexagonal c_h axis perpendicular to the deposition surface is thus obtained. This part is entirely carried out in Leuven. After this step, we have to extract a slice and thin it to make it transparent to the electron beam; a thickness of 100 nm or less is required to probe it in transmission by the electron beam.

This thinning process was performed by Dr. Laura Bocher, a researcher in the STEM group of the LPS, thanks to the Focused Ion Beam (FIB) instrument of the NANOTEM platform (Equipex TEMPOS project) and which exploits a Scios Dual Beam equipment of the manufacturer ThermoFischer [82]. First, carbon and platinum (Pt) are deposited to protect the surface of the area of interest. The extra thickness created by the platinum deposit is also used to define this zone of interest. Then, a slice (cut parallel to c_h) a few micrometers thick is extracted from the sample thanks to gallium beam ions that dig around the zone of interest. Thanks to Pt, the extracted slice is subsequently stuck onto a copper half-grid (omniprobe). Finally, the gallium ion beam is

[7] In this thesis, 4D-STEM data are analysed on a computer with a RAM of 128 GB.

used again to complete the thinning process and obtain a slice of a few tens of nanometers (see figure 3.13). The V_2O_3 thin films thus obtained and that we have studied have a cross-section of approximately 60 nm in thickness. The samples prepared from Leuven thin films are probed statically, either at room temperature in the PM phase of V_2O_3 or at low temperature under liquid nitrogen in the AFI phase.

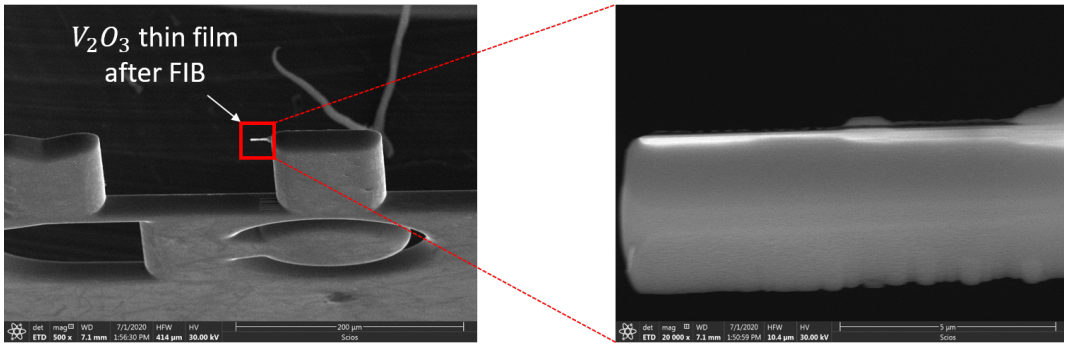

FIGURE 3.13: V_2O_3 thin film stuck on the omniprobe, after FIB preparation.

The single crystals from the IMN were prepared using a sulfur-assisted chemical-vapor transport method. The synthesis is performed in two steps. A V_2O_5 powder (Aldrich, >99.6 %) is placed in an oven at 900°C for 10 h under a 95 % Ar – 5 % H_2 gas flow. Half a gram of the single phase V_2O_3 powder obtained was then introduced in a silica tube (inner diameter 10 mm, typical length 10 cm), with 40 mg of sulfur as a vapor phase transport agent. The tube was vacuum sealed, heated up to T_{max} (950 - 1050°C) in a furnace with a temperature gradient ($\approx$ 10°C/cm), slowly cooled down to 900°C (from - 0.5 to - 2° C.h^{-1}) and finally fast cooled (- 300° C.h^{-1}) to room temperature. Such treatment allows obtaining small single crystals (typical size < 300 μm) within the preparation. Energy-dispersive X-ray spectroscopy (EDXS) analyses carried out using a scanning electron microscope JEOL 5800 confirmed the absence of sulfur in the single crystals. The IMN entirely carries out this part. These single crystals must also be thinned to be transparent to the electron beam. This step, still carried out by Dr. Laura Bocher, is performed in the same way as in the case of the thin films of V_2O_3 described above. However, in the context of our *in situ* experiments carried out exclusively with

theV_2O_3 thin lamellas from the IMN, the sample is no longer stuck to the omniprobe but rather to a MEMS thanks to lateral Pt contacts (see figure 3.14). The MEMS system, coupled with the HennyZ sample holder [15] from NION CHROMATEM, will thus allow us to vary the temperature of the sample between 125 K and 300 K.

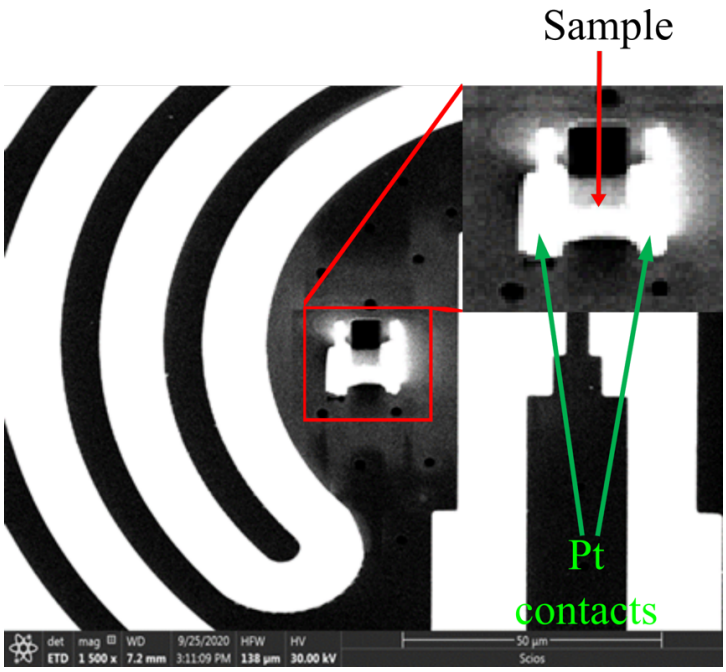

FIGURE 3.14: V_2O_3 thin lamella stuck on the MEMS used for variable temperature experiments, after FIB preparation.

In situ variable temperature experiments with HennyZ sample holder

The observation of both electronic and structural properties through the PM-AFI transition was made possible by the double-tilt sample holder HennyZ used on NION CHROMATEM. Indeed, recent instrumental developments in sample holders allow today, under cryo conditions, the observation in real time of the physical properties of materials in continuous variable temperature experiments; this down to the atomic scale. The double-tilt sample holder HennyZ, coupled to the JEOL ARM 200 F electron microscope under cryo conditions[8], allowed Tyukalova *et al.* to image at atomic resolution and

[8]The tip of the sample holder was approximately at 140 K

to study the phenomenon responsible for the degradation of $LiNi_{0.5}Mn_{0.5}O_4$ and $ZnCo_{1.8}Ni_{0.2}O_4$ nanoparticles [103]. Another cryo double-tilt sample holder, the GATAN 636, coupled to the FEI TITAN THEMIS electron microscope, also allowed El Baggari *et al.* to study the charge order in $Bi_{1-x}Sr_{1-y}Ca_yMnO_3$ (BSCMO) manganites at 93 K, still with atomic resolution [14].

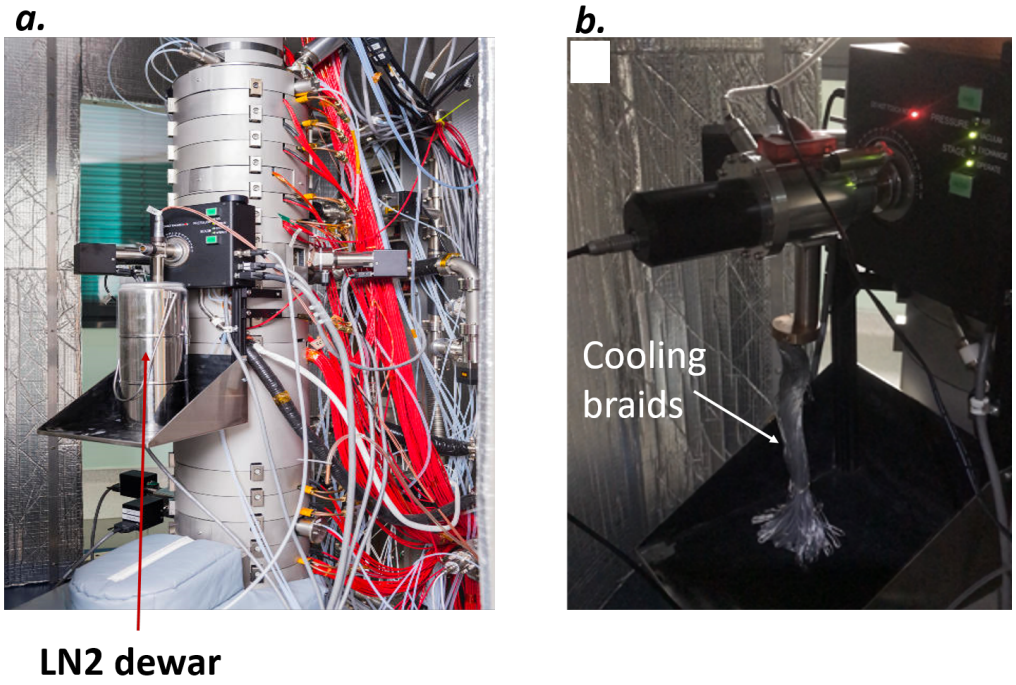

FIGURE 3.15: *a*. The sample holder HennyZ inserted in the NION CHROMATEM with the copper braid dipped in the liquid nitrogen dewar. This is the single tilt version shown in the picture, but the principle remains the same as with the double-tilt version. *b*. The double-tilt sample holder HennyZ inside the NION CHROMATEM.

The sample holder developed by HennyZ and used here is an original system. Its titanium tube allows the connection between the tip of the sample holder (where the sample is located) and the outer cylinder of the rod without any thermal coupling between these two parts [15] (see figure 3.16). This decoupling ensures the thermal equilibrium of the system by keeping the outer cylinder at the temperature of the microscope and minimizing thermal drift due to thermal contraction or expansion of the rod during variable

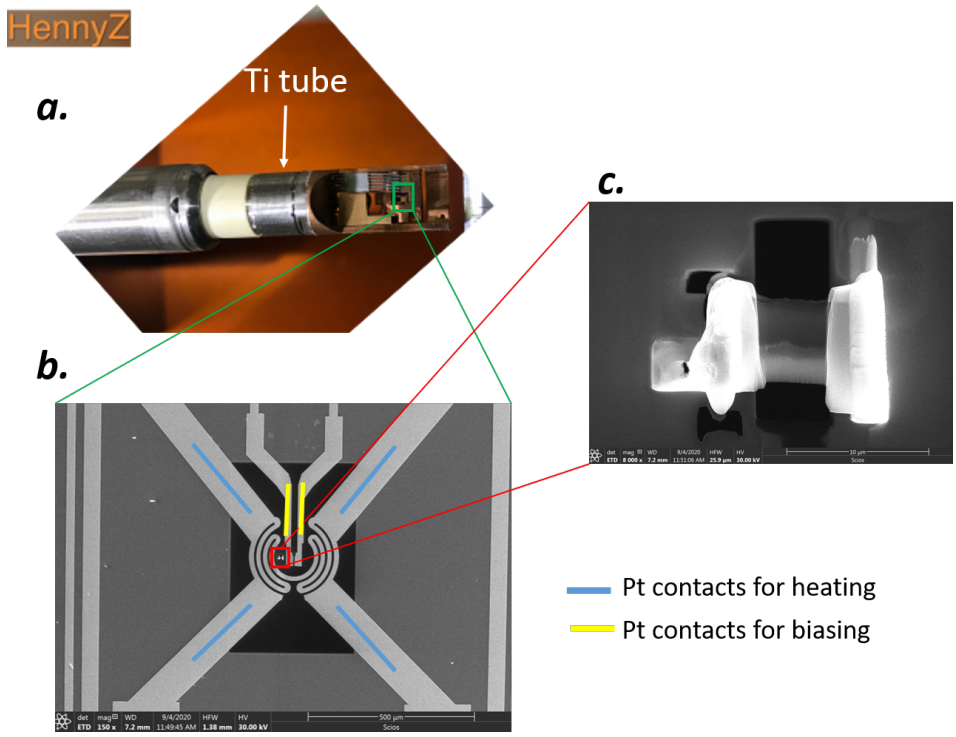

FIGURE 3.16: *a*. Tip of the HennyZ double-tilt sample holder. *b*. MEMS used for variable temperature experiments. The 4 Pt contacts used for heating are shown in blue. The 2 contacts for the biasing experiments are shown in yellow. *c*. View of the V_2O_3 thin film on the MEMS.

temperature experiments. The MEMS system used on this sample holder also allows the sample inside to be heated locally while ensuring thermal equilibrium conditions [15]. MEMS consists of a Si_3N_4 membrane in thermal contact with Pt electrodes, designed as a Heater coil. Among the Pt electrodes shown in the figure, only 4 of them are used for the variable temperature experiments. The 2 others are used for biasing experiments (see figure 3.16). By calibrating the system, i.e., thanks to the knowledge of the existing relationship between the resistance and the temperature of the heating Pt element [9], the sample deposited on the MEMS is heated to the desired temperature by injecting current through the sample holder. This step is controlled via the control system interface, the MMI (Man Machine Interface), connected directly to the sample holder.

[9]The injection of current through the Pt leads to the heating of the latter by the Joule effect.

The HennyZ sample holder rod is also connected via copper braids to the cryogenic nitrogen liquid (see figure 3.15). This has the consequence of minimizing the mechanical coupling between this rod and the cryogenic liquid [15]. The dewar used, containing the cryogenic liquid, is installed on the microscope column to protect it from possible vibrations from the electron microscope room. With this system, the sample can be cooled down to about 125 K in our *in situ* experiments.

The double-tilt HennyZ sample holder with its MEMS system, coupled with the NION CHROMATEM, has thus enabled us to carry out investigations under stable conditions. These structural and electronic investigations at variable temperatures, between 125 K and 300 K, have been performed at spatial resolutions of the order of nm and spectral resolutions of a few tens of meV.

This sample holder can also be used statically, at room temperature or under liquid nitrogen, when samples stuck on omniprobes are explored. There is also a single-tilt version with the same operating principle as the double-tilt version.

3.3 . Tools for data analysis

In the following sections, we present the tools we used to analyse and interpret the data acquired on our electron microscopes.

3.3.1 . Geometric phase analysis (GPA)

Structural defects such as dislocations or strain effects can alter the physical properties of thin films. Therefore, it seems essential to study them to better understand these films' behavior.

Methods such as GPA allow the determination of local deviations or displacements in an atomic lattice with respect to a reference lattice, from the acquisition of HAADF or BF images [104]. The intensity of these images for crystalline materials can be represented by the expression :

$$H = \sum_{\mathbf{g}} H_g(\mathbf{r}) e^{2\pi i \mathbf{g}.\mathbf{r}} \tag{3.6}$$

where

$$H_g(\mathbf{r}) = A_g(\mathbf{r})e^{iP_g(\mathbf{r})} \tag{3.7}$$

In these expressions, $\mathbf{g}$ represent the periodicities in the reciprocal space, $\mathbf{r}$ the position, H_g the associated Fourier coefficients, A_g the amplitude of the fringes or atomic planes associated with $\mathbf{g}$, and P_g the geometric phase. This geometric phase P_g represents the lateral position associated with these atomic lattice planes. This is the parameter at the heart of GPA, since it is directly related to the displacement field $\mathbf{u}$ (and therefore to strains) according to the expression [104]: $P_g(\mathbf{r}) = -2\pi\mathbf{g}.\mathbf{u}$. The knowledge of the geometric phase can thus help to quantify the strains in the atomic lattice.

In GPA, the geometric phase is determined by calculating the Fast Fourier transform (FFT) associated with the image and selecting only the Bragg reflection corresponding to $\mathbf{g}$ in the reciprocal space. A mask is employed for this purpose. From this selection and by applying the inverse Fourier transform, the intensity of the image is then reduced to [104] :

$$H_g^{'}(\mathbf{r}) = H_g(\mathbf{r})e^{2\pi i\mathbf{g}.\mathbf{r}} \tag{3.8}$$

Taking into account the equation 3.7, the expression 3.8 becomes :

$$H_g^{'}(\mathbf{r}) = A_g(\mathbf{r})e^{2\pi i\mathbf{g}.\mathbf{r}+iP_g(\mathbf{r})} \tag{3.9}$$

The amplitude and phase images can therefore be deduced and are :

$$A_g(\mathbf{r}) = Module[H_g^{'}(\mathbf{r})] \tag{3.10}$$

$$P_g(\mathbf{r}) = Phase[H_g^{'}(\mathbf{r})] - 2\pi\mathbf{g}.\mathbf{r} \tag{3.11}$$

Now, with this geometric phase, we can retrieve the value of the displacement field in the lattice, by using the relationship between these two quantities, as mentionned previously. However, calculating the quantity u of coordinates (u_x, u_y) requires two geometric phase images associated with non-collinear vectors $\mathbf{g_1}$ and $\mathbf{g_2}$, that we can determine by proceeding as above [104]. Finally, the in-plane ($e_{xx} = \frac{\partial u_x}{\partial x}$) and out-of-plane ($e_{yy} = \frac{\partial u_y}{\partial y}$) strains

we are interested mainly in our investigations, are derived from the calculation of the displacement field **u**. The strains determined in GPA are relative strains. We, therefore, need to define a reference lattice for this purpose.

GPA is applied in our case on V_2O_3 thin films in the zone axis $[100]_h$, using HAADF images of 4096 x 4096 px^2, acquired at atomic resolution. The algorithm calculates the FFT and selects, using 2 masks, the reflections associated with the non-collinear **g** necessary for strains determination. Each mask applied considers the reflections of the V_2O_3 film and the Al_2O_3 substrate, this latter of hexagonal structure and taken here as the reference area. The lattice parameters of Al_2O_3, where there is almost no strain, are $a_{sub} = 4.760$ Å and $c_{sub} = 12.993$ Å. The choice of mask size also influences the results obtained in GPA. Indeed, a small mask improves the accuracy of the strain measurements and reduces the noise, but at the expense of spatial resolution. Earlier studies carried out by Zhu *et al.* [105] in a cubic lattice showed that a mask size of $1/2a_{sub}$ seems reasonable. In our case, a mask of size $1/2a_{sub} = 1.05$ nm^{-1} achieves a good compromise. In the following, the calculated geometric phase images are refined in the reference region by minimizing the phase gradient in this area. The geometric phase images of the whole (film + substrate) are calculated again, and the relative strain maps in the plane e_{xx} and out-of-plane e_{yy} are deduced.

Generally, images acquired with scanning directions at 0° and 90° of the same region are used for GPA strain determination. Indeed, acquisitions in the slow scan direction can be influenced by flyback error, which occurs when the probe beam passes from the end of one scan line to another [82, 105]. The drift of the probed sample and scan instabilities [106] (producing vertical streaks on the FFT) can also influence the strains determined in the slow scan direction. An example of strain determination by GPA is given in Figure 3.17.

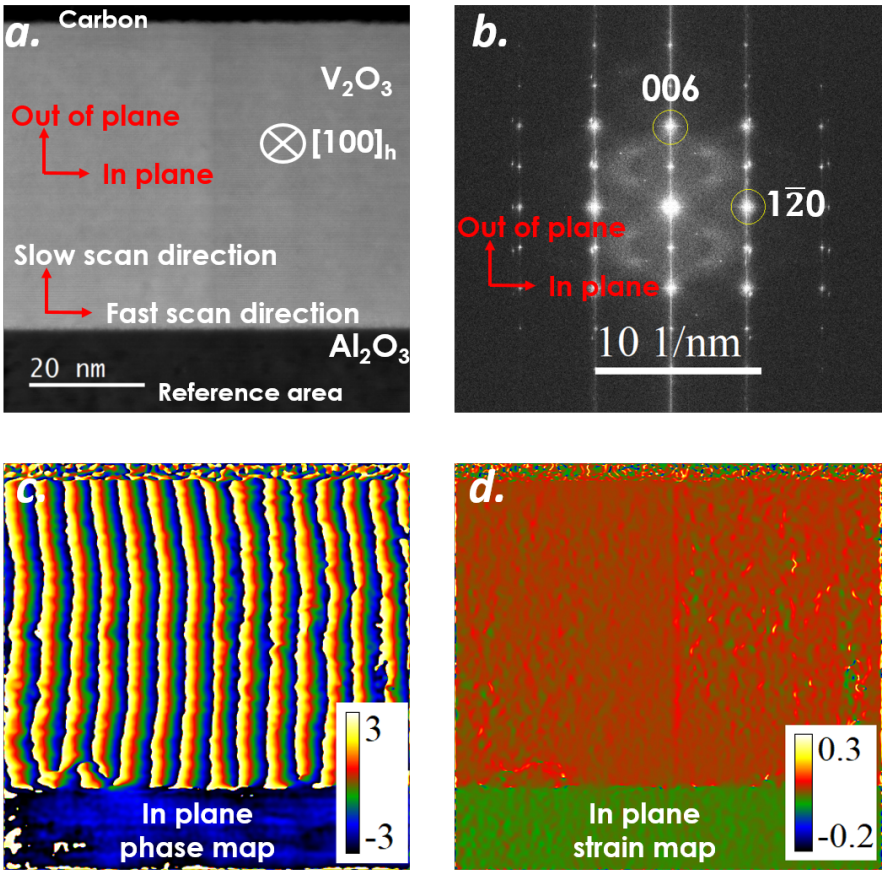

FIGURE 3.17: a. HAADF image of 4096 x 4096px^2, acquired at room temperature on a V_2O_3 thin film. b. FFT associated to the HAADF image. One can observe the vertical lines or streaks associated with the drift or scan instabilities [106] in the slow scan direction. c. Associated in-plane geometric phase map. d. Associated in-plane strain map.

3.3.2 . Principal component analysis (PCA)

PCA is a factorial multivariate statistical analysis method that reorganizes data according to existing correlations between them, following a linear orthogonal transformation [89]. It is generally used in EELS to limit the influence of noise in the interpretation of data, assuming that the relevant signals or information have a significant variance compared to the noise [89]. The PCA decomposition represents the spim by a matrix, where rows and columns are associated with energy loss channels and spectra, respectively. The variance-covariance matrix, representing the quantitative variation of

each element of the previous matrix with respect to the others, is then determined. The diagonalization of this variance-covariance matrix will allow the representation of these data in a new orthogonal basis of eigenvectors corresponding here to the principal components. Eigenvalues associated with these principal components are the variance explained by these components. Finally, denoising is obtained by taking into account only the principal components with a high variance in the signal recomposition. These components are selected by observing the scree plot, representing the principal components by decreasing eigenvalues or explained variances. The stopping criterion consists in selecting only the components located above the slope change. However, the first components below this slope are inspected due to the increase in principal components, often caused by the non-linearity of the EELS data. This non-linearity may, for example, originate from multiple scattering in the sample [89].

PCA can also be used to estimate the number of phases present in the sample, if linearity of the data is assumed [89]. An example is given in Figure 5.8. The scree plot obtained in PCA was extracted from a spim acquired in the low-loss region, on V_2O_3 thin lamella, when phase coexistence is observed. Several pre-processing steps, such as ZLP removal or signal normalization, have been performed before PCA. 3 principal components, reflecting the presence of AFI, PM, and interfacial phases, on which we will give more details in chapter 5, emerge from this scree plot.

The components deduced from the PCA are difficult to interpret, generally because of the non-orthogonality of the physically meaningful components [89]. Following the same decomposition principle as in EELS, PCA has also been used in 4D-STEM data processing to improve the performance of K-means clustering with respect to noise, for instance.

3.3.3 . Non-negative matrix factorization (NMF), vertex component analysis (VCA) and multiple linear-least square (MLLS) fitting

The NMF, VCA and MLLS fitting techniques have also been used in the analysis of spims. NMF, also a multivariate analysis method, is a technique

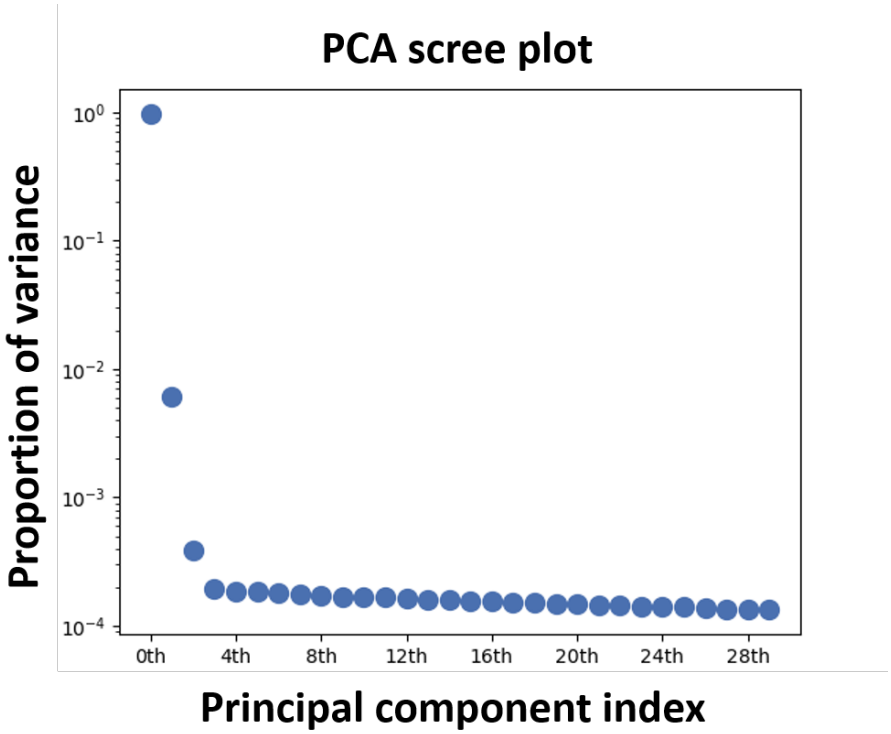

FIGURE 3.18: Scree plot obtained in PCA in the electronic coexistence region, during the variable temperature experiments on V_2O_3 thin films. 3 principal components are clearly visible.

used in EELS for spectral unmixing [107]. NMF performs a linear decomposition of the spim, applying a positivity constraint, in order to obtain decomposition components that are physically meaningful and more easily interpretable. Thus, with this technique, the spectral information and maps associated with the distinct phases present in the sample, and thus in each pixel of our spim, can be recovered. However, particular attention must be paid to the interpretation of the data, as the NMF is primarily a mathematical decomposition. NMF has been successfully used, for example, to map the phonon modes observed in EELS in MgO cubes, as observed on the figure 3.19.

VCA, also exploited in this thesis, uses the assumption of the presence of pure pixels (representing a single phase, for instance) to perform a linear decomposition [109, 110] of the spectra contained in the spim. It gave us good results, especially in the core-loss region, where the previously mentioned

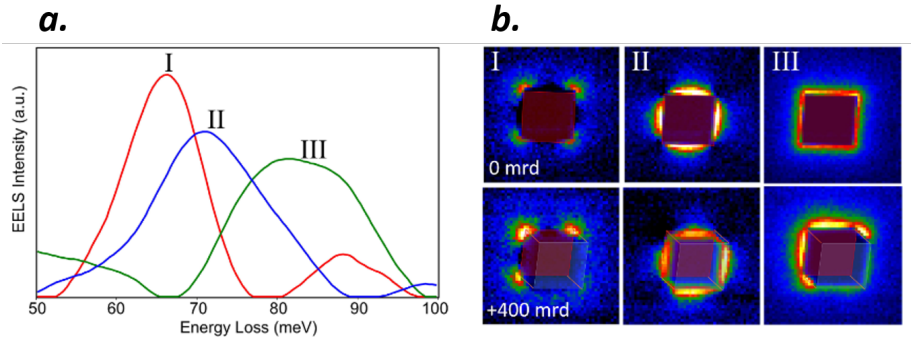

FIGURE 3.19: *a*. Spectra associated with phonon modes in the Mgo cubes, obtained in NMF. *b*. Corresponding maps of phonon modes, also obtained in NMF. The figure is adapted from [108].

electron probe delocalization effects are less important.

Finally, the MLLS fitting technique exploits the linear combination of reference spectra [83], which may be spectra representing pure phases in the sample, to map their spatial distribution in the region under investigation. Reference spectra are required for the application of this technique.

3.3.4 . Richardson-Lucy (R-L) deconvolution

R-L deconvolution has been employed in these investigations to reduce the contribution of the ZLP tail in the spectroscopic region around 1 eV. Indeed, as we will see in the next chapter, the low intensity of the spectroscopic signature at 1 eV in V_2O_3 thin films may be partly hidden under the ZLP tail. R-L deconvolution is necessary here despite using a monochromator, this latter allowing the acquisition of spectra with a ZLP FWHM of a few meV and therefore with a much smaller tail. In the probed V_2O_3 thin films, a minimum probe current of 10 pA must be ensured to successfully probe the sample and observe the spectral feature at 1 eV. This minimum current imposes a monochromation limit [10].

In order to describe R-L deconvolution, we recall that the signals or spectra acquired in EELS result from the convolution between the PSF and the original spectrum, i.e., the perfect or intrinsic spectrum resulting from the

[10]The monochromation and thus the reduction of the ZLP FWHM is accompanied by a reduction of the probe current.

electron-sample interaction. According to Gloter *et al.* [111], this PSF results from three factors: spectrometer aberrations, the energy spread of the primary beam, and the PSF intrinsic to the camera. R-L deconvolution, based on a Bayesian approach[11] and the principle of maximizing likelihood[12] [112], will make it possible to iteratively obtain an estimate of the original spectrum [111]. It requires prior knowledge of the PSF.

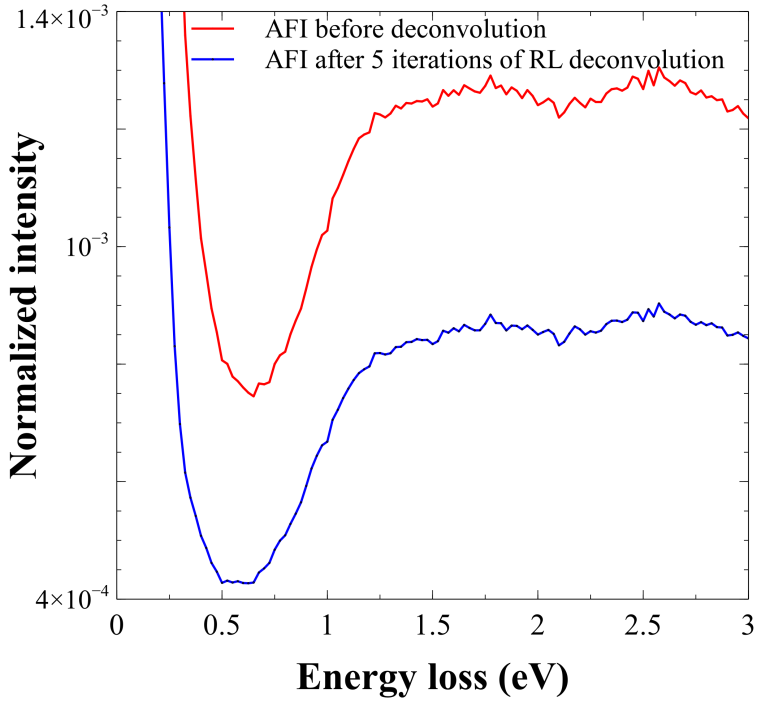

FIGURE 3.20: Representation of the spectra in the AFI phase of V_2O_3, before and after 5 iterations of R-L deconvolution.The spectrum acquired in vacuum is taken as PSF.

R-L deconvolution, like all deconvolution, is a technique that amplifies noise. Moreover, it is likely to introduce artifacts such as ring effects towards the tail of the ZLP or false spectroscopic signatures in the deconvolved spectrum beyond a certain number of iterations. The spectrum acquired in the vacuum is generally used as the PSF. However, the instrumental response function of the spectrometer may vary depending on whether the spectrum

[11] In the Bayesian approach, the observation of an event can be traced back to its origins [112]. By analogy, the observation of the spectrum convolved with the PSF can lead back to the original spectrum.

[12] Maximizing the likelihood means maximizing the degree of compatibility between the observed (convoluted) spectrum and the original or intrinsic spectrum.

is acquired with or without a sample [113, 114]. This difficulty often leads to using Gaussian, Lorentzian, or pseudo-Voigt functions to approximate the ZLP in the sample and then use it as the PSF. An example of R-L deconvolution, after 5 iterations, with the PSF taken in vacuum, is given in figure 3.20. We do observe a reduction in the tail of the ZLP after deconvolution.

3.3.5 . K-means clustering

Clustering analysis has previously been successfully applied in EELS by Torruella *et al.* to retrieve information on the composition and oxidation state of Fe_3O_4/MnO_4 core/shell nanoparticles [115]. This technique also allowed Teurtrie to study the distribution of iron in octahedral and tetrahedral sites of Bismuth Iron Garnet (BIG) [82].

K-means clustering is a classification technique that aims to group a dataset into different clusters according to their similarities. This similarity is determined using, in our case, the Euclidean distance metric. An interesting fact about this technique is that it does not modify the original data. The artifacts produced come from the wrong grouping of the data. Indeed, the calculation of similarity (with the Euclidean distance) can diverge because of the non-normalization of the data, for instance, but also because the metric is not necessarily adapted to the data type. In our case, the tests carried out previously by Teurtrie made it possible to ensure this method's robustness beforehand [82].

K-means clustering has been applied in this thesis, on EELS spims and 4D-STEM nanodiffraction and microdiffraction data. It allowed us to study the spatial distributions of the electronic and structural phases during the transitions between PM and AFI in V_2O_3. In K-means clustering, a spim and a 4D-STEM data can be represented as collections of K and L points, respectively. These points correspond to the number of pixels in the spim and the 4D-STEM data. Each of these points is associated with a p-dimensional space. For the spim, p represents the number of channels in the EELS spectrum, and the coordinates associated with the p dimensions correspond to the intensities observed in these channels. For the 4D-STEM data, p represents the number of pixels in the reciprocal diffraction space (k_x, k_y), and the coordinates in this p-dimensional space are the intensities observed at each pixel in

this (k_x, k_y) space. In the following, the K-means algorithm initializes some points (centroids), i.e., the number of clusters we have to choose and whose coordinates are randomly determined in the same p-dimensional space described above. Each point of the spim or 4D-STEM data is then attached to the nearest centroid by performing a similarity calculation via the Euclidean distance[13]. Clusters are thus formed. At the end of this step, the average point attached to each cluster is calculated and updated as the new centroid. Again, similarity calculations are performed for each point of the spim or 4D-STEM data, with the centroids that have just been updated. Several loops are performed. The final result is the one that minimizes the inertia of the clusters. Much more explanation of the K-means clustering method used in this thesis can be found in [82].

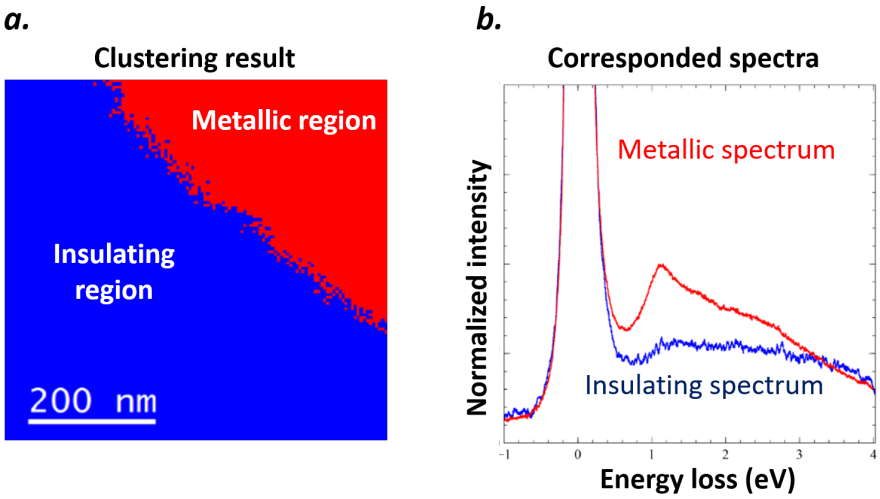

FIGURE 3.21: *a.* K-means clustering mapping of the different electronic regions in the phase coexistence zone, during the variable temperature experiments on V_2O_3 at T = 152 K. *b.* Low-loss spectra corresponding to the metallic and insulating regions.

An example is given in Figure 3.21. The spim used was acquired at 152 K, in the electronic coexistence region observed in V_2O_3 thin lamella, during the AFI to PM phase transition. For this analysis, we chose two clusters. The

[13]The Euclidean distance for two points c with coordinates $(c_1, c_2, ..., c_p)$ and e with coordinates $(e_1, e_2, ..., e_p)$ is given by $d = \sqrt{(c_1 - e_1)^2 + (c_2 - e_2)^2 + ... + (c_p - e_p)^2}$

choice of this number is usually made by estimating the number of components in PCA (if the linearity assumption holds, which is not always verified) and by directly inspecting the data. After removing the ZLP and normalizing the spim, we mapped the metallic and insulating regions in the phase coexistence regime by K-means clustering.

3.3.6 . About Pyxem, Hyperspy, JEMS software and Digital micrograph

Pyxem is a python library that we used to analyze the 4D-STEM data [101]. It allowed us to determine, for instance, the lattice parameters associated with the structural phases in V_2O_3 during the variable temperature experiments. Hyperspy is also a python library allowing the processing of multidimensional data such as spims [116]. K-means clustering analyses on spims and 4D-STEM data, R-L deconvolution, PCA, and NMF were performed using Hyperpsy. The JEMS software [98] is a crystallographic software allowing to determine zone axes, to simulate diffraction patterns, or determining the position of the CLC, for instance. Finally, Digital Micrograph (DM), also exploited, is a software package that accompanies some electron microscopes and allows the analysis of spims, BF, or HAADF images. It is used for chemical mapping, the realization of fits such as MLLS, or the execution of GPA thanks to specific plugins, for example.

3.4 . Conclusion

In this chapter, we have presented the analytical techniques and tools that enabled us to carry out our investigations in this thesis. EELS spectroscopy in the low-loss region makes it possible to investigate the electronic properties of our samples, where only the metallic state is characterized by the presence of a spectroscopic signature at about 1 eV. It is also possible to investigate the electronic properties in the EELS core-loss region, thanks to the changes observed in the V-$L_{2,3}$ and O-K edges. Nanodiffraction and microdiffraction techniques used in 4D-STEM, or the HAADF imaging mode, also allow the observation of the structural properties of the sample. Coupled with analysis tools such as GPA, R-L deconvolution, or K-means clustering, information

can be deduced to accurately characterize the electronic or structural states of the material. The NION ULTRASTEM 200 microscope, with its double-tilt sample holders for atomic resolution, and the NION CHROMATEM coupled to the HennyZ cryo double-tilt sample holder for variable-temperature experiments at the nanometric resolution, allow these investigations to be carried out. Their EELS spectrometers, fitted with Medipix 3 direct detection cameras, also acquire spectra with good SNR. These microscopes are, therefore, essential tools in this study.

Chapter 4

Local electronic, structural, and chemical properties in V_2O_3 thin films

4.1 . Introduction

Previous studies on V_2O_3 thin films have raised various questions about understanding the underlying mechanisms related to the phase transition between PM and AFI phases. The possibility of a 6 K thermal decoupling between electronic and structural transitions from PM to AFI, and thus the presence of metallic monoclinic domains, has been suggested, for instance, in V_2O_3 thin films, by McLeod *et al.* [6]. The vanishing of the PM to AFI phase transition has also been observed by Dillemans *et al.* [12] in V_2O_3 ultrathin films (around 4 nm) deposited on Al_2O_3 substrates. In addition, Schuler *et al.* [117] showed that the electronic properties of V_2O_3 thin films on Al_2O_3 substrates could vary as a function of substrate temperature and deposition rate. The electronic properties of these films could even tend towards the insulating properties of the chromium-doped V_2O_3 PI phase at room temperature. Describing the behavior of thin films is challenging, as several considerations must be taken into account when investigating these films. Indeed, epitaxial thin films may exhibit structural defects, vacancies or chemical interdiffusion at the film/substrate interface, for instance, highly likely to modify or induce new physical properties in these systems [118]. A study of these different parameters could therefore help in understanding the physical phenomena that occur within these materials.

In this chapter, we investigate the structural (by GPA) and electronic (by EELS low-loss and EELS core-loss) properties in V_2O_3 thin films and explore the elemental distribution at the film/substrate interface, with a particular focus on the room temperature PM phase. We highlight electronic and structural inhomogeneities over domains of a few tens of nanometers. Our results suggest the existence in the room temperature phase of a large volume insulating hexagonal phase coexisting with the PM phase.

4.2 . Structural properties investigation by GPA

As explained in chapter 3, GPA is a method to study the local strains or displacements in an atomic lattice with respect to a reference one. From the 56 nm V_2O_3 thin film deposited on an Al_2O_3 substrate, also already presented in chapter 3 [1], we have acquired 4096 x 4096 px^2 HAADF images at atomic resolution (all obtained on the NION ULTRASTEM microscope) and at room temperature. We have then applied GPA to investigate the structural properties of the V_2O_3 thin film. The Al_2O_3 substrate is taken here as the reference area. The lattice parameters reported in XRD based on data are $a_h = 4.972$ Å and $c_h = 13.967$ Å for the V_2O_3 thin film, and $a_h = 4.760$ Å and $c_h = 12.993$ Å for the Al_2O_3 substrate. The substrate lattice parameters observed in XRD almost coincide with those of the sapphire bulk ($a_h = 4.758$ Å and $c_h = 12.991$ Å [119]), which is not the case for the thin film. Indeed, the V_2O_3 bulk has been reported in the literature to have lattice parameters $a_h = 4.951$ Å and $c_h = 14.003$ Å [3]. The discrepancies observed here at the macroscopic scale would result from residual thermal strains in the film [120]. Due to the difference in the thermal expansion coefficient between the film and the substrate, and the clamping of the film to the substrate, the film is cooled to room temperature after deposition with a thermal expansion coefficient imposed by the substrate. This would result, for the thin film, in an increase and decrease in the a_h and c_h lattice parameters, respectively, compared to those of V_2O_3 bulk samples.

The local contrast inhomogeneities already observed in the HAADF images (figure 4.1) reveal the presence of nano-columnar structures in the V_2O_3

[1] The sample is obtained from a collaboration the KU Leuven.

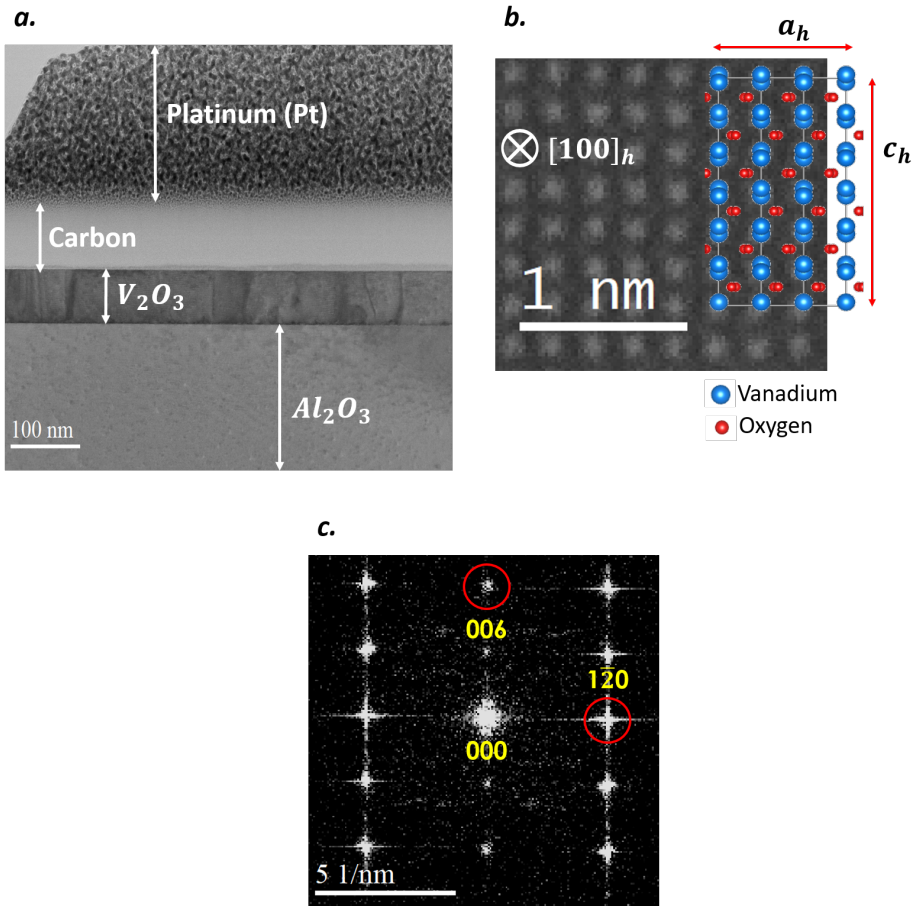

FIGURE 4.1: *a*. Low magnification HAADF image of the sample at room temperature. Nano-columnar structures seem to be observed in the film. b. HAADF image at atomic resolution in the V_2O_3 thin film, along the $[100]_h$ zone axis. *c*. FFT performed in the Al_2O_3 substrate taken here as the reference area in GPA. Reflections (006) and $(1\bar{2}0)$ are used to determine the substrate lattice parameters.

thin film. From these HAADF images acquired in the $[100]_h$ zone axis (see figure 4.1), in-plane and out-of-plane strain maps are obtained. These maps can then be used to derive the local lattice parameters a_h^{loc} and c_h^{loc} and the local (c_h^{loc}/a_h^{loc}) ratio. Indeed, the local lattice parameters are related to the in-plane (e_{xx}) and out-of-plane (e_{yy}) strains according to the expressions :

$$e_{xx} = \frac{a_h^{loc} - a_h^{sub}}{a_h^{sub}} \tag{4.1}$$

$$e_{yy} = \frac{c_h^{loc} - c_h^{sub}}{c_h^{sub}} \tag{4.2}$$

Here, a_h^{sub} and c_h^{sub} represent the substrate lattice parameters in the reference region. They are calculated by determining the inter-reticular distances d_{hkl} associated with the reflections (006) and (1$\bar{2}$0) on the FFT performed in this region (see figure 4.1). These distances are then used to derive the lattice parameters in the substrate according to the expression for the hexagonal lattice:

$$d_{hkl} = \frac{1}{\sqrt{\frac{4}{3a_h^2}(h^2 + k^2 + hk) + \frac{l^2}{c_h^2}}} \tag{4.3}$$

Typical examples of local in-plane (a_h^{loc}), out-of-plane (c_h^{loc}), and c_h/a_h ratio maps are presented in figures 4.3 and 4.6. The corresponding HAADF images for these different regions are also shown in figures 4.2 and 4.5. In figure 4.3, we notice the presence of defects towards the top of the film in region B (see the in-plane map). These defects could serve as film relaxation mechanisms, in addition of the dislocation cores near the interface and observed on the enlarged image of the interface in the in-plane map (figure 4.4). The average in-plane a_h^{mean} lattice parameters, deduced from the profiles [2] in the thin film, are 4.964 Å in region A and 4.983 Å in region B. On the out-of-plane map, we observe a significant increase in the c_h^{loc} lattice parameters towards the interface. These maxima could correspond to a deformation of the V_2O_3 unit cell, due to the accommodation of the in-plane lattice parameter to that of the (much smaller) substrate, during the first few nanometers of the film growth. This would thus induce an increase in the out-of-plane c_h^{loc} lattice parameter. We can also try to estimate the critical thickness, i.e., the thickness at which the film starts to relax via the introduction of dislocations. From the profiles carried out on the in-plane and out-of-plane maps, we observe the beginning of lattice relaxation at about 2 nm from the film/substrate interface. Our collaborators in Leuven also obtained a critical thickness value of

[2] All GPA profiles are carried out perpendicularly across the film/substrate interface.

the order of nanometer [120], from the Matthews-Blakeslee [121] relationship giving the evolution of the critical thickness as a function of the lattice mismatch between the film and the substrate (4.2 % between V_2O_3 and Al_2O_3 in the present case). The mean c_h^{mean} lattice parameters obtained from the out-of-plane map in the thin film are 13.864 Å in region A and 13.861 Å in region B. These values are much smaller compared to those obtained in XRD. Finally, the average c_h/a_h ratios in V_2O_3, deduced in regions A and B are 2.793 and 2.782 (figure 4.3), respectively. The film c_h/a_h ratio deduced in XRD, which is 2.809, is also larger than those obtained in these regions.

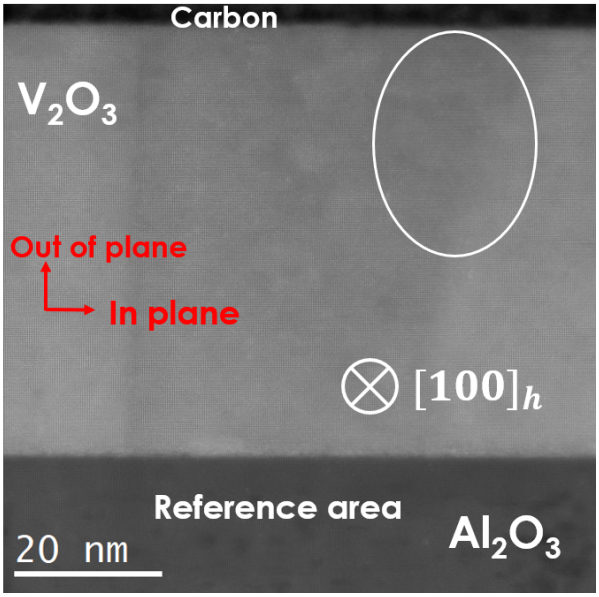

FIGURE 4.2: HAADF image corresponding to regions A and B investigated in GPA (see figure 4.3). The area indicated by a white circle corresponds to the region with defects on the in-plane map (figure 4.3).

In figure 4.6, by probing other regions of interest in the film, defects are observed towards region D, again on the in-plane local lattice parameter evolution map. These defects are associated with the dark contrast area on the HAADF image corresponding to the probed region (see figure 4.5). The mean in-plane a_h^{mean} lattice parameters deduced from regions C and D profiles, in

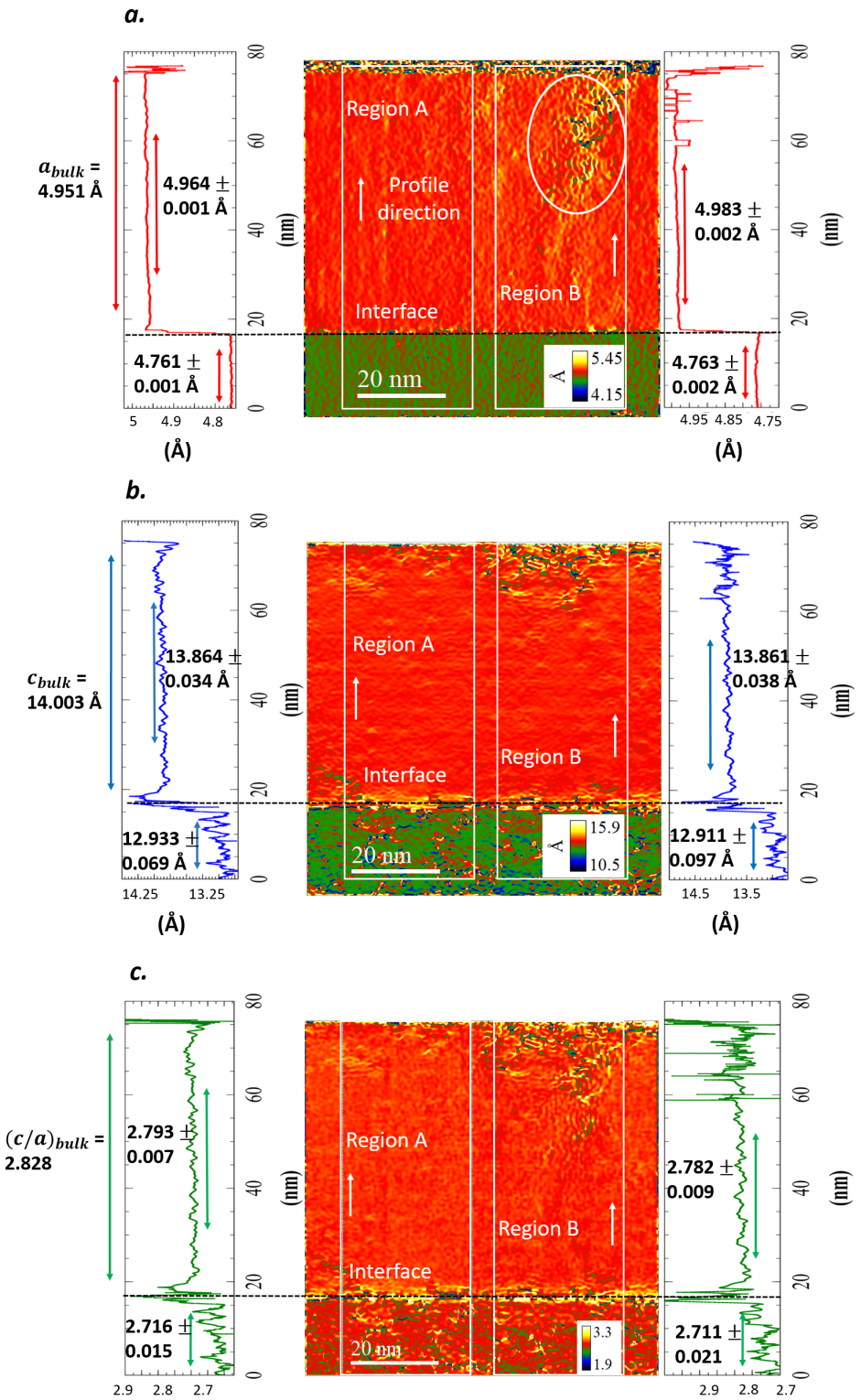

FIGURE 4.3: *a*. In-plane a_h^{loc} local lattice parameters. The region indicated by a white circle appears to have defects. The profiles carried out in regions A (left) and B (right) are also shown. *b*. Out-of-plane c_h^{loc} local lattice parameters. Profiles from regions A (left) and B (right) are shown. *c*. c_h/a_h ratio map. The profiles in regions A (left) and B (right) are shown.

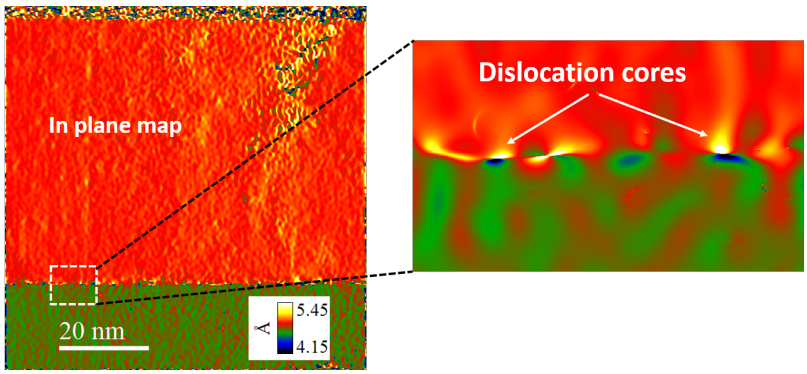

FIGURE 4.4: In-plane map where dislocation cores are located at the interface.

the film, are 4.946 Å and 4.949 Å, respectively. These values are smaller than those obtained previously in regions A and B, or compared to that obtained in XRD. These variations reflect quite well the structural inhomogeneities at the nanoscale present in the V_2O_3 thin film. On the out-of-plane map, as in figure 4.3, we also notice an increase of c_h^{loc} close to the interface, similarly as previously mentionned. The profiles realized also allow us to observe the beginning of film relaxation at about 2 nm from the interface, as previously. The deduced average c_h^{mean} lattice parameters in the thin film, also smaller than that in XRD, are 13.919 Å for region C and 13.924 Å for region D. The resulting c_h/a_h ratio values, smaller than in regions A or B, are 2.814 for region C and 2.813 for region D.

We have also performed GPA analyses in film regions that show almost no structural defects (see figure 4.7). The values obtained for a_h, c_h, and c_h/a_h ratio also show variations compared to the previous situations. Thus, in region I, we find 4.957 Å, 13.988 Å, and 2.822 for these three parameters, respectively. In region J, these parameters are respectively 4.963 Å, 13.968 Å, and 2.814. A summary of the values obtained in GPA in these different regions is presented in Table 4.1. The values deduced from these GPA analyses in the film are between 4.946 Å and 4.988 Å for the in-plane lattice parameter , between 13.759 Å and 14.061 Å for the out-of-plane lattice parameter, and between 2.777 and 2.838 for c_h/a_h ratio. These in-plane and out-of-plane lattice parameter variations in GPA can be seen in Figure 4.8. From all the V_2O_3 thin film regions analyzed by GPA, it also appears that the film relaxation starts

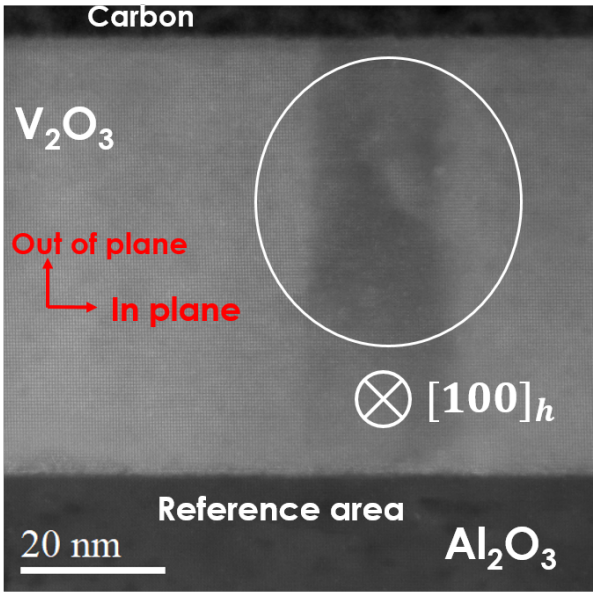

FIGURE 4.5: HAADF image corresponding to regions C and D (see figure 4.6) investigated in GPA. The region indicated by a white circle corresponds to the region with defects on the in-plane map of figure 4.6.

at about 2 nm from the interface. Structural inhomogeneities such as the local variations of the in-plane lattice parameter (a_h) observed here could be correlated to the presence of electronic inhomogeneities in the thin film. Indeed, as Homm *et al.* [67] show, an increase in the in-plane lattice parameter (by epitaxy) in pure V_2O_3 and chromium-doped V_2O_3 thin films can lead to a less metallic state, and eventually to the large volume [3] PI phase (volume $\approx$ 301.145 Å^3 for a chromium doping of about 1.1 %) at room temperature when $a_h \approx 5$ Å. The volumes determined in the thin film, up to 301.850 Å^3 (from the GPA data), also suggest the presence of a large volume hexagonal phase [4] similar to PI. Furthermore, the observations of Sakai *et al.* [122] would support this idea. They show that V_2O_3 thin films with a c_h/a_h ratio lower than about 2.80 at room temperature exhibit electronic properties similar to those of an insulator.

[3] The volume in the hexagonal phase is given by : $v = a_h^2 c_h sin(60°)$.

[4] The bulk volume in V_2O_3 is 297.261 Å^3. The volume deduced from the Leuven XRD data is also 299.017 Å^3.

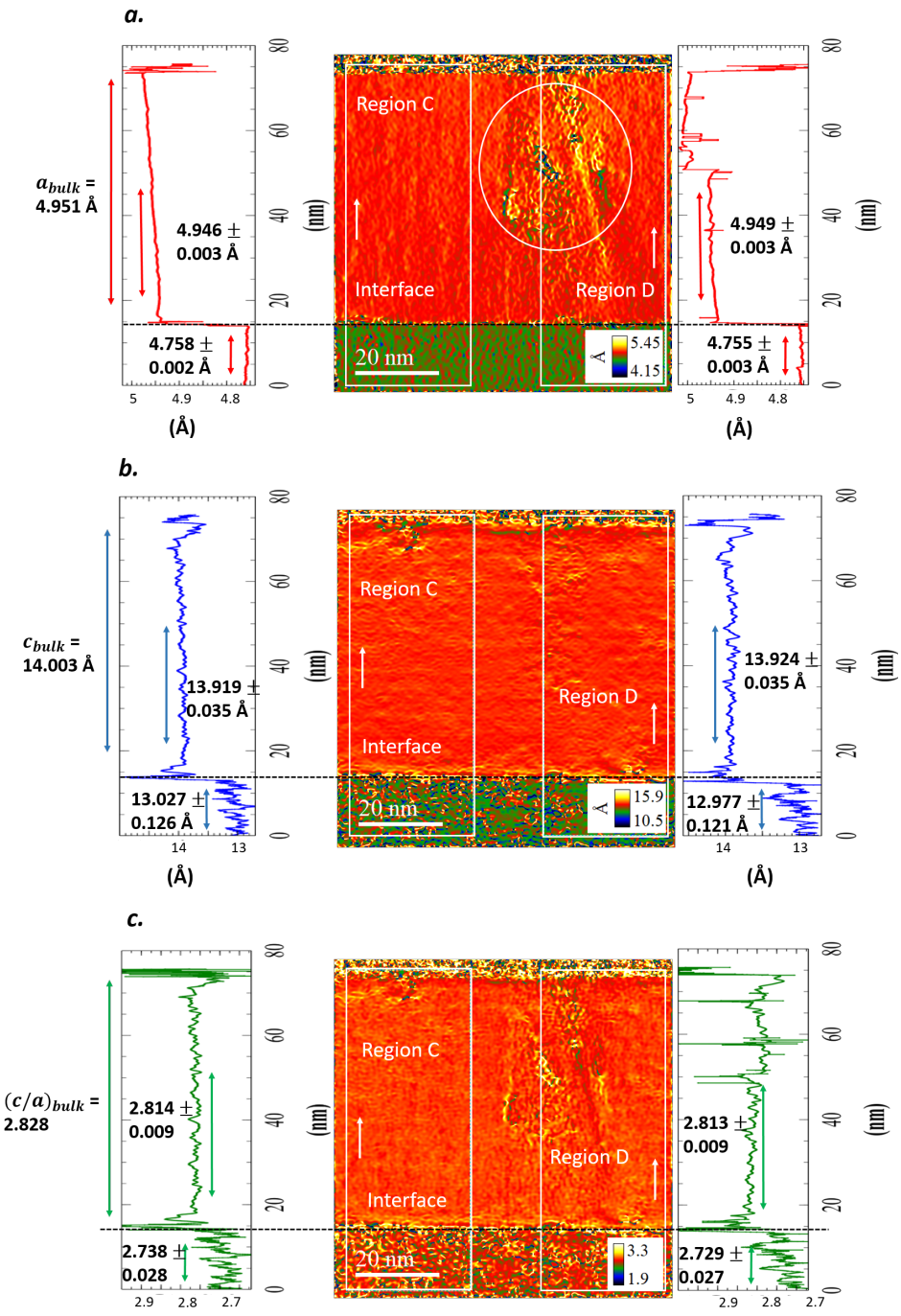

FIGURE 4.6: *a*. In-plane a_h^{loc} local lattice parameters. The region indicated by a white circle appears to have defects. The profiles carried out in regions C (left) and D (right) are also shown. *b*. Out-of-plane c_h^{loc} local lattice parameters. Profiles from regions C (left) and D (right) are shown. *c*. c_h/a_h ratio map. The profiles in regions C (left) and D (right) are shown.

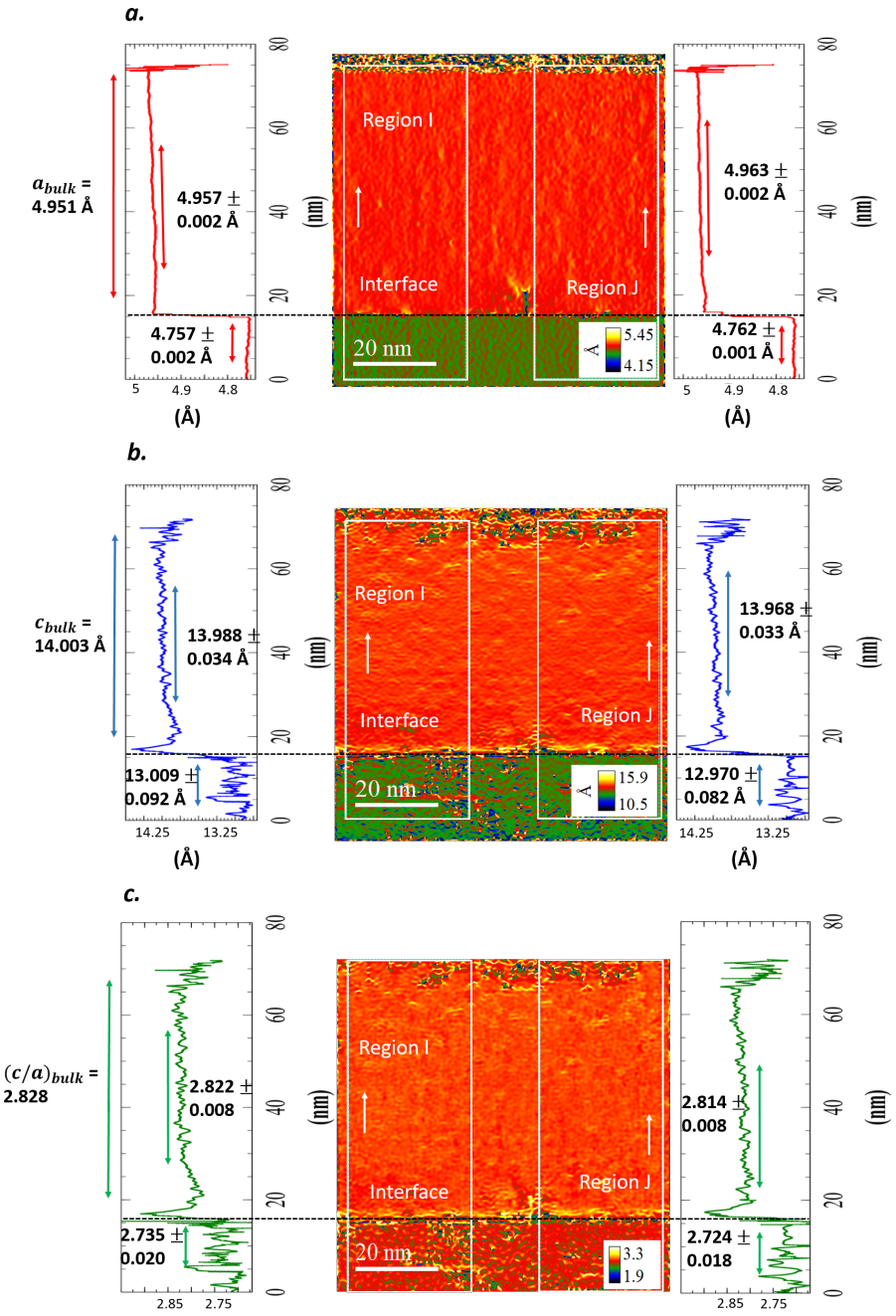

FIGURE 4.7: *a*. In-plane a_h^{loc} local lattice parameters. The profiles carried out in regions I (left) and J (right) are also shown. *b*. Out-of-plane c_h^{loc} local lattice parameters. Profiles from regions I (left) and J (right) are shown. *c*. c_h/a_h ratio map. The profiles in regions I (left) and J (right) are shown.

Sample	a_h (Å)	c_h (Å)	c_h/a_h	Volume (Å^3)
Al_2O_3 (bulk) [119]	4.758	12.991	2.730	254.696
Al_2O_3 (XRD Leuven)	4.760	12.993	2.730	254.949
V_2O_3 (bulk) [3]	4.951	14.003	2.828	297.261
V_2O_3 (XRD Leuven)	4.972	13.967	2.809	299.017
V_2O_3 (GPA in the region A)	4.964	13.864	2.793	295.857
V_2O_3 (GPA in the region B)	4.983	13.861	2.782	298.062
V_2O_3 (GPA in the region C)	4.946	13.919	2.814	294.881
V_2O_3 (GPA in the region D)	4.949	13.924	2.813	295.345
V_2O_3 (GPA in the region I)	4.957	13.988	2.822	297.662
V_2O_3 (GPA in the region J)	4.963	13.968	2.814	297.957

TABLE 4.1: Lattice parameters obtained for bulk Al_2O_3 [119] and bulk V_2O_3 [3], for Al_2O_3 and V_2O_3 thin film from Leuven XRD measurements, and for V_2O_3 thin film in GPA.

We would also like to note that this columnar structuration (observed on the low magnification HAADF image) in the thin film could be due to the large lattice mismatch between the film and the substrate (about 4.2 %). Indeed, according to Schuler *et al.* [117], the growth of V_2O_3 on a Al_2O_3 substrate would induce the formation of grains in the film (see figure 4.9). This particular structuration would result from the island growth mode favored here to minimize the strains induced by the significant lattice mismatch between the film and the substrate. In their proposed model, as shown in figure 4.9, the film would gradually relax the in-plane compressive strains induced by the substrate down to about 30 nm. Then, the film would exhibit evolving tensile strains up to about 50 nm due to the growth mode. Although in our case, the film relaxes very quickly and adopts an almost constant in-plane a_h lattice parameter after the growth first few nms, we nevertheless observe a behavior quite similar to the proposed model beyond a given thickness in some regions of the film. For example, beyond about 15 nm from the interface, in region C (see figure 4.6), we observe a quasi-continuous increase in the a_h lattice parameter. The structural defects in some regions, higher up

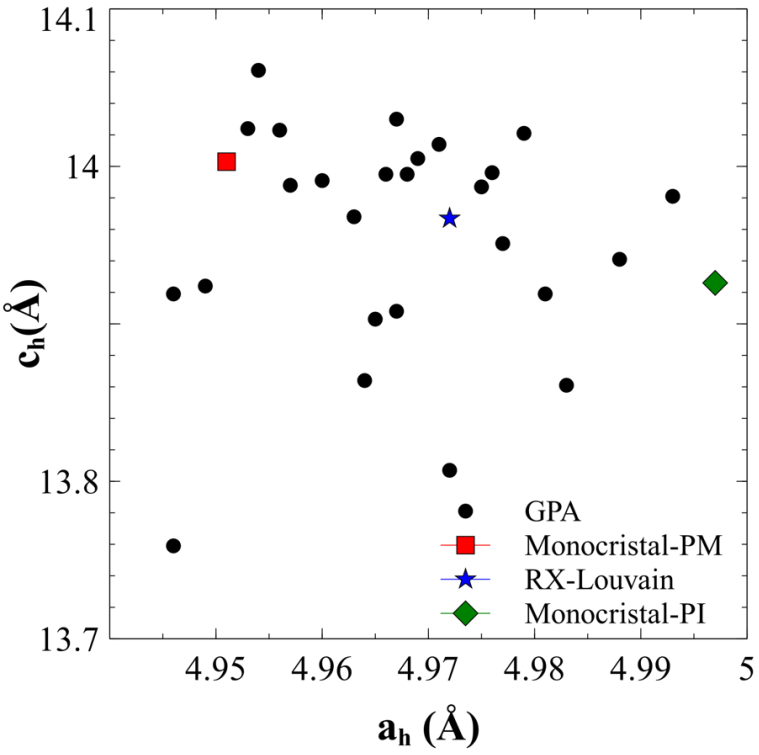

FIGURE 4.8: Evolution of V_2O_3 in-plane and out-of-plane lattice parameters deduced from GPA analyses, and those obtained in XRD by Leuven, for the bulk 1.1 % Cr-doped V_2O_3 in the PI phase and the bulk V_2O_3 in the PM phase.

in the film, could additionally result from these in-plane tensile strains, but also from possible oxygen vacancies. Indeed, the work of Ha *et al.* [123] indicates that the presence of oxygen vacancies in V_2O_3 thin films could be correlated to the generation of structural defects in these systems. This can be understood by the fact that the few V^{2+} ions induced to respect the electrical neutrality in the lacunar system have an ionic radius (0.92 Å) much larger than that of V^{3+} (0.78 Å) [124]. Finally, the respective arrangement of these grains could induce local strains in the film and thus influence probably the electronic properties.

From all these investigations carried out in GPA, the exploration of electronic properties is necessary for a better understanding of the physical behavior of our thin film. We will address this in the next section by performing EELS low-loss and core-loss investigations.

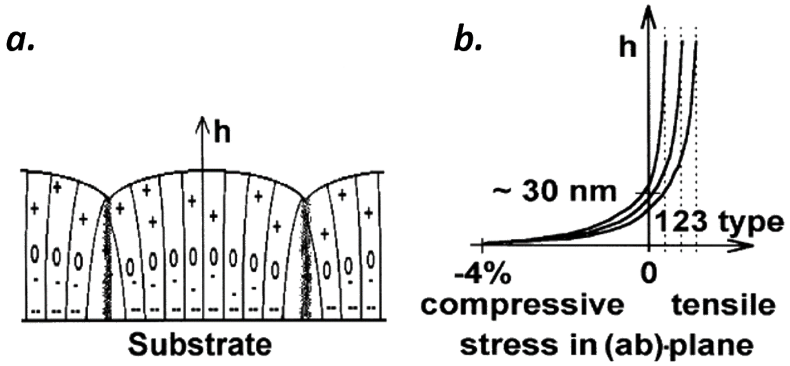

FIGURE 4.9: *a*. V_2O_3 growth representation on the Al_2O_3 substrate. We observe the formation of grains in the film. The signs "-," "0", and "+" observed in the film represent in-plane compressive strains, zero strains, and in-plane tensile strains, respectively. *b*. Representation of the in-plane strains evolution in the film as a function of its thickness. The figures are adapted from [117].

4.3 . EELS spectroscopic studies in V_2O_3 thin film.

As discussed in the introductory section, the electronic properties are investigated by a combination of spatially resolved measurements in the low-loss and core-loss spectral regions on the NION CHROMATEM. From our thin film, we have acquired spims in the low-loss region at 300 K, in the PM phase. These acquisitions were performed at the nanometer spatial resolution, with an acquisition time of 50 ms/px, an EELS dispersion of 3.1 meV/ch, and a ZLP FWHM of about 60 meV. These spims allowed us to extract and investigate spectroscopic signatures in small domains of about 15 nm x 15 nm, as shown in figure 4.10. The resistivity versus temperature curve obtained by our Leuven collaborators [12] is also shown in figure 4.11.

The spectra observed in regions 1 and 2 on figure 4.10 have almost the same shape, except around 1 eV, where region 2 seems to be characterized by the vanishing of the spectroscopic signature occurring at this 1 eV energy loss. In order to gain a better understanding of the electronic properties of the film, spims were acquired in the low-loss region, at low temperature under liquid nitrogen, in the AFI phase. The spectra deduced from these spims were compared with the spectroscopic signatures in regions 1 and 2, as

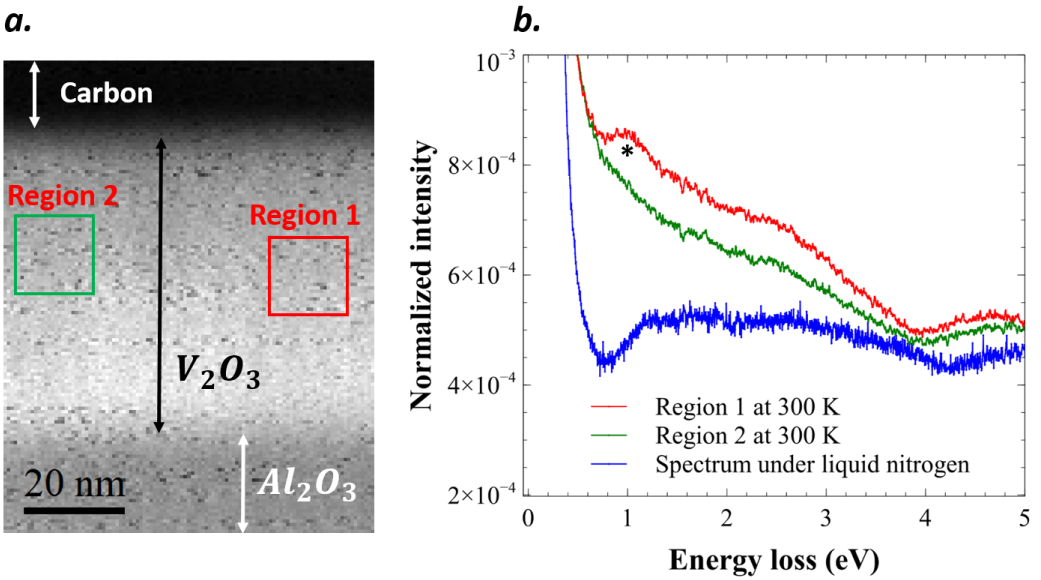

FIGURE 4.10: *a*. HAADF map showing different probed regions of the sample in EELS low-loss at room temperature. *b*. EELS low-loss spectra corresponding to regions 1 and 2, and the low temperature phase. * indicates the spectroscopic signature at 1 eV.

shown in the figure 4.10. It is clear here that the spectrum observed in region 2 is different from that obtained in the AFI insulating state. Therefore, at first glance, the potential absence of this spectral feature at 1 eV in region 2 may not be associated with the insulating state occurring in the low-temperature phase. Note also that the spectroscopic inhomogeneities observed in the film in the PM phase give way to homogeneous spectral signatures throughout the film in the AFI phase.

K-means clustering was used in the following to map the spatial distribution of these spectral inhomogeneities at 300 K. However, two important steps must be performed before applying the K-means clustering algorithm. First, the ZLP must be removed from our spectra. Indeed, as the ZLP is the most intense peak in our spectra and several orders of magnitude more important than any other spectroscopic signature, any variation on this feature becomes mathematically preponderant, as explained by Kalinin *et al.* [125]. In our case, these variations or fluctuations on the ZLP may strongly

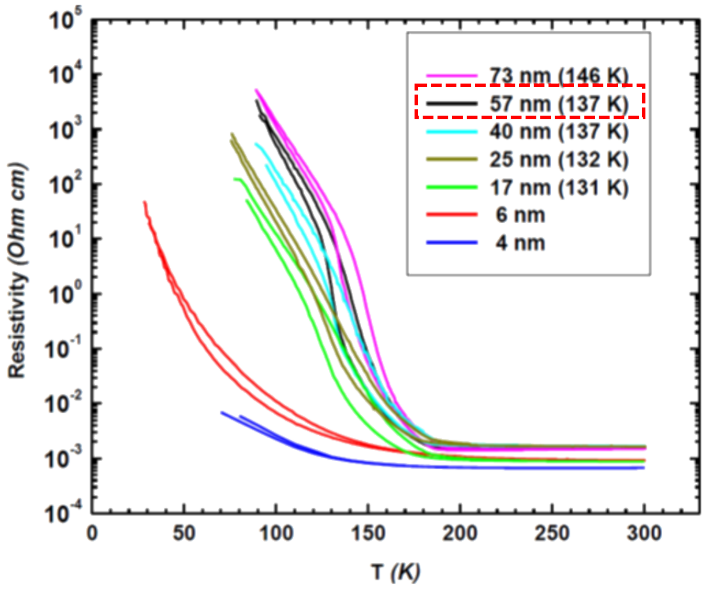

FIGURE 4.11: Resistivity versus temperature curves obtained on different V_2O_3 thin films by Leuven group. The film of interest in this chapter corresponds to the 57 nm-thick. The figure is adapted from [12].

affect the determination of the clusters via the Euclidean distance calculation, hence the need to remove this feature. This is done by considering only the energy channels beyond the ZLP in our spectra. Secondly, a normalization of the EELS spectra must be carried out. Indeed, as pointed out by Torruella *et al.* [115], spectra acquired in regions of similar composition with identical shapes but with different intensities (due, for instance, to thickness variation) will tend to form different clusters due to the Euclidean distance metric employed. By normalizing each of these spectra by the sum of the intensities of all the energy channels of the corresponding spectra, they were able to correct or minimize this clustering problem and successfully map the composition of Fe_3O_4/MnO_4 core/shell nanoparticles using this technique. In our case, we adopted a similar approach by dividing each of the spectra (after removal of the ZLP) contained in our spims by the integrated intensity over all energy channels of the corresponding spectra. Note that this normalization operation would also minimize the effects of elastic scattering on the spectra intensities variation acquired in EELS, as indicated by Venkatraman *et al.* [126]. Assuming that the EELS aperture is adjusted so that there is

no diffracted beam entering the EELS spectrometer (which is our case), the intensity variations in EELS could be partly related to the diffraction effects [127] that are more or less important in the different regions of the sample probed. This normalization operation would, thus, in some way minimize these diffraction effects. The scree plot associated with the PCA decomposition, before and after removal of the ZLP and normalization of the spectra, are shown in figure 4.12. We note that the presence of the ZLP adds additional components to the decomposition before the slope change in the scree plot. These observed components could be due to the variations occurring on the ZLP, as we have just discussed.

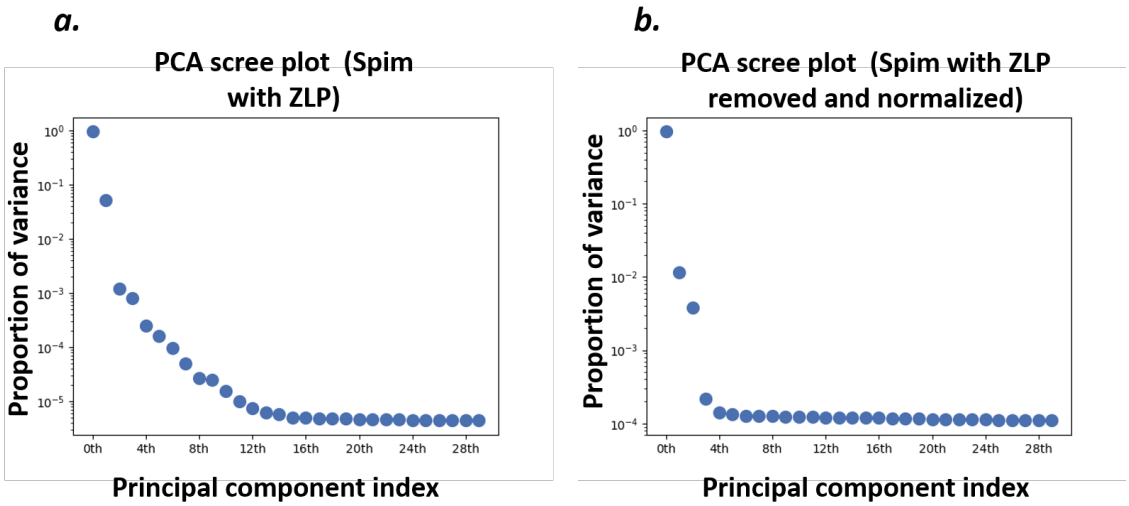

FIGURE 4.12: *a*. Scree plot of the PCA decomposition before ZLP removal. *b*. Scree plot of the PCA decomposition after ZLP removal and spim normalization.

K-means clustering was first applied by selecting 3 clusters. The regions and spectroscopic signatures corresponding to the Al_2O_3 substrate, the V_2O_3 thin film, and the carbon layer on top of it, are clearly identified by the clustering, as shown in figure 4.13. However, the choice of 4 clusters for applying the K-means algorithm does not allow finding or mapping the spectroscopic inhomogeneities occurring in the thin film. Instead, we find a fourth component towards the film/substrate interface (see figure 4.14). The appearance

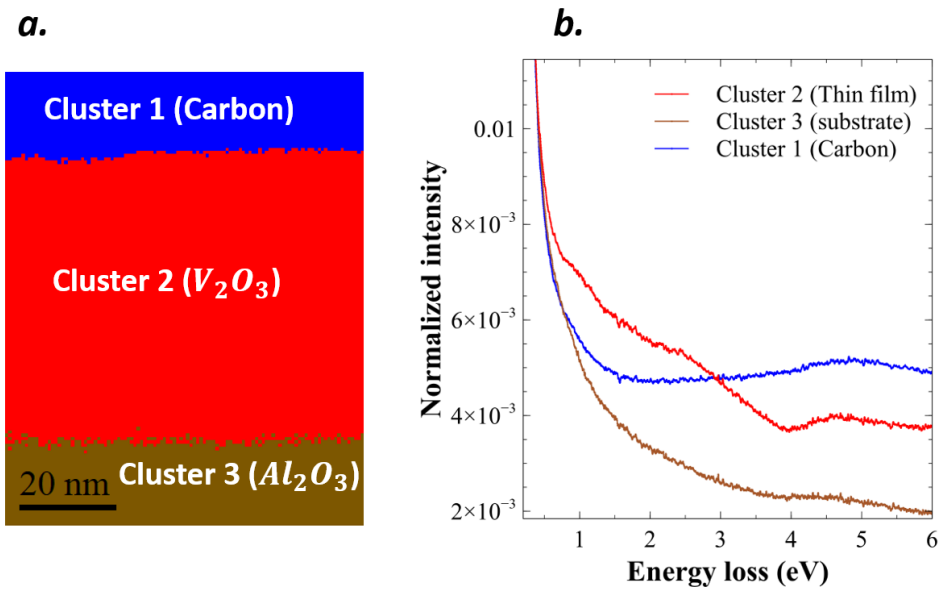

FIGURE 4.13: *a*. Map obtained by K-means clustering with 3 clusters, identifying the carbon, the Al_2O_3 substrate, and the V_2O_3 thin film. *b*. Spectra corresponding to the different clusters, also obtained by K-means clustering.

of the fourth cluster in this region is probably due to the relatively small variations of the Euclidean distance in the thin film.

To cope with this problem, we subsequently cut our spim, keeping only the region corresponding to the V_2O_3 thin film. The PCA decomposition used here for estimating the number of phases present in the sample (in addition to the direct inspection of the data) revealed about 2 principal components on the scree plot (see figure 4.15). The application of K-means clustering with 2 clusters allowed this time to identify and map the spectroscopic inhomogeneities in the film (see figure 4.16). The maps and spectra deduced from the clustering are in perfect agreement with the raw data, with the different mapped areas showing or not the spectral signature at about 1 eV.

These spectroscopic inhomogeneities observed in the V_2O_3 thin film could result from attenuation or damping of the spectral feature occurring at 1 eV, due to defects such as grain boundaries in the film. Indeed, defects are highly likely to affect the intensity of plasmonic signatures [128], if we obviously admit the plasmonic character of the feature at 1 eV. This feature, due to its

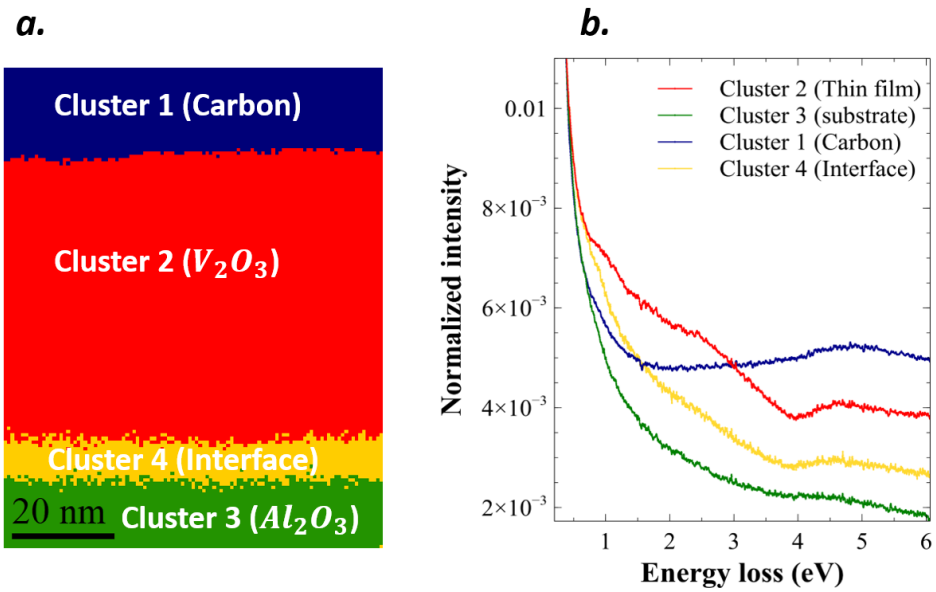

FIGURE 4.14: *a*. Map obtained by K-means clustering with 4 clusters. The cluster 4 is obtained at the film/substrate interface. *b*. Spectra corresponding to the different clusters, obtained by K-means.

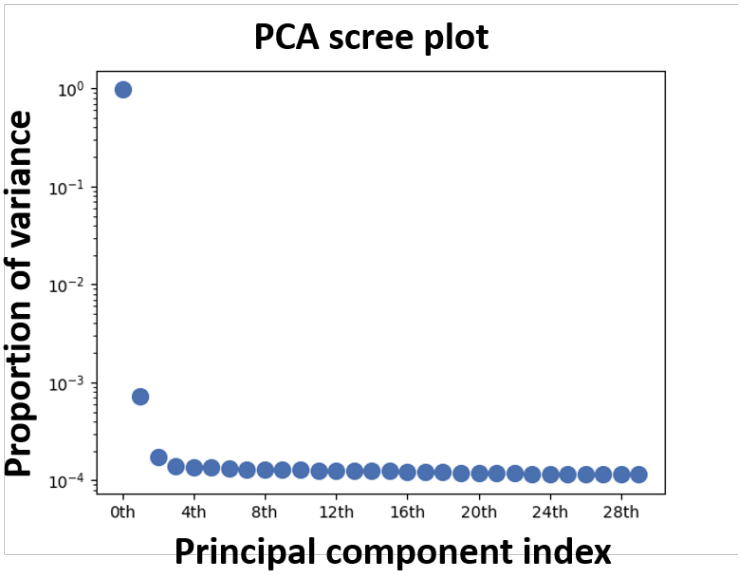

FIGURE 4.15: Scree plot of the PCA decomposition, cutting off spatially the spim and considering only the V_2O_3 thin film. The ZLP is removed here, and the spim is normalized.

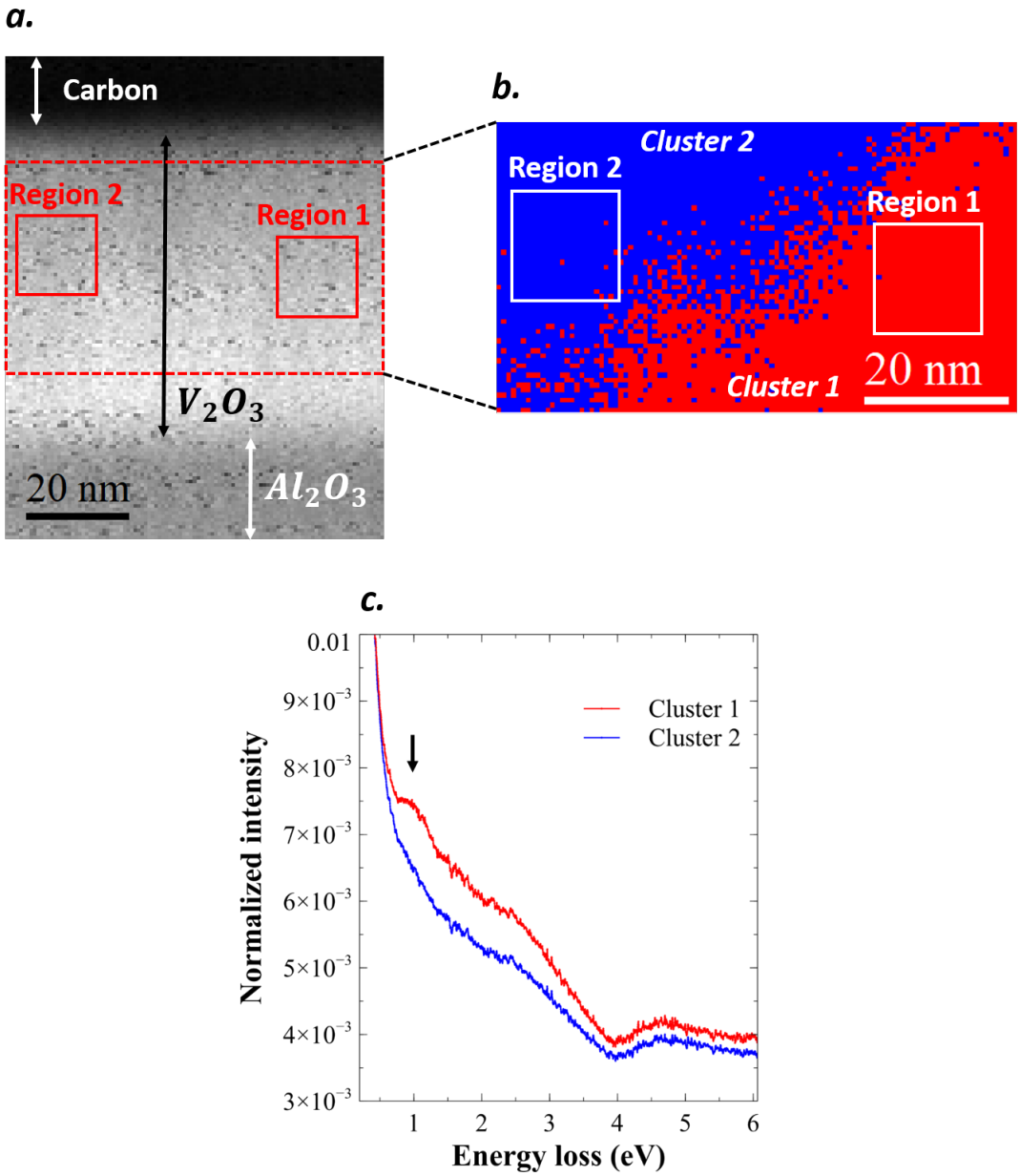

FIGURE 4.16: *a*. HAADF map showing the selected area in the thin film. *b*. Map obtained by K-means clustering in the thin film, with 2 clusters. The observed clusters correspond well to the spectroscopic inhomogeneities observed in the film. *c*. Spectra corresponding to the different clusters, with the presence of the spectroscopic signature at about 1 eV (indicated by an arrow) for cluster 1.

very low intensity in some regions, could be hidden under the tail of the ZLP.

Another possibility to explain this attenuation of the signature at 1 eV would be the local variations of the in-plane a_h lattice parameter in the thin film, as observed in GPA. Indeed, as discussed previously with Homm *et al.*, variations in the in-plane lattice parameter can induce inhomogeneities of electronic properties in the thin film. This is what we observe in figure 4.17, where we present the evolution of the quantity $Im(-1/\epsilon)$ (which is the quantity measured by EELS spectroscopy) as a function of the a_h lattice parameter for a 1.5 % Cr-doped V_2O_3 thin film. The quantity $Im(-1/\epsilon)$ is deduced here from the refractive indices (n) and extinction coefficients (k) [5] given by Homm *et al.*. Concerning the spectroscopic signature at 1 eV, which is of main interest, we observe a decrease in its intensity on the calculated spectra when a_h increases and we tend more and more towards the PI insulating state. This result, similar to what we observe experimentally in different regions of our thin film, could therefore reflect electronic inhomogeneities in our sample at room temperature.

Finally, the existence of an effective medium in which nanodomains of the PM phase could coexist with nanodomains of a larger volume hexagonal phase (like the PI phase, for instance) could also support these observations. We would then see a damping of the plasmon intensity at 1 eV, which only occurs in the PM phase. This effective medium, with higher or lower contributions from these possible PM and PI phases per region or domain, would therefore give rise to the spectroscopic variations observed at 1 eV in the film.

To test the damping hypothesis, we applied Richardson-Lucy deconvolution to remove any doubt about whether the 1 eV spectroscopic signature is present in all film regions. Since deconvolution requires the presence of the ZLP, the entire EELS spectrum is used in the deconvolution step. Using the spectrum acquired in the vacuum for the R-L deconvolution as the PSF or instrumental response, we cannot perform the deconvolution operation cleanly. On the contrary, the R-L deconvolution application induces artifacts appearance after 3 iterations, with sawtooth-shaped spectra, as shown in the figure 4.18. These artifacts result from the noisy spectra acquired in

[5] Indeed, $\epsilon_1 = Re(\epsilon) = n^2 - k^2$ and $\epsilon_2 = Im(\epsilon) = 2nk$.

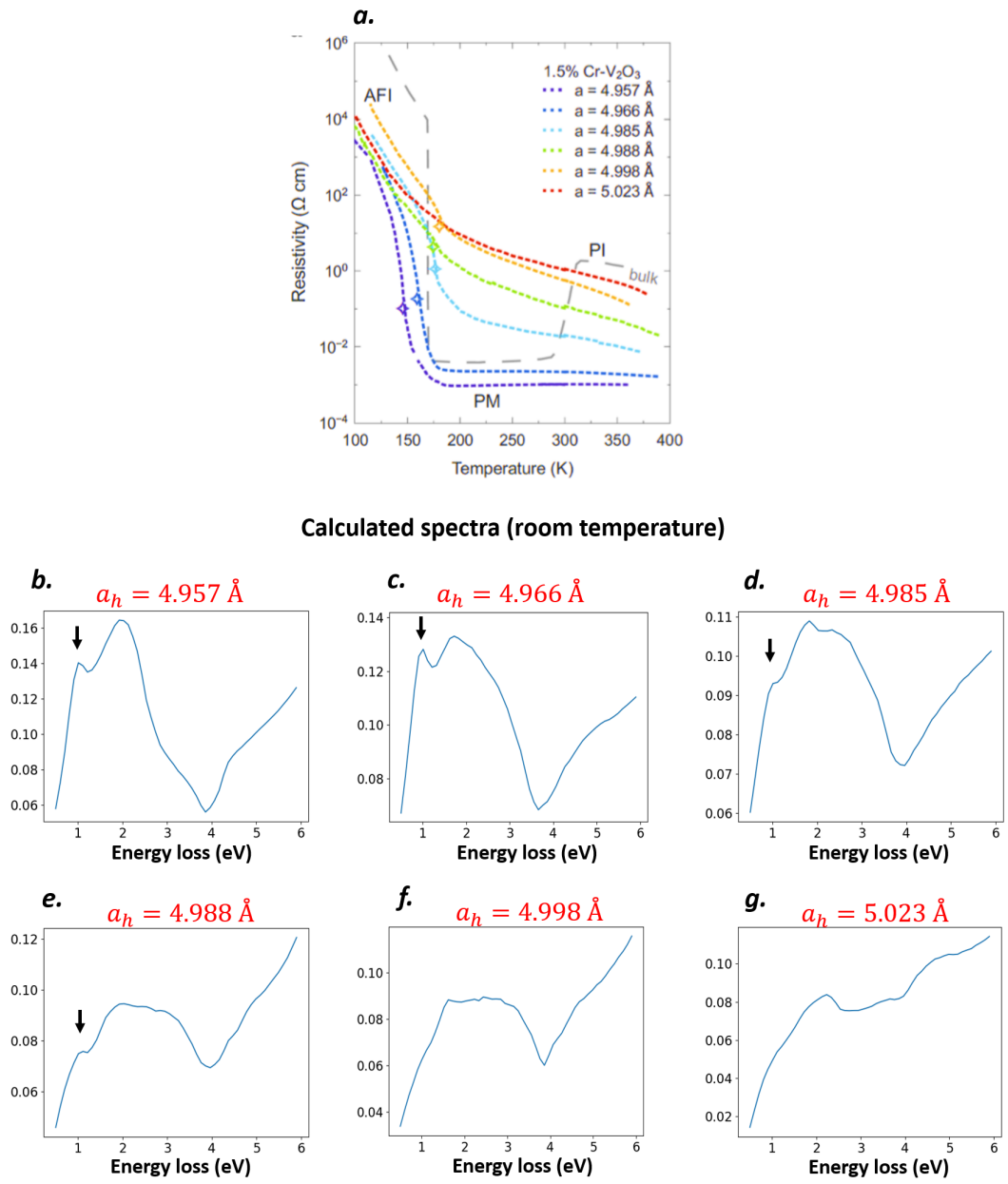

FIGURE 4.17: *a*. Resistivity versus temperature curve for different in-plane lattice parameters at room temperature in 1.5 % *Cr*-doped V_2O_3, adapted from [67]. *b* to *g*. Calculated spectra at room temperature for $Im(-1/\epsilon)$, following the different lattice parameters given in *a*.

the vacuum used as PSF, which induce noise amplification by deconvolution, as mentioned in the previous chapter. Spectra acquired in the vacuum may also not be very good PSFs. Indeed, the instrumental response of the EELS spectrometer can be different depending on whether the spectra are acquired with or without the presence of the sample. We used, therefore, as PSF, a pseudo-Voigt [6] function of FWHM equal to that of the ZLP in the film. This function was chosen to obtain a better approximation of the symmetric tail of the ZLP [7], which in our case is more and less significant than those of Gaussian and Lorentzian functions, respectively.

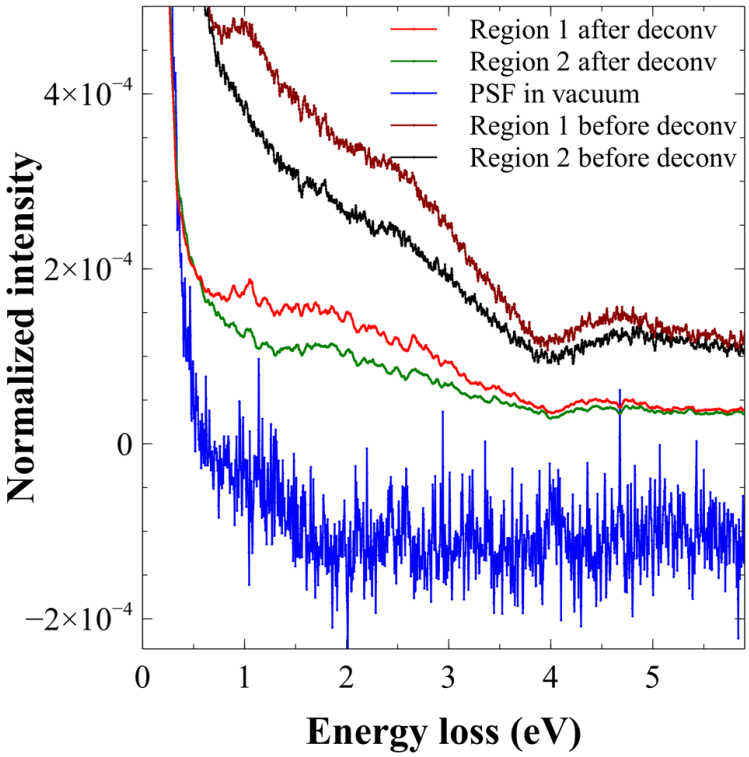

FIGURE 4.18: Spectra in regions 1 and 2 before and after 3 iterations of R-L deconvolution, with the PSF taken in vacuum. The PSF in vacuum is very noisy.

The results of R-L deconvolution with the pseudo-Voigt function as PSF, after 3 iterations, are presented in figure 4.19. We observe an effective decrease in the tail of the ZLP on the obtained spectra. Moreover, no artifact associated with deconvolution is observed on these spectra. Region 2

[6] The pseudo-Voigt function is the weighted sum of a Gaussian and a Lorentzian.
[7] The ZLP obtained from a monochromator is generally symmetric

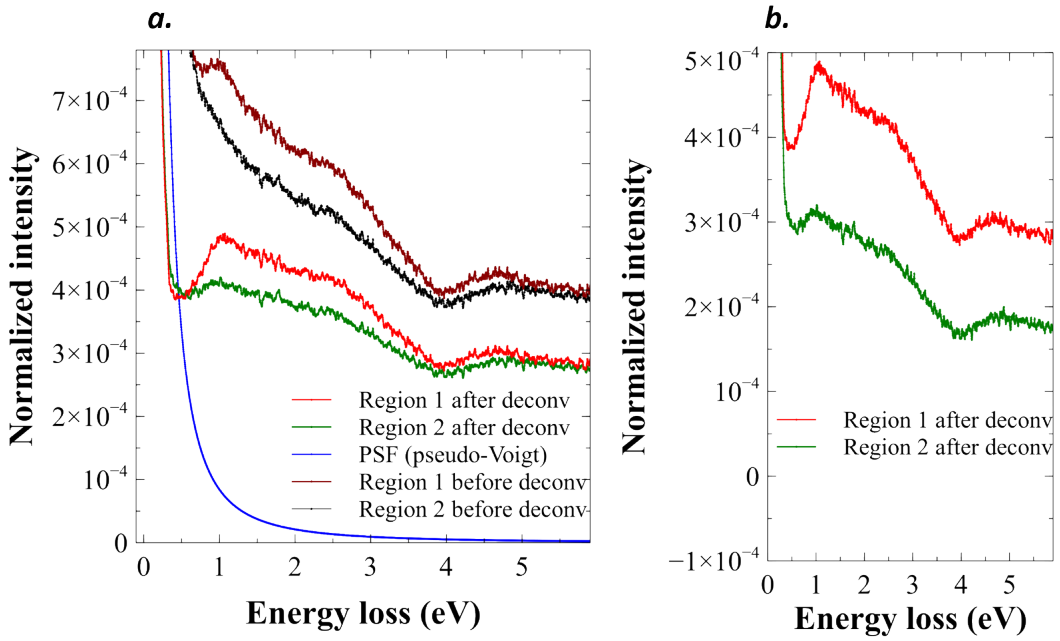

FIGURE 4.19: *a*. Spectra in regions 1 and 2 before and after 3 iterations of R-L deconvolution, with the pseudo-Voigt function taken as PSF. No artifacts are observed. The spectral feature at 1 eV is revealed in region 2. *b*. Enlarged view of the spectra in regions 1 and 2 after deconvolution. The spectra presented are vertically shifted relative to each other.

presents this time, as in region 1, an almost similar spectroscopic characteristic at about 1 eV. However, this feature has a much lower intensity in this region. Finally, the spectral signature at 1 eV is present throughout the film, with a fluctuating amplitude in the latter. After this successful R-L deconvolution, we applied the K-means clustering technique by limiting only to the V_2O_3 thin film region and always choosing 2 clusters. As explained above, the ZLP is removed from our spectra, and the spectra are normalized before clustering. The same spatial distribution (see figure 4.20) as in figure 4.16, observed previously in K-means clustering before deconvolution, is obtained. This result reflects the robustness of the clustering method in identifying and mapping these spectroscopic inhomogeneities in our thin film, in EELS low-loss.

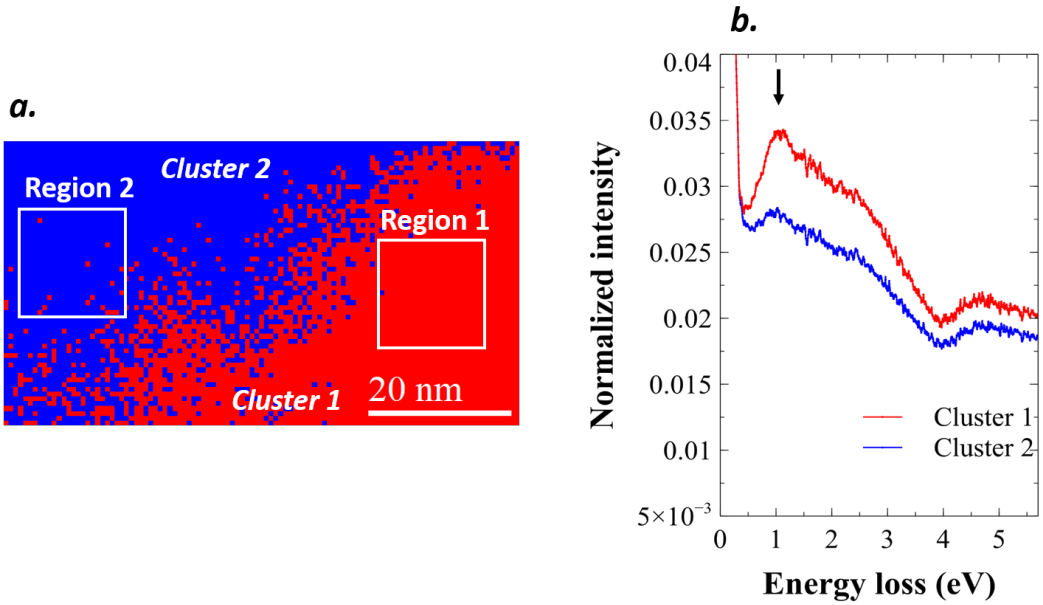

FIGURE 4.20: *a*. Map obtained by K-means clustering in the V_2O_3 film with 2 clusters, after R-L deconvolution (the pseudo-Voigt function taken as PSF). A result identical to that in figure 4.16 is obtained. *b*. Spectra corresponding to the clusters, with the spectroscopic feature at 1 eV indicated by an arrow.

We also applied K-means Clustering to other spims acquired in EELS low-loss at room temperature, following the previous methodology (i.e. considering only the thin film region). As we can see in figures 4.21 and 4.22, we still find this domain distribution with more or less important variations of the 1 eV intensity feature. The domains observed on almost all our acquisitions are columnar and have widths of about 40 nm-50 nm.

Following these results in the low-loss region, we also looked at the core-loss region through the acquisition of spims at room temperature in the PM phase and at low temperature under liquid nitrogen in the AFI phase, as shown in figure 4.23. In the latter, the spim acquired at room temperature is obtained at the spatial nanometric resolution, with an acquisition time of 50 ms/px and an EELS dispersion of 21 meV/ch. The spim acquired in the AFI phase is also obtained at the spatial nanometric resolution, with an acquisition time of 70 ms/px and an EELS dispersion of 21 meV/ch. As before, spectroscopic inhomogeneities are observed at room temperature (see

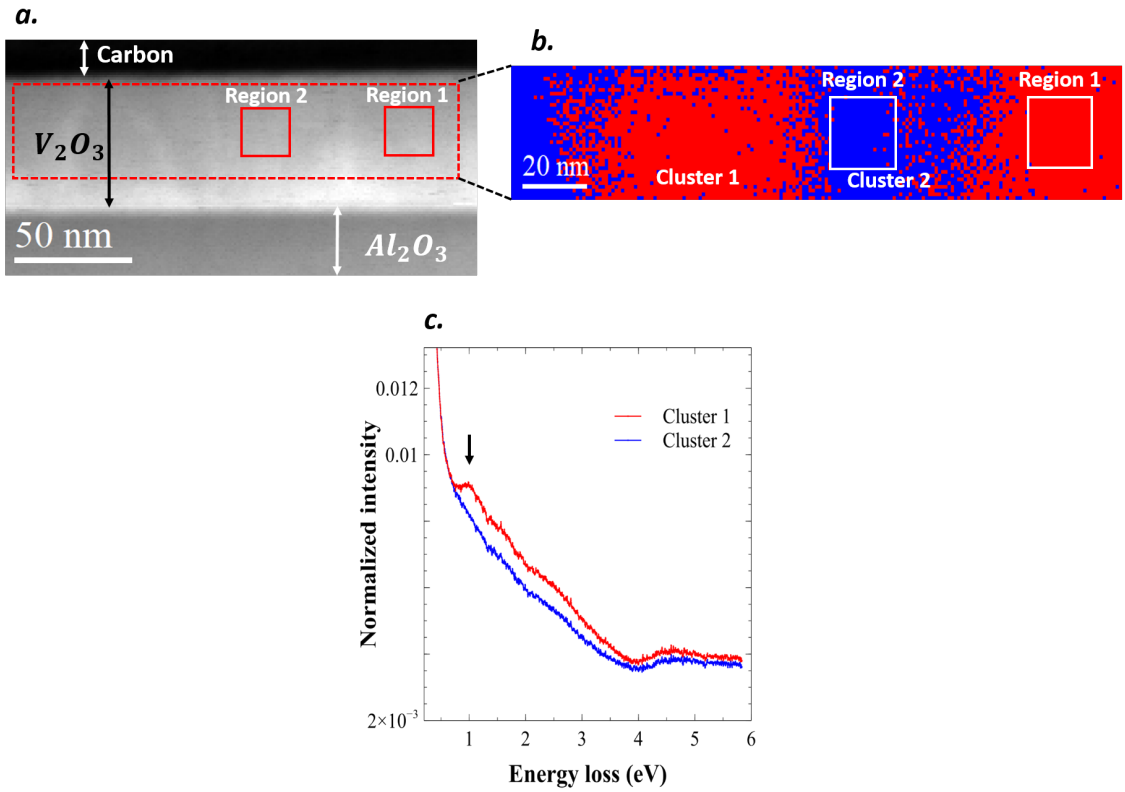

FIGURE 4.21: *a*. HAADF map showing the selected area in the thin film. *b*. Map obtained by K-means clustering in the thin film, with 2 clusters. *c*. Spectra corresponding to the different clusters, with the presence of the spectroscopic signature at about 1 eV (indicated by an arrow) for cluster 1.

arrows in figure 4.23). The spectral signature obtained in region 3 at 300 K is almost identical to that of Abe *et al.* [70] (see figure 3.8 in chapter 3) at this temperature and reflects the expected behavior in the PM phase . In region 4, still in the spim acquired at room temperature, the shoulder previously observed around 520 eV in region 3 and indicated by an arrow, is almost replaced by a peak. The shoulder around 514 eV (also indicated by an arrow) on V-L_3 edge is much more pronounced in region 4 than in region 3. In addition, a change in the shape of V-L_2 peak between regions 3 and 4 is observed. All these spectroscopic changes observed between these two regions represent some transition features between the metallic (PM) and the insulating states (PI and AFI) in V_2O_3, already discussed extensively in the previous chapter 3. Finally, an upward shift (around 171 meV) concerning

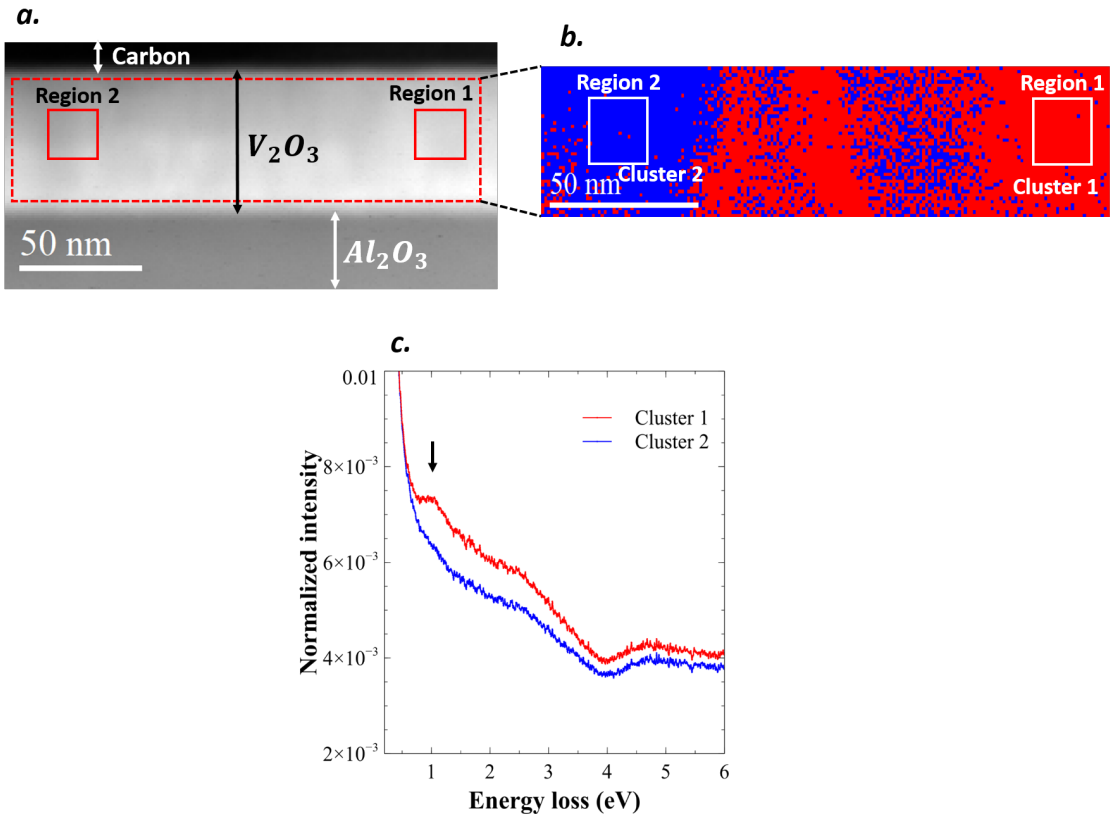

FIGURE 4.22: *a*. HAADF map showing the selected area in the thin film. *b*. Map obtained by K-means clustering in the thin film, with 2 clusters. *c*. Spectra corresponding to the different clusters, with the presence of the spectroscopic signature at about 1 eV (indicated by an arrow) for cluster 1.

the O-*K* edge seems to occur from region 4 to region 3. However, even if this value is smaller than the one observed during the transition from PM to AFI, or PM to PI (around 0.4 eV), the spectroscopic behavior in region 4 seems to be similar to that of the AFI or PI phases (see figure 3.9 in chapter 3). Thus, the spectroscopic signatures of regions 3 and 4 suggest potential electronic inhomogeneities in the film. As in the low-loss region, the spectra acquired in core-loss at low temperatures show homogeneous spectroscopic features throughout the film. The homogeneous spectra observed in the low-temperature phase could rule out the contribution of oxygen vacancies in explaining the structural defects observed in GPA. These vacancies (in oxygen

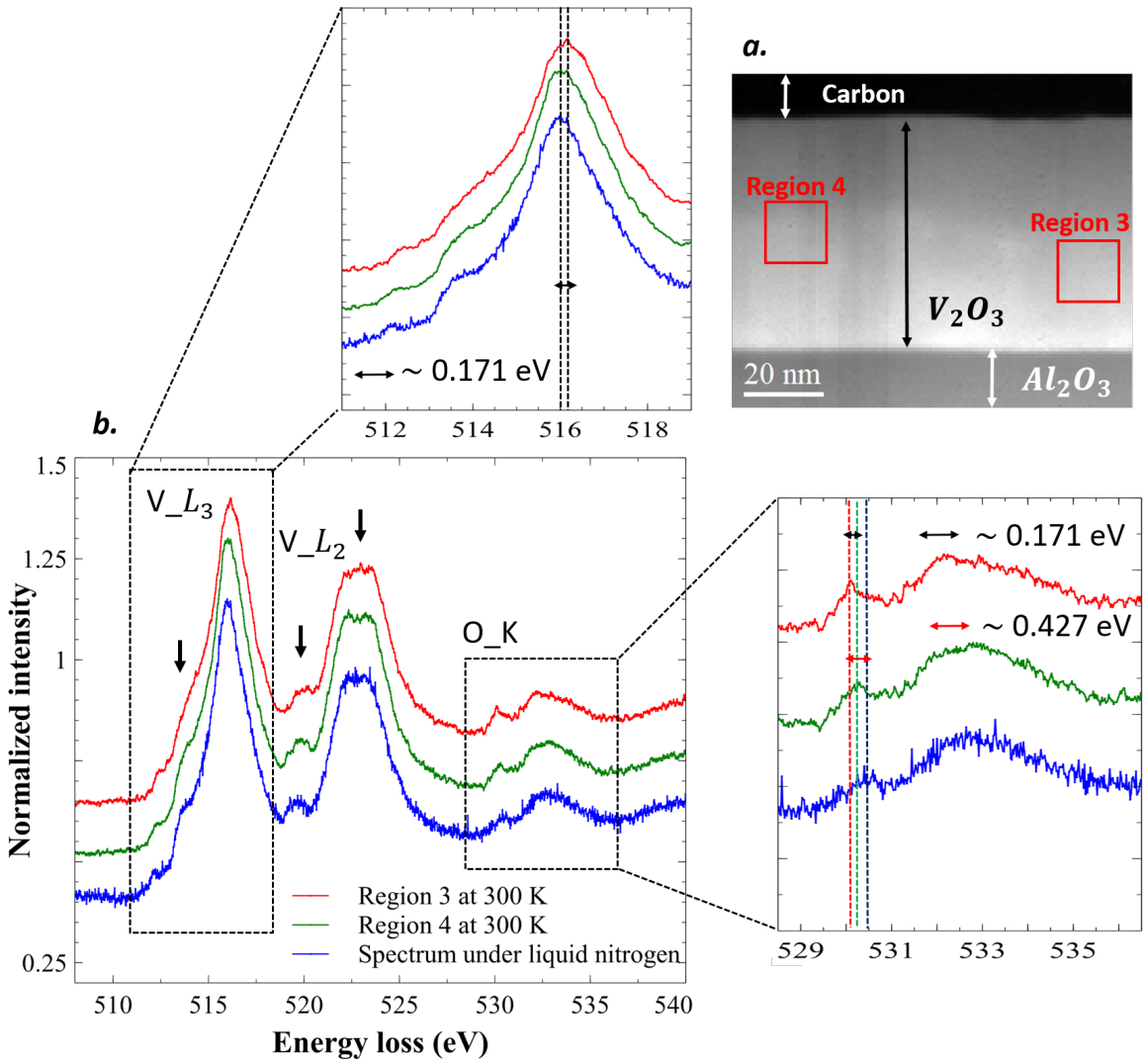

FIGURE 4.23: *a*. HAADF map showing different regions probed in the sample, in EELS core-loss at room temperature. *b*. Core-loss spectra corresponding to regions 3 and 4, and to the AFI phase obtained under liquid nitrogen. V-L_3 and O-*K* edges enlarged views are also shown.

or vanadium), which would be expected to occur in both the room temperature and low-temperature phases, for instance, by a shift on the vanadium edge, are not observed. These results lead us to say that even if we cannot rule out the possibility of oxygen (or vanadium) vacancies, they are in very low proportion, making them almost undetectable by our spectroscopic measurements. The observed spectra at low-temperature are also identical to those of Abe *et al.* in the AFI phase. Compared to that obtained in region 3, the spectra acquired at low temperature seem to show an upward shift of about 427 meV on the O-*K* edge, very close to the one expected (see figure 4.23).

In the following, we applied K-means Clustering on the spims acquired in the core-loss to map the spectroscopic inhomogeneities in this region. Unfortunately, despite the normalization of our data and considering only the thin film region, the clustering results remain strongly dependent on the thickness variations in the film, as shown in appendix A. Indeed, the distribution of clusters follows the contrast variations observed on the HAADF map. Moreover, the spectra associated with the clusters show almost no differences, as observed previously, except for the small change in shape on the V-L_2 edge. We, therefore, took several slices of relatively constant thickness in the film based on the contrast of the HAADF map. In one of them (see appendix B), we can see the results of applying K-means Clustering (with 2 clusters). We find almost the same columnar domains observed previously in EELS low-loss. However, the spectroscopic signatures resulting from the clustering treatment do not still show significant differences like those observed previously between regions 3 and 4. We observe, almost solely, a change in shape [8], slightly more pronounced than previously, still on the V-L_2 edge.

There could also be a mixture of "more metallic" and "less metallic" spectroscopic contributions in some pixels of our spim. For example, region 4, which tends more towards an insulating state, could have a majority of this "less metallic" contribution compared to other regions of the spim. These

[8] Remember that this change in shape observed on the L_2 edge is a transition feature between the PM and AFI, or PM and PI phases, as mentioned earlier.

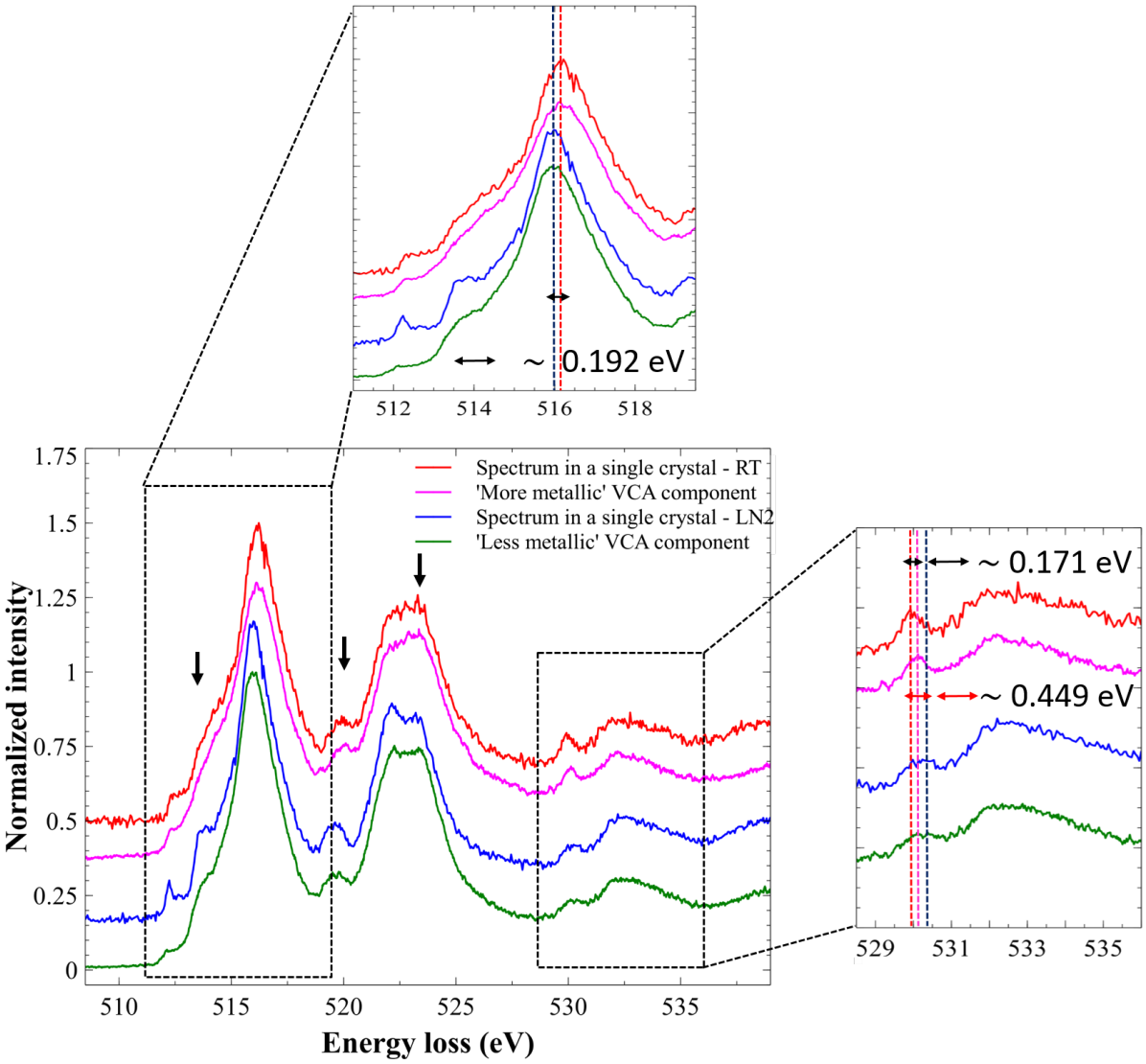

FIGURE 4.24: Spectra ("more metallic" and "less metallic") obtained after application of the VCA, and reference spectra in the PM and AFI phases. The V-L_3 and the O-K edges enlarged views are shown.

variations in proportion would explain the less significant differences observed previously in clustering, almost exclusively on V-L_2 edge. Unfortunately, K-means Clustering being a classification method [9], it is not able to unmix the spectral information found in a given pixel. We, therefore, need to find other tools to verify the spectral mixing hypothesis, hence the use of vertex component analysis or VCA in our case.

The VCA application on the different slices allows us to observe mainly 2 spectroscopic contributions in the thin film (see figure 4.24). Compared to the reference spectra we acquired in the pure V_2O_3 single crystal in the PM, and AFI phases [10], the components observed in VCA are broadly similar to the spectroscopic signatures of the insulating and metallic states, as shown in figure 4.24. We refer to these components in the following as the "more metallic" VCA component (for that which shows similarities to the PM metallic spectrum) and the "less metallic" VCA component (for that which shows similarities to the AFI insulating spectrum). On the V-L_3 edge maximum, we observe a shift of about 192 meV towards lower energies, from the "more metallic" VCA component to the "less metallic" VCA component. We also observe a shift of about 278 meV towards higher energies on the O-K edge, less important than in the case of the PM to AFI transition (around 449 meV for our reference spectra), from the "more metallic" VCA component to the "less metallic" VCA component. This shift is associated with an intensity decrease on the O-K pre-peak at about 530 eV. However, we observe on this same edge, an upward shift of about 171 meV from the PM reference spectrum to the "more metallic" VCA component. This shift could be related to a hybridization change between the 2p oxygen and 3d vanadium orbitals in the thin film. It could also be related to the fact that the unmixing in VCA is not totally perfect, and that there is still a small contribution from the insulating component on this edge.

The spectra observed for the "less metallic" VCA component and the single crystal AFI phase are relatively similar. However, the peak at 512 eV and

[9] Here, all the spectral information contained in a pixel is assigned to a specific domain.

[10] The reference spectra presented here are much better spectrally resolved as they were acquired with the Medipix 3 direct detection camera, which has a better PSF. The spims presented in the thin film were obtained with the old CMOS camera when it was still installed on the CHROMATEM.

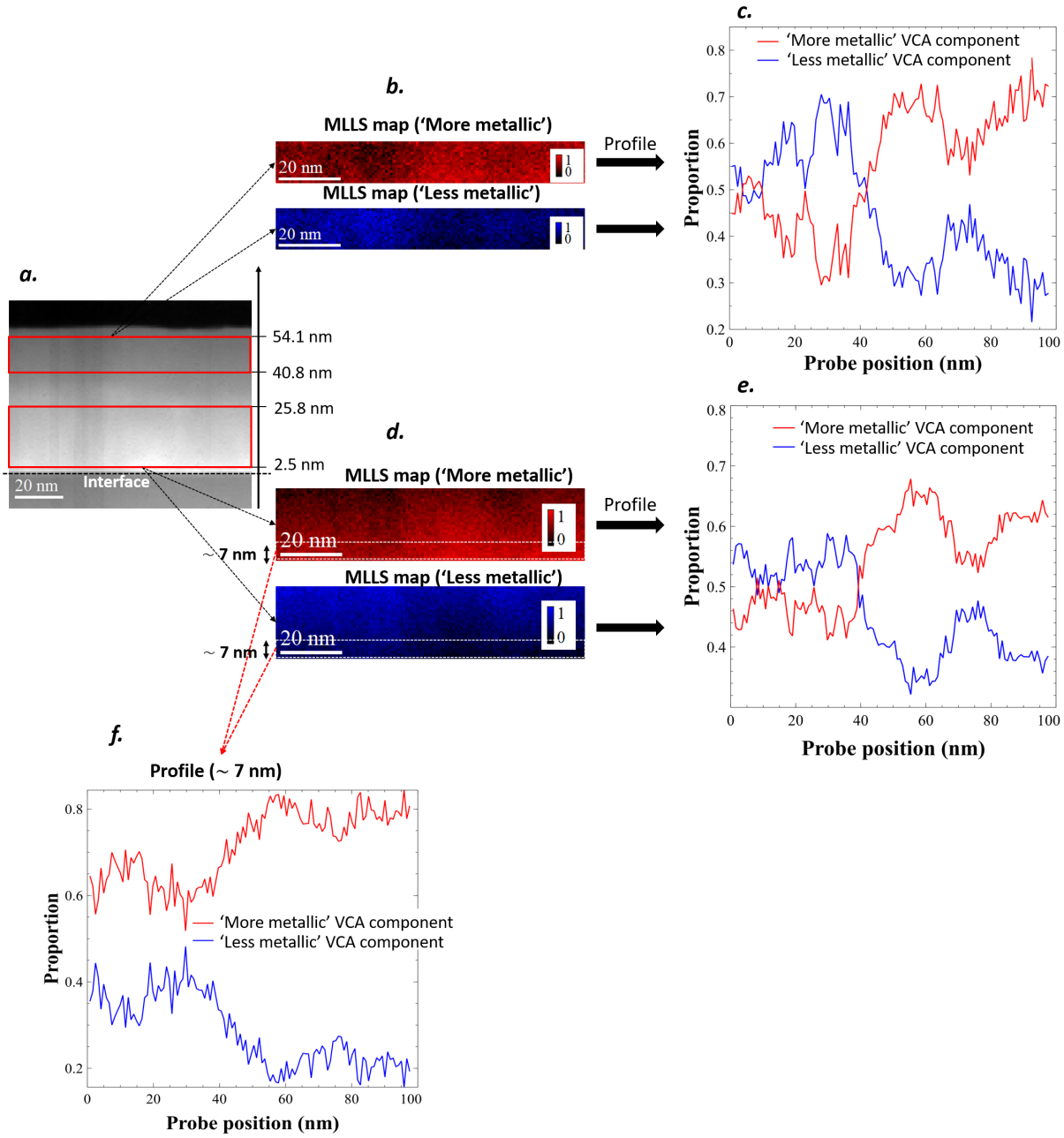

FIGURE 4.25: *a.* HAADF map showing the slices considered in the film for the VCA application. *b.* and *d.* MLLS maps obtained in the slices from the "more metallic" and "less metallic" components deduced in VCA. *c.* and *e.* Distribution profiles of the "more metallic" and "less metallic" components deduced in VCA. *f.* Distribution profiles of the VCA components over the first 7 nm of the MLLS map obtained in *d.* (close to the interface).

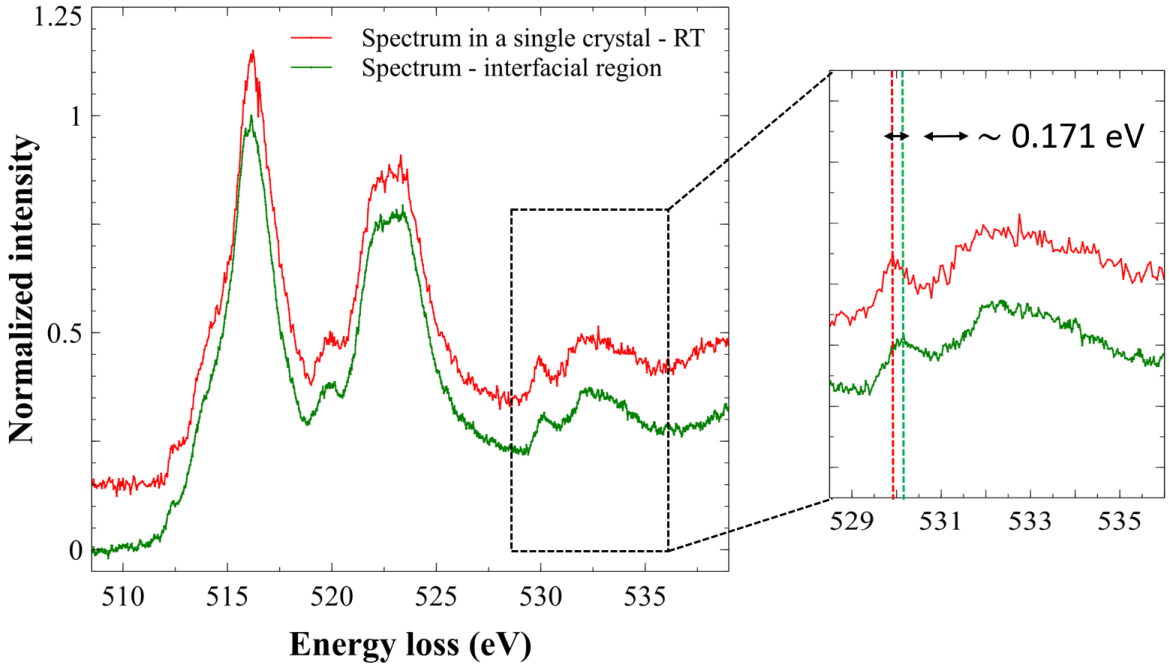

FIGURE 4.26: Core-loss spectrum obtained in the interfacial region and reference spectrum at room temperature. The O-*K* edge enlarged view is also shown.

the change in the shape of the V-L_2 edge at 522 eV are much less marked for the "less metallic" VCA component. These differences could be explained by using different cameras to acquire these data (Medipix for the reference AFI phase and KURO CMOS for the VCA spectra). They could also be due to the presence of the PI phase at room temperature in the sample. Indeed, even if we cannot directly interpret the fine structures of the vanadium threshold, as noted earlier in Chapter 3, the partial contribution of the a_{1g} orbitals to these structures and whose occupancy rate in the ground state is higher in the PI phase, allows us to make this interpretation.

The map intensities resulting from multivariate analysis techniques such as VCA can be defined by a more or less arbitrary factor. Therefore, the spectra obtained with VCA [11] are used as reference spectra to establish relatively reliable component maps by applying Multiple Linear Least Square Fitting

[11] The spectra used here are normalized by the sum of the intensities of all energy channels.

(MLLS). As shown in figure 4.25, we find on the maps and profiles thus obtained this distribution of columnar domains of about 40 nm - 60 nm. However, this time, each domain is made up of the spectroscopic contributions of the "more metallic" VCA component and the "less metallic" VCA component, each with more or less important proportions. Given the EELS core-loss analyses, there would therefore appear to be, as previously observed in low-loss, electronic inhomogeneities in the V_2O_3 thin film. The spectra observed in the interfacial region of the thin film are almost homogeneous. They show strong similarities with the metallic reference spectrum acquired in the PM phase, as shown in figure 4.26. However, we observe, as before, for the "more metallic" VCA component, an upward shift of about 171 meV on the O-*K* edge from the PM reference spectrum to the interfacial region spectrum. The profiles obtained from the MLLS maps in the region close to the interface (see figure 4.25) also show a spectroscopic contribution predominantly of the "more metallic" VCA component. Therefore, the film would be relatively much more "metallic" over the first 10 nm from the interface. These observations could be correlated with a constant evolution of the in-plane lattice parameter in this region.

We would also like to comment the possible lattice deformation at the interface, previously indicated in GPA. This possible deformation is hardly noticeable in the EELS core-loss spectroscopic signature of this region. Indeed, as we have shown, the spectra acquired in the interfacial region show strong similarities with the metallic PM phase spectra in pure V_2O_3 single crystals and the "more metallic" VCA component. It should also be noted that the regions whose electronic state tends most towards the insulating state could act as nucleation sites during phase transitions, as pointed out by Lupi *et al.* [5] in the case of $(V_{0.989}Cr_{0.011})_2O_3$ single crystals during the PM-PI transition (discussed in Chapter 2). These electronic inhomogeneities could, therefore, somehow hide the intrinsic degrees of freedom associated with these phase transitions.

After investigating the structural properties by GPA and the electronic properties by monochromated EELS spectroscopy at the nanoscale, we will, in the next section, explore the chemical distribution in our V_2O_3 thin film, with a particular focus on the film/substrate interface.

4.4 . Chemical investigation in the interfacial region

As mentioned above, the physical properties of the thin film can be altered by the electronic or atomic structure, or the chemical diffusion at the film/substrate interface. In our case, for instance, aluminium diffusion in the V_2O_3 thin film could induce a PI phase, as V_2O_3 is known to stabilise this phase by aluminium doping [129], hence the importance of the latter's characterization.

For this purpose, we have acquired spims in the interfacial zone at atomic resolution in the core-loss region (including V-$L_{2,3}$ and Al-K edges), still at room temperature. The acquisitions in this section are all performed on the NION ULTRASTEM (with the Medipix 3 camera). First, the spims are corrected for gain variations in the Medipix 3 direct detection camera by dividing them by the gain image acquired in the vacuum at 100 kV. Denoising by PCA is then carried out to obtain the best possible SNR. From these spims, we finally extracted chemical maps in this interfacial region. These chemical maps are obtained by applying an integration window on the edge of the corresponding chemical elements and subtracting by a power law the background on which the signal is superimposed, as shown in appendix C. This background results from the tails of valence or core excitations manifesting, for instance, before the edge of interest.

Typical HAADF and resulting aluminum and vanadium chemical maps are given in figure 4.28. The spims from which they derive were acquired in different regions, which we call here region E and region F. Oxygen chemical maps were not performed in the present case due to the hybridization differences between oxygen and vanadium (a transition metal) on the one part, and oxygen and aluminum (not a transition metal) on the other part. These differences can be seen in the EELS core-loss spectra by a change in the oxygen signal shape between the film and the substrate, which makes signal extraction difficult and unreliable. In data presented in figure 4.28, denoising by PCA is obtained by considering only the first 9 principal components for the recomposition of the signal. This number of components is chosen by inspection of the scree plot (see figure 4.27), the maps, and the spectra associated with the decomposition components, as shown in appendix D for region

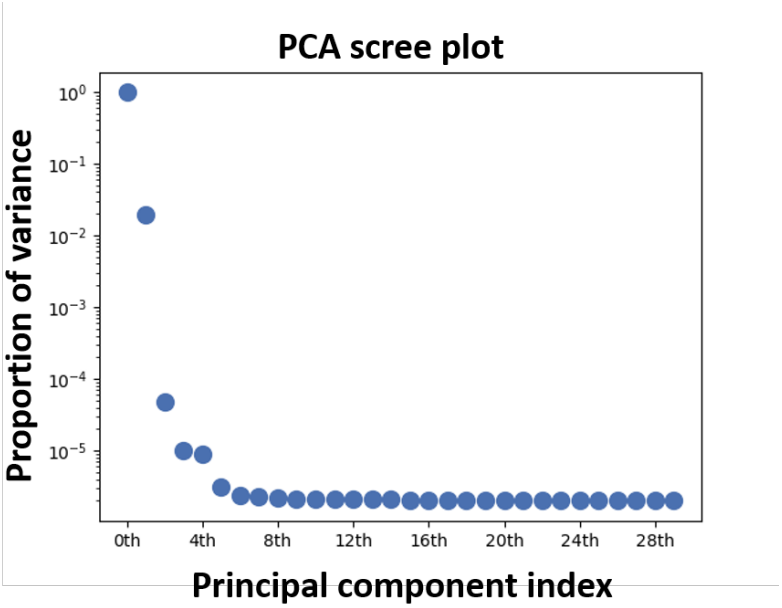

FIGURE 4.27: Scree plot of the PCA decomposition obtained in an interfacial region (called here region F).

F. On the HAADF maps observed in figure 4.28, the film/substrate interface does not seem to have any significant defects. We can also distinguish the aluminum and vanadium atomic columns. Due to spatial drift when probing the insulating substrate (charge effect) during the spim acquisition, the presented maps present shifted columns which does not represent the exact atomic arrangement at the interface. These effects are nevertheless small or insignificant in the present case and should not prevent us from making reliable chemical distribution profiles across the interface.

The distribution profiles of V-$L_{3,2}$ and Al-K across the interface, derived from the chemical maps, are shown in figure 4.29. Each of these profiles is normalized to the maximum of the corresponding one. We observe, within the uncertainty of the inelastic delocalization effects of the electron probe, a chemical interdiffusion at the interface of about 3.5 nm, i.e., less than 3 V_2O_3 unit cells. The most striking observation here is the fluctuation or variation in vanadium distribution in the film at various interfacial regions. Indeed, the vanadium proportions obtained from the chemical maps at different interfacial regions show inhomogeneities over at least 2 nm in the film. These inhomogeneities could result from the presence of vanadium vacancies in the

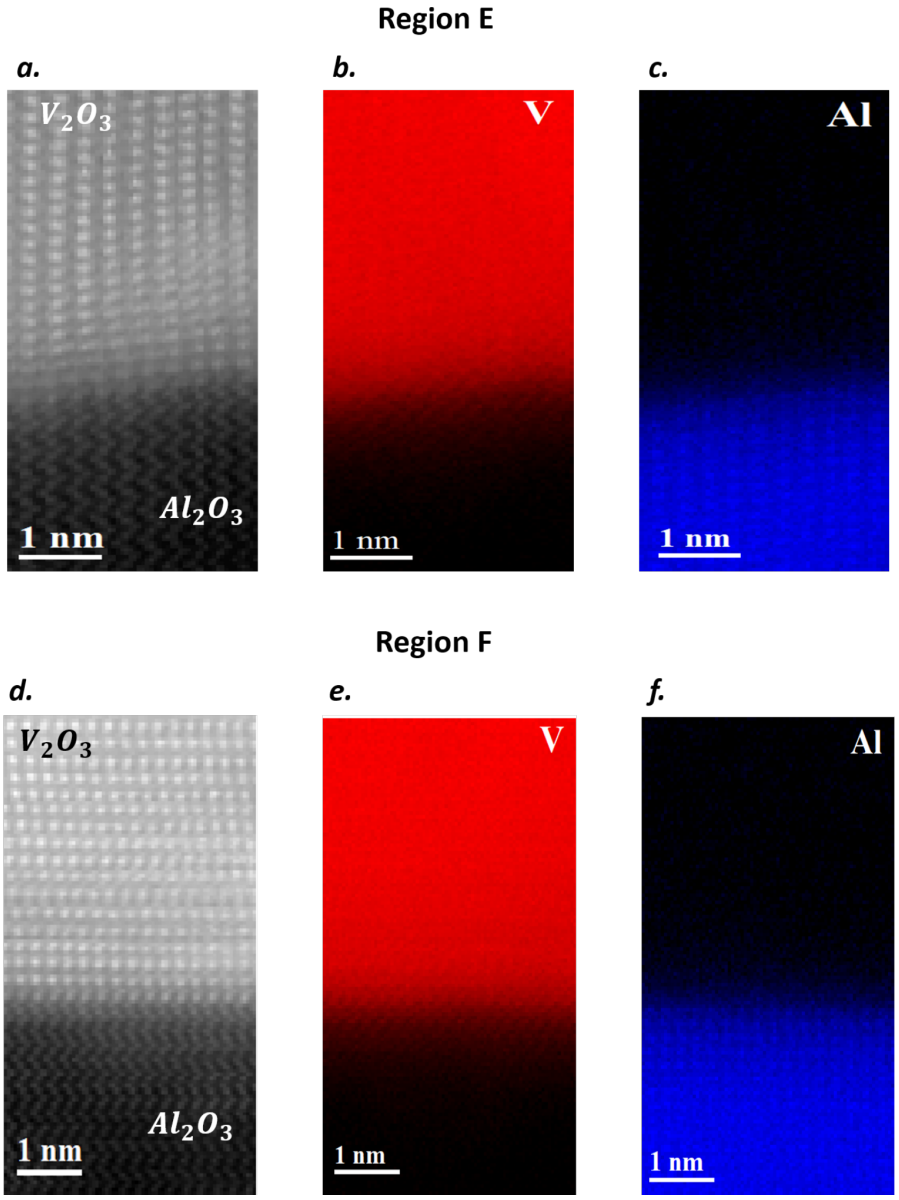

FIGURE 4.28: *a*. Corresponding HAADF map of Region E. *b*. Vanadium chemical map in Region E. *c*. Aluminum chemical map in Region E. *d*. Corresponding HAADF map of region F. *e*. Vanadium chemical map in region F. *f*. Aluminum chemical map in region F.

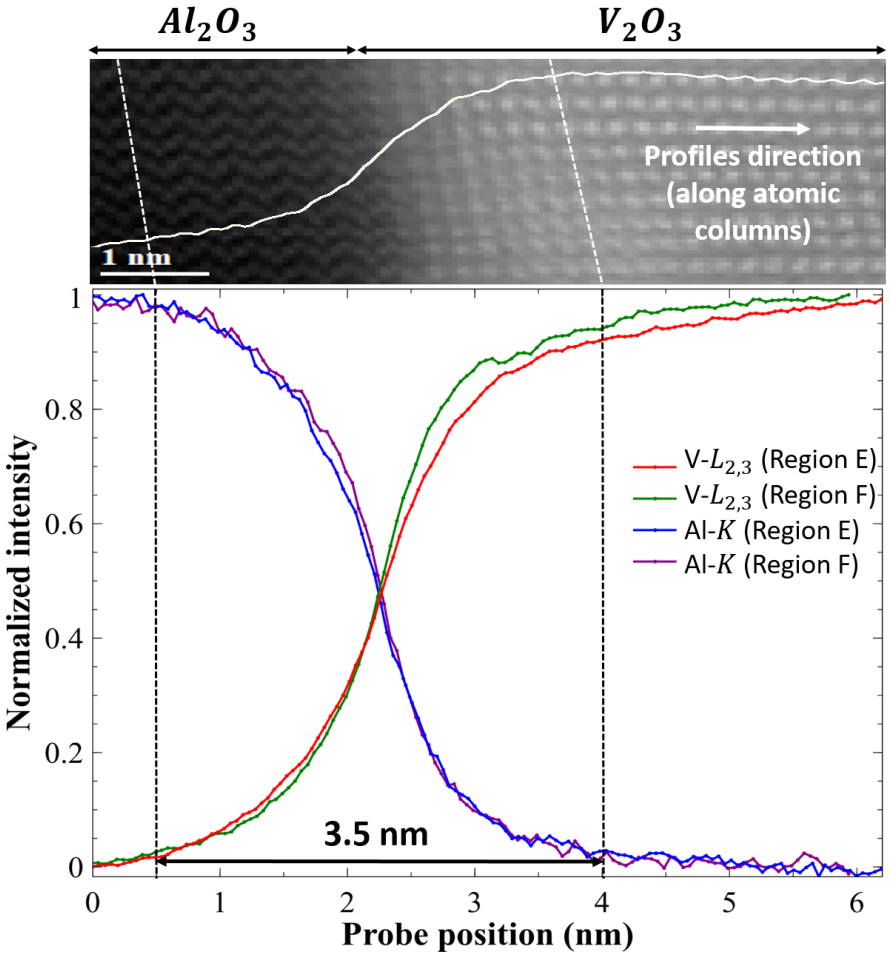

FIGURE 4.29: V-$L_{2,3}$ and Al-K chemical diffusion profiles for regions E and F. A proportion variation for vanadium is observed between these regions.

thin film. However, these results contrast with those carried out in the interfacial region in EELS core-loss, where the spectroscopic signature is relatively homogeneous and similar to the PM phase. These discrepancies could be due to the relative insensitivity of our EELS core-loss measurements to these proportion variations or also to very localized variations of vanadium in the sample, not probed in our core-loss investigations.

As noted throughout this chapter, several parameters, such as structural and electronic inhomogeneities, or possible vacancies, could influence the physical behavior of the V_2O_3 thin film grown on the sapphire substrate. This could also influence our understanding on the intrinsic parameters associated with the PM-AFI phase transition we would like to investigate. We, therefore, need to find a model system for the *in situ* variable temperatures study of the PM-AFI phase transition. The V_2O_3 thin lamellas obtained from the single crystals (IMN Nantes) constitute a candidate of choice. They show almost no structural defects and are not subject to chemical interdiffusion effects at the interface since there is no substrate.

4.5 . Conclusion

In this chapter, we have studied the electronic, structural and chemical properties in a V_2O_3 thin film on an Al_2O_3 substrate. We have highlighted structural inhomogeneities in GPA, characterized by lattice parameter variations and c_h/a_h ratio variations between 2.777 and 2.838. These lattice parameter variations, particularly in-plane (often with values greater than those of the bulk), suggest the presence of a large-volume hexagonal phase (such as the PI phase) in the sample. HAADF imaging observations also suggest the presence of columnar structures in the film. We also found a critical thickness of about 2 nm, which shows a fast beginning of the V_2O_3 film relaxation on the Al_2O_3 substrate. Regarding the investigations in EELS low-loss and EELS core-loss, we have shown the presence of electronic domains where more or less metallic phases, which could be assimilated to PM and a phase analogous to PI, coexist at room temperature probably as nanodomains in variable proportions. These electronic domains of about 50 nm, as determined by clustering and VCA, also have a columnar character. All these results, which

indicate the predominant role of structure in determining electronic properties, suggest strong correlations between these two degrees of freedom. The less metallic domains observed here could also act as nucleation sites during the phase transition between PM and AFI. All these findings add additional degrees of freedom to the description of the thin film physical properties, which is already quite challenging due to electronic correlations. We have therefore chosen to work with a system less subject to these different parameters, i.e., the thin lamellas made from V_2O_3 single crystals. They will be used for the *in situ* variable temperature investigation of the electronic and structural properties during the PM-AFI phase transition.

Chapter 5

In situ variable temperature investigation of the electronic and structural properties across the temperature-induced MIT in V_2O_3 single crystal.

5.1 . Introduction

The existence of structural precursors in the PM-AFI transition has been discussed in the past [6, 56–58], both in thin films and single crystals. However, the study of these systems, in particular thin films, has proven to be challenging. Indeed, as we have just seen in the case of thin films, the triggering of the electronic and structural properties can be subject to many factors, such as structural defects, lattice distortions or possible vacancies. In addition, the spatial resolutions used to investigate the correlations between electronic and structural properties can lead to different interpretations of this phase transition. The works of McLeod *et al.* [6] and Kalcheim *et al.* [7] perfectly illustrate this. While some (McLeod *et al.*) observe in micro-XRD and nano-IR (25 nm probe size) the decoupling between the electronic and structural transitions from PM to AFI, the others (Kalcheim *et al.*) observe instead in XRD (penetration depth of $\sim$ 13 μm) and IR-spectroscopy (penetration depth up to 760 nm) a strong coupling between these two degrees of freedom.

Many questions remain regarding understanding the PM-AFI phase transition, mainly about the nucleation and growth mechanisms that involves heterogeneities at the nanoscale. What are the eventual nanoscale mechanisms behind this transition under the same experimental conditions? Is there a strong coupling between electronic and structural degrees of freedom at this scale, and if not, which degree of freedom drives the transition?

In this chapter, we investigate in pure V_2O_3 single crystals, the simultaneous evolution at the nanoscale of electronic and structural properties during this PM-AFI temperature-induced phase transition. We combine nanoscale resolved monochromated EELS low-loss measurements (for electronic characterization) with 4D-STEM microdiffraction and nanodiffraction measurements (for structural characterization) in these *in situ* variable temperature experiments.

5.2 . Spectroscopic fingerprints for metallic and insulating phases

As explained in Chapter 3, the variable temperature experiments for investigating the PM-AFI transition are performed with the monochromated electron microscope NION CHROMATEM. The microscope is equipped with the double-tilt HennyZ cryo holder, using a MEMS system to vary the temperature continuously between 125 K and 300 K. The EELS data presented in this chapter was also acquired, at the spatial nanometric resolution, before and after the installation of the Medipix 3 direct detection camera. Due to limited signal-to-noise ratio (SNR) in core-loss as a consequence of a larger thickness of the lamella, we restricted our spectroscopic acquisitions to the low-loss region. We would also like to recall that the V_2O_3 thin lamella used (from IMN Nantes) was obtained by FIB cutting along the $[\bar{1}\bar{1}0]_h$ zone axis. The lamella was deposited and maintained by platinum (Pt) contacts on our MEMS, as shown in figure 3.14 of Chapter 3.

The EELS low-loss spectra of V_2O_3 , acquired on the MEMS (with the Medipix 3), in the PM phase at ambient temperature (metallic) and AFI phase at low temperature (insulating), are shown in figure 5.1. Overall, it should be mentioned that the spectra display clearer and sharper features than in the

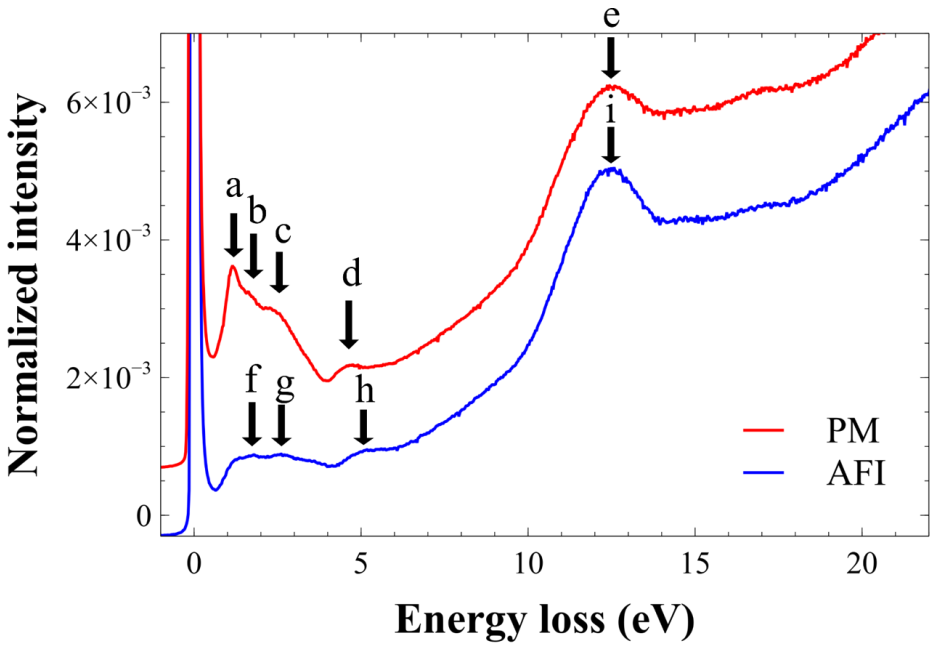

FIGURE 5.1: EELS low-loss spectra of PM (metallic) and AFI (insulating) phases. The letters stand for the spectroscopic features in the spectra.

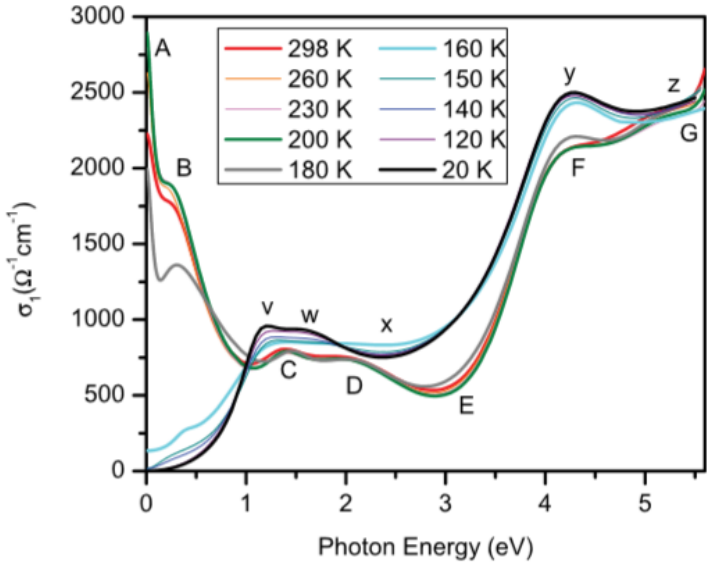

FIGURE 5.2: Real part of the optical conductivity for a V_2O_3 thin film. The figure is adapted from [130].

case of thin films (see chapter 4) and that the measurements are in perfect

agreement with the previous ones by Abe *et al.* on a V_2O_3 crystal [69]. According to the latter, the feature around 12.5 eV (indicated by the letters e and i in figure 5.1) is assigned to interband plasmons associated with transitions from oxygen 2p to vanadium 3d levels, so as the feature at $\sim$ 5 eV (d and h in figure 5.1). Moreover, a shift of $\sim$ 0.3 eV, not discussed by Abe *et al.*, is observed for this latter feature (at 5 eV) between the PM and AFI phases (shift toward higher energy loss for AFI). A similar feature, with the same trend between PM and AFI, is shown by Stewart *et al.* [130] in the real part of the optical conductivity obtained by ellipsometric measurements, but at lower energy, around $\sim$ 4 eV (see figure 5.2). Note that the real part of the optical conductivity is related to the imaginary part of the dielectric function ϵ, and the EELS low-loss region to the ($Im(-1/\epsilon)$) response function. Therefore, due to the contribution of the real part of ϵ in EELS low-loss, some similar features present in the real part of the optical conductivity and in EELS low-loss may experience a shift depending on the technique used. Additonal features, not assigned by Abe *et al.*, can also be discussed in the light of measurements performed for the real part of the optical conductivity. Thus, the features around $\sim$ 1.8 eV (feature b) and $\sim$ 2.5 eV (feature c) in the PM phase could correspond respectively to the transition from the vanadium e_g^π lower Hubbard band to the vanadium t_{2g} quasiparticle peak and to the transition from the vanadium t_{2g} quasiparticle peak to the vanadium a_{1g} upper Hubbard band. In the AFI phase, the features around $\sim$ 1.8 eV and $\sim$ 2.6 eV (f and g, respectively) could be assigned to transitions within the vanadium t_{2g} lower Hubbard bands. Finally, we observe the sharp peak at $\sim$ 1 eV (feature a) already mentioned in the previous chapters, corresponding to an interband plasmon, according to Abe *et al.*, and present only in the PM phase.

During the cooling process, we observe the presence and the vanishing of the 1 eV spectroscopic feature before and after the electronic transition, respectively, as already observed by Abe *et al.* and reported in chapter 3 (figure 5.3**.a**). This metal-to-insulator transition (MIT) appears at 138 K, almost at the same value as Abe *et al.* (140 K) for pure V_2O_3. During heating (figure 5.3**.b**), the same behavior is observed, with the absence or the presence of the 1 eV feature, before and after the electronic transition, respectively. At 153 K, the

sample is entirely metallic, as shown in Figure 5.3**.b** . The thermal hysteresis deduced from the spectroscopic measurements during cooling and heating is $\sim$ 15 K (figure 5.3**.c**), in the same order of magnitude as in bulk materials [37].

EELS core-loss spectra also reveal an upward shift of $\sim$ 0.4 eV on the O-K edge during the MIT between PM and AFI phases (figure 5.4). Again, this shift value is consistent with that of Abe *et al.* and that observed for thin films in the previous chapter. However, these spectra are less spectrally resolved than those obtained previously for the thin film due to the KURO CMOS camera used here (worse PSF than the Medipix 3) and the accumulation of several spectra in order to obtain a good SNR. We point out that this shift value is almost identical to that previously reported on the EELS low-loss interband transition near 5 eV. We also observe, on the V $L_{2,3}$ edge, all the fine structure changes related to the phase transition (indicated by arrows), as mentioned in the previous chapter.

5.3 . Structural texture across the transition

During cooling, the homogenous contrast observed on HAADF images above the transition, as shown in figure 5.5**.a** (139 K), gives way to the abrupt appearance at the MIT of quasi-periodic stripes with alternating dark and bright contrasts (138 K in Figure 5.5**.b**). The dark and bright stripes have about $\sim$ 80 nm - 100 nm and 30 nm - 40 nm widths, respectively. However, when we move away from the lamella edge, we notice a contrast inversion, probably due to thickness variation. In the following, the dark stripes refer to the larger regions and the bright stripes to the thinner regions. Interestingly, we note that, according to our associated spectroscopic measurements and mapped by applying K-means clustering, (see figure 5.6) , the electronic transition appears to be also abrupt during this process. In these images (at 139 K and 138 K), the homogeneous contrast is associated with the metallic state (see figures 5.5 and 5.6), and the stripy one with the insulating state. Upon heating, these stripes change to a homogeneous HAADF contrast at

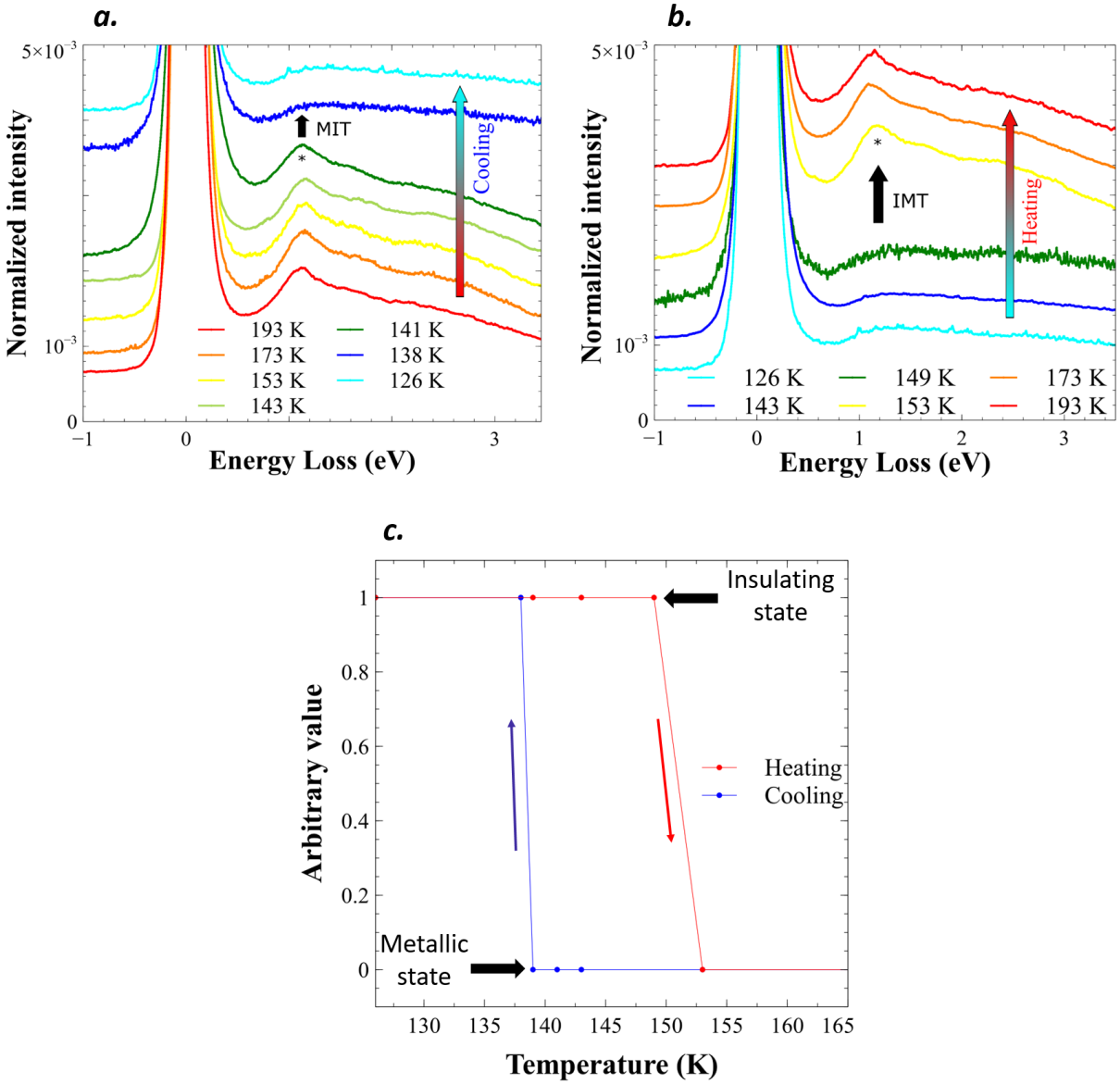

FIGURE 5.3: *a*. EELS low-loss spectra probed upon cooling across the PM -> AFI transition. *b*. EELS low-loss spectra probed upon heating across the AFI -> PM transition. *c*. The thermal hysteresis, deduced from the spectroscopic measurements ($\sim$ 15 K).

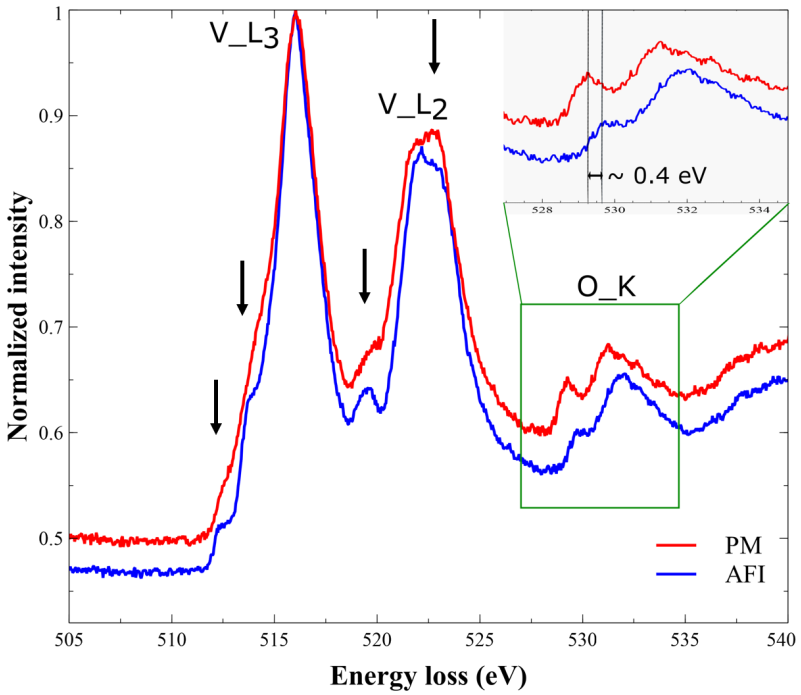

FIGURE 5.4: EELS core-loss from the PM and AFI phases, where a $\sim$ 0.4 eV shift for the O-K edge is observed from PM to AFI.

the insulator-to-metal transition (IMT) (see figures 5.5**.c**, 5.5**.d**, 5.5**.e**). However, over a $\sim$ 3 K temperature range, there is a coexistence of stripy and homogeneous contrasts regions separated by a propagating wall inclined with respect to the direction of the stripes (151 K and 152 K in figures 5.5**.c** and 5.5**.d**). Finally, according to our spectroscopic measurements, we notice an electronic phase coexistence for the same temperature range, where stripy regions correspond again to the insulating state and homogeneous contrast region to the metallic one.

We have performed electron nanodiffraction (spatial resolution $\sim$ 5 nm) and microdiffraction (spatial resolution $\sim$ 10 nm) experiments in 4D-STEM acquisition mode to fully characterize this nanostructuration. We observe, in nanodiffraction, in the metallic state at 139 K, one First-Order Laue Zone (FOLZ) centered on the position of the transmitted beam (figure 5.7**.a**). As shown in figure 5.7**.c** in the insulating state (138 K), 2 FOLZs, are present in dark and bright stripes, but with different intensities. One is centered on the transmitted beam position, and the other is shifted from that position. We used the JEMS software to determine the zone axis corresponding to each

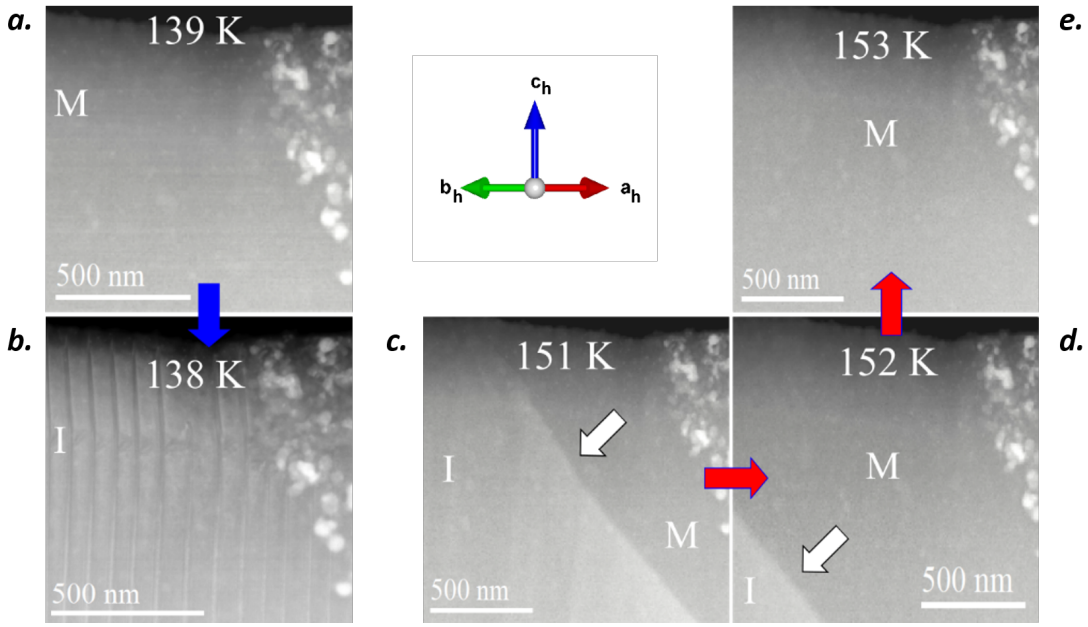

FIGURE 5.5: Letters I and M denote respectively insulating and metallic states. HAADF image acquired : *a*. at 139 K, upon cooling (M state). *b*. at 138 K (I state), upon cooling. Appearance of abrupt stripes at this temperature. *c*. at 151 K upon heating. A domain wall is observed, separating stripy regions (I state) and homogeneous contrast regions (M state). *d*. at 152 K upon heating. The domain wall propagates into the sample. *e*. at 153 K, acquired upon heating. A homogeneous contrast is observed throughout the sample.

FOLZ (as indicated in figure 5.7). The deduced zone axis at 139 K in the metallic state corresponds well to the $[\bar{1}\bar{1}0]_h$. In the insulating state (at 138 K), the centered FOLZ also corresponds to the $[\bar{1}\bar{1}0]_h$ zone axis, but not the shifted one found in the [1$\bar{9}$7 1$\bar{9}$7 $\bar{1}$] zone axis configuration. It is well known that upon cooling, 3 monoclinic twins can form in V_2O_3, resulting from the possibility for the hexagonal c_h axis to tilt towards the 3 equivalent basal plane axes at the transition [33]. This configuration should result in the observation of 3 FOLZs in nanodiffraction, where the FOLZs centers would be shifted from the position of the transmitted beam. However, we would like to point out that depending on the sample growth process or sample preparation method, only 2 monoclinic twins [6] or even a single monoclinic domain

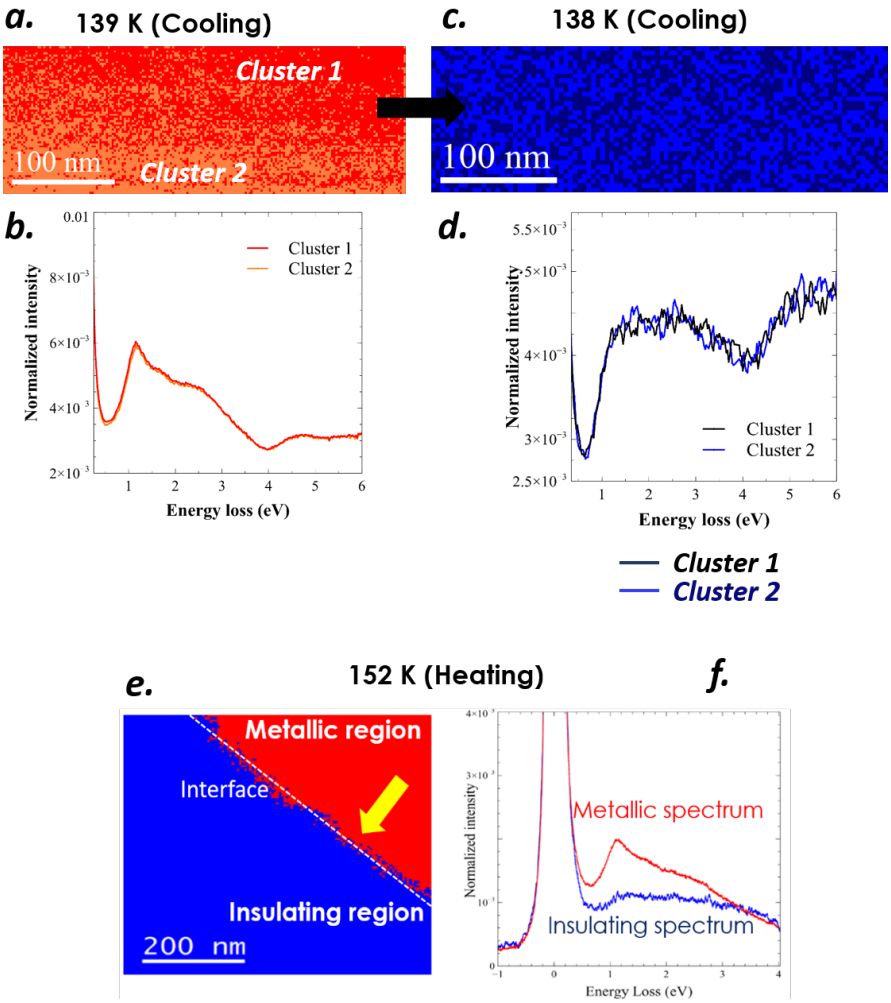

FIGURE 5.6: Maps obtained in clustering : *a*. at 139 K, upon cooling. *c*. at 138 K, upon cooling. *e*. at 152 K, upon heating. Spectra deduced in the clustering regions : *b*. at 139 K. *d*. at 138 K. *f*. at 152 K.

[131] can form. Indeed, when extracting a FIB lamella from the crystal parallel to the c_h axis and in particular directions for the basal plane, basal plane axes become inequivalent due to edge effects [131]. In these conditions, the transition results in the formation of a single monoclinic domain. We believe the latter configuration is reached during the FIB cutting along the $[\bar{1}\bar{1}0]_h$ zone axis. Hence, in the insulating state, we assign the shifted FOLZ to this single monoclinic domain characterized by a $\sim 1°$ tilt of the c_h axis (as determined using the JEMS software) and the second FOLZ where no shift is

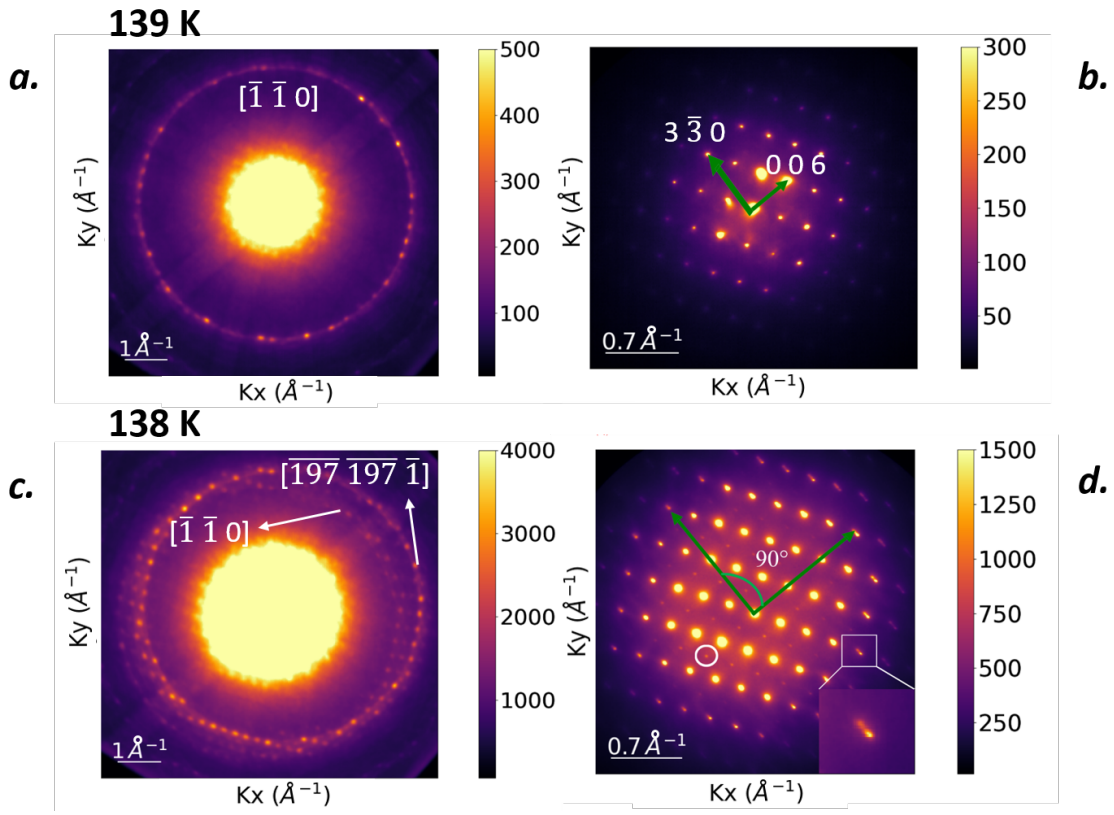

FIGURE 5.7: *a*. Electron nanodiffraction pattern acquired at 139 K. *b*. Electron microdiffraction pattern acquired at 139 K. *c*. Electron nanodiffraction pattern acquired at 138 K. *d*. Electron microdiffraction pattern acquired at 138 K. Two splitted spots are present (white square). Spots with 1/2 periodicity are also shown (in white circle). Data presented here are acquired in the thin lamella on the MEMS.

observed to the hexagonal structure.

As discussed above, the 2 FOLZS observed in the insulating state (the centered and the shifted FOLZs) show different intensities depending on whether the probe seats in a bright or dark stripe. However, we would like to point out that the dark stripe observed in the HAADF image showed almost only the shifted FOLZ (attributed to the monoclinic structure) during the first temperature cycles. The appearance of the second centered FOLZ (attributed to the hexagonal structure) in these dark regions (with much lower intensity), which occurred during the following *in situ* experiments, could be due to the

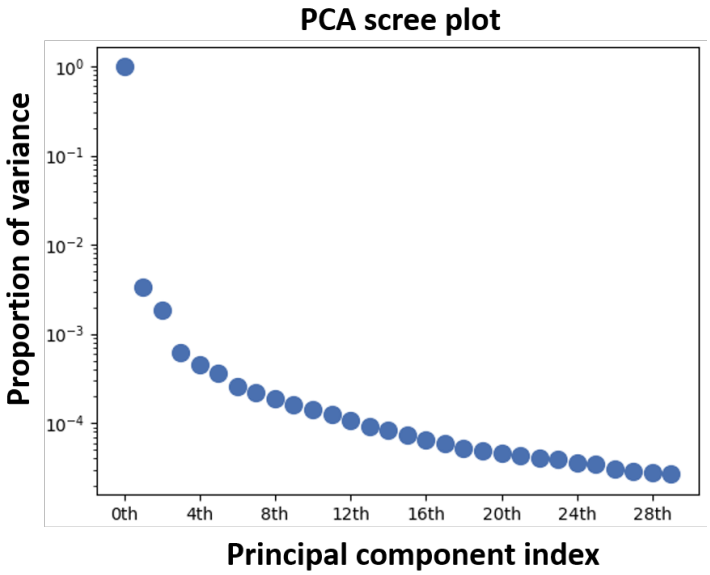

FIGURE 5.8: PCA scree plot obtained from the 4D-STEM nanodiffraction data (138 K) during cooling.

successive thermal cycles applied to the sample. Apart from this fact, all observations made in EELS spectroscopy or diffraction are almost identical over all thermal cycles performed in this thesis, thus ensuring the reproducibility and reliability of our data.

We applied K-means clustering to our 4D-STEM nanodiffraction acquisitions to map the structural inhomogeneities observed in the sample at 138 K. As we can see in figure 5.8, the scree plot of the PCA decomposition applied to our data shows more than 2 principal components before the slope change criterion. These observations could be due to the diffraction dynamical effects (multiple diffractions, for instance, in the sample), which would add additional components before the slope change on the scree plot. Nevertheless, applying K-means clustering with 2 components does not recover the periodic spatial distribution of structural inhomogeneities in the sample, especially in the left area of the probed region, as observed in figure 5.9. To solve this issue, we decided to apply, this time, the K-means clustering algorithm not in the dimensional space associated with the raw 4D-STEM data (2048 x 2048 px^2) but instead in the much smaller dimensional space associated with the PCA decomposition. Such an approach, also used by

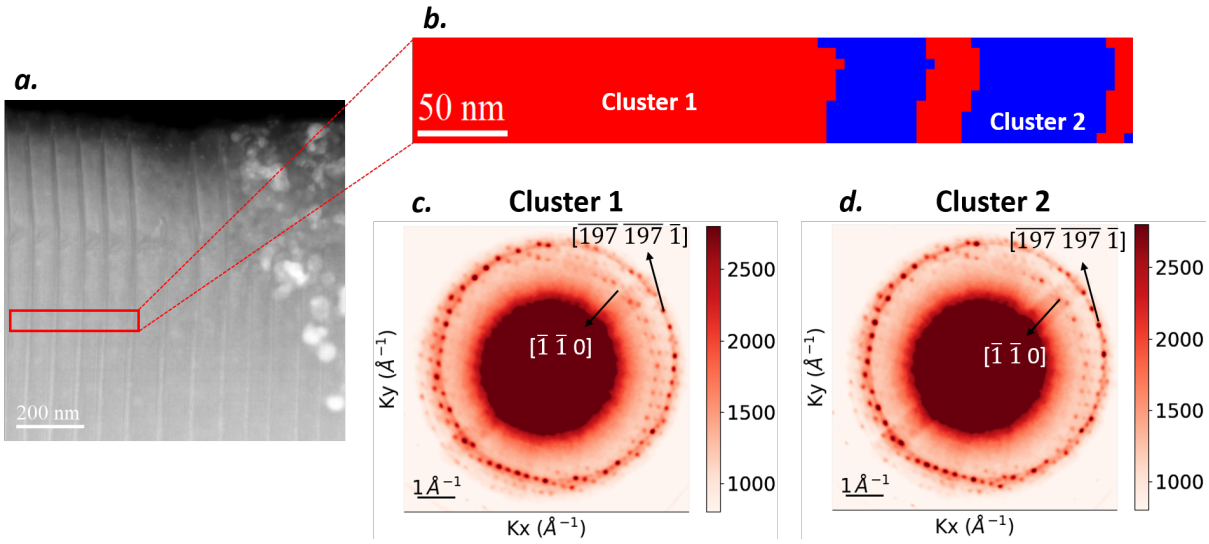

FIGURE 5.9: *a.* HAADF image showing the probed region in nanodiffraction at 138 K (cooling). *b.* Map obtained in clustering for the probed region in nanodiffraction. *c.* and *d.* FOLZs associated with the clusters.

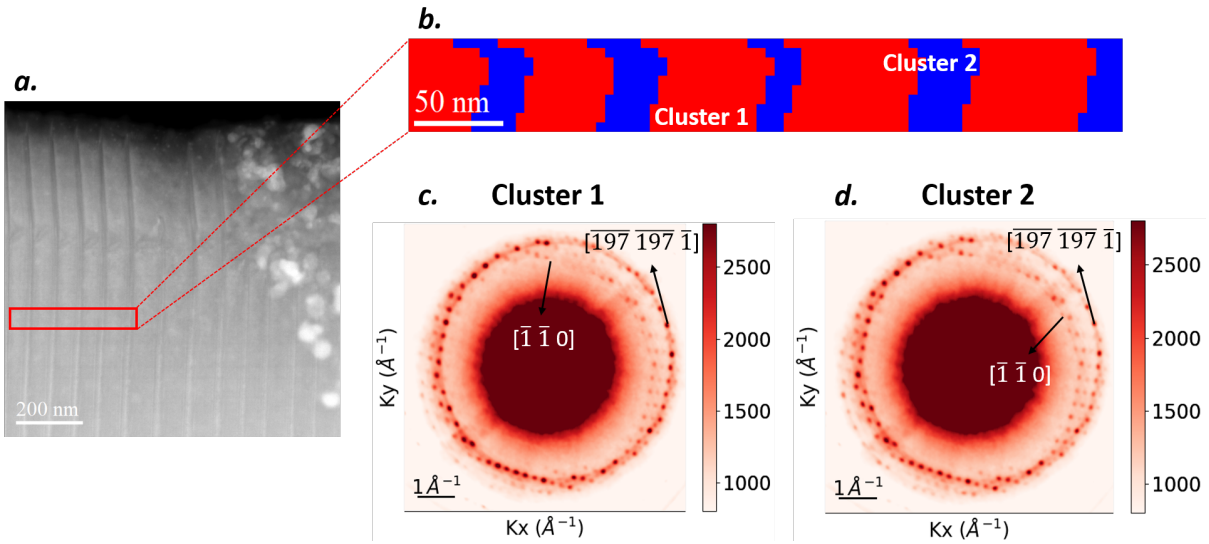

FIGURE 5.10: *a.* HAADF image showing the probed region in nanodiffraction at 138 K (cooling). *b.* Map obtained in clustering by using the first 10 components of PCA decomposition. *c.* FOLZs associated with the clusters. The intensity of the centered FOLZ appears more intense for cluster 2.

Torruella *et al.* [115], improves the K-means algorithm's performance since

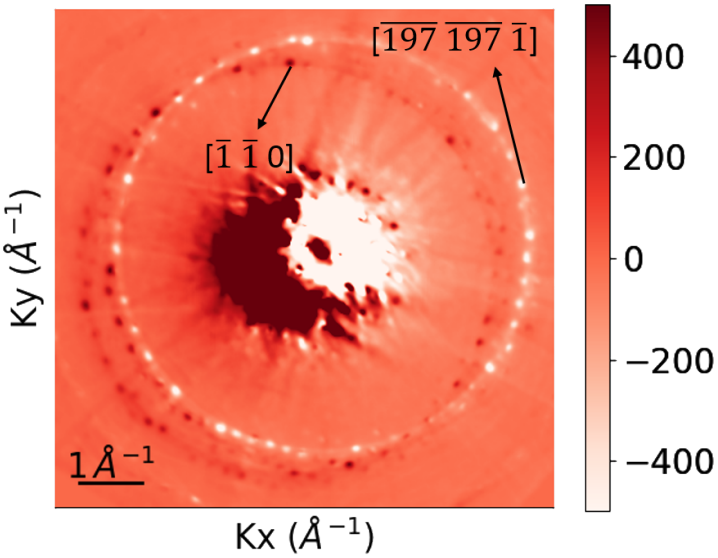

FIGURE 5.11: 2D difference signal obtained by subtracting the FOLZ contribution of cluster 1 from that of cluster 2.

the euclidean distance metric becomes less precise when the dimension of the space considered becomes large. Moreover, this approach not only improves the data clustering with respect to noise, but also greatly reduces the data processing time (from about 20 min on raw 4D-STEM data to about 1 min on PCA decomposed data). Finally, by applying K-means clustering from the first 10 principal components of the PCA decomposition [1] (which is now equivalent to working in a 10-dimensional space), we successfully mapped these structural inhomogeneities with 2 components in the insulating state. We find this periodic distribution (see figure 5.10), whose different regions mapped in clustering correspond almost to those observed on the raw data. The large dark stripes (cluster 1) show lower intensities for the centered FOLZ than the small bright stripes (cluster 2), as discussed previously. The difference signal between the components obtained by clustering (see figure 5.11) also shows, on the one hand, a relative majority contribution of the centered FOLZ for cluster 2 (bright stripe), compared to cluster 1 (dark stripe). On the other hand, a relative majority contribution of the shifted FOLZ for cluster 1 is observed, compared to cluster 2. These results could

[1] The number of PCA components chosen here is determined by inspecting the maps and spectra associated with the decomposition, as discussed in previous chapters.

reflect the relative proportions of these hexagonal and monoclinic phases observed in the stripes.

In order to corroborate this hypothesis (about the structural coexistence), we performed microdiffraction measurements. In the metallic state, the microdiffraction pattern (figure 5.7**.b**) matches perfectly with the hexagonal symmetry in the $R\bar{3}C$ space group (still determined using the JEMS software). In the insulating state, we observe two splitted spots (figure 5.7**.d**). Again one pattern matches well with the hexagonal structure, and the second, even if it cannot be perfectly indexed, seems to be consistent with a V_2O_3 monoclinic pattern, in agreement with the $\sim 1°$ split between the spots along the c_h^* direction. The impossibility of indexing this monoclinic pattern comes from the fact that all experiments performed on the MEMS in the metallic or insulating state are done in the $[\bar{1}\bar{1}0]_h$ hexagonal zone axis. This second pattern resembles that of V_2O_3 in $[020]_m$ monoclinic zone axis, one of the zone axes derived from the hexagonal to monoclinic structural transition relationship. Indeed, the equivalences between the hexagonal and monoclinic zone axes before and after the structural transition can be derived from the relationships given by Dernier *et al.* [33] :

$$\begin{pmatrix} \mathbf{a_m} \\ \mathbf{b_m} \\ \mathbf{c_m} \end{pmatrix} = \begin{pmatrix} 2/3 & 4/3 & 1/3 \\ 1 & 0 & 0 \\ 1/3 & 2/3 & -1/3 \end{pmatrix} \begin{pmatrix} \mathbf{a_h} \\ \mathbf{b_h} \\ \mathbf{c_h} \end{pmatrix} \tag{5.1}$$

or

$$\begin{pmatrix} \mathbf{a_m} \\ \mathbf{b_m} \\ \mathbf{c_m} \end{pmatrix} = \begin{pmatrix} -4/3 & -2/3 & 1/3 \\ 0 & 1 & 0 \\ -2/3 & -1/3 & -1/3 \end{pmatrix} \begin{pmatrix} \mathbf{a_h} \\ \mathbf{b_h} \\ \mathbf{c_h} \end{pmatrix} \tag{5.2}$$

or

$$\begin{pmatrix} \mathbf{a_m} \\ \mathbf{b_m} \\ \mathbf{c_m} \end{pmatrix} = \begin{pmatrix} 2/3 & -2/3 & 1/3 \\ -1 & -1 & 0 \\ 1/3 & -1/3 & -1/3 \end{pmatrix} \begin{pmatrix} \mathbf{a_h} \\ \mathbf{b_h} \\ \mathbf{c_h} \end{pmatrix} \tag{5.3}$$

In these expressions, $\mathbf{a_m}$, $\mathbf{b_m}$, and $\mathbf{c_m}$ are the monoclinic lattice's basis vectors. $\mathbf{a_h}$, $\mathbf{b_h}$ and $\mathbf{c_h}$ are those of the hexagonal lattice.

Thus, from these relations, we would have obtained from the $[\bar{1}\bar{1}0]_h$ hexagonal zone axis, the $[\bar{2}\bar{1}\bar{1}]_m$, $[\bar{2}\bar{1}1]_m$, and $[020]_m$ zone axes if we had observed twinning at the structural transition (which is not the case). Only $[020]_m$ comes nearest to the observed monoclinic structure of these 3 zone axes [2]. Beyond these splittings, in the insulating state, we observe additional spots with ½ periodicity (in the small white circle in figure 5.7.**d**). These additional spots seem to correspond to double diffraction, according to the indexed diffraction pattern in the insulating state observed in figure 5.12. They fit quite well with the simulated double diffraction spots of the hexagonal structure in the $[\bar{1}\bar{1}0]_h$ zone axis (still obtained using JEMS).

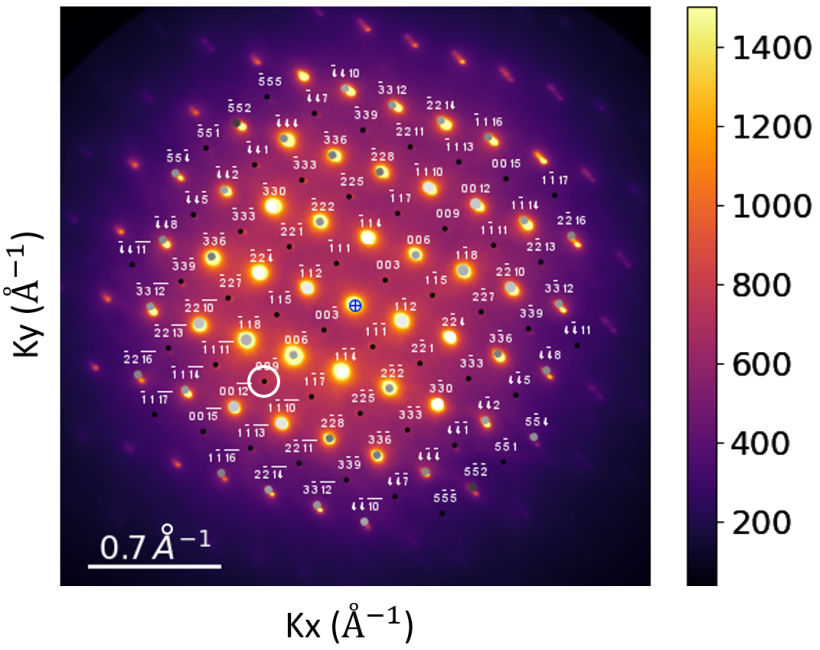

FIGURE 5.12: Microdiffraction pattern obtained at 138 K during cooling (structural coexistence). Here, the pattern is indexed from the hexagonal structure in the $[\bar{1}\bar{1}0]_h$ zone axis. The spots associated with the double diffraction fit well with those of 1/2 periodicity observed in microdiffraction (see spot in the white circle).

To understand the origin of the nanotexturation observed in the insulating state, we designed a "flag geometry" lamella (figure 5.13). This lamella

[2]Some experiments carried out under the monoclinic conditions zone axis at the structural transition have verified that the zone axis effectively obtained is $[020]_m$.

is extracted by FIB within the same zone axis ($[\bar{1}\bar{1}0]_h$), then stuck and maintained only on one lateral side ("flag geometry") on an omniprobe grid. By cooling the latter, we observe stripes appearance at the transition, but only on the maintained side (figure 5.13**.a**). The other free edge, near vacuum, does not show these patterns (figure 5.13**.b**). Here, the sample is probed under monoclinic zone axis conditions ($[020]_m$). In the stripy region, we observe almost the same features as previously, i.e., the observation of the 2 centered and shifted FOLZs. In the region without stripes, nanodiffraction patterns from the insulating state display only one FOLZ, related to the single monoclinic domain (figure 5.14**.a**). In microdiffraction, we obtain, this time, only one pattern which fits well with the monoclinic structure in the $I2/a$ space group (figure 5.14**.b**). Particularly, we do not observe the additional spots with $1/2$ periodicity (indicated in the white circle previously). Finally, we attribute these additional features to double diffraction, resulting from the diffraction dynamical effects due to sample thickness, or the disorientation between the 2 coexisting structures at low temperatures in the MEMS sample.

Note also that some splitted spots are present in the microdiffraction pattern from the stripes-free region (enlarged view on figure 5.13**.b**), but share the same monoclinic symmetries and correspond to the same $[020]_m$ zone axis. Such observations are possible in electron microdiffraction when the beam is in the vicinity of a discontinuity [132], which suggests the presence of a small mosaicity in the sample.

5.4 . Structural parameter evolution across the phase transition

From the present analysis, the stripes generated in the insulating phase result from the coexistence of monoclinic and hexagonal structures. The existence of this hexagonal structure in the insulating state suggests the presence of a phase anlogous to PI; the other insulating phase of V_2O_3. In order to check this assumption, we determined the lattice parameters and the c_h/a_h ratio of the hexagonal structure in metallic and insulating states (figure 5.16)

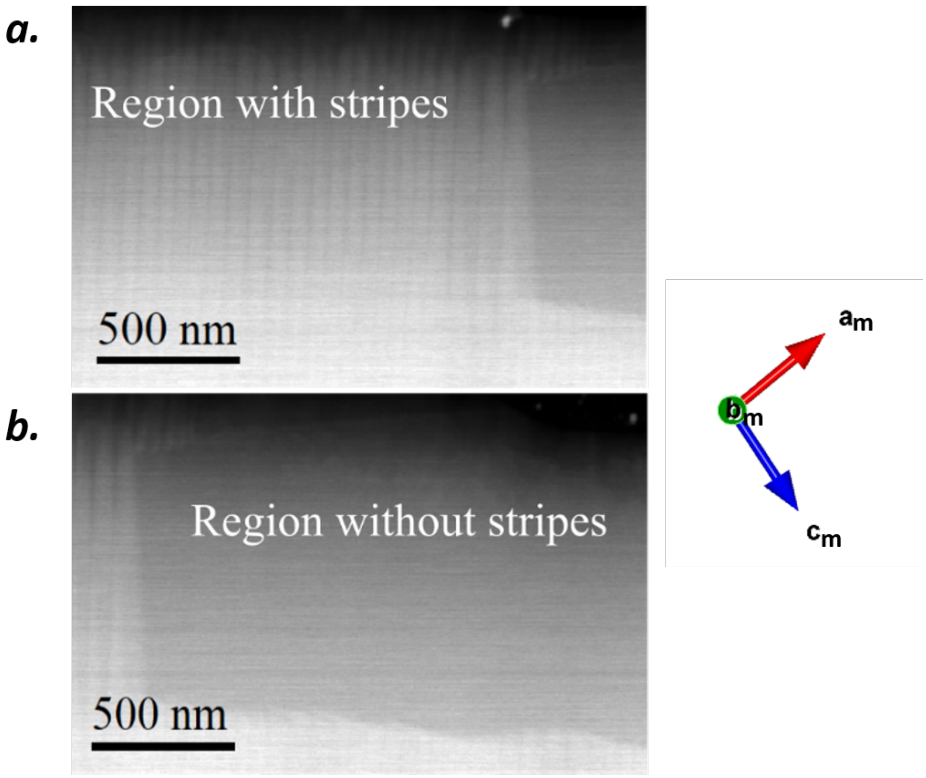

FIGURE 5.13: HAADF images acquired under liquid nitrogen for "flag geometry" lamella. *a*. HAADF image of the region with stripes, close to maintained side. *b*. HAADF image of the region without stripes, near vacuum.

from microdiffraction [3] acquisitions. According to Rodolakis *et al.* [133] (see figure 5.15), the transition from PM to PI phases under pressure, temperature, or chromium doping, is characterized by a decrease in the c_h lattice parameter, an increase in the a_h lattice parameter, and a decrease and a jump in the c_h/a_h ratio. However, for titanium-doped V_2O_3, the decrease in the c_h/a_h ratio does not lead to an insulating state, as observed by Ishiwata *et al.* [134]. In some works [37, 134], it is argued that c_h is rather the pertinent lattice parameter that should be considered in the MIT mechanism. Qualitatively, we observe in our case (figure 5.16) a jump of the c_h lattice parameter at IMT and MIT, with the same behavior (increase or decrease), as shown by Rodolakis *et al.*. Also, a jump and a small variation (increase or decrease as in

[3] The microdiffraction data used here were acquired with a spatial resolution of about 120 nm away from the phase transition and about 10 nm near the transition ($\sim$ 10 K).

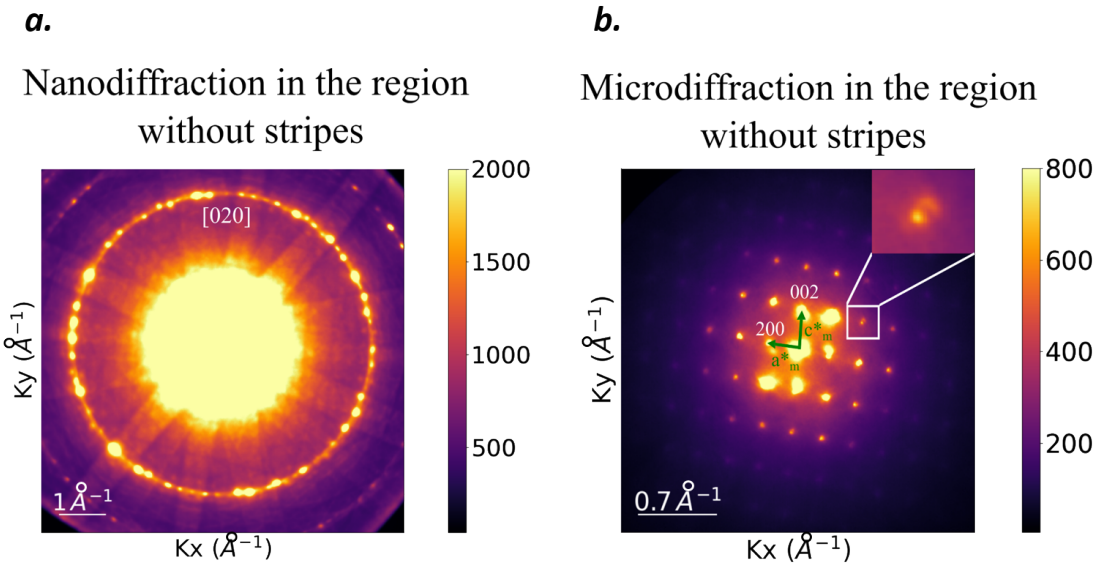

FIGURE 5.14: *a*. Electron nanodiffraction pattern acquired under liquid nitrogen for the "flag geometry" lamella in the $[020]_m$ monoclinic zone axis. Only one FOLZ is observed. *b*. The corresponding microdiffraction pattern, with the monoclinc symmetry in the $[020]_m$ zone axis for $I2/a$ space group. Some splitted spots are observed (inset).

[133]) are observed respectively at IMT and MIT, in the a_h lattice parameter and the c_h/a_h ratio. However, upon cooling, almost $\sim$ 10 K after MIT, the small variation gives way to a jump in the a_h lattice parameter and c_h/a_h ratio. This delay in jump for a_h and c_h/a_h is not observed at IMT, upon heating. This is probably due to the fact that the data point after IMT, in figure 5.16, is acquired for the complete electronic transition of the sample, perhaps a few Kelvins after the transition of the probed region. These significant changes in the c_h lattice parameter before those of a_h, during MIT, could indicate the decisive role of c_h in the electronic transition. Finally, from all these observations, the present results suggest a first-order transition towards a phase similar to PI in the insulating state.

Surprisingly, spectroscopic investigations in EELS low-loss reveal only one spectroscopic signature in the insulating state (see figure 5.17). There is also almost no difference in this signature with that acquired in homogeneous contrast regions for the "flag geometry" lamella in the insulating

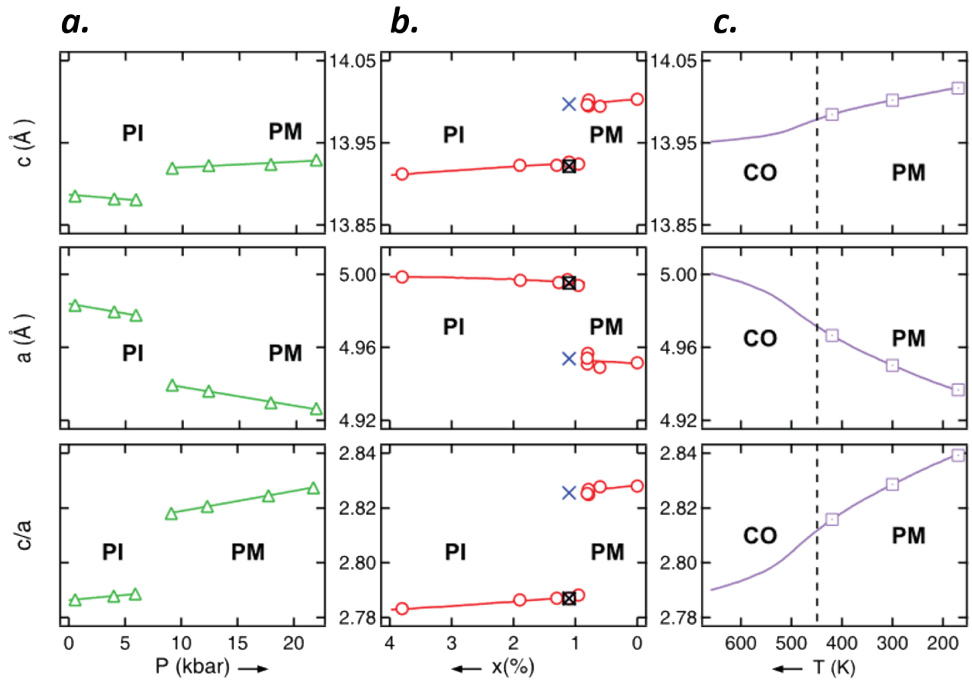

FIGURE 5.15: *a*. Lattice parameters evolution during the pressure-induced transition between PM and PI phases in 2.8 % Cr-doped V_2O_3. *b*. Lattice parameters evolution between the PM and PI phases, depending on the chromium doping. *c*. Lattice parameters evolution as a function of temperature in V_2O_3. "CO" refers to the crossover region. In this region, the PM and PI phases are no longer clearly differentiated. The figures are adapted from [133].

state, where only the AFI phase (associated to monoclinic structure) is detected. Therefore, it seems that the PI and AFI phases coexisting in this state are spectroscopically similar. Recently, the PI phase, usually obtained by chromium doping, has been stabilized in pure V_2O_3 by heteroepitaxy at room temperature by Homm *et al.* [67]. In this case, the optical conductivity was shown to be very similar to that of the AFI phase, with a bandgap of up $\sim$ 0.5 eV in contrast to 0.12 eV [52, 67] measured in the PI chromium-doped V_2O_3. It is suggested that this difference could be explained by local inhomogeneities due to chromium doping, which would subsequently affect the optical properties of the sample. Our observations corroborate these results showing strong similarities in the optical conductivity between both PI and

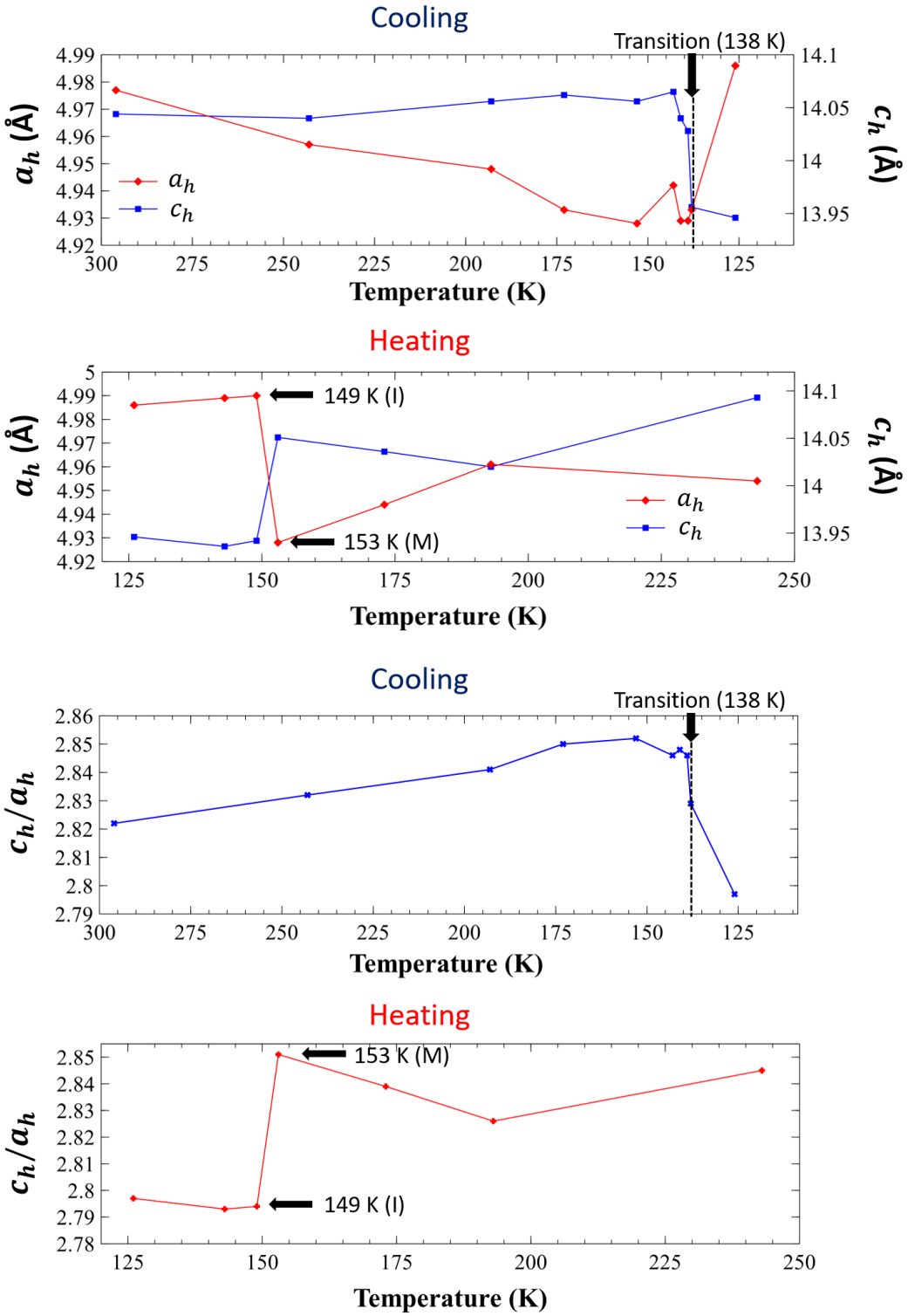

FIGURE 5.16: Evolution of a_h , c_h and c_h/a_h ratio during cooling and heating : *a*. during cooling (for a_h and c_h). *b*. during heating (for a_h and c_h). *c*. during cooling (c_h/a_h). *d*. during heating (c_h/a_h).

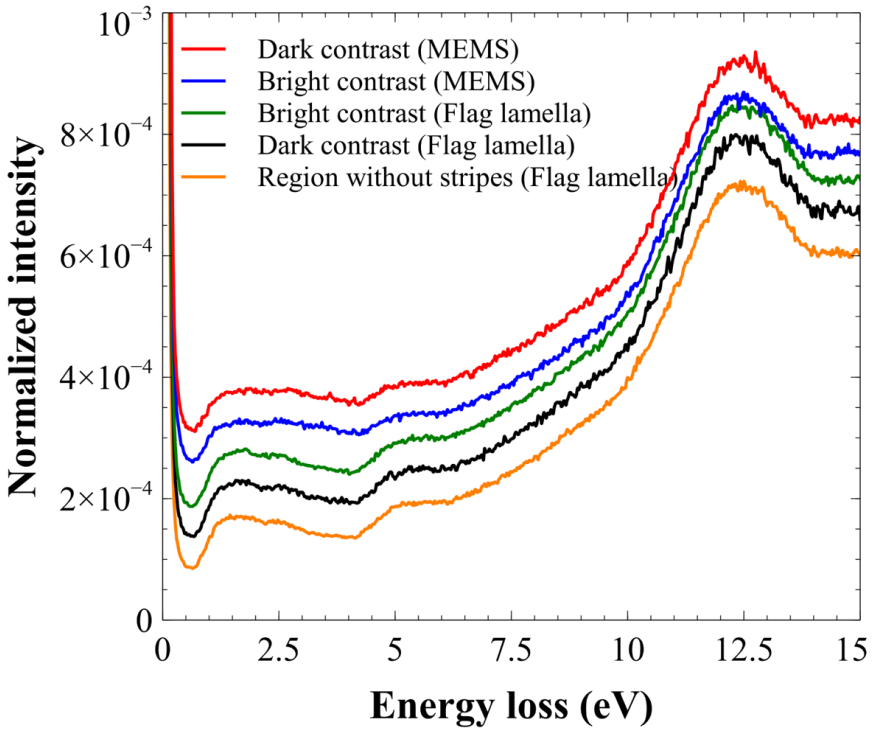

FIGURE 5.17: Spectra obtained at low temperature in the stripy regions and the regions without stripes (on the MEMS and the flag lamella).

AFI phases in pure V_2O_3.

5.5 . Spatial evolution of the structural and electronic phases during the IMT.

As explained previously, the temperature-induced transition is abrupt during cooling, but there exists a phase coexistence range ($\sim$ 3 K) during heating. We now focus on this coexistence regime. At 151 K, we can observe on the HAADF image (figure 5.18**.a**) an interfacial region separating the region with stripes from the region with homogeneous contrast. We performed EELS low-loss together with microdiffraction and nanodiffraction measurements across such an interfacial area to probe stripes (region 1), interface (region 2), and homogeneous (region 3) contrast regions (figure 5.18**.a**). The spatial resolutions used in low-loss, nanodiffraction, and microdiffraction are

approximately 1 nm, 5 nm, and 10 nm, respectively.

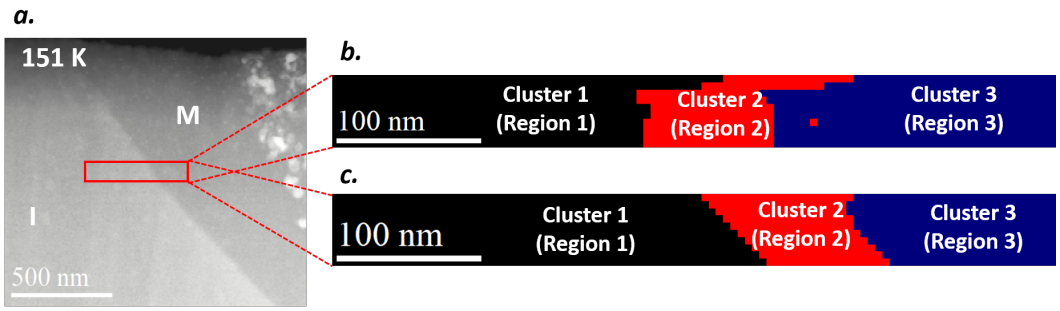

FIGURE 5.18: *a*. HAADF image obtained at 151 K during heating, showing the regions probed by nanodiffraction and microdiffraction. *b* and *c*. Clustering maps obtained by nanodiffraction and microdiffraction respectively, through the interfacial region.

K-means clustering (with 3 clusters) was also applied in these regions, especially on the nanodiffraction and microdiffraction data. As shown in figure 5.18, the clusters observed on the maps coincide quite well with these different regions. The morphology differences observed at the interface on the nanodiffraction map (domain wall not tilted) are due to spatial drift during this data acquisition. We also note that the microdiffraction data presented in figure 5.19 are obtained in specific regions within each cluster. This representation choice was intended to highlight better the characteristics associated with the different domains established in clustering.

In region 1, we observe now 3 FOLZs in the nanodiffraction patterns (figure 5.19**.a**) instead of the 2 previously identified . The corresponding zone axes derived by using JEMS software are [$1\bar{1}0$ $1\bar{1}0$ $\bar{1}$]; [$11\bar{7}75$ $11\bar{6}18$ 75] and [$8\bar{9}$ $8\bar{8}$ 0]. We notice that even if the h and k indices characterizing the [hkl] zone axis are not identical in some cases (contrary to expectations, as there is only a tilt of the c_h axis), they are very close. These small differences could be explained by the arrangement of coexisting domains, inducing possibly structural deformations, and also could be due to the precision of the measurement tools. However, this does not affect our results, as these effects

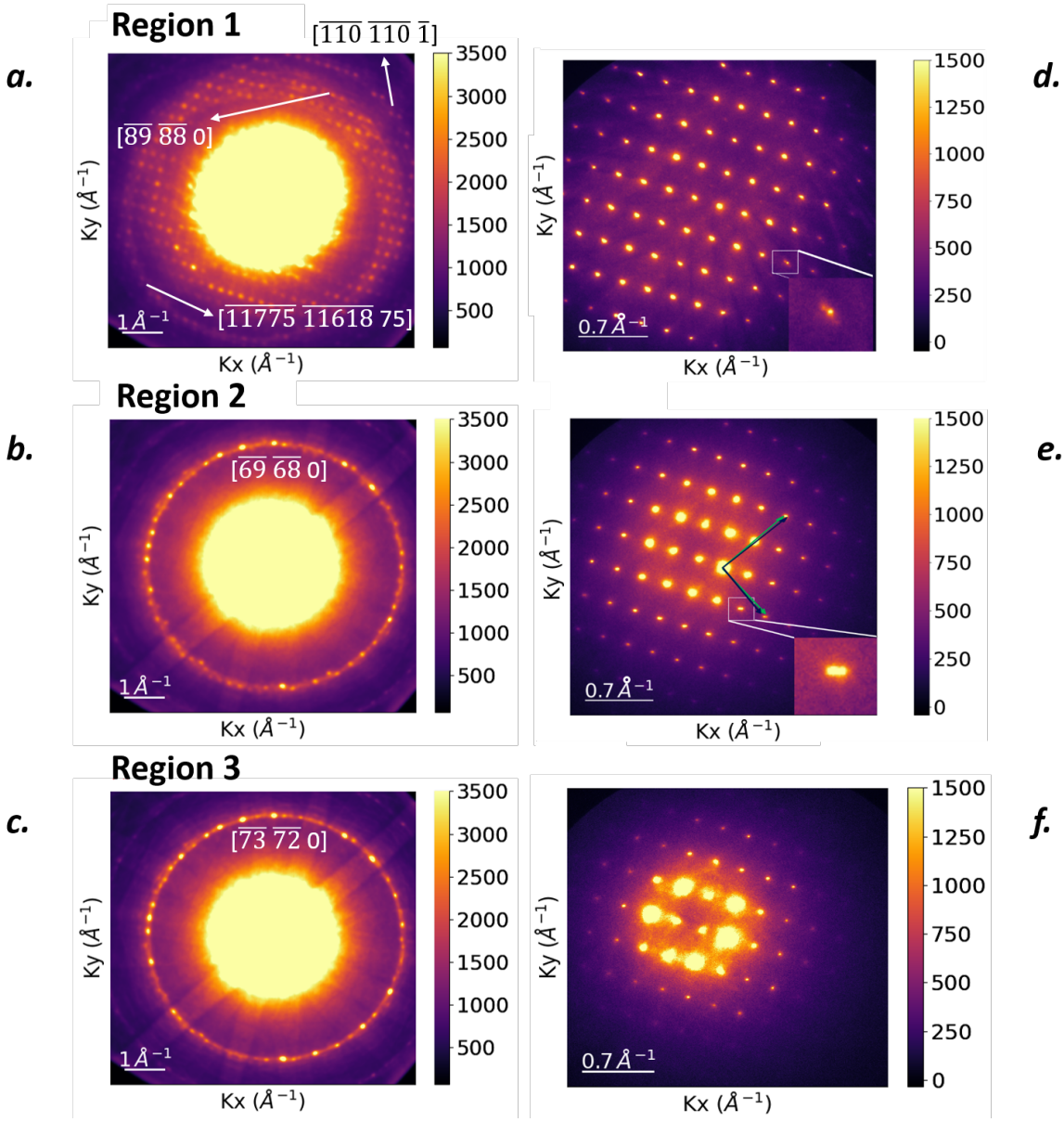

FIGURE 5.19: Electron nanodiffraction patterns acquired at 151 K : *a*. in region 1. Three FOLZs (one centered and two shifted) are observed. *b*. in region 2. This FOLZ seems to be more diffuse than the one in region 3. *c*. in region 2. One FOLZ is observed. Electron microdiffraction patterns acquired at 151 K : *d*. in region 1. Three splitted spots are present (inset). *e*. in region 2. Two splitted spots are present (inset). The two patterns have the hexagonal symmetry. *f*. in region 3. The hexagonal symmetry is observed.

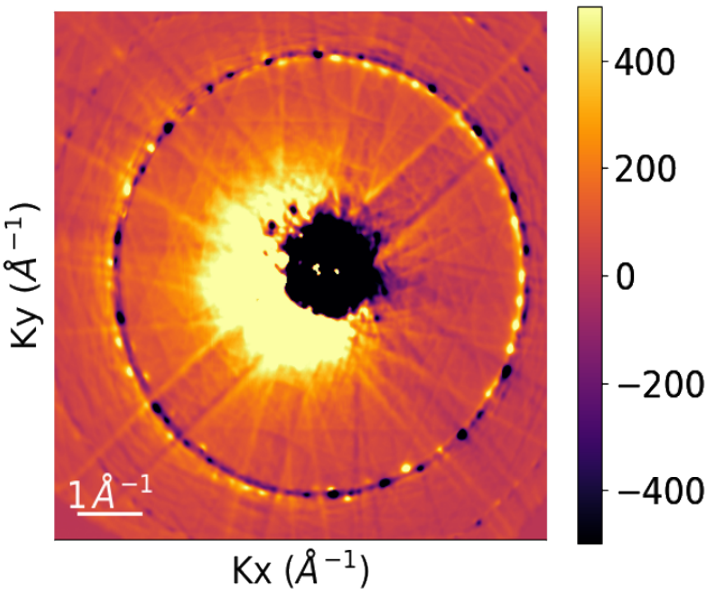

FIGURE 5.20: Map obtained by subtracting the contribution of region 3 from that of region 2.

occur only in the basal plane, perpendicular to the c_h axis. Finally, we observe, in region 1, one FOLZ centered on the transmitted beam (the hexagonal case); a second FOLZ shifted where the c_h axis is tilted in the same direction as in figure 5.7**.c**, and a third FOLZ also shifted but with the c_h axis tilted in the opposite direction to the second. The third situation suggests the presence of antiphase domains in this region, which break the translational symmetry [136]. Apparently, this symmetry breaking occurs along the $\mathbf{a_m}$ direction of the monoclinic lattice, as shown in the model presented in figure 5.21. It should be noted that the direction of antiphase domain boundaries that form coincides quite well with that of the interfacial plane direction (50° $\sim$ 55° from the horizontal position and along the $\mathbf{c_m}$ monoclinic axis). The existence of these domains is also confirmed in microdiffraction, where we obtain 3 splitted spots (see inset on figure 5.19**.d**). In EELS low-loss, the insulating spectroscopic signature is the only one observed (figure 5.22). Thus, we can assign the 3 regions as follows :

Region 1 would correspond to coexisting AFI-PI phases.

Region 3 is associated with the PM phase. Only one FOLZ (centered) and one microdiffraction pattern corresponding to the hexagonal case in the

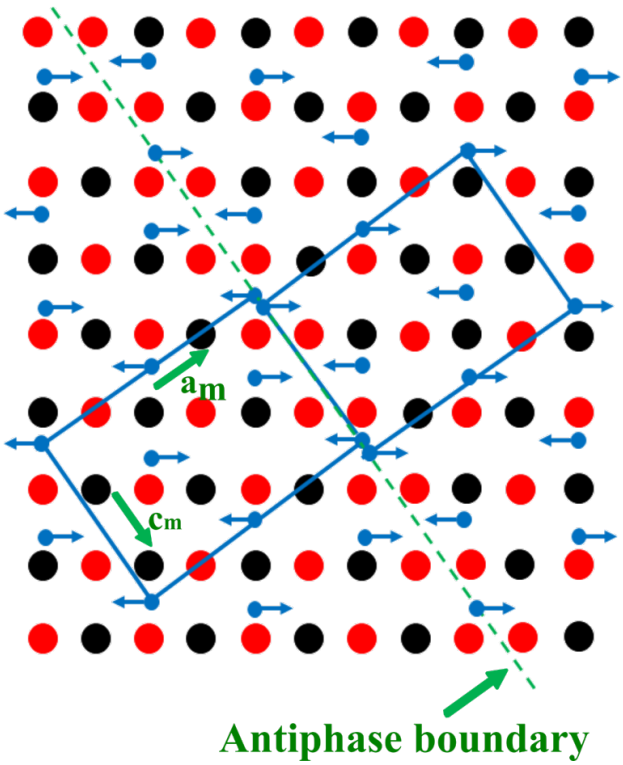

FIGURE 5.21: A model of the antiphase domains that form during heating, near the phase transition. Oxygen atoms are in red (in front of the plane) and in black (behind the plane). Vanadium atoms are in blue (the arrows indicate their movement in the monoclinic structure). The structural model is adapted from [135].

space group $R\bar{3}C$ (figures 5.19**.c** and 5.19**.f**) are observed, together with the spectroscopic signature of the metallic state (figure 5.22).

For region 2 (with a width of about 80 nm, according to the clustering maps), we now observe one FOLZ in the nanodiffraction pattern centered on the transmitted beam position (figure 5.19**.b**). However, this FOLZ appears to be more diffuse than the one in region 3, suggesting several contributions. The 2D signal subtraction between the components of regions 2 and 3 in nanodiffraction (see figure 5.20), where we seem to distinguish 2 contributions, could also support this interpretation. In microdiffraction, we observe 2 patterns, both with hexagonal symmetry (figure 5.19**.e**). The determination of the lattice parameters associated with these patterns suggests the coexistence of a PI phase (a_h = 5.070 Å; c_h = 13.925 Å) and a PM phase (a_h

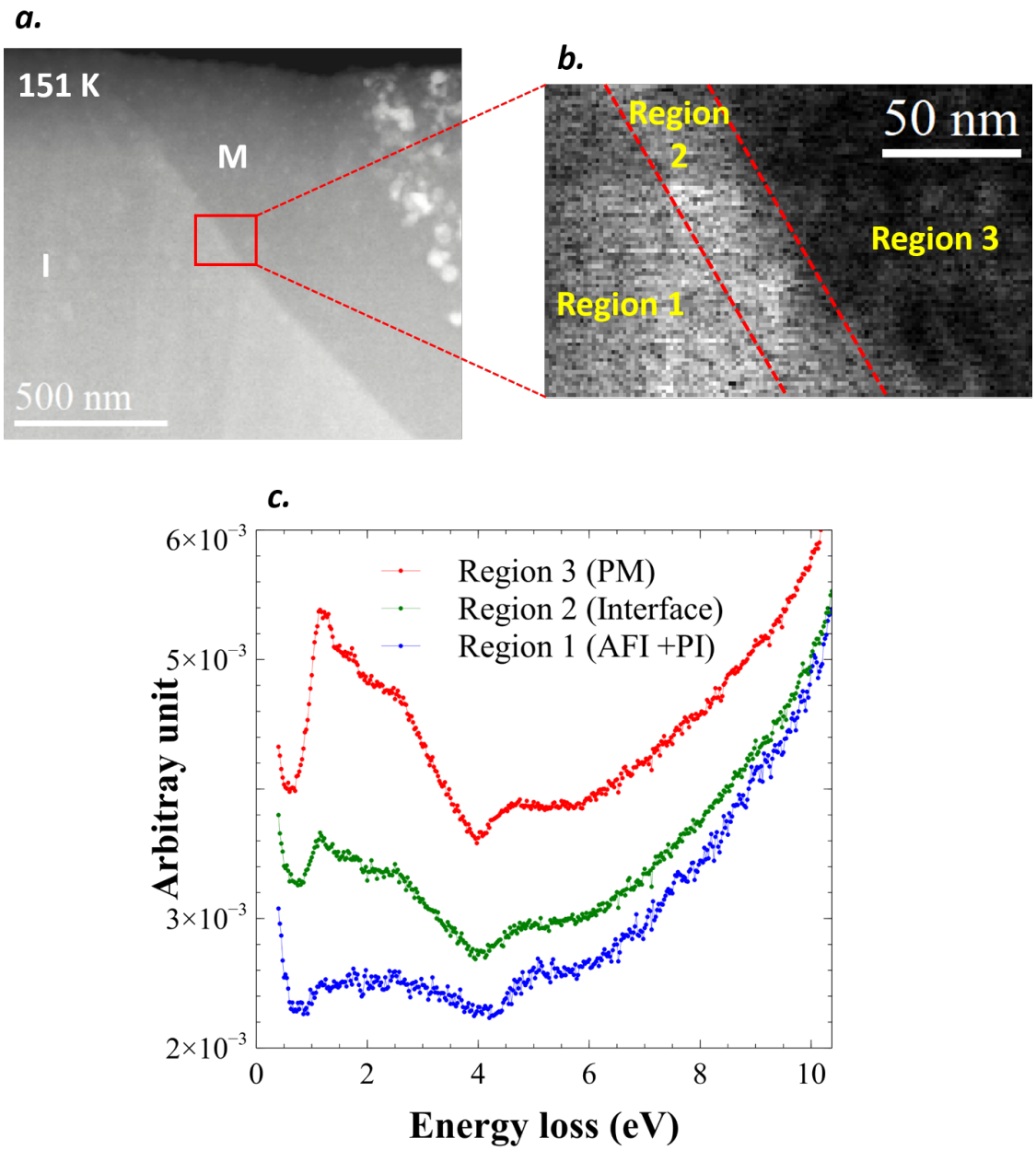

FIGURE 5.22: *a*. HAADF image obtained at 151 K during heating, showing the regions probed in EELS low-loss. *b*. HAADF map of stripy region (region 1), interface (region 2) and homogeneous contrast region (region 3). *c*. The corresponded spectroscopic signatures in these regions.

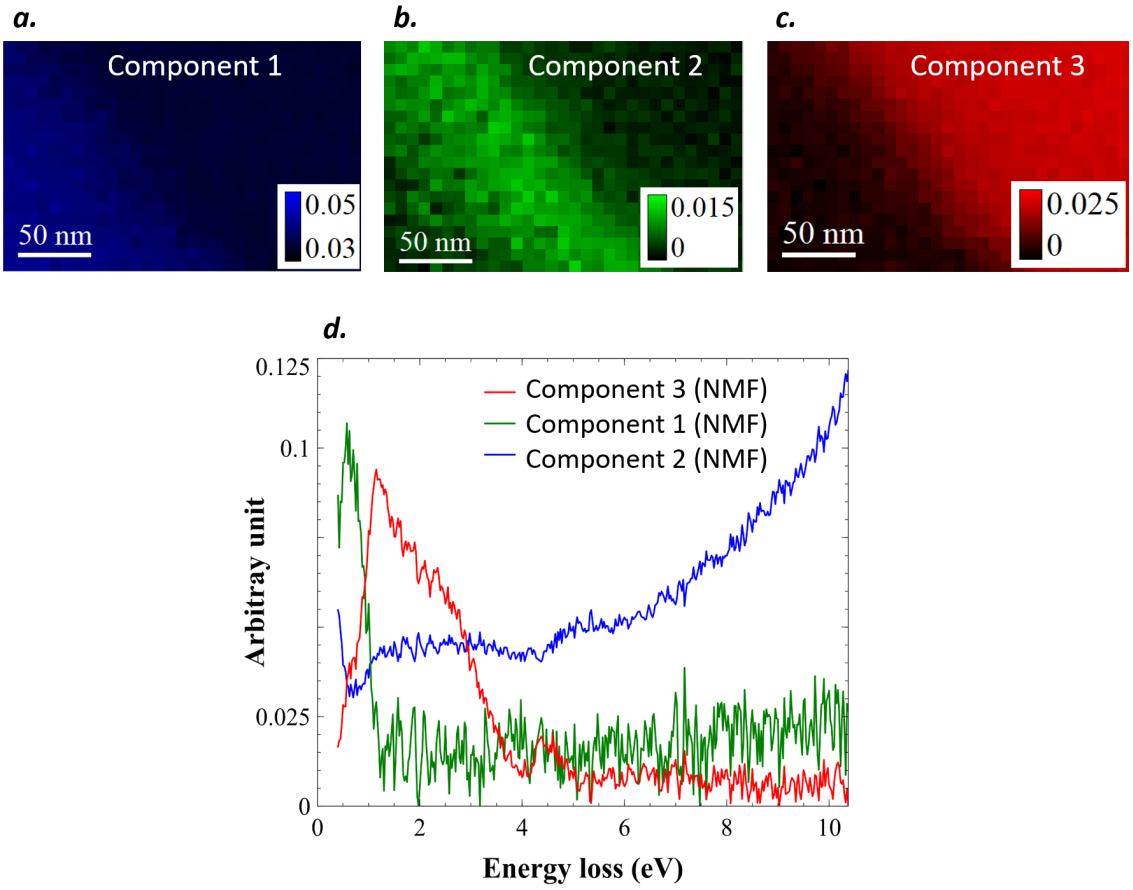

FIGURE 5.23: *a.*, *b.* and *c.* NMF maps obtained in the interfacial region, after binning. *d.* Spectra associated with the maps obtained in NMF.

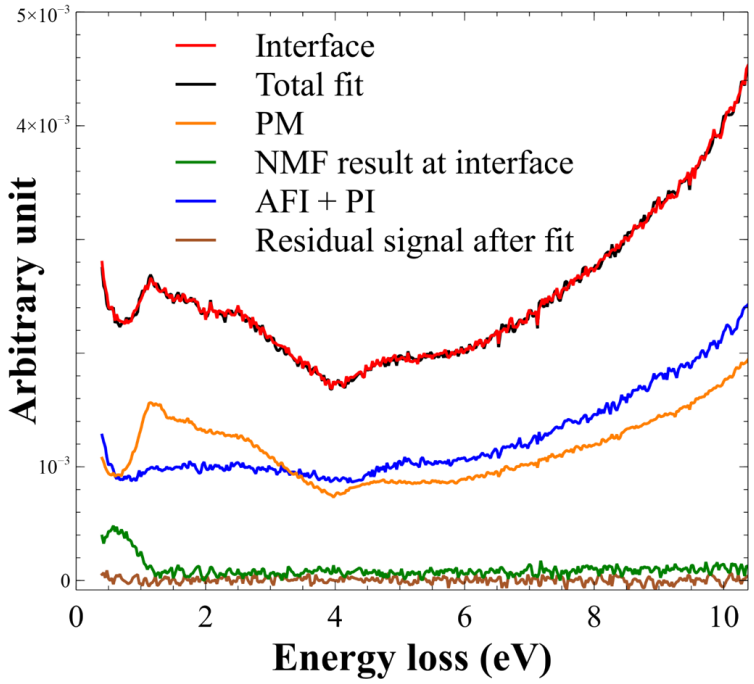

FIGURE 5.24: Fit of the interfacial spectroscopic signature with PM, AFI+PI and NMF result at the interface spectra. The fit obtained is in good agreement with the interfacial spectrum.

= 4.965 Å; c_h = 14.029 Å). Indeed, the differences between these two lattice parameters are relatively similar to what we have previously shown for the transition between PM (smaller a_h and larger c_h) and PI (larger a_h and smaller c_h). The low-loss spectroscopic signature in this region shows both spectral features from insulating and metallic states but does not fully fit with a linear contribution of both, particularly in the region below 1 eV, as shown in appendix E.1. We, therefore, used non-negative matrix factorization (NMF) decomposition to separate the different spectroscopic contributions in our spim. Unfortunately, as shown in apendix E.2, NMF has difficulty performing this task due to the non-negligible noise level in our data. Following the binning [4], i.e., summing up the adjacent pixels in the spim to improve the SNR, and applying NMF again, we do not successfully separate the metallic and insulating contributions, as we can see in figure 5.23. For instance, component 3 associated with the PM metallic region has almost no signal

[4]Binning is used here because the NMF decomposition, even after PCA, remains quite similar to that observed in figure E.2.

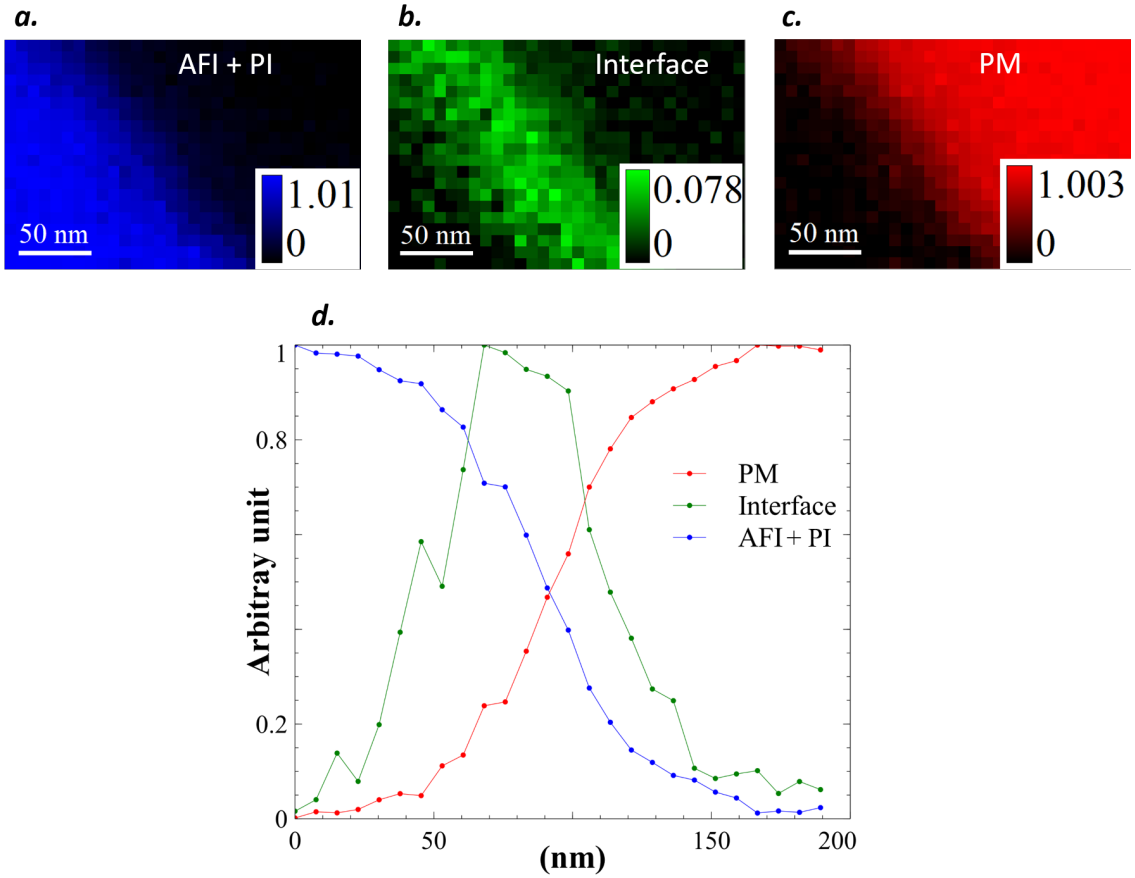

FIGURE 5.25: *a*. Map from MLLS fit for (AFI+PI) spectroscopic signature. *b*. Map from MLLS fit for the NMF spectrum at the interface. *c*. Map from MLLS fit for the PM spectrum. *d*. Profiles (normalized by the maximum) deduced from the corresponding MLLS maps.

above 5 eV. However, we extract an extra spectroscopic feature at the interface marked only by the presence of a peak around 0.7 eV. A fit performed by taking into account the latter feature and the pure metallic and insulating signatures in the spim fairly reproduces, this time, the spectroscopic signature at the interface (Figure 5.24). Finally, by using the NMF spectral feature at the interface, and the pure metallic and insulating signatures as reference spectra for fitting the experimental spectra with their linear combinations (MLLS fit), we map their occurrence regions (see figures 5.25**.a**, 5.25**.b** and 5.25**.c**). The intensity profiles deduced from these maps are also presented in figure 5.25**.d**. The NMF interface spectral feature could be the contribution of an interface plasmon. This excitation can be generated when the electron beam passes near an interface separating different dielectric constant media [137] (regions 1 and 2 here). Located near the interface, it decreases away from the latter following a Bessel function [138]. Finally, region 3 would correspond to a mixture of PI and PM phases, on the verge of becoming a PM phase entirely.

5.6 . Discussion

In fact, transport studies on pure annealed V_2O_3 single crystals suggested the occurrence of a PI phase under hydrostatic pressure at low temperatures [45] (see figure 5.26). This phase is either transient or can persist at very low temperatures ($\sim$ 50 K), depending on the pressure imposed to the material (persistence above 15 kbars). In our situation, the sample is maintained on the MEMS by Pt contacts on the 2 lateral sides. Since the structural transition (PM towards AFI) is also accompanied by a volume increase of 1.4 %, the sample cannot expand laterally and is subject to uniaxial pressure at the transition. The material reacts by forming stripes perpendicular to the strain direction. This assumption is also supported by the observations on the "flag geometry" lamella, where only the maintained side produces stripes. Thus, it seems that at the transition, uniaxial pressure induces the self-organization of the material in relaxed domains (AFI phase) and strained domains stabilizing a PI phase. The stripes are finally only the consequence of this organization, with contrasts depending on the relative proportions of these AFI and PI

domains as observed in nanodiffraction and microdiffraction, and probably appearing in this way to minimize the free energy of the system.

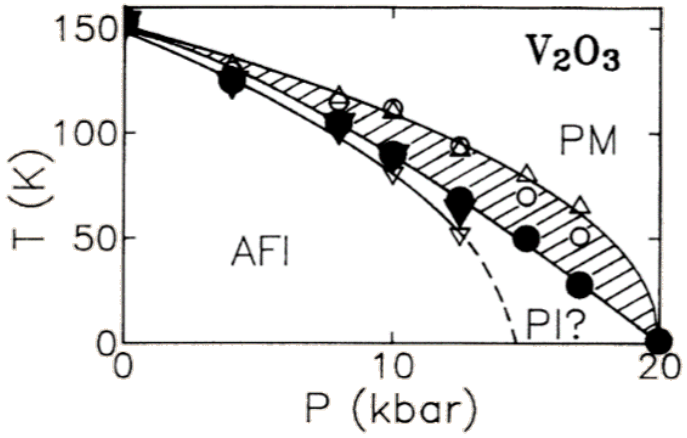

FIGURE 5.26: V_2O_3 Phase diagram as a function of temperature and pressure. This diagram, proposed by Carter *et al.*, is adapted from [45].

It has also been shown in ultrasonic sound waves measurements [5] on pure V_2O_3 single crystals, that the c_{44} elastic shear constant (shear perpendicular to the c_h axis direction) does not soften in the PM phase when temperature decreases, which is in contrast with the case of chromium-doped V_2O_3 in the PI phase [41, 42]. Since the monoclinic structure arises from the c_h axis tilt, and hence from the displacement of vanadium atoms in a direction almost normal to the c_h axis, the stiffness of c_{44} for pure V_2O_3 led to the prediction of an intermediate or a precursor PI phase during the transition [42]. This PI phase should immediately give rise to the AFI phase after its occurrence [42, 44]. Indeed, according to the phase diagram, this PI phase should be very unstable, with the PI to AFI transition occurring around 180 K for chromium-doped V_2O_3. However, under hydrostatic or uniaxial pressure like in this case, it seems possible to stabilise it at the transition.

From our analyses, we are able to suggest a scenario for the transition during heating and cooling. During cooling, the PM-AFI transition occurs via a PI phase, hence a Mott-Hubbard transition, due to the stiffness of the

[5] These ultrasonic sound waves measurements were also discussed in section 3 of Chapter 1.

c_{44} shear constant in PM. This PI phase, induced by the electronic degrees of freedom, immediately gives rise to the AFI phase due to its instability at this temperature. However, as in the FIB sample, it is possible to observe the PI-AFI coexistence at low temperatures under uniaxial pressure. Recently, a study carried out by Ronchi *et al.* [139] showed in x-ray photoemission electron microscopy and optical spectroscopy measurements on V_2O_3 thin films, that the metallic phase nucleated at twin boundaries that form in AFI, these locations known to be subject to high mechanical strains [140]. Hence, during heating, the PI phase can also be stabilized at these locations, and then grow to finally give rise to the PM phase under the impulse of the electronic degrees of freedom. In our case, the sample forms a single monoclinic domain (no twinning), but we observe the appearance of antiphase domains during heating. We, therefore, suggest that antiphase domain boundaries, generating also strains in their vicinity [141, 142], stabilize a PI phase that serves for the nucleation of the metallic phase. In this configuration, the insulating/metal domain wall, viewed on our HAADF images in the temperature coexistence regime, appears in a direction (along monoclinic c_m axis) related to these antiphase domain boundaries (APBs). The observation of a well-defined domain wall oriented along the APBs suggests that the nucleation sites for the PM phase are solely the APBs. The PI sites already present in the AFI/PI stripes region due to the uniaxial strain are not involved in this process, probably because of their non-percolative nature.

This scenario, where PI is precursor to PM during heating, is consistent with some previous pump-probe experiments. A temporary photoinduced phase, similar structurally to PI, was observed by Singer *et al.* [76] before the PM phase's occurrence. Also, it is shown that metallic domains grow in the ballistic limit, where their growth rates are limited to that of sound, suggesting that the metallic state is formed after the complete hexagonal symmetry restoration [7, 143]. The link between AFI and PI under pressure, suggesting a magnetoelastic effect, would confirm the strong relation between magnetism, symmetry, and lattice parameters observed in Neutron scattering and density functional theory (DFT) calculations, unveiling magnetic frustration for the PI phase [62].

We can also put our findings in perspective with recent results related

to the observation of magnetic fluctuations preceding the transition between PM and AFI phases. More specifically, Neutron scattering measurements have evidenced a magnetic pair distribution function (magnetic PDF) decrease, at least 25 K before the AFI towards PM structural transition [61]. In this work, the authors suggested that the spin degree of freedom is preponderant over the lattice degree of freedom. We suggest an alternative mechanism, where the transition involves an intermediate PI phase, indicated as magnetically frustrated in [62], and mediating a Mott-Hubbard transition.

5.7 . Conclusion

In this chapter, we investigated the electronic and structural properties of a V_2O_3 thin lamella, using coupled 4D-STEM nanodiffraction and microdiffraction experiments on the one hand and monochromated EELS low-loss experiments on the other. These experiments were carried out *in situ*, between 125 K and 300 K, thanks to the HennyZ sample holder using a MEMS system on which Pt contacts hold the sample. In these variable temperature experiments in pure V_2O_3 single crystal, we observed abrupt electronic and structural transitions upon cooling. However, a different process holds during heating, involving structural and electronic coexistence regions over about 3 K. After the transition, during cooling, we suggest that stripes appearing due to the volume increase result from the uniaxial strain imposed by the lateral Pt contacts that maintained our sample. These stripes would indicate the coexistence of an AFI phase and a phase similar to PI, resulting from strong correlations between magnetism and structure, and thus from a magnetoelastic effect. Our observations also suggest the role of the PI phase as the precursor phase in this temperature-induced transition, highlighting an intermediate Mott-Hubbard transition. Finally, following [35], these results suggest the driving character of electronic degrees of freedom in this transition.

Chapter 6

Conclusions and perspectives

6.1 . Conclusions

V_2O_3, belonging to the family of strongly correlated systems, presents a very rich phase diagram depending on external stimuli such as temperature, pressure, or chemical substitution. In this thesis, we first studied, especially at room temperature, V_2O_3 thin films (56 nm thick) on Al_2O_3 substrates (from a collaboration with the KU Leuven). We investigated the structural properties by GPA using HAADF image acquisitions at atomic resolution with the NION ULTRASTEM electron microscope. We also studied the electronic properties employing ultra-high spectral resolution ($\sim$ a few tens of meV) and spatial resolution ($\sim$ 1 nm) experiments in EELS spectroscopy with the NION CHROMATEM microscope. We also investigated the chemical properties in the thin film/substrate interfacial region using EELS spectroscopy with the NION ULTRASTEM. We have demonstrated, in GPA, structural inhomogeneities in the film, characterized by variations in the in-plane lattice parameter (a_h between 4.946 Å and 4.988 Å), out-of-plane lattice parameter (c_h between 13.759 Å and 14.061 Å), and c_h/a_h ratio (between 2.777 and 2.838). The Al_2O_3 substrate, which imposes significant in-plane strains during the growth of the film (4.2 % lattice mismatch between substrate/film), would be at the origin of these observations. The substrate would favor the formation of grains and the increase of the film in-plane lattice parameter with the increasing evolution of the thickness of the latter [117]. We have also highlighted a critical thickness of about 2 nm, which supports the fact that V_2O_3 films on Al_2O_3 substrates begin to relax after a few nanometers of growth [12, 120].

As for spectroscopic measurements in core-loss and low-loss, they clearly show spatial electronic inhomogeneities in the thin film. Indeed, the maps carried-out by clustering in the low-loss region show intensity variations of the spectroscopic signature at 1 eV (characteristic signature of the PM state) over domains of about 50 nm. The evolution of this spectroscopic feature can be directly linked to the variations of the in-plane lattice parameter, but also to the electronic properties of the film, as we have shown on calculated spectra. The results obtained in the core-loss region further confirm these observations. The variations observed on the vanadium (V-$L_{2,3}$) and oxygen (O-K) fine structures suggest the presence of metallic but also insulating contributions in the film. The maps obtained in MLLS in this region, from the decomposition performed in VCA (for spectral unmixing), establish electronic domains of almost identical widths to those previously observed in low-loss experiments. All these results suggest the existence of a large volume hexagonal phase similar to the PI phase in the sample at room temperature. The core-loss spectra in the interfacial region, even over the first 10 nm, are also homogeneous and relatively identical to the metallic spectroscopic signature, which may appear to contrast with the modulations in vanadium proportion observed in some interfacial regions. The results suggest strong correlations between structural and electronic properties in V_2O_3 thin films at room temperature.

In the second step, we studied, *in situ*, the local evolution of structural and electronic properties in V_2O_3 thin lamellas extracted from single crystals (from IMN Nantes) during the temperature-induced transition between PM and AFI. We investigated the structural properties by 4D-STEM nanodiffraction (spatial resolution of about 5 nm) and 4D-STEM microdiffraction (spatial resolutions of about 120 nm and 10 nm). In parallel, we studied also the electronic properties, using EELS spectroscopy with spatial and spectral resolutions of the order of nm and a few tens of meV, respectively. We also implemented all these experiments using the NION CHROMATEM fitted with the cryo sample-holder HennyZ, allowing *in situ* variable temperature investigations and ensuring high stability and spatial resolution down to the nanometer. We have highlighted different mechanisms of this phase transition while cooling, i.e., toward the AFI state, and while heating, i.e., toward

the PM state. The phase transition during cooling is marked by the abrupt vanishing of the 1 eV spectroscopic signature associated with the PM state, concomitant with the sudden appearance of bright and dark quasi-periodic stripes of tens of nm width in HAADF imaging. These stripes, which appear in the insulating state, corresponds to the coexistence of monoclinic and hexagonal structures, as evidenced by 4D-STEM nanodiffraction and microdiffraction. The presence of the hexagonal structure in the insulating state, which contrasts with the unique presence of the monoclinic structure in the AFI phase, as reported in the literature [33], suggests the existence of a phase analogous to PI, i.e., the other insulating phase of V_2O_3. The jumps in lattice parameters and c_h/a_h ratio observed at the phase transition, during heating and cooling, similar to those of the phase transition between PM and PI, support this idea. The low-loss spectroscopic signature at low temperatures is relatively homogeneous throughout the sample. This result, suggesting spectral similarities between this possible PI and AFI phases, and contrasting with those of the chromium-doped PI phase, is also supported by recent ellipsometry investigations [67]. At the phase transition involving an abrupt increase in volume (1.4 %), the uniaxial strains (perpendicular to $\mathbf{c_h}$) imposed by the Pt lateral contacts holding the thin lamella would be at the origin of these observations (structural coexistence).

During heating, a completely different mechanism is observed, involving the propagation of a domain wall separating stripy and homogeneous HAADF contrast regions associated, respectively, with the insulating and metallic states. The complete characterization of the interfacial region suggests the presence of a phase analogous to PI at the domain boundary, which would be induced here by the strains generated around the antiphase domain boundaries formed along the domain wall. This possible coexistence of AFI and PI phases under the strain effect would imply a magnetoelastic effect in V_2O_3. The PI phase, also stabilized under strains, would suggest a precursor role of the latter in the phase transition. It is also important to note that only one monoclinic domain is formed in the lamella at low temperatures instead of the expected three monoclinic twins. This is due to the

cutting orientation of the single crystal by FIB along the $[\bar{1}\bar{1}0]_h$ direction, favoring one twin direction more than the others in the low-temperature monoclinic phase. All these observations again indicate the PI phase's precursor role at a local scale during the temperature phase transition between PM and AFI. The results, therefore, suggest the electronic degrees of freedom as the driving degrees of freedom of this temperature-induced phase transition.

6.2 . Perspectives

The role of PI as a precursor phase for the PM-AFI phase transition calls for a better electronic, structural, and also magnetic characterization of the PI-AFI phase transition, especially in pure V_2O_3 and chromium-doped samples. Indeed, real part measurements of the optical conductivity performed by spectroscopic ellipsometry [67] indicate relative similarities between the PI (for pure V_2O_3 thin films obtained by heteroepitaxy) and AFI phases, which is not the case for chromium-doped V_2O_3. These differences would be due to chromium doping which would induce inhomogeneities in the physical properties of V_2O_3. It would therefore be interesting to investigate the phase transition between PI and AFI, on the one hand in chromium-doped samples, and on the other hand in pure V_2O_3 samples stabilized in the PI phase (thanks to thin films engineering). This would allow a better understanding of the role of chromium doping in V_2O_3, and the precursor role of the possible PI intermediate phase that appears during the phase transition between PM and AFI. This comparative study could also be carried out during the PI-PM-AFI phase transition, which is also possible to achieve for low chromium doping (about 1.2 %), or by strain generation in pure V_2O_3 thin films [66].

The role of strains in the phase transition during heating is also indicated by the experimental results. The strains generated at the antiphase domain boundaries would be at the origin of this transition's possible PI precursor phase. It would be interesting to perform the same experiment, but this time using monoclinic twin samples and see the evolution of the phase transition. Indeed, the twin domain boundaries can be subject to very high shear strains [140]. This experiment will allow us to know if the nucleation mechanisms during heating are the same for V_2O_3 samples that form a single monoclinic

domain at low temperatures in AFI, and those that form twins in this phase. This will require a peculiar FIB extraction of V_2O_3 samples to be probed in the direction perpendicular to the hexagonal c_h axis (or parallel to the basal plane) to avoid favoring any direction in the basal plane at the phase transition. It is also essential to investigate the low-temperature AFI phase under hydrostatic or uniaxial pressure to study better the possible magnetoelastic effects that occur there. The application of complementary experimental techniques on samples prepared with the same geometry as ours, such as muon spin relaxation (μsr), for instance, could also allow us to probe the local magnetic states [59] that occur there . All these findings on thin lamellas could also be used for the *in situ* variable temperature investigation of V_2O_3 thin films.

The Mott-Hubbard transition between the PM and PI phases, which has not been investigated directly in this thesis, presents interesting technological aspects such as ReRAMs or neuromorphic applications, discussed extensively in Chapter 2. The technological opportunities envisaged here would result from creating conductive filaments under intense electrical pulses (around 6 kV/cm) in the $(V_{1-x}Cr_x)_2O_3$ PI phase at room temperature. The carried-out modelization (figure 6.1) indicates, after the pulse, the creation of metallic sites, which finally percolate to give rise to the stabilization of conductive filaments or the dissolution of the latter, depending on whether they reach a critical size or not [72]. The compressive strains generated in the insulating matrix would be the origin of these observations [124]. However, the local stabilization mechanisms of these filaments or even the local evolution of the strains at the interface between the conductive filaments and the insulating matrix remain unresolved issues.

It would therefore be interesting to provide some answers to these concerns using electron spectromicroscopy. We now have the tool, i.e., the NION CHROMATEM coupled to the cryo sample holder HennyZ using a MEMS system, which can provide us local structural, electronic, and chemical information in and around these filaments. The MEMS system used here has two Pt electrodes dedicated specifically to biasing experiments. The inter-electrode distances of up to 20 μm can also allow the creation of conductive filaments in the insulating $(V_{0.95}Cr_{0.05})_2O_3$ lamella under typical electric

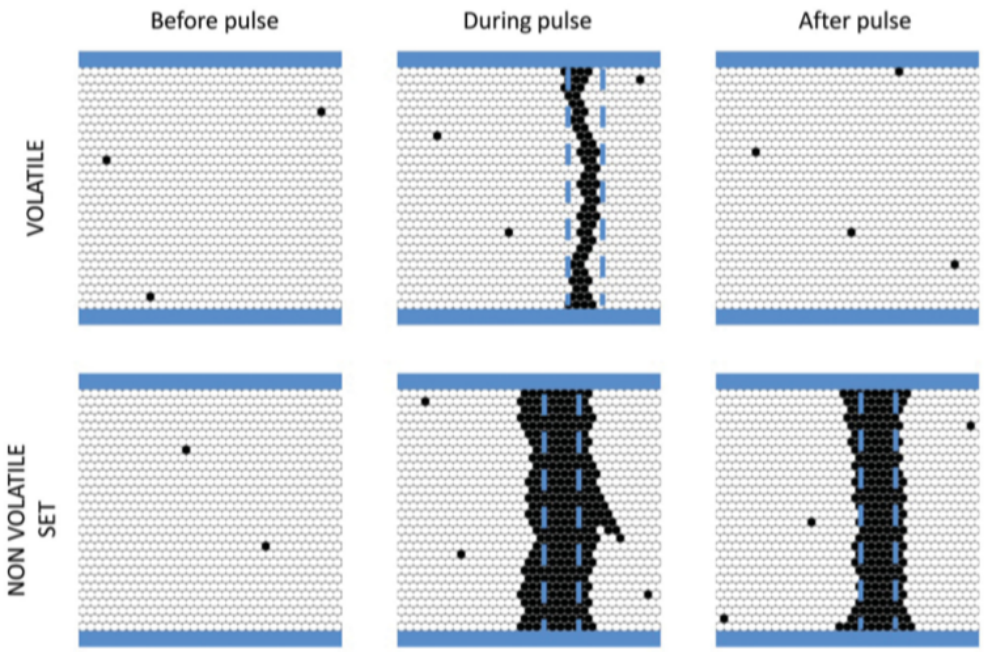

FIGURE 6.1: Schematic evolution of the metallic filament within the insulating matrix, before, during and after the pulse. The black dots represent the metallic sites. The blue dashed lines indicate the critical size to be reached to stabilize the filament. The figure is adapted from [72].

fields of around 10 kV/cm. Thanks to the collaboration with IMN (Nantes), which already has several years of experience in these areas, we can set up, with our electron microscope, the tools necessary for the creation and investigation of these conductive filaments in $(V_{0.95}Cr_{0.05})_2O_3$ lamellas [144]. Indeed, thanks to a pulse generator (Agilent 8114 A), we can send electrical pulses of up to 10 ns onto the thin lamella, also producing the typical voltages necessary for creating metallic filaments. The insertion of a load resistor ($R_{sample}/R_{load} = 10$), in series with the sample, should also limit the current that could damage the sample during the transition to the low resistance state. In addition, the oscilloscope, with a bandwidth of 500 MHz, will allow us to follow the current and voltage evolution across the sample. Finally, the integration of a measurement source (Keithley 236) at the sample terminals, controllable by relays, will allow us to carry-out measurements at low currents to measure the sample resistance in between pulses (to ensure

non-volatile transition or not). The electron microscope, the NION CHROMATEM, will then allow us to investigate locally the physical properties of the sample using the experimental techniques described in this thesis.

Chapter 7

Résumé en français

Le V_2O_3 appartient à la famille des oxydes fortement corrélés. Dans ces matériaux, les corrélations électroniques, relativement importantes, occupent une place de choix quant à la description des propriétés physiques du système. Le V_2O_3 présente deux types de transition métal-isolant [2–4] (MIT), comme observé sur le diagramme de phase de la figure 7.1. Le système non dopé présente d'une part, par exemple, la transition du premier ordre de la phase paramagnétique métallique (PM) vers la phase antiferromagnétique isolante (AFI) autour de 150K – 160 K. Cette transition est accompagnée d'une augmentation abrupte de la résistivité de sept ordres de grandeur et d'une transition de l'état paramagnétique vers l'état antiferromagnétique. Une brisure de symétrie, de la structure hexagonale vers la structure monoclinique, est également observée. La distorsion structurale s'illustre principalement par l'inclinaison de l'axe hexagonal c_h (perpendiculaire au plan basal) d'environ 1.8 ° [33] vers les directions du plan basal. Cette inclinaison est induite ici par le déplacement des atomes de vanadium le long de l'axe c_h vers les sites octaédriques non occupés à la transition de phase. Finalement, cette transition s'accompagne d'une augmentation abrupte du volume d'environ 1.4 %. D'autre part, la transition de Mott-Hubbard du premier ordre de la phase PM vers la phase paramagnétique isolante (PI) est également observée. Elle peut se produire, par exemple, à température ambiante pour une substitution en chrome au-delà de 1 %. Cette transition, isostructurale, est accompagnée d'une augmentation abrupte de la résistivité de deux ordres de grandeur.

Les récentes observations dans le V_2O_3, s'illustrant par une séparation de phases électronique à des résolutions spatiales allant jusqu'à quelques

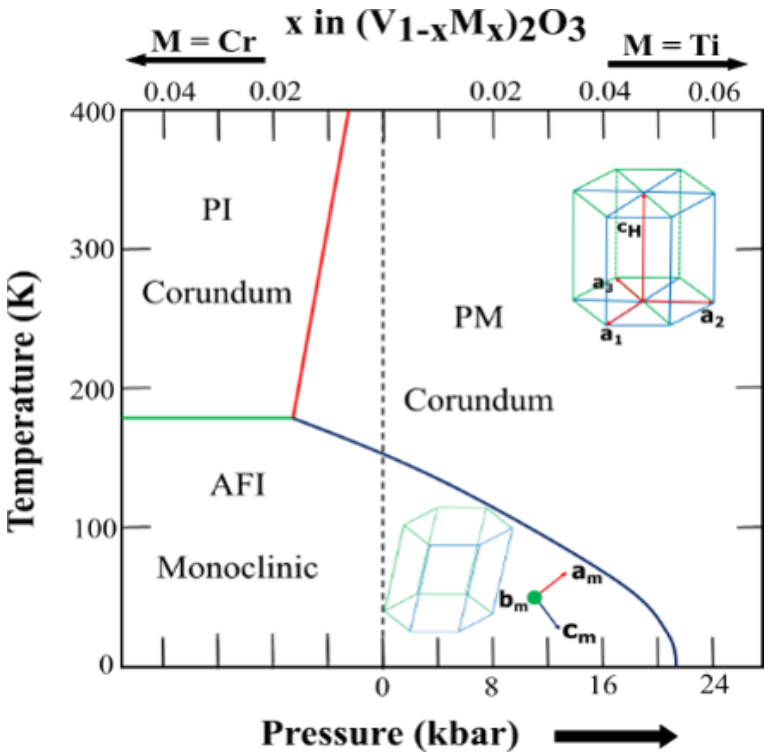

FIGURE 7.1: Diagramme de phase du $(V_{1-x}M_x)_2O_3$ (M pour Cr or Ti), en fonction des paramètres extérieurs (température, pression, dopage chimique). Cette figure est adaptée des travaux pionniers de McWhan *et al.* [2–4].

dizaines de nanomètres [5, 6], particulièrement pendant la transition de phase de PM vers AFI, amènent à nous interroger sur les mécanismes de nucléation structuraux et/ou électroniques associés à cette transition. L'objectif de ce travail de thèse est de répondre aux problématiques portant sur les propriétés locales (à des résolutions spatiales nanométriques) structurales, électroniques et chimiques dans les films minces de V_2O_3, mais également de comprendre les mécanismes de nucléation structuraux et/ou électroniques pendant la transition de phase en température entre PM et AFI, dans les monocristaux de V_2O_3, à l'échelle nanométrique.

Les outils de la microscopie électronique utilisés ici dans le cadre de nos

investigations, sont des outils adéquats pour répondre à de telles préoccupations. En effet, les microscopes électroniques modernes corrigés des aberrations sphériques et disposant de monochromateurs peuvent atteindre des résolutions spectrales allant jusqu'à quelques meV et spatiales allant du nanomètre à l'angström, en spectroscopie des pertes d'énergie des électrons (EELS) [13]. Grâce à ces performances, les propriétés locales optiques, électroniques et chimiques du matériau ainsi sondé peuvent être obtenues. De plus, les modes d'imagerie tel que le mode d'imagerie en fond noir grand angle (HAADF) ou encore les techniques de diffraction électronique permettent également d'accéder, avec des résolutions spatiales allant de la dizaine de nanomètre à l'angström, aux propriétés locales structurales de l'échantillon investigué. Les récents développements instrumentaux en ce qui concerne les porte-objets Cryo [14, 15] qui accompagnent les microscopes électroniques permettent également de réaliser *in situ* en température variable de telles expériences, en assurant une grande stabilité et une résolution spatiale allant du nanomètre à l'angström. Finalement, les techniques d'analyse de données telles que la 'vertex component analysis' (VCA) [109, 110] ou encore le 'K-means clustering' [82, 115], appliquées de plus en plus aux expériences de microscopie électronique, peuvent également permettre de cartographier les éventuels domaines structuraux et/ou électroniques observés au sein du matériau sondé.

Nous nous sommes d'abord intéressés au cours de ces travaux de thèse, notamment à température ambiante, à un film mince de V_2O_3 sur un substrat de Al_2O_3, de 56 nm d'épaisseur et obtenu grâce à une collaboration avec le KU Leuven. Nous y avons étudié les propriétés structurales, grâce à l'analyse en phase géométrique (GPA), en utilisant des acquisitions d'images HAADF à résolution atomique avec un microscope STEM équipé d'un correcteur d'aberrations sur la sonde (le microscope NION ULTRASTEM). Nous y avons également étudié les propriétés électroniques en réalisant des expériences à ultra haute résolution spectrale ($\sim$ quelques dizaines de meV) et spatiale ($\sim$ 1 nm) en spectroscopie EELS avec un microscope corrigé des aberrations en mode sonde et d'un monochromateur permettant une résolution spectrale de l'ordre de 5-10 meV (microscope NION CHROMATEM).

Nous avons également étudié les propriétés chimiques dans la région interfaciale du film grâce à la spectroscopie EELS, ceci avec le NION ULTRASTEM. Nous avons mis en évidence, en GPA, des inhomogénéités structurales dans le film, caractérisées par des variations du paramètre de maille dans le plan (entre 4.946 Å et 4.988 Å), du paramètre de maille hors plan (entre 13.759 Å et 14.061 Å), et du rapport c_h/a_h (entre 2.777 et 2.838). Le substrat de Al_2O_3, qui impose des contraintes importantes dans le plan lors de la croissance du film, de l'ordre de 4.2 %, serait à l'origine de ces observations. Il favoriserait la formation de grains et l'augmentation du paramètre de maille dans le plan du film avec l'évolution croissante de l'épaisseur de ce dernier [117]. Nous avons également mis en évidence une épaisseur critique d'environ 2 nm, qui soutient le fait que les films de V_2O_3 sur des substrats de Al_2O_3 commencent à se relaxer après quelques nanomètres de croissance [12, 120].

Quant aux mesures spectroscopiques en EELS dans la région des pertes proches et des pertes de cœur, elles montrent clairement des inhomogénéités électroniques spatiales dans la couche mince. En effet, les cartes réalisées par application de la classification en K-moyennes (K-means clustering) dans la région des pertes proches montrent des variations d'intensité de la signature spectroscopique à 1 eV sur des domaines d'environ 50 nm (voir Figure 7.2). L'évolution de cette caractéristique spectroscopique peut être directement corrélée aux variations du paramètre de maille dans le plan, mais aussi aux propriétés électroniques du film, comme nous l'avons montré sur les spectres calculés à partir des indices de réfraction et des coefficients d'extinction du V_2O_3 dopé en chrome à 1.5 %. Les résultats obtenus dans la région de pertes du cœur confirment encore ces observations. Les variations observées sur les structures fines du vanadium (V-$L_{2,3}$) et de l'oxygène (O-K) suggèrent, elles aussi, la présence de contributions métalliques et isolantes dans le film. Les cartes obtenues grâce à l'ajustement linéaire des moindres carrés (MLLS) dans cette région, à partir de la décomposition spectrale effectuée en analyse en composantes de sommet (VCA) , établissent des domaines électroniques de largeurs presque identiques à ceux précédemment observés dans la région des pertes faibles. Toutes les observations structurales et électroniques réalisées ici suggèrent la coexistence d'une phase PM et d'une phase de grand volume similaire à la phase PI. Les spectres obtenus dans la région des pertes

de cœur, dans la région interfaciale, sont également homogènes sur environ les 10 premiers nanomètres et relativement identiques à la signature spectroscopique métallique, même si des variations de proportion du vanadium sont observées dans certaines régions à l'interface. Les résultats suggèrent de fortes corrélations entre les degrés de liberté électroniques et structuraux dans les films minces de V_2O_3 à température ambiante.

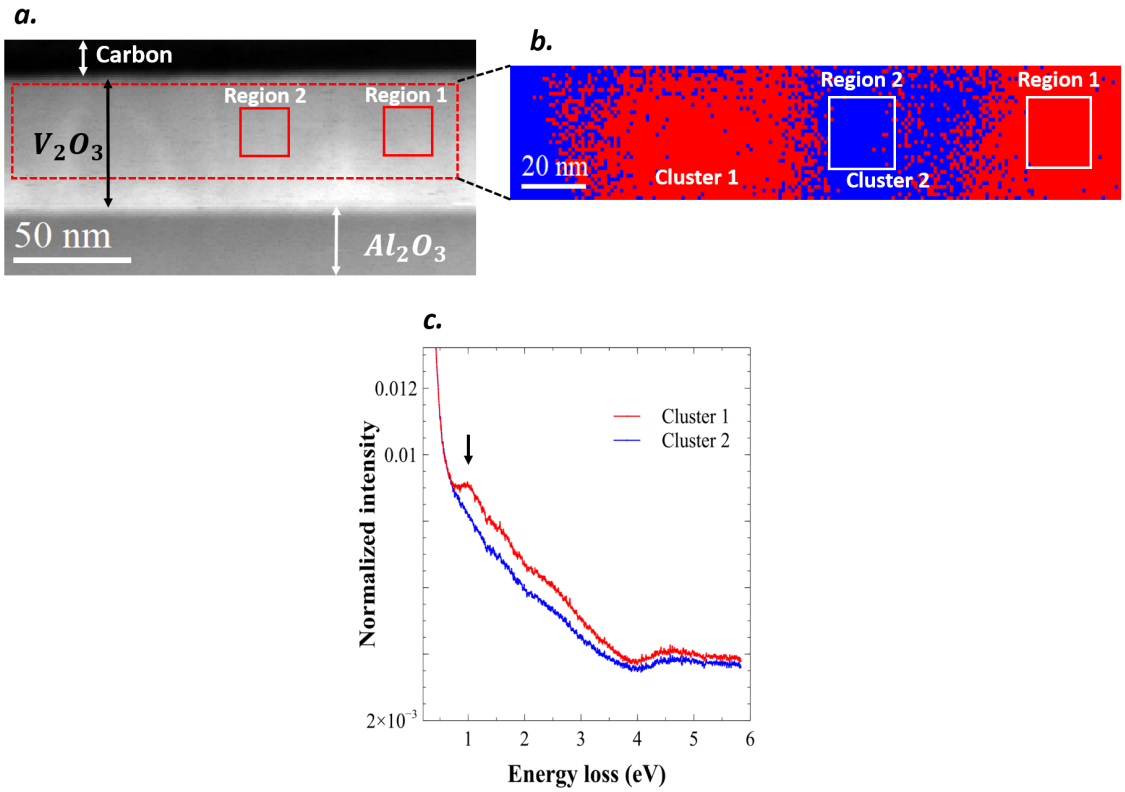

FIGURE 7.2: *a*. Carte HAADF montrant la région sélectionnée pour application du clustering. *b*. Carte obtenue en k-means clustering dans le fim mince, avec 2 clusters *c*. Spectres correspondants aux différents clusters, avec la présence de la signature spectroscopique à 1 eV (indiqué par une flêche) pour le cluster 1.

Dans la suite, nous avons investigué l'évolution locale des propriétés structurales et électroniques dans des lames minces de V_2O_3 (extraites de monocristaux provenant d'une collaboration avec l'IMN Nantes) pendant la transition induite en température entre PM et AFI. Nous avons étudié les propriétés structurales en réalisant des expériences de nanodiffraction 4D-STEM (résolution

spatiale d'environ 5 nm) et microdiffraction 4D-STEM (résolutions spatiales d'environ 120 nm et 10 nm). Les propriétés électroniques ont quant à elles été étudiées grâce à la spectroscopie EELS dans la région des pertes proches, avec respectivement des résolutions spatiale et spectrale de l'ordre du nm et de quelques dizaines de meV. Ces expériences ont été mises en œuvre en utilisant le microscope électronique NION CHROMATEM équipé du porte-objet Cryo HennyZ, permettant des investigations *in situ* à température variable et assurant une grande stabilité et une résolution spatiale jusqu'au nanomètre. Grâce à ces conditions, nous avons mis en évidence différents mécanismes de cette transition de phase pendant le refroidissement (de PM vers AFI) et pendant le chauffage (de AFI vers PM). La transition de phase lors du refroidissement est marquée par la disparition abrupte de la signature spectroscopique à 1 eV associée à l'état PM, et l'apparition soudaine de bandes quasi-périodiques claires et sombres en imagerie HAADF (voir figure 7.3). Ces bandes, qui apparaissent dans l'état isolant, indiquent la coexistence de structures monoclinique et hexagonale, comme le montrent les expériences de nanodiffraction et de microdiffraction 4D-STEM. La présence de la structure hexagonale dans l'état isolant, qui contraste avec la présence unique de la structure monoclinique dans la phase AFI, comme rapporté dans la littérature [33], suggère l'existence d'une phase analogue à PI, l'autre phase isolante du V_2O_3.

Les sauts des paramètres de maille et du rapport c_h/a_h observés à la transition de phase, lors du chauffage et du refroidissement, similaires à ceux de la transition de phase entre PM et PI, supportent cette interprétation. La signature spectroscopique dans la région des pertes faibles à basse température est relativement homogène dans l'ensemble de l'échantillon. Ce résultat, suggérant des similitudes spectrales entre cette phase analogue à PI et la phase AFI, est également soutenu par des études récentes d'ellipsométrie [67], montrant des similarités en ce qui concerne la partie réelle de la conductivité optique de la phase AFI et de la phase PI obtenue par ingénierie de contraintes sans dopage. La coexistence structurale observée résulte ici des contraintes uniaxiales lors de cette transition de phase impliquant une augmentation brutale du volume (1.4 %), imposées par les contacts en platine qui maintiennent l'échantillon. Lors du chauffage, un mécanisme complètement

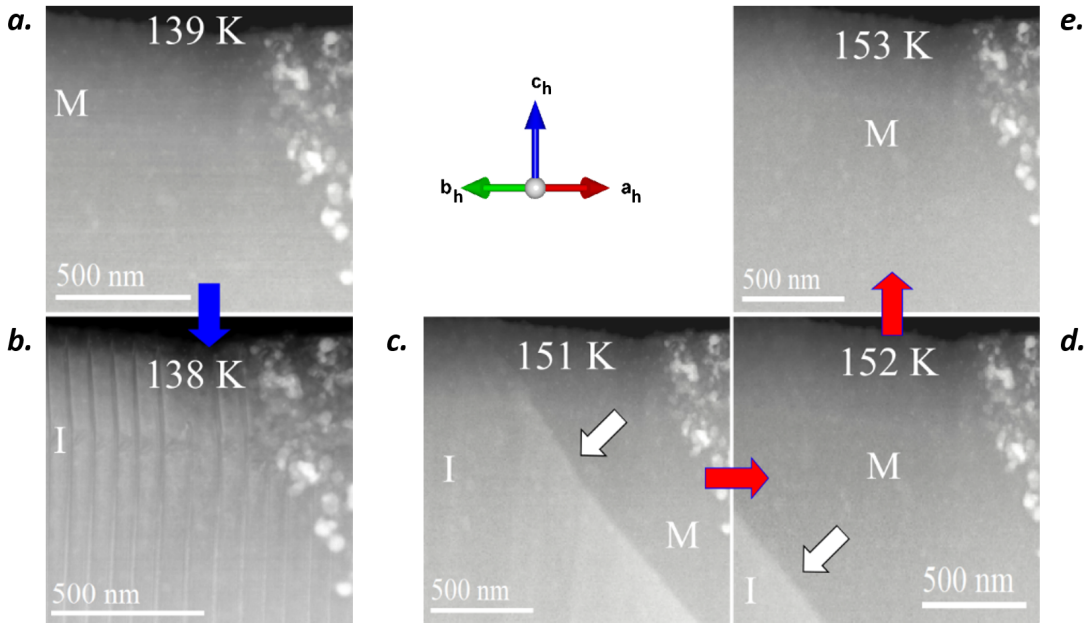

FIGURE 7.3: Les lettres I et M expriment, respectivement, les états isolant et métallique. *a*. Image HAADF acquise à 139 K, pendant refroidissement (état M). *b*. Image HAADF acquise à 138 K (état I), pendant refroidissement. Apparition abrupte de bandes à cette température. *c*. Image HAADF acquise à 151 K pendant chauffage. Une paroi de domaines est observée, séparant les régions présentant des bandes (état I) et les régions de contraste homogène (état M). *d*. Image HAADF acquise à 152 K pendant chauffage. La paroi de domaines se propage à travers l'échantillon. *e*. Image HAADF acquise à 153 K, acquise pendant chuaffage. Un contraste homogène est observé dans tout l'échantillon.

différent est observé, impliquant la propagation d'une paroi de domaines séparant les régions de contraste HAADF présentant des bandes et les régions de contraste homogène (voir figure 7.3). Ces régions sont également associées, respectivement, aux états isolant et métallique. La caractérisation complète de la région interfaciale suggère encore la présence d'une phase analogue à PI au niveau de la paroi de domaine, qui serait induite ici par les contraintes générées autour des frontières de domaine en antiphase formées le long de cette paroi. Cette possible coexistence des phases AFI et PI sous l'effet des contraintes impliquerait un effet magnétoélastique dans le V_2O_3. Toutes ces observations indiquent le rôle précurseur de cette phase PI lors

de la transition de phase en température entre PM et AFI. Ces résultats suggèrent également les degrés de liberté électroniques comme degrés de liberté pilotes de cette transition de phase induite en température.

Appendix A

K-means clustering applied in the core-loss region (thin film region selected)

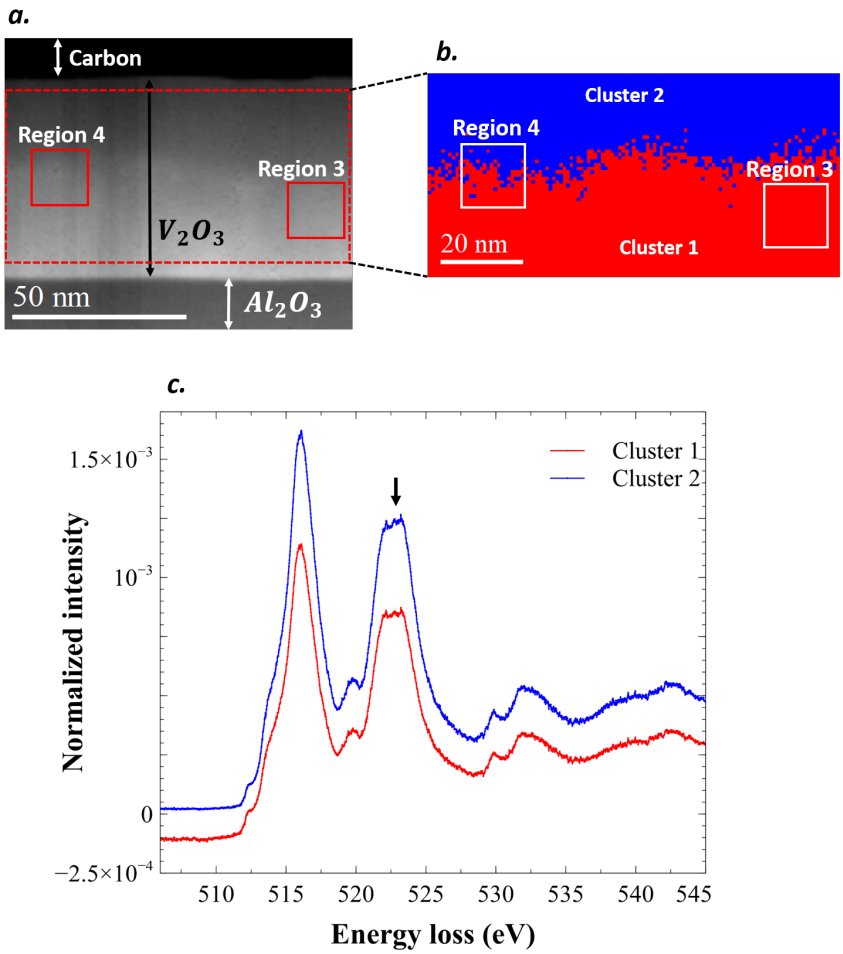

FIGURE A.1: *a*. HAADF map showing the selected area in the thin film. *b*. Map obtained by K-means clustering in the thin film, with 2 clusters. *c*. Spectra corresponding to the different clusters. A small change in shape on the V-L_2 edge can be observed.

Appendix B

K-means clustering applied in the core-loss region (slice selected in the thin film)

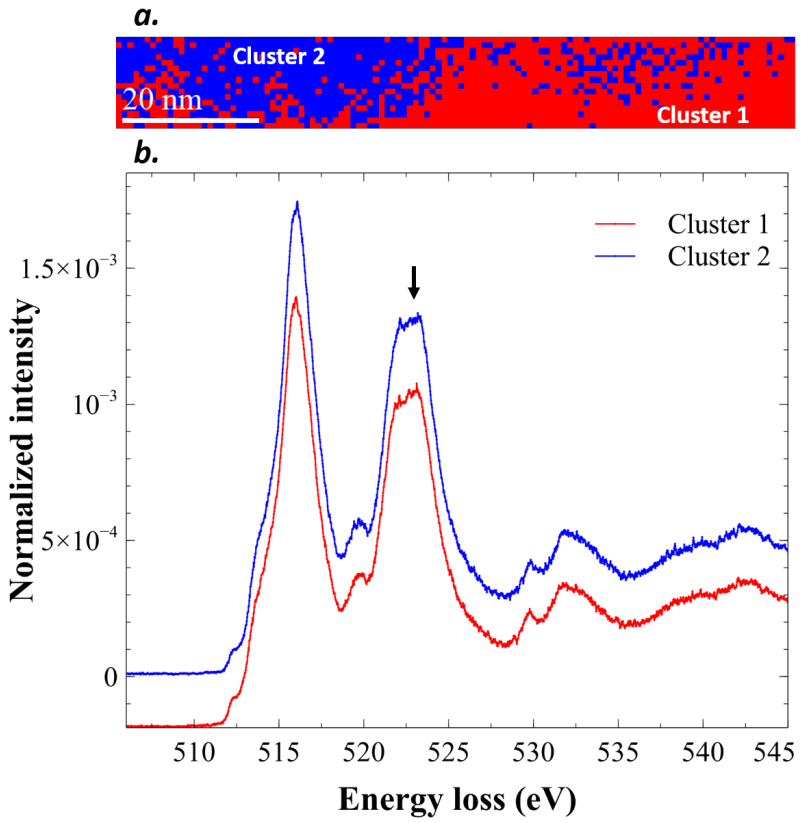

FIGURE B.1: *a*. Map obtained by K-means clustering in a slice of the thin film, with 2 clusters. *b*. Spectra corresponding to the different clusters. A small change in shape on the V-L_2 edge is also observed.

Appendix C

Background subtraction by a power law and signal integration for chemical mapping in the core-loss region.

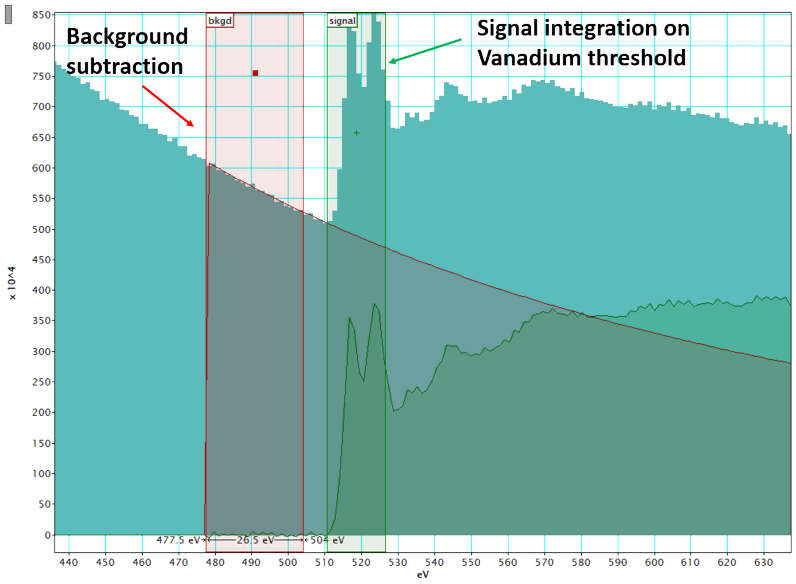

FIGURE C.1: Core-loss spectrum showing background subtraction and signal integration (on the V-$L_{2,3}$ edge) for chemical mapping.

Appendix D

Maps and spectra associated with the PCA decomposition, inspected for spim denoising.

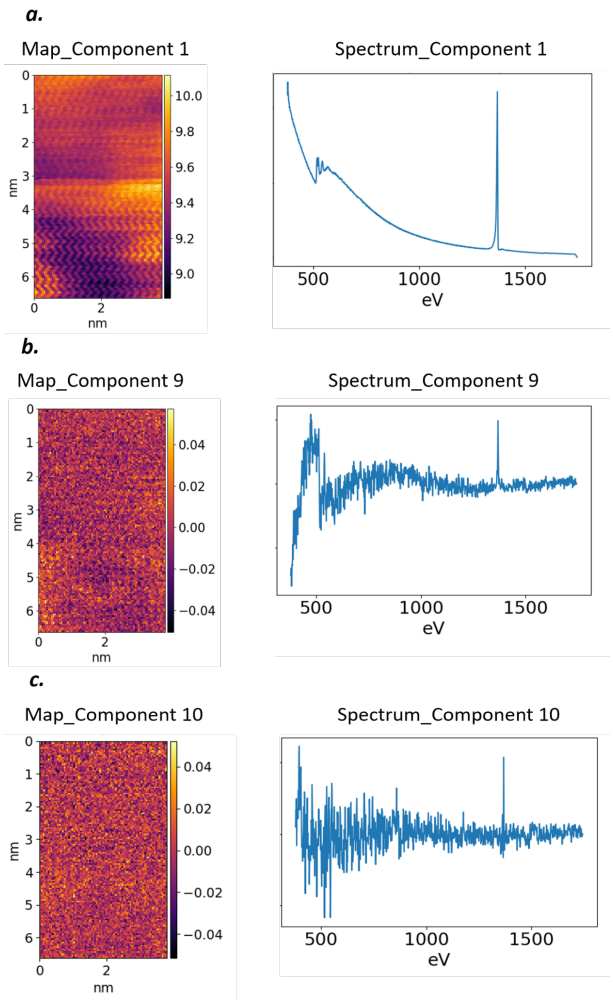

FIGURE D.1: Maps and spectra (region F) of the PCA decomposition for : *a*. the first principal component. *b*. the 9th principal component. *c*. the 10th principal component. There is almost only noise for this component. The signal is recomposed, taking into account only the first 9 principal components.

Appendix E

Fit of the spectrum acquired in the interfacial region during heating and results of the NMF decomposition applied in this region.

E.1 . Spectroscopic signature in the interfacial region fitted from the spectrum in the PM region (homogeneous HAADF contrast) and the spectrum in the coexistence stripy region (AFI + PI-like phase)

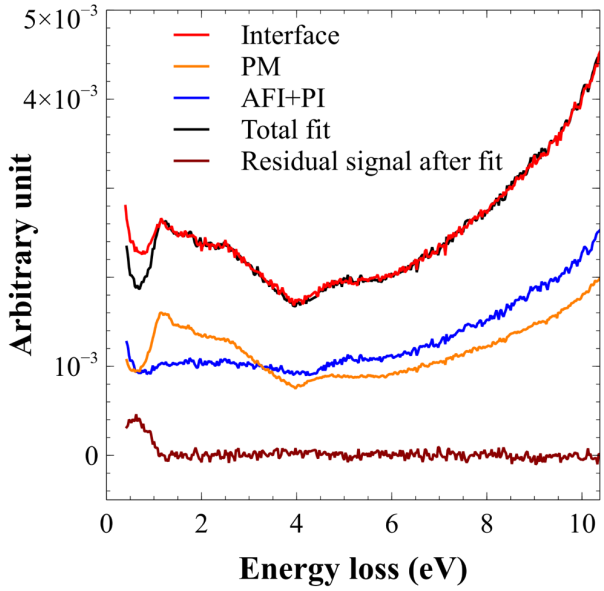

FIGURE E.1: Fit of the interfacial spectroscopic signature with PM and AFI+PI spectra. The fit obtained is not in good agreement with the interfacial spectrum, particularly under 1 eV.

E.2 . NMF decomposition applied to a spim acquired across the interfacial region during heating.

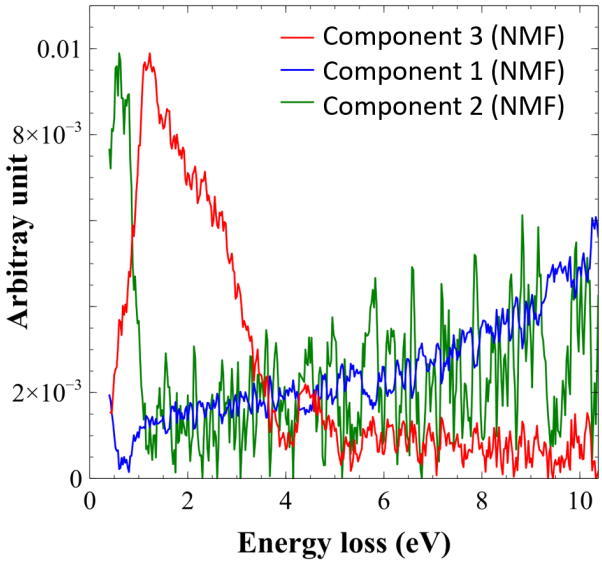

FIGURE E.2: NMF components obtained in the interfacial region, before binning.

Bibliography

1. Morosan, E., Natelson, D., Nevidomskyy, A. H. & Si, Q. Strongly Correlated Materials. *Advanced Materials* **24,** 4896–4923. ISSN: 1521-4095 (2012).
2. McWhan, D. B. & Remeika, J. P. Metal-Insulator Transition in $(V_{1-x}Cr_x)_2O_3$. *Physical Review B* **2,** 3734–3750 (Nov. 1970).
3. McWhan, D. B., Menth, A., Remeika, J. P., Brinkman, W. F. & Rice, T. M. Metal-Insulator Transitions in Pure and Doped V_2O_3. *Physical Review B* **7,** 1920–1931 (Mar. 1973).
4. McWhan, D. B., Rice, T. M. & Remeika, J. P. Mott Transition in Cr-Doped V_2O_3. *Physical Review Letters* **23,** 1384–1387 (Dec. 1969).
5. Lupi, S. *et al.* A Microscopic View on the Mott Transition in Chromium-Doped V_2O_3. *Nature Communications* **1,** 105. ISSN: 2041-1723 (Nov. 2010).
6. McLeod, A. S. *et al.* Nanotextured Phase Coexistence in the Correlated Insulator V_2O_3. *Nature Physics* **13,** 80–86. ISSN: 1745-2481 (Jan. 2017).
7. Kalcheim, Y. *et al.* Robust Coupling between Structural and Electronic Transitions in a Mott Material. *Physical Review Letters* **122,** 057601 (Feb. 2019).
8. Bocher, L. *et al.* Atomic and Electronic Structure of the $BaTiO_3$/Fe Interface in Multiferroic Tunnel Junctions. *Nano Letters* **12,** 376–382. ISSN: 1530-6984 (Jan. 2012).
9. Valencia, S. *et al.* Interface-Induced Room-Temperature Multiferroicity in $BaTiO_3$. *Nature Materials* **10,** 753–758. ISSN: 1476-4660 (Oct. 2011).
10. Popova, E. *et al.* Bismuth Iron Garnet $Bi_3Fe_5O_12$: A Room Temperature Magnetoelectric Material. *Applied Physics Letters* **110,** 142404. ISSN: 0003-6951 (Apr. 2017).
11. Hébert, S. *et al.* From Oxides to Selenides and Sulfides: The Richness of the CdI_2 Type Crystallographic Structure for Thermoelectric Properties. *physica status solidi (a)* **210,** 69–81. ISSN: 1862-6319 (2013).
12. Dillemans, L. *et al.* Evidence of the Metal-Insulator Transition in Ultrathin Unstrained V_2O_3 Thin Films. *Applied Physics Letters* **104,** 071902. ISSN: 0003-6951 (Feb. 2014).

13. Krivanek, O. L., Lovejoy, T. C., Dellby, N. & Carpenter, R. Monochromated STEM with a 30 meV-wide, Atom-Sized Electron Probe. *Microscopy* **62,** 3–21. ISSN: 2050-5698 (Feb. 2013).

14. El Baggari, I. *et al.* Nature and Evolution of Incommensurate Charge Order in Manganites Visualized with Cryogenic Scanning Transmission Electron Microscopy. *Proceedings of the National Academy of Sciences* **115,** 1445–1450 (Feb. 2018).

15. Goodge, B. H., Bianco, E., Schnitzer, N., Zandbergen, H. W. & Kourkoutis, L. F. Atomic-Resolution Cryo-STEM Across Continuously Variable Temperatures. *Microscopy and Microanalysis* **26,** 439–446. ISSN: 1431-9276, 1435-8115 (June 2020).

16. Gebhard, F. *The Mott Metal-Insulator Transition: Models and Methods* ISBN: 978-3-540-61481-4 978-3-540-14858-6 (Springer, Berlin, Heidelberg, 1997).

17. Pavarini, E., Koch, E., Scalettar, R. & Martin, R. *The Physics of Correlated Insulators, Metals, and Superconductors Schriften Des Forschungszentrums Jülich. Reihe Modeling and Simulation* **7.** ISBN: 978-3-95806-224-5 (Forschungszentrum Jülich GmbH Zentralbibliothek, Verlag, Jülich, 2017).

18. Rodolakis, F. *Spectroscopies à l'aide du rayonnement synchrotron appliquées aux systèmes fortement corrélés : Transition métal-isolant dans les oxydes de vanadium* PhD thesis (Université Paris Sud - Paris XI, Dec. 2009).

19. Imada, M., Fujimori, A. & Tokura, Y. Metal-Insulator Transitions. *Reviews of Modern Physics* **70,** 1039–1263 (Oct. 1998).

20. Hubbard, J. & Flowers, B. H. Electron Correlations in Narrow Energy Bands. *Proceedings of the Royal Society of London. Series A. Mathematical and Physical Sciences* **276,** 238–257 (Nov. 1963).

21. Hubbard, J. & Flowers, B. H. Electron Correlations in Narrow Energy Bands. II. The Degenerate Band Case. *Proceedings of the Royal Society of London. Series A. Mathematical and Physical Sciences* **277,** 237–259 (Jan. 1964).

22. Hubbard, J. & Flowers, B. H. Electron Correlations in Narrow Energy Bands III. An Improved Solution. *Proceedings of the Royal Society of London. Series A. Mathematical and Physical Sciences* **281,** 401–419 (Sept. 1964).

23. Fotso, H. F., Tam, K.-M. & Moreno, J. Beyond Quantum Cluster Theories: Multiscale Approaches for Strongly Correlated Systems. *Quantum Science and Technology* **7,** 033001. ISSN: 2058-9565 (May 2022).

24. Pavarini, E., Koch, E., Lichtenstein, A. & Vollhardt, D. *The LDA+DMFT Approach to Strongly Correlated Materials Schriften Des Forschungszentrums Jülich. Reihe Modeling and Simulation* **1** (Forschungszenrum Jülich GmbH Zentralbibliothek, Verlag, Jülich, 2011).

25. Mansart, B. *Dynamique des électrons et des phonons dans les systèmes fortement corrélés : transition de Mott dans V_2O_3 et supraconductivité dans les pnictures de fer* PhD thesis (Université Paris Sud - Paris XI, Oct. 2010).

26. Lieb, E. H. & Wu, F. Y. Absence of Mott Transition in an Exact Solution of the Short-Range, One-Band Model in One Dimension. *Physical Review Letters* **20,** 1445–1448 (June 1968).

27. Georges, A., Kotliar, G., Krauth, W. & Rozenberg, M. J. Dynamical Mean-Field Theory of Strongly Correlated Fermion Systems and the Limit of Infinite Dimensions. *Reviews of Modern Physics* **68,** 13–125 (Jan. 1996).

28. Georges, A. & Kotliar, G. Hubbard Model in Infinite Dimensions. *Physical Review B* **45,** 6479–6483 (Mar. 1992).

29. Kotliar, G. & Vollhardt, D. Strongly Correlated Materials: Insights From Dynamical Mean-Field Theory. *Physics Today* **57,** 53–59. ISSN: 0031-9228 (Mar. 2004).

30. Mo, S.-K. *et al.* Prominent Quasiparticle Peak in the Photoemission Spectrum of the Metallic Phase of V_2O_3. *Physical Review Letters* **90,** 186403 (May 2003).

31. Grotendorst, J., Marx, D. & Muramatsu, A. *Quantum Simulations of Complex Many-Body Systems: From Theory to Algorithms, Lecture Notes ; Winter School, 25 February - 1 March 2002, Rolduc Conference Centre, Kerkrade, The Netherlands NIC Series* **10.** ISBN: 978-3-00-009057-8 (John von Neumann Institute for Computing, Jülich, 2002).

32. Grygiel, C. *Etude multi-échelle de la transition métal-isolant de films minces du composé V_2O_3* PhD thesis (Université de Caen, Sept. 2008).

33. Dernier, P. D. & Marezio, M. Crystal Structure of the Low-Temperature Antiferromagnetic Phase of V_2O_3. *Physical Review B* **2,** 3771–3776 (Nov. 1970).

34. Moon, R. M. Antiferromagnetism in V_2O_3. *Journal of Applied Physics* **41,** 883–883. ISSN: 0021-8979 (Mar. 1970).

35. Hassan, S. R., Georges, A. & Krishnamurthy, H. R. Sound Velocity Anomaly at the Mott Transition: Application to Organic Conductors and V_2O_3. *Physical Review Letters* **94,** 036402 (Jan. 2005).

36. Rodolakis, F. *et al.* Inequivalent Routes across the Mott Transition in V_2O_3 Explored by X-Ray Absorption. *Physical Review Letters* **104,** 047401 (Jan. 2010).

37. Ueda, Y., Kosuge, K. & Kachi, S. Phase Diagram and Some Physical Properties of V_2O_{3+x}($0 \leq x \leq 0.080$). *Journal of Solid State Chemistry* **31,** 171–188. ISSN: 0022-4596 (Feb. 1980).

38. Andreev, V. N. & Klimov, V. A. Effects of Electron Localization in $V_{2-y}O_3$. *Physics of the Solid State* **48,** 2328–2331. ISSN: 1090-6460 (Dec. 2006).

39. Rúa, A. *et al.* Toward Reproducible Metal-Insulator Transition Characteristics in V_2O_3 Thin Films Sputter-Deposited on Glass. *Journal of Applied Physics* **124,** 205301. ISSN: 0021-8979 (Nov. 2018).

40. Brockman, J. *et al.* Increased Metal-Insulator Transition Temperatures in Epitaxial Thin Films of V_2O_3 Prepared in Reduced Oxygen Environments. *Applied Physics Letters* **98,** 152105. ISSN: 0003-6951 (Apr. 2011).

41. Yang, H., Sladek, R. J. & Harrison, H. R. Shear Elastic Constant Softening in $(V_{1-x}Cr_x)_2O_3$: Second-order Nature of the Low Temperature Phase Transition. *Solid State Communications* **47,** 955–957. ISSN: 0038-1098 (Sept. 1983).

42. Yethiraj, M., Werner, S. A., Yelon, W. B. & Honig, J. M. Phonon Anomalies and the Magnetic Transition in Pure and Cr-doped V_2O_3. *Physical Review B* **36,** 8675–8686 (Dec. 1987).

43. Mouhat, F. & Coudert, F.-X. Necessary and Sufficient Elastic Stability Conditions in Various Crystal Systems. *Physical Review B* **90,** 224104 (Dec. 2014).

44. Yethiraj, M. Pure and Doped Vanadium Sesquioxide: A Brief Experimental Review. *Journal of Solid State Chemistry* **88,** 53–69. ISSN: 0022-4596 (Sept. 1990).

45. Carter, S. A. *et al.* Magnetic and Transport Studies of Pure V_2O_3 under Pressure. *Physical Review B* **49,** 7898–7903 (Mar. 1994).

46. Nateprov, A. *Investigation of Growth, Structural and Electronic Properties of V_2O_3 Thin Films on Selected Substrates* PhD thesis (Universität Augsburg, Aug. 2006).

47. Castellani, C., Natoli, C. R. & Ranninger, J. Insulating Phase of V_2O_3: An Attempt at a Realistic Calculation. *Physical Review B* **18,** 4967–5000 (Nov. 1978).

48. Thees, M. *et al.* Imaging the Itinerant-to-Localized Transmutation of Electrons across the Metal-to-Insulator Transition in V_2O_3. *Science Advances* **7,** eabj1164 (Nov. 2021).

49. Park, J.-H. *et al.* Spin and Orbital Occupation and Phase Transitions in V_2O_3. *Physical Review B* **61,** 11506–11509 (May 2000).

50. Keller, G., Held, K., Eyert, V., Vollhardt, D. & Anisimov, V. I. Electronic Structure of Paramagnetic V_2O_3: Strongly Correlated Metallic and Mott Insulating Phase. *Physical Review B* **70,** 205116 (Nov. 2004).

51. Poteryaev, A. I. *et al.* Enhanced Crystal-Field Splitting and Orbital-Selective Coherence Induced by Strong Correlations in V_2O_3. *Physical Review B* **76,** 085127 (Aug. 2007).

52. Mo, S.-K. *et al.* Photoemission Study of $(V_{1-x}M_x)_2O_3$ $(M = Cr, Ti)$. *Physical Review B* **74,** 165101 (Oct. 2006).

53. Guo, Y., Clark, S. J. & Robertson, J. Calculation of Metallic and Insulating Phases of V_2O_3 by Hybrid Density Functionals. *The Journal of Chemical Physics* **140,** 054702. ISSN: 0021-9606 (Feb. 2014).

54. Thomas, G. A. *et al.* Observation of the Gap and Kinetic Energy in a Correlated Insulator. *Physical Review Letters* **73,** 1529–1532 (Sept. 1994).

55. Qazilbash, M. M. *et al.* Electrodynamics of the Vanadium Oxides VO_2 and V_2O_3. *Physical Review B* **77,** 115121 (Mar. 2008).

56. Frenkel, A. I., Stern, E. A. & Chudnovsky, F. A. Local Structure Changes in V_2O_3 below and above the Metal-Insulator Transition. *Solid State Communications* **102,** 637–641. ISSN: 0038-1098 (June 1997).

57. Pfalzer, P., Obermeier, G., Klemm, M., Horn, S. & denBoer, M. L. Structural Precursor to the Metal-Insulator Transition in V_2O_3. *Physical Review B* **73,** 144106 (Apr. 2006).

58. Majid, S. S. *et al.* Stabilization of Metallic Phase in V_2O_3 Thin Film. *Applied Physics Letters* **110,** 173101. ISSN: 0003-6951 (Apr. 2017).

59. Frandsen, B. A. *et al.* Intertwined Magnetic, Structural, and Electronic Transitions in V_2O_3. *Physical Review B* **100,** 235136 (Dec. 2019).

60. Trastoy, J. *et al.* Magnetic Field Frustration of the Metal-Insulator Transition in V_2O_3. *Physical Review B* **101,** 245109 (June 2020).

61. Fletcher, E. R. A., Higashi, K., Kalcheim, Y., Kageyama, H. & Frandsen, B. A. Uniform Structural Phase Transition V_2O_3 without Short-Range Distortions of the Local Structure. *Physical Review B* **104,** 184115 (Nov. 2021).

62. Leiner, J. C. *et al.* Frustrated Magnetism in Mott Insulating $(V_{1-x}Cr_x)_2O_3$. *Physical Review X* **9,** 011035 (Feb. 2019).

63. Ding, Y. *et al.* Novel High-Pressure Monoclinic Metallic Phase of V_2O_3. *Physical Review Letters* **112,** 056401 (Feb. 2014).

64. Hansmann, P. *et al.* Mott–Hubbard Transition in V_2O_3 Revisited. *physica status solidi (b)* **250,** 1251–1264. ISSN: 1521-3951 (2013).

65. Lechermann, F., Bernstein, N., Mazin, I. I. & Valentí, R. Uncovering the Mechanism of the Impurity-Selective Mott Transition in Paramagnetic V_2O_3. *Physical Review Letters* **121,** 106401 (Sept. 2018).

66. Hu, L. *et al.* Unveiling the Mechanisms of Metal-Insulator Transitions in V_2O_3: The Role of Trigonal Distortion. *Physical Review B* **103,** 085119 (Feb. 2021).

67. Homm, P., Menghini, M., Seo, J. W., Peters, S. & Locquet, J. .-. Room Temperature Mott Metal–Insulator Transition in V_2O_3 Compounds Induced via Strain-Engineering. *APL Materials* **9,** 021116 (Feb. 2021).

68. Polewczyk, V. *et al.* Tuning the Magnetic Properties of $V_2O_3/CoFeB$ Heterostructures across the V_2O_3 Structural Transition. *Physical Review Materials* **5,** 034413 (Mar. 2021).

69. Abe, H. A. H., Terauchi, M. T. M., Tanaka, M. T. M. & Shin, S. S. S. Electron Energy-Loss Spectroscopy Study of the Metal-Insulator Transition in V_2O_3. *Japanese Journal of Applied Physics* **37,** 584. ISSN: 1347-4065 (Feb. 1998).

70. Abe, H. A. H., Terauchi, M. T. M., Tanaka, M. T. M. & Shin, S. S. S. Electron Energy-Loss Spectroscopy Study of the Metal-Insulator Transition in $(V_{1-x}Cr_x)_2O_3$ (X= 0.012). *Japanese journal of applied physics* **38,** 1403 (1999).

71. Müller, O. *et al.* Spectroscopy of Metallic and Insulating V_2O_3. *Physical Review B* **56,** 15056–15061 (Dec. 1997).

72. Janod, E. *et al.* Resistive Switching in Mott Insulators and Correlated Systems. *Advanced Functional Materials* **25,** 6287–6305. ISSN: 1616-3028 (2015).

73. Querré, M. *et al.* Non-Volatile Resistive Switching in the Mott Insulator $(V_{1-x}Cr_x)_2O_3$. *Physica B: Condensed Matter* **536,** 327–330. ISSN: 0921-4526 (May 2018).

74. Stoliar, P. *et al.* A Leaky-Integrate-and-Fire Neuron Analog Realized with a Mott Insulator. *Advanced Functional Materials* **27,** 1604740. ISSN: 1616-3028 (2017).

75. Adda, C. *et al.* Mott Insulators: A Large Class of Materials for Leaky Integrate and Fire (LIF) Artificial Neuron. *Journal of Applied Physics* **124,** 152124. ISSN: 0021-8979 (Oct. 2018).

76. Singer, A. *et al.* Nonequilibrium Phase Precursors during a Photoexcited Insulator-to-Metal Transition in V_2O_3. *Physical Review Letters* **120,** 207601 (May 2018).

77. Ronchi, A. *et al.* Nanoscale Self-Organization and Metastable Non-Thermal Metallicity in Mott Insulators. *Nature Communications* **13,** 3730. ISSN: 2041-1723 (June 2022).

78. Egerton, R. *Electron Energy-Loss Spectroscopy in the Electron Microscope* ISBN: 978-1-4419-9582-7 978-1-4419-9583-4 (Springer US, Boston, MA, 2011).

79. Otero, A. C. *Optics and Structure of Metal Clusters at the Atomic Scale* PhD thesis (Université Paris Saclay (COmUE), Oct. 2018).

80. Morniroli, J.-P. *Large-Angle Convergent-Beam Electron Diffraction Applications to Crystal Defects* (CRC Press, 2004).

81. Brydson, R. *Aberration-Corrected Analytical Transmission Electron Microscopy* (Wiley Online Library, 2011).

82. Teurtrie, A. *Towards a Magnetic Semiconductor Using Ca and Y Co-Substituted Bismuth Iron Garnet Thin Films* PhD thesis (Université Paris Saclay (COmUE), Nov. 2019).

83. Pennycook, S. J. & Nellist, P. D. *Scanning Transmission Electron Microscopy: Imaging and Analysis* (Springer Science & Business Media, 2011).

84. Krivanek, O. L. *et al.* An Electron Microscope for the Aberration-Corrected Era. *Ultramicroscopy* **108,** 179–195. ISSN: 0304-3991 (Feb. 2008).

85. Dellby, N. *et al.* Dedicated STEM for 200 to 40 keV Operation*. *The European Physical Journal - Applied Physics* **54,** 33505. ISSN: 1286-0042, 1286-0050 (June 2011).

86. Gatan. *Spectrum Imaging* https://www.gatan.com/techniques/spectrum-imaging.

87. Auad, Y. *et al.* Event-Based Hyperspectral EELS: Towards Nanosecond Temporal Resolution. *Ultramicroscopy* **239,** 113539. ISSN: 0304-3991 (Sept. 2022).

88. Ballabriga, R. *et al.* Medipix3: A 64k Pixel Detector Readout Chip Working in Single Photon Counting Mode with Improved Spectrometric Performance. *Nuclear Instruments and Methods in Physics Research Section A: Accelerators, Spectrometers, Detectors and Associated Equipment. 11th International Workshop on Radiation Imaging Detectors (IWORID)* **633,** S15–S18. ISSN: 0168-9002 (May 2011).

89. De la Peña Manchón, F. J. *Advanced Methods for Electron Energy Loss Spectroscopy Core-Loss Analysis* These de Doctorat (Paris 11, Jan. 2010).

90. Colliex, C. From Early to Present and Future Achievements of EELS in the TEM. *The European Physical Journal Applied Physics* **97,** 38. ISSN: 1286-0042, 1286-0050 (2022).

91. García de Abajo, F. J. & Kociak, M. Probing the Photonic Local Density of States with Electron Energy Loss Spectroscopy. *Physical Review Letters* **100,** 106804 (Mar. 2008).

92. Howie, A. Image Contrast And Localized Signal Selection Techniques. *Journal of Microscopy* **117,** 11–23. ISSN: 1365-2818 (1979).

93. Gloter, A. *et al.* Atomically Resolved Mapping of EELS Fine Structures. *Materials Science in Semiconductor Processing. Advanced Transmission Electron Microscopy for Semiconductor and Materials Science* **65,** 2–17. ISSN: 1369-8001 (July 2017).

94. de Groot, F. M. F., Fuggle, J. C., Thole, B. T. & Sawatzky, G. A. 2p X-Ray Absorption of 3d Transition-Metal Compounds: An Atomic Multiplet Description Including the Crystal Field. *Physical Review B* **42,** 5459–5468 (Sept. 1990).

95. Sahoo, S. *et al.* Realizing Low-Temperature Charge-Transfer-Type Insulating Ground State in Strained V_2O_3 Thin Film. *ACS Applied Electronic Materials* **4,** 3036–3048 (June 2022).

96. Gries, K. *et al.* Correlation of the Orientation of Stacked Aragonite Platelets in Nacre and Their Connection via Mineral Bridges. *Ultramicroscopy* **109,** 230–236. ISSN: 0304-3991 (Feb. 2009).

97. Houdellier, F. *Contribution Au Développement Du CBED et de l'holographie HREM Pour l'analyse Des Déformations de Couches Épitaxiées* These de Doctorat (Toulouse, INSA, Jan. 2006).

98. *JEMS* https://www.jems-swiss.ch/.

99. Benner, G. & Probst, W. Köhler Illumination in the TEM: Fundamentals and Advantages. *Journal of Microscopy* **174,** 133–142. ISSN: 1365-2818 (1994).

100. Cautaerts, N. *et al.* Free, Flexible and Fast: Orientation Mapping Using the Multi-Core and GPU-accelerated Template Matching Capabilities in the Python-based Open Source 4D-STEM Analysis Toolbox Pyxem. *Ultramicroscopy* **237,** 113517. ISSN: 0304-3991 (July 2022).

101. *Pyxem* https://github.com/pyxem/pyxem. Nov. 2022.

102. Ophus, C. Four-Dimensional Scanning Transmission Electron Microscopy (4D-STEM): From Scanning Nanodiffraction to Ptychography and Beyond. *Microscopy and Microanalysis* **25,** 563–582. ISSN: 1431-9276, 1435-8115 (June 2019).

103. Tyukalova, E. & Duchamp, M. Atomic Resolution Enabled STEM Imaging of Nanocrystals at Cryogenic Temperature. *Journal of Physics: Materials* **3,** 034006. ISSN: 2515-7639 (May 2020).

104. Hÿtch, M. J., Snoeck, E. & Kilaas, R. Quantitative Measurement of Displacement and Strain Fields from HREM Micrographs. *Ultramicroscopy* **74,** 131–146. ISSN: 0304-3991 (Aug. 1998).

105. Zhu, Y., Ophus, C., Ciston, J. & Wang, H. Interface Lattice Displacement Measurement to 1pm by Geometric Phase Analysis on Aberration-Corrected HAADF STEM Images. *Acta Materialia* **61,** 5646–5663. ISSN: 1359-6454 (Sept. 2013).

106. Velazco, A., Nord, M., Béché, A. & Verbeeck, J. Evaluation of Different Rectangular Scan Strategies for STEM Imaging. *Ultramicroscopy* **215,** 113021. ISSN: 0304-3991 (Aug. 2020).

107. Shiga, M. *et al.* Sparse Modeling of EELS and EDX Spectral Imaging Data by Nonnegative Matrix Factorization. *Ultramicroscopy* **170,** 43–59. ISSN: 0304-3991 (Nov. 2016).

108. Li, X. *et al.* Three-Dimensional Vectorial Imaging of Surface Phonon Polaritons. *Science* **371,** 1364–1367 (Mar. 2021).

109. Dobigeon, N. & Brun, N. Spectral Mixture Analysis of EELS Spectrum-Images. *Ultramicroscopy* **120,** 25–34. ISSN: 0304-3991 (Sept. 2012).

110. Nascimento, J. & Dias, J. Vertex Component Analysis: A Fast Algorithm to Unmix Hyperspectral Data. *IEEE Transactions on Geoscience and Remote Sensing* **43,** 898–910. ISSN: 1558-0644 (Apr. 2005).

111. Gloter, A., Douiri, A., Tencé, M. & Colliex, C. Improving Energy Resolution of EELS Spectra: An Alternative to the Monochromator Solution. *Ultramicroscopy. Proceedings of the International Workshop on Strategies and Advances in Atomic Level Spectroscopy and Analysis* **96,** 385–400. ISSN: 0304-3991 (Sept. 2003).

112. Fouetilloux, R., Ferro-Famil, L. & Méric, S. *Amélioration de La Résolution Angulaire d'un Radar FMCW Panoramique* in *Journées URSI, "géolocalisation et Navigation Dans l'espace et Le Temps"* (Meudon, France, Mar. 2018).

113. Egerton, R. F., Qian, H. & Malac, M. Improving the Energy Resolution of X-ray and Electron Energy-Loss Spectra. *Micron* **37,** 310–315. ISSN: 0968-4328 (June 2006).

114. Lazar, S., Botton, G. A. & Zandbergen, H. W. Enhancement of Resolution in Core-Loss and Low-Loss Spectroscopy in a Monochromated Microscope. *Ultramicroscopy. Proceedings of the International Workshop on Enhanced Data Generated by Electrons* **106,** 1091–1103. ISSN: 0304-3991 (Oct. 2006).

115. Torruella, P. *et al.* Clustering Analysis Strategies for Electron Energy Loss Spectroscopy (EELS). *Ultramicroscopy* **185,** 42–48. ISSN: 0304-3991 (Feb. 2018).

116. De la Peña, F. *et al. Hyperspy/Hyperspy: Release v1.7.1* Zenodo. June 2022.

117. Schuler, H., Klimm, S., Weissmann, G., Renner, C. & Horn, S. Influence of Strain on the Electronic Properties of Epitaxial V_2O_3 Thin Films. *Thin Solid Films* **299,** 119–124. ISSN: 0040-6090 (May 1997).

118. *Thin Films and Heterostructures for Oxide Electronics* ISBN: 978-0-387-25802-7 (Springer-Verlag, New York, 2005).

119. Wen, Q., Wei, X., Jiang, F., Lu, J. & Xu, X. Focused Ion Beam Milling of Single-Crystal Sapphire with A-, C-, and M-Orientations. *Materials* **13,** 2871. ISSN: 1996-1944 (Jan. 2020).

120. Homm Jara, P. *Electronic, Structural and Optical Phase Transitions in Strongly Correlated Oxide Thin Films Grown by Molecular Beam Epitaxy* PhD thesis (KU Leuven, Feb. 2019).

121. Matthews, J. W. & Blakeslee, A. E. Defects in Epitaxial Multilayers: I. Misfit Dislocations. *Journal of Crystal Growth* **27,** 118–125. ISSN: 0022-0248 (Dec. 1974).

122. Sakai, J., Limelette, P. & Funakubo, H. Transport Properties and c/a Ratio of V_2O_3 Thin Films Grown on C- and R-plane Sapphire Substrates by Pulsed Laser Deposition. *Applied Physics Letters* **107,** 241901. ISSN: 0003-6951 (Dec. 2015).

123. Ha, J.-H., Kim, H.-W., Jo, Y.-S., Kim, S.-W. & Hong, J.-I. Tunable Metal-Insulator Transition of V_2O_3 Thin Films Strained by Controlled Inclusion of Crystallographic Defect. *Applied Materials Today* **22,** 100984. ISSN: 2352-9407 (Mar. 2021).

124. Babich, D. *et al.* Lattice Contraction Induced by Resistive Switching in Chromium-Doped V_2O_3: A Hallmark of Mott Physics. *arXiv preprint arXiv:2105.05093* (Oct. 2021).

125. Kalinin, S. V. *et al.* Separating Physically Distinct Mechanisms in Complex Infrared Plasmonic Nanostructures via Machine Learning Enhanced Electron Energy Loss Spectroscopy. *Advanced Optical Materials* **9,** 2001808. ISSN: 2195-1071 (2021).

126. Venkatraman, K., Levin, B. D. A., March, K., Rez, P. & Crozier, P. A. Vibrational Spectroscopy at Atomic Resolution with Electron Impact Scattering. *Nature Physics* **15,** 1237–1241. ISSN: 1745-2481 (Dec. 2019).

127. Eccles, J. W. *An Electron Energy Loss Spectroscopy Study of Metallic Nanoparticles of Gold and Silver* (The University of Manchester (United Kingdom), 2010).

128. Bosman, M. *et al.* Encapsulated Annealing: Enhancing the Plasmon Quality Factor in Lithographically–Defined Nanostructures. *Scientific Reports* **4,** 5537. ISSN: 2045-2322 (July 2014).

129. Pfalzer, P. *et al.* Local Symmetry Breaking in Paramagnetic Insulating $(Al, V)_2O_3$. *Physical Review B* **66,** 085119 (Aug. 2002).

130. Stewart, M. K. *et al.* Insulator-to-Metal Transition and Correlated Metallic State of V_2O_3 Investigated by Optical Spectroscopy. *Physical Review B* **85,** 205113 (May 2012).

131. Andreev, V. N. & Chudnovskii, F. A. Cause and prevention of fracture of V_2O_3 single crystals due to metal-semiconductor phase transition. *Soviet physics. Solid state* **17,** 1966 (1976).

132. Cowley, J. M. & Spence, J. C. H. Convergent Beam Electron Microdiffraction from Small Crystals. *Ultramicroscopy* **6,** 359–366. ISSN: 0304-3991 (Jan. 1981).

133. Rodolakis, F. *et al.* Evolution of the Electronic Structure of a Mott System across Its Phase Diagram: X-ray Absorption Spectroscopy Study of $(V_{1-x}Cr_x)_2O_3$. *Physical Review B* **84,** 245113 (Dec. 2011).

134. Ishiwata, Y. *et al.* Corundum Insulating Phases in Highly Ti-doped V_2O_3 Nanocrystals. *Physical Review B* **101,** 035415 (Jan. 2020).

135. Van Landuyt, J., Amelinckx, S. & Remeika, J. P. Domain Formation Accompanying the Metal-Insulator Transition in $V_{2-x}Cr_xO_3$. *Materials Research Bulletin* **7,** 845–856. ISSN: 0025-5408 (Aug. 1972).

136. Howe, J. M. in *Physical Metallurgy (Fifth Edition)* (eds Laughlin, D. E. & Hono, K.) 1317–1451 (Elsevier, Oxford, Jan. 2014). ISBN: 978-0-444-53770-6.

137. Couillard, M., Yurtsever, A. & Muller, D. A. Competition between Bulk and Interface Plasmonic Modes in Valence Electron Energy-Loss Spectroscopy of Ultrathin SiO_2 Gate Stacks. *Physical Review B* **77,** 085318 (Feb. 2008).

138. Howie, A. Valence Excitations in Electron Microscopy: Resolved and Unresolved Issues. *Micron. Zeitler Festschrift* **34,** 121–125. ISSN: 0968-4328 (Apr. 2003).

139. Ronchi, A. *et al.* Early-Stage Dynamics of Metallic Droplets Embedded in the Nanotextured Mott Insulating Phase of V_2O_3. *Physical Review B* **100,** 075111 (Aug. 2019).

140. Chudnovskii, F. A. *et al.* Acoustic Emission during Metal–Insulator Phase Transition in V_2O_3. *Journal of Solid State Chemistry* **133,** 430–433. ISSN: 0022-4596 (Nov. 1997).

141. Rychetský, I. Deformation of Crystal Surfaces in Ferroelastic Materials Caused by Antiphase Domain Boundaries. *Journal of Physics: Condensed Matter* **9,** 4583. ISSN: 0953-8984 (June 1997).

142. Studer, P. *et al.* Model System for Controlling Strain in Silicon at the Atomic Scale. *Physical Review B* **84,** 041306 (July 2011).

143. Abreu, E. *et al.* Dynamic Conductivity Scaling in Photoexcited V_2O_3 Thin Films. *Physical Review B* **92,** 085130 (Aug. 2015).

144. Babich, D. *Electron-Lattice Coupling at the Mott Transition Driven by Electric and/or by Light Pulse* These de Doctorat (Nantes, Dec. 2020).